Mapping Earth Surface Deformation using New Time Series Satellite Radar Interferometry

Author:
Du, Zheyuan

Publication Date:
2017

DOI:
https://doi.org/10.26190/unsworks/20454

Mapping Earth Surface Deformation using New Time Series Satellite Radar Interferometry

By

Zheyuan Du

A thesis submitted to The University of New South Wales in partial fulfilment of the requirements for the degree of Doctor of Philosophy

Geoscience and Earth Observing Systems Group (GEOS)
School of Civil and Environmental Engineering
Faculty of Engineering
The University of New South Wales
Sydney, NSW 2052, Australia

August 2017

PLEASE TYPE

THE UNIVERSITY OF NEW SOUTH WALES
Thesis/Dissertation Sheet

Surname or Family name: **DU**

First name: **ZHEYUAN**

Other name/s:

Abbreviation for degree as given in the University calendar: **PhD**

School: **School of Civil and Environmental Engineering**

Faculty: **Faculty of Engineering**

Title: **Mapping Earth Surface Deformation Using New Time Series Satellite Radar Interferometry**

Abstract 350 words maximum: (PLEASE TYPE)

Land subsidence is an environmental, geological phenomenon that often refers to gradual settling or rapid sinking of the ground surface as a result of subsurface movement of earth materials. Satellite-based interferometric synthetic aperture radar (InSAR) has been proved to be an excellent technique for monitoring the subsidence at various temporal and spatial scales. Differential Interferometric Synthetic Aperture Radar (DInSAR) method has been used to observe such events over the past three decades. However, its result can be affected by spatial/temporal decorrelation and atmospheric disturbance. In recent decade, Time Series InSAR (TS-InSAR) was proposed to minimise these biases by taking advantage of the principle of temporal and spatial statistical analysis. Nevertheless, TS-InSAR has issues due to the tropospheric stratification in high elevation regions and insufficient measurement pixels over rapid subsiding zones.

This dissertation mainly focused on optimisation of the TSInSAR-based technique for land subsidence measuring induced by the extraction of natural resources, such as coal, coalbed methane (CBM) and groundwater. Firstly, TS-InSAR has the problem dealing with the rapid surface subsidence and consequently gaps would appear in such areas. A new method has been proposed to fill these gaps by integrating DInSAR and TS-InSAR. Secondly, ALOS-1 PALSAR and ENVISAT ASAR based TS-InSAR has been conducted to monitor the subsidence over underground mining regions. Nevertheless, the result of the counterpart ENVISAT failed to produce reasonable outcome due to the underground mining effect. An approach has been developed and implemented to address this issue through an IDW (Inverse Distance Weighted)-based integration method. Thirdly, TS-InSAR was being exploited to monitor groundwater and CBM extraction induced subsidence in Beijing Municipality and Liulin County, respectively, by taking both tropospheric stratification and turbulence into consideration. Good correlations were observed between InSAR and levelling derived measurements. Fourthly, Gravity Recovery and Climate Experiment (GRACE) is a joint scientific project between NASA and DLR, which can be used to monitor the groundwater depletion rate. Given the fact that TSInSAR-derived result and GRACE-based outcome have a vast difference in spatial resolution, i.e. GRACE (~ 300 km) vs. TS-InSAR (~ 10 meters), a solution to combine both measurements has been suggested.

ORIGINALITY STATEMENT

‘I hereby declare that this submission is my own work and to the best of my knowledge it contains no materials previously published or written by another person, or substantial proportions of material which have been accepted for the award of any other degree or diploma at UNSW or any other educational institution, except where due acknowledgement is made in the thesis. Any contribution made to the research by others, with whom I have worked at UNSW or elsewhere, is explicitly acknowledged in the thesis. I also declare that the intellectual content of this thesis is the product of my own work, except to the extent that assistance from others in the project's design and conception or in style, presentation and linguistic expression is acknowledged.’

Signed ……………………………………………..............

Date ……………………………………………..............

COPYRIGHT STATEMENT

‘I hereby grant the University of New South Wales or its agents the right to archive and to make available my thesis or dissertation in whole or part in the University libraries in all forms of media, now or here after known, subject to the provisions of the Copyright Act 1968. I retain all proprietary rights, such as patent rights. I also retain the right to use in future works (such as articles or books) all or part of this thesis or dissertation.

I also authorise University Microfilms to use the 350 word abstract of my thesis in Dissertation Abstract International (this is applicable to doctoral theses only).

I have either used no substantial portions of copyright material in my thesis or I have obtained permission to use copyright material; where permission has not been granted I have applied/will apply for a partial restriction of the digital copy of my thesis or dissertation.'

Signed ……………………………………………...........................

Date ……………………………………………...........................

AUTHENTICITY STATEMENT

‘I certify that the Library deposit digital copy is a direct equivalent of the final officially approved version of my thesis. No emendation of content has occurred and if there are any minor variations in formatting, they are the result of the conversion to digital format.’

Signed ……………………………………………...........................

Date ……………………………………………...........................

Abstract

Land subsidence is an environmental, geological phenomenon that often refers to gradual settling or rapid sinking of the ground surface as a result of subsurface movement of earth materials. Satellite-based interferometric synthetic aperture radar (InSAR) has been proved to be an excellent technique for monitoring the subsidence at various temporal and spatial scales.

Differential Interferometric Synthetic Aperture Radar (DInSAR) method has been used to observe such events over the past three decades. However, its result can be affected by spatial/temporal decorrelation and atmospheric disturbance. In recent decade, Time Series InSAR (TS-InSAR) was proposed to minimise these biases by taking advantage of the principle of temporal and spatial statistical analysis. Nevertheless, TS-InSAR has issues due to the tropospheric stratification in high elevation regions and insufficient measurement pixels over rapid subsiding zones.

This dissertation mainly focused on optimisation of the TSInSAR-based technique for land subsidence measuring induced by the extraction of natural resources, such as coal, coalbed methane (CBM) and groundwater. Firstly, TS-InSAR has the problem dealing with the rapid surface subsidence and consequently gaps would appear in such areas. A new method has been proposed to fill these gaps by integrating DInSAR and TS-InSAR. Secondly, ALOS-1 PALSAR and ENVISAT ASAR based TS-InSAR has been conducted to monitor the subsidence over underground mining regions. Nevertheless, the result of the counterpart ENVISAT failed to produce reasonable outcome due to the underground mining effect. An approach has been developed and implemented to address this issue through an IDW (Inverse Distance Weighted)-based integration method. Thirdly, TS-InSAR was being exploited to monitor groundwater and CBM extraction induced subsidence in Beijing Municipality and Liulin County, respectively, by taking both tropospheric stratification and turbulence into consideration. Good correlations were observed between InSAR and levelling derived measurements. Indeed, by applying several established TS-InSAR techniques to different areas, and these significant findings

from the TS-InSAR analysis have led to new insights into the processes causing the deformation.

List of Abbreviations

ALOS	Advanced Land Observation Satellite
APS	Atmospheric Phase Screen
ASAR	Advanced Synthetic Aperture Radar
ASI	Italian Space Agency
CSA	Canadian Space Agency
DEM	Digital Elevation Model
DInSAR	Differential Interferometric Synthetic Aperture Radar
DLR	German Aerospace Center
DS	Distributed Scatterer
ECMWF	European Centre for Medium-Range Weather Forecasts
ESA	European Space Agency
ENVISAT	Environmental Satellite
ERSDAC	Earth Remote Sensing Data Analysis Center
ERS	European Remote Sensing
EWH	Equivalent Water Height
FBD	Fine beam dual-polarisation
FBS	Fine beam single-polarisation
FFT	Fast Fourier Transform
GAM	Global Atmospheric Model
GIS	Geographic Information Science
GLDAS	Global Land Data Assimilation System
GPS	Global Positioning System
GRACE	Gravity Recovery and Climate Experiment
GWS	ground water storage
IFG	Interferogram
InSAR	Interferometric Synthetic Aperture Radar
IWS	Interferometric Wide Swath
JAXA	Japan Aerospace Exploration Agency
LAMBDA	Least-squares AMBiguity Decorrelation Adjustment
LANDSAT	Land Remote-Sensing Satellite
LOS	Line of Sight

MCF	Maximum Cost Flow
MERIS	Medium Resolution Imaging Spectrometer
MERRA	Modern Era-Retrospective Analysis
MODIS	Moderate-Resolution Imaging Spectroradiometer
MS	Measurement Scatterer
MSE	Mean Square Error
NARR	North American Regional Reanalysis
NASA	National Aeronautics and Space Administration
PS	Persistent Scatterer
PSI	Persistent Scatterer Interferometry
PALSAR	Phased Array type L-band Synthetic Aperture Radar
RADARSAT	Radar Satellite
RMSE	Root Mean Square Errors
ROI	Region of Interest
SRTM	Shuttle Radar Topography Mission
SIS	snow and ice storage
SLC	Single Look Complex
SAR	Synthetic Aperture Radar
SBAS	Short Baseline Subset
SMS	soil moisture storage
SNR	Signal-to-Noise Ratio
SVD	Singular Value Decomposition
TSInSAR	Time Series Interferometric SAR
TWS	total water storage

Acknowledgements

This research was conducted in the Geoscience and Earth Observing Systems Group (GEOS), School of Civil and Environmental Engineering at the University of New South Wales (UNSW Australia), Sydney, Australia from August 2014 to August 2017 under the supervision of Associate Professor Linlin Ge and Dr Xiaojing Li. They have been encouraging, inspirational, and have challenged me to think through research ideas in various ways that I would never imagine by myself. I am very thankful for their gentle guidance and reassurance on supporting this work that makes this journey so enjoyable.

I would like to express my thanks to our current and former GEOS group members, including Liam Liyuan Li, Tim Youtian Liu, Associate Professor Kubic Kui Zhang, Dr Alex Zhe Hu, Dr Henry Yan Wang, for numerous discussions. Particularly, I would like to thank Associate Professor Alex Hay-Man Ng, a mentor and a good friend of mine, for sharing his knowledge in the field of radar interferometry. He is always there whenever I needed advice, and he is truly an inspiration for me. I would not achieve that much without his help. I would also like to acknowledge the assistance of Dr Yincai Zhou, Dr Craig Roberts, Gwyn Jones, and Dr Scott Hensley. Also, I would like to thank reviewers for their valuable suggestions.

The Earth Remote Sensing Data Analysis Centre is acknowledged for providing the ALOS-1 PALSAR and ALOS-2 PALSAR data. METI and JAXA retain the ownership of the ALOS-1/2 PALSAR original data. The European Space Agency is acknowledged for providing data from the ENVISAT ASAR and Sentinel-1 missions. The Canadian Space Agency is acknowledging for providing data from the RADARSAT-2 mission.

Finally, I would like to express my sincere gratitude to my parents, my uncles and aunts, my grandparents and girlfriend Esther Qinggaozi Zhu for their emotional support. Thanks to all the people who love me and whom I love.

List of Publications

Several journal and conference papers have been accepted for publishing, published or submitted during the journey of research study. The publication list is shown as follows:

Journal Papers:

Du, Z., Ge, L., Ng, A.H.M., Zhu, Q., Yang, X. and Li, L., 2018. Correlating the subsidence pattern and land use in Bandung, Indonesia with both Sentinel-1/2 and ALOS-2 satellite images. *International Journal of Applied Earth Observation and Geoinformation*, *67*, pp.54-68.

Du, Z., Ge, L., Ng, A.H.M., Li, X. and Li, L., 2018. Investigation on mining subsidence over Appin-West Cliff Colliery using time-series SAR interferometry. *International Journal of Remote Sensing*, 39, 1528-1547.

Ge, L., Ng, A.H.M., **Du, Z**., Chen, H.Y. and Li, X., 2017. Integrated space geodesy for mapping land deformation over Choushui River Fluvial Plain, Taiwan. *International Journal of Remote Sensing*, *38*(22), pp.6319-6345.

Du, Z., Ge, L., Ng, A.H.M., Xiaojing, L. and Li, L., 2017. Mapping land subsidence over the eastern Beijing city using satellite radar interferometry. *International Journal of Digital Earth*, pp.1-16.

Ng, A.H.M., Ge, L., **Du, Z**., Wang, S. and Ma, C., 2017. Satellite radar interferometry for monitoring subsidence induced by longwall mining activity using Radarsat-2, Sentinel-1 and ALOS-2 data. *International Journal of Applied Earth Observation and Geoinformation*, *61*, pp.92-103.

Du, Z., Ge, L., Ng, A.H.M., Li, X. and Li, L., 2017. Monitoring of ground deformation in Liulin district, China using InSAR approaches. *International Journal of Digital Earth*, pp.1-20.

Du, Z., Ge, L., Li, X. and Ng, A.H.M., 2016. Subsidence monitoring over the Southern Coalfield, Australia using both L-Band and C-Band SAR time series analysis. *Remote Sensing*, *8*(7), p.543-559.

Du, Z., Ge, L., Li, X. and Ng, A.H.M., 2016. Subsidence monitoring in the Ordos basin using integrated SAR differential and time-series interferometry techniques. *Remote Sensing Letters*, *7*(2), pp.180-189.

Ge, L., Ng, A.H.M., Li, X., Liu, Y., **Du, Z**. and Liu, Q., 2015. Near real-time satellite mapping of the 2015 Gorkha earthquake, Nepal. *Annals of GIS*, *21*(3), pp.175-190.

Conference Papers:

Du, Z. Ge, L., Ng, A.H.M. and Li, X., 2017, July. Ground Deformation Monitoring in Beijing using both Sentinel and ALOS. In *Geoscience and Remote Sensing Symposium (IGARSS), 2017 IEEE International* (in press). IEEE.

Du, Z. Ge, L., Ng, A.H.M. and Li, X., 2017, July. An Innovative Distributed Scatterer based Time-Series InSAR method over underground mining region. In *Geoscience and Remote Sensing Symposium (IGARSS), 2017 IEEE International* (in press). IEEE.

Du, Z., Ge, L., Ng, A.H.M. and Li, X., 2016, July. Time series interferometry integrated with groundwater depletion measurement from GRACE. In *Geoscience and Remote Sensing Symposium (IGARSS), 2016 IEEE International* (pp. 1166-1169). IEEE.

Du, Z., Ge, L., Ng, A.H.M. and Li, X., 2016, July. Three dimensional subsidence monitoring in the south of Sydney. In *Geoscience and Remote Sensing Symposium (IGARSS), 2016 IEEE International* (pp. 1186-1189). IEEE.

Du, Z., Ge, L., Li, X. and Ng, A.H.M., 2015, July. Land subsidence characteristics of Ordos using differential interferometry and persistent scatterer interferometry. In *Geoscience and Remote Sensing Symposium (IGARSS), 2015 IEEE International* (pp. 314-317). IEEE.

Du, Z., Ge, L., Li, X., & Ng, A. H. M. 2015. Improving Differential Interferometry using Global Atmospheric Models. In *2015 Australian Space Research Conference (ASRC 2015)*, 195-206.

Statement on collaboration

In general, Associated Professor Linlin Ge and Dr. Xiaojing Li proposed the topic; I performed the entire analysis, evaluated the accuracy of the results and wrote the manuscript; Professor Alex Hay-Man Ng helped with the TS-InSAR analysis.

Table of Contents

Abstract i

List of Abbreviations... iii

Acknowledgements v

List of Publications vii

Table of Contents xi

List of Figures xv

List of Tables..xxi

Chapter 1 1

Introduction 1

1.1 Objective and contributions 3

1.2 Thesis outline 5

Chapter 2 7

Background 7

2.1 Traditional surface deformation mapping methods 7

2.2 Recent advancement in mapping technique 8

2.2.1 The basic principle of Synthetic Aperture Radar 8

2.2.2 Synthetic Aperture Radar Interferometry..13

2.2.3 Differential Synthetic Aperture Radar Interferometry 14

2.2.4 Time series Synthetic Aperture Radar Interferometry 16

Chapter 3 19

Technical Highlights of Differential SAR Interferometry and Time series SAR Interferometry 19

3.1 The principle of DInSAR 19

3.2 Time series InSAR Interferometry..25

3.2.1 SAR images co-registration and interferogram generation.......................25

3.2.2 Measurement scatterer pixel selection 29

3.2.3 Parameters estimation 40

3.2.4 Parameters integration 47

3.2.5 Including less reliable measurement points 50

3.2.6 Removal of orbit and topography-dependent atmospheric error 51

3.2.7 Temporal-spatial filtering operation 53

3.3 Tropospheric turbulence and stratified phase delay.. 55

3.4 InSAR tropospheric stratification correction with GAMs 61

Chapter 4 .... **Error! Bookmark not defined.**

Tropospheric turbulent phase correction with TS-InSAR 64

4.1 Groundwater induced subsidence in Beijing City 64

4.2 Geological settings and data description... 67

4.3 Result and analysis... 69

4.3.1 Mapping land subsidence with ALOS-1/2 and Sentinel.................................. 69

4.3.2 InSAR data validation.. 72

4.3.3 Spatial-temporal analysis of land subsidence 73

4.4 Discussion and conclusion... 80

Chapter 5.. 83

Tropospheric stratified and turbulent phase correction for TS-InSAR..................... 83

5.1 Tropospheric stratified phase correction with DInSAR.................................. 83

5.2 Introduction... 89

5.3 Geological setting and dataset 91

5.4 Methodology flowchart.. 94

5.5 Experimental results and discussion 97

5.5.1 L-band InSAR result interpretation 100

5.5.2 Compare L-band result with C-band result over CBM sites.......................... 102

5.5.3 Errors respect to TS-InSAR measurement... 109

5.6 Concluding remarks 111
Chapter 6 113
C-band and L-band based TS-InSAR method over coalmine 113
6.1 Study regions within southern coalfield and dataset 114
6.2 Experimental results and analyses 117
6.2.1 Deformation over Wollongong City 120
6.2.2 Deformation over Tahmoor 123
6.2.3 Deformation over Appin underground mining Site 125
6.2.4 Conclusion remarks 127
Chapter 7 130
DInSAR and TS-InSAR for mining subsidence detection 130
7.1 Integration of DInSAR with TS-InSAR 130
7.1.1 Geological settings and dataset 131
7.1.2 Tropospheric stratified phase mitigation for DInSAR 133
7.1.3 Result and analysis 134
7.1.4 Integration of DInSAR and TS-InSAR 139
7.2 Modified TS-InSAR method for C-band SAR images 140
7.2.1 Dataset and study region 142
7.2.2 Add less reliable MS pixels 144
7.2.3 Experimental result and discussion 150
7.2.4 ATS-InSAR methods with less reliable MS pixels 161
Chapter 8 165
Comparison between GRACE and InSAR 165
8.1 Overview of the GRACE satellite mission 166
8.2 Geological settings 168
8.3 The procedure to generate GRACE time series measurements 171
8.4 InSAR time series measurement 177

8.5 Further work..183
Chapter 9...185
Concluding Remarks...185
9.1 Summary...185
9.2 Future directions 187
Reference 190

List of Figures

Figure 2.1 The side-looking geometry of synthetic aperture radar system……...…10

Figure 3.1 Geometry of repeat-pass InSAR System .. **Error! Bookmark not defined.**

Figure 3.2 Processing flowchart of DInSAR technique**Error! Bookmark not defined.**

Figure 3.3 Reflected signals received from PS, DS, CS, refined DS and Incoherent Scatterers pixels. .... **Error! Bookmark not defined.**

Figure 3.4 Amplitude dispersion simulation result modified from (Ferretti et al., 2001; Ng, 2010). .... **Error! Bookmark not defined.**

Figure 3.5 Comparison of the (a) individual ALOS-1 Intensity image, (b) after temporal mean filtering, (c) after the SH filtering (20 × 10), and (d) after the spatial mean filtering (20 × 10)... **Error! Bookmark not defined.**

Figure 3.6 The Ordinary Least-Squares fit is more influenced by the outlier than the Robust Regression fit 48

Figure 3.7 Representation of atmospheric layers 57

Figure 4.1 (a) The coverage of ALOS-1 (blue), ALOS-2 (yellow) and Sentinel-1 A/B (red) image stacks. The white pink cross represents the reference point. (b) Land cover classification result with respect to the coverage study region. 68

Figure 4.2 Three InSAR-derived subsidence rate maps over the eastern Beijing region on three-time spans were generated from SAR images acquired by: (a) ALOS-1, (b) Sentinel-1, and (c) ALOS-2 satellites. The blue circle represents the Tongzhou District, which is located in the eastern part of Beijing City. The resolution is 100 m × 100 m for all sub-maps. 70

Figure 4.3 Histogram of the measured mean velocity maps in ALOS-1's LOS direction generated from (a) ALOS-1, (b) Sentinel-1 and (c) ALOS-2 dataset, respectively, over the ROI region. .... **Error! Bookmark not defined.**

Figure 4.4 (a) Four levelling points (black triangles) superimposed onto ALOS-1 TS-InSAR derived velocity map (b) comparison of the land subsidence rate in ALOS-1's LOS direction between levelling and TS-InSAR measurements.**Error! Bookmark not defined.**

Figure 4.5 Pixel-by-pixel comparison between (a) Sentinel-1 and ALOS-1, and (b) Sentinel-1 and ALOS-2 mean velocity maps both in the ALOS-1's LOS direction,

mean velocity differences of (c) Sentinel-1 – ALOS-1, and (d) Sentinel-1 – ALOS-2 73
Figure 4.6 Four subsiding zones were marked with rectangle boxes I, II, III and IV, respectively (a) The relative locations with respect to these township centres, (b) ALOS-1 LOS displacement rate map, (c) Sentinel-1 displacement rate map and (d) ALOS-2 displacement rate map. Both (c) and (d) were converted into the ALOS-1's LOS direction. 75
Figure 4.7 Five measurement points within each zone and two profile lines a-a' and b-b' crossing the targeted subsiding regions. 78
Figure 4.8 Subsidence profile: (a) along the profile line a-a' within Zone 1, and (b) along the profile line b-b' within Zone 2. 78
Figure 4.9 Time series deformation over the five measurement points; (left) ALOS-1 based measures; (b) ALOS-2 and Sentinel-1 based measures. 80
Figure 5.1 (a) DEM over Qinghai Mount; (b) The primary differential IFG; (c) The de-ramped differential IFG without denoising; (d) The de-ramped differential IFG; (e) TSPD derived from MERRA; (f) Differential IFG after TSPD correction. The de-ramped IFG is generated from the ALOS-1 pair of 13 June 2009 and 29 July 2009. 84
Figure 5.2 (a) DEM over Ordos Basin (b) The de-ramped differential IFG (c) TSPD derived from MERRA (d) Differential IFG after TSPD correction. The de-ramped IFG is generated from ENVISAT pairs of 4 December 2011 and 2 February 2012. 86
Figure 5.3 (a) DEM over North China Plain; (b) The de-ramped differential IFG; (c) TSPD derived from ERA-Interim; (d) Differential IFG after TSPD correction. The de-ramped IFG is generated from ALOS-1 pair of 9 August 2009 and 9 February 2010. 87
Figure 5.4 The coverage of Liulin County superimposed on SRTM DEM map **Error! Bookmark not defined.**
Figure 5.5 Stratigraphic column of the coal-bearing sequences in Liulin area (modified from (Meng et al., 2014)) .... **Error! Bookmark not defined.**
Figure 5.6 The flowchart of Time series InSAR approach used in this study .... **Error! Bookmark not defined.**
Figure 5.7 (a) Time-baseline plot of the 21 ALOS PALSAR scenes, the red dash lines represent the consecutive interferometric pair combinations out of 67. (b) Time-baseline plot of the 14 ENVISAT ASAR images, the red dash lines represent the

consecutive interferometric pair combinations out of 36.**Error! Bookmark not defined.**

Figure 5.8 Three selected interferometric pairs in radar coordinates for L-band ALOS-1: (a) 25 December 2007 and 26 March 2008; (b) 2 July 2010 and 17 November 2010; and (c) 2 October 2010 and 17 November 2010 from the preliminary differential IFG, corrected for TSPD, corrected for TSPD and LOPD. .... **Error! Bookmark not defined.**

Figure 5.9 InSAR-derived linear deformation rate map with respect to coherent targets. (a) L-band ALOS PALSAR (b) C-band ENVISAT ASAR. Three regions with noticeable subsidence are marked with blue, red and black dash line rectangular boxes, respectively. 98

Figure 5.10 Three InSAR products derived from L-band ALOS-1 dataset (a) DInSAR IFG generated with two images acquired on 9 February 2008 and 26 March 2008 (b) InSAR-derived linear deformation rate map around AOI 1, AOI 2 and AOI 3 within Figure 5.12 and (c) DInSAR IFG generated with two images acquired on 30 December 2009 and 14 February 2010, Black cross represents the reference point. .... **Error! Bookmark not defined.**

Figure 5.11 Coal mining sites identified on the optical images acquired from Google Earth (© Google Earth) near (a) Haojiapocun and Zhaizeshangcun (b) Gaomingcun, (c) Guantoucun and (d) Shuangzaogetacun and Kangzhecun.**Error! Bookmark not defined.**

Figure 5.12 Twenty CBM sites superimposed on InSAR-derived linear deformation rate map (a) L-band outcome (b) C-band outcome.... **Error! Bookmark not defined.**

Figure 5.13 Time series measurements over eight selected CBM sites.............**Error! Bookmark not defined.**

Figure 6.1 The coverage of ALOS-1 PALSAR image stacks (1) and ENVISAT ASAR image pairs (2)... **Error! Bookmark not defined.**

Figure 6.2 (a) ALOS-1 PALSAR mean velocity result in LOS direction. (b) ENVISAT ASAR mean velocity result in LOS direction. The pink star represents the reference point while regions marked with red, blue and purple rectangular boxes are Wollongong city area, Appin mining sites and Tahmoor town region, respectively. The displacement results are resampled onto a grid of 100 m × 100 m resolution. (c) Slope Map generated from SRTM DEM. .... **Error! Bookmark not defined.**

Figure 6.3 L-band (a) and C-band (b) measurement over Wollongong city region in the vertical direction (c) time series evolution over one MS pixel marked with the red cross. .... **Error! Bookmark not defined.**
Figure 6.4 Comparison over Wollongong between L-band and C-band TS-InSAR results. .... **Error! Bookmark not defined.**
Figure 6.5 (a) L-band and (b) C-band measurements over Tahmoor region, the resolution of each pixel is 30 m × 30 m (c) Google map over Tahmoor town (© Google Earth) (d) the profile line through Tahmoor town.**Error! Bookmark not defined.**
Figure 6.6 Three selected IFGs within the study region of Figure 6.5 (a–c) interferometric phase after the interferometric phase optimization; (d–f) unwrapped phase from deformation; (a, d) 3 February 2008 and 18 January 2009; (b, e) 9 November 2008 and 18 January 2009; (c, f) 18 January 2009 and 1 August 2010. .... **Error! Bookmark not defined.**
Figure 6.7 Comparison over Appin mining site between (a) L-band and (b) C-band, the resolution of each pixel is 30 m × 30 m. .... **Error! Bookmark not defined.**
Figure 6.8 Typical patterns of underground mining subsidence in (a) DInSAR differential IFG. (b) TS-InSAR velocity map (Du et al., 2016b).**Error! Bookmark not defined.**
Figure 7.1 (a) Ordos region superimposed with DEM (b) Deformation maps over Ordos using GEOS-PSI with D_A < 0.4. The blue rectangle indicates the region with Advance Time Series Analysis (GEOS-ATSA) analysis. The red rectangle indicates the relatively stable region, which will be used for further analysis. ....**Error! Bookmark not defined.**
Figure 7.2 (a) The de-ramped differential IFGs, (b) TSPD obtained from the ERA-Interim, and (c) After TSPD correction. The de-ramped differential IFGs of (a) is generated from SAR pair of 16 July 2009 and 31 August 2009.**Error! Bookmark not defined.**
Figure 7.3 Deformation mapping result with the GEOS-ATSA for Ordos over the blue rectangle region in Figure 5.1 (b)....................... **Error! Bookmark not defined.**
Figure 7.4 (a) GEOS-PSI time series deformation map for Ordos (A) Huo Luo Wan coalmine (B) Qu Jia Liang coalmine (b-g) Accumulated DInSAR subsidence map for Qu Jia Liang coalmine within Ordos where no signal detected by TS-InSAR from

February 2008 to (b) April 2008 (c) July 2008 (d) February 2009 (e) July 2009 (f) January 2010 (g) July 2010 The two black stars are selected points 'a' and 'b'.**Error! Bookmark not defined.**

Figure 7.5 (a) Ground deformation at points 'a' and 'b' within Qu Jia Liang coalmine with no signal detected by TS-InSAR between 26 February 2008 and 19 July 2010. (b) and (c) Deformation results along two profiles denoted in Figure 5.4 (b-g): (b) Profile A-A′ along one of the long wall over Qu Jia Liang coalmine. (c) Profile B-B′ perpendicular to the long wall direction. The solid black lines indicate the deformation over these two profiles. .... **Error! Bookmark not defined.**

Figure 7.6 DInSAR results (a) Original (b) After TSPD correction are generated from SAR pairs of 13 June 2009 and 29 July 2009. The red rectangular boxes are stable region identified by GEO-PSI (Figure 5.1). .... **Error! Bookmark not defined.**

Figure 7.7 (a) GEOS-ATSA deformation map for Ordos (February 2007 ~ February 2011) near Qu Jia Liang coalmine (b) GEOS-ATSA deformation map for Ordos incorporating information from DInSAR output (February 2008 ~ April 2008)**Error! Bookmark not defined.**

Figure 7.8 Geographical location of the Appin & West Cliff Colliery at Southern Coalfield in Australia overlaid on ©Google Map. Longwall panels highlighted with blue colour were mining active between June 2007 and January 2011 while panels marked with yellow colour were mining active between July 2015 and June 2016. .... **Error! Bookmark not defined.**

Figure 7.9 Flowchart of the proposed method .... **Error! Bookmark not defined.**

Figure 7.10 Simple geometry of including less reliable MS pixels**Error! Bookmark not defined.**

Figure 7.11 Correlation between the maximum detectable subsidence rate and maximum cycles within single-master stacks .... **Error! Bookmark not defined.**

Figure 7.12 The MVM derived from ALOS-1 based ATS-InSAR method superimposed onto a DEM layer. .... **Error! Bookmark not defined.**

Figure 7.13 ENVISAT derived MVM using both traditional and modified ATS-InSAR method over Southern Sydney with different threshold settings (a) $D_A < 0.25$ or $\gamma_P > 0.55$ (b) $D_A < 0.25$ or $\gamma_P > 0.6$ & $0.6 \geq \gamma_P > 0.55$, and (c) Correlation between (a) and (b). .... **Error! Bookmark not defined.**

Figure 7.14 ENVISAT ATS-InSAR result over the longwall panel marked with blue colour with $D_A < 0.25$ or a) $\gamma_P > 0.5$, b) $\gamma_P > 0.4$, c) modified ATS-InSAR with $\gamma_P > 0.4$ and $0.4 \geq \gamma_P > 0.25$, and d) ALOS-1 with $\gamma_P > 0.75$. P1 is the selected hot-spot. .... **Error! Bookmark not defined.**
Figure 7.15 Sentinel TS-InSAR result over the longwall panel marked with yellow colour in Figure 1 with $D_A < 0.25$ or a) $\gamma_P > 0.7$, b) $\gamma_P > 0.6$, c) $\gamma_P > 0.5$ and d) modified ATS-InSAR with $\gamma_P > 0.5$ and $0.5 \geq \gamma_P > 0.4$. P2 is the selected hot-spot. .... **Error! Bookmark not defined.**
Figure 7.16 Time series displacement over two hot-spots P1 (Figure 7.14 (a) and (b)) and P2 (Figure 7.15 (a) and (c)), respectively. .... **Error! Bookmark not defined.**
Figure 7.17 (a) – (b) 1-cm-interval contour maps superimposed on ENVISAT and Sentinel-1 based SMVMs, respectively. (c) – (d) 1-cm-interval contour maps superimposed on ©Google Map. .... **Error! Bookmark not defined.**
Figure 8.1 The area covered by TS-InSAR analysis is indicated by the rectangle with black solid lines. The light green rectangle refers to the coverage of GRACE product. Regions covered with red solid-line is known as Haolebaoji.**Error! Bookmark not defined.**
Figure 8.2 the *TWS* acquired on 16 June 2012 derived from (a) CSR, (b) GFZ, (c) JPL, and (d) CSR+GFZ+JPL, respectively............... **Error! Bookmark not defined.**
Figure 8.3 components included in *TWS* acquired on 01 June 2012 derived from (a) *RSW*, (b) *LWS*, (c) *SIS*, and (d) *SMS*, respectively..... **Error! Bookmark not defined.**
Figure 8.4 The 2003 – 2012 time series soil moisture variation over Ordos Basin estimated from four GLDAS models (including the averaged result)................**Error! Bookmark not defined.**
Figure 8.5 (a) *SMS*, *TWS* and *RSW*+*LWS* time series measurements and (b) groundwater depletion rate form GRACE between Sep. 2006 and Jun. 2012 (c) the monthly rainfall over Ordos Basin............................ **Error! Bookmark not defined.**
Figure 8.6 TS-InSAR mean velocity map in LOS direction superimposed on SRTM DEM map (SAR images acquired from 08 January 2007 to 19 January 2011) .**Error! Bookmark not defined.**
Figure 8.7 The histogram of TS-InSAR velocity over the common region (a) Frame 780; (b) Frame 790; marked with red rectangle dash-line box in Figure 8.6. ....**Error! Bookmark not defined.**

Figure 8.8 (a) (d) Subsidence rate map generated with ALOS-1 PALSAR data with optical image (© Google Earth) at the highlighted region AOI 1 and AOI 2 in Fig. 5. (b) represents the DInSAR IFG generated with two RADARSAT-2 images acquired on 13 February 2012 and 8 March 2012. (c) and (e) are optical image obtained from Google Earth. .... **Error! Bookmark not defined.**
Figure 8.9 Twelve gap regions derived from TS-InSAR result**Error! Bookmark not defined.**

List of Tables

Table 2-1 Overview of the most commonly used space-borne platforms for InSAR (modified from (Moreira et al., 2013))...................... **Error! Bookmark not defined.**
Table 3-1 The value of K_a for the most common levels of $\boldsymbol{\alpha}$**Error! Bookmark not defined.**
Table 5-1 Detailed information of the interferometric pairs..................................... 83
Table 5-2 Standard deviations of phase value for coherent points ($\boldsymbol{\gamma}$>0.7 with respect to each IFG) with various phase correction, the detailed information about these three IFG can be found in Figure 5.9. 97
Table 5-3 Average subsidence derived from L-band InSAR over CBM sites (Unit mm year^{-1}) .... **Error! Bookmark not defined.**
Table 5-4 Average subsidence derived from C-band InSAR over CBM sites (Unit mm year^{-1}) .... **Error! Bookmark not defined.**
Table 5-5 Mean and SDV derived from InSAR over CBM sites (Unit mm year^{-1}) .... **Error! Bookmark not defined.**
Table 6-1 ALOS and ENVISAT dataset. .... **Error! Bookmark not defined.**
Table 7-1 ALOS-1, ENVISAT and Sentinel-1 dataset**Error! Bookmark not defined.**

Table 7-2 SAR satellite characteristics relevant to the expected detected subsidence .... **Error! Bookmark not defined.**
Table 9-1 ScanSAR Data information for the radar satellites that are still operating .... **Error! Bookmark not defined.**

Chapter 1

Introduction

Land subsidence has gradually become a global issue and researchers from all across the world are investigating to identify the causes of deformation and its further influences. From the perspective of common causes of land subsidence, it can be segregated into two categories: 1) anthropogenic involved subsidence and 2) non-human related subsidence. While the reason behind anthropogenic involved subsidence is the collapse of the geological structure beneath the land surface, typically induced by a variety of human-involved operations like underground mining activities, natural resources extraction, and underground tunnel construction, the non-human related subsidence includes earthquake deformation and volcano eruption. On the other hand, the level of land subsidence can be categorised into three groups – rapid, moderate and slow changes, if one only considers the potential effects of subsidence.

It should also be noticed that the impact of land subsidence can be seen in two forms, including structural damage to infrastructures and its effect on the serviceability of environmental assets. More specifically, land subsidence may:

- Damage the buildings, houses, sewers and buried pipes;
- Reduce the stability of structure of buildings and towers;
- Affect the serviceability of railways and roads due to distortion of rail foundation and road surface;

- Increase the exposure to flooding in regions near the coast;
- Affect the storage and effectiveness of drainage channels and dams;
- Lead to loss of surface water drainage to deeper strata;
- Shear the groundwater supply wells.

These above mentioned hazards can not only threaten an individual's everyday life and properties, but also lead to massive impacts on the national economy in a big way. In Bandung Basin, Indonesia, acceleration of ground subsidence has been reported by many researchers due to excessive groundwater extraction and the largest subsidence reached to as much as –24 cm yr^{-1} (Ge et al., 2014). Moreover, during the processing of hard rock and underground coal mining, many miners die every year all across the world as a direct result of long-term accumulated subsidence (Zhao and Jiang, 2015). Nevertheless, these catastrophic events are often predictable to some extent since they often follow a natural cycle. Timely displacement information, which can provide strong indicators of these future disasters, is often used to identify the severely affected area. A recent example is UC Berkeley's ShakeAlert System, which detected the South Napa Earthquake ten seconds earlier by using p-wave for monitoring displacement of earth surface (Lindsey, 2014). Therefore, having the ability to measure the earth surface deformation over an extended period of time can enable us to have a better understanding of natural hazards. Eventually, this can also help the local government or associated councils to minimise the impacts and make better decisions.

1.1 Objective and contributions

This dissertation aims to identify ways to overcome the drawbacks of the TS-InSAR method for dealing with the moderate and rapid ground subsidence, as well as to investigate the potential cause of the subsidence by applying several established TS-InSAR techniques to different areas.

The key contributions of this thesis is summarised as follows:

- The problem with TS-InSAR technique is that some rapid surface subsidence within a short period of time can lead to loss of InSAR coherence and consequently gaps would appear in such areas. A new way to integrate TS-InSAR with DInSAR over mining regions in Ordos, China has been suggested.

- A modified single-master-based TS-InSAR approach was invented by selecting less reliable Measurement Scatterer (MS) pixels through an IDW-based integration module. The generic term MS is the total sum of Persistent Scatterer (PS) and Distributed Scatterer (DS). The proposed method was being used to monitor the underground mining induced land subsidence in Appin & West Cliff Colliery, Australia.

- Several established TS-InSAR techniques have been applied to different areas, and these significant findings from the TS-InSAR analysis have led to new insights into the processes causing the deformation.

1.2 Thesis outline

There are in total nine chapters in this dissertation.

The objective and contribution are given in Chapter 1.

Chapter 2 gives a brief history of the background of SAR imaging and InSAR mapping methods.

Chapter 3 provides a brief overview of the fundamental principles of DInSAR. The detailed processing strategies for both single- and multi-master based TS-InSAR methods are described.

Chapter 4 and 5 demonstrates the performance of global atmospheric model and TS-InSAR method in correcting both tropospheric stratification and turbulence. This chapter is drafted based on materials published in *International Journal of Digital Earth* (Du et al., 2017a) and *International Journal of Digital Earth* (Du et al., 2017b).

Chapter 6 and 7 illustrates the feasibility of using both DInSAR and TS-InSAR for monitoring the subsidence phenomenon over underground mining regions. This chapter is drafted based on materials published in *Remote Sensing* (Du et al., 2016a), *Remote Sensing Letters* (Du et al., 2016b) and *International Journal of Remote Sensing* (Du et al., 2018).

Chapter 8 demonstrates the potential usage of GRACE-derived measurement and TS-InSAR outcome.

Chapter 9 presents the concluding remarks of this dissertation and recommendations for the future work.

Chapter 2

Background

This chapter starts with an overview of Interferometric Synthetic Aperture Radar (InSAR), as well as the Differential Interferometric SAR (DInSAR) and Time series SAR Interferometry (TS-InSAR) techniques, which are the extension of InSAR methods.

2.1 Traditional surface deformation mapping methods

Conventionally, mapping of earth surface deformation is achieved by using field survey techniques, such as digital levels, total stations and Global Positioning Systems (GPS) in Real Time Kinematic (RTK) and static surveys. Both total stations and digital levels can achieve 0.1 mm accuracy in the vertical direction, while static GPS can deliver 5 mm height change resolution and RTK with the corresponding accuracy of 20 to 30 mm (Ge et al., 2007). However, these ground survey methods have limitations. 1) It could be extremely labour-intensive and time-consuming once the measurement regions become large as well as the revisit time is short, and 2) these techniques are based on a point-to-point measurement, which means it is tough to obtain a reasonable interpretable topographic surface deformation over the whole region (Zhang et al., 2011). For example, the GEONET (GPS Earth Observation Network) is the largest and best instrumented continuous GPS (CGPS) network in the world, which consists of about 1, 200 GPS static stations, and the equivalent spatial resolution is approximate ~20 km. Nevertheless, a CGPS network with such density is still not good enough to perform accurate monitoring of the dynamic ground changes over wide area (Ge et al., 2000).

2.2 Recent advancement in mapping technique

Interferometric Synthetic Aperture Radar (InSAR) is a relatively new imaging method that has been widely used over the past three decades to measure large-scale land surface subsidence, earth fissures, as well as faults caused by natural and anthropogenic activities (Rosen et al., 2000), and it has a wide range of benefits compared to traditional field survey methods. First of all, InSAR is fully capable of monitoring the wide-area continuous ground movement with the accuracy of centimetre to millimetre (Massonnet and Feigl, 1998), for example, a standard InSAR scene covers an area of ~ 10, 000 km^2 at a pixel spatial resolution of 1 ~ 30 meters. Secondly, SAR is an all-weather electronic system, which can be operated 24 hours a day since it mainly depends on the coherent active microwave (Graham, 1974). Thirdly, it has the quickest access to any sites, especially those flooded regions or earthquake zones. The detailed literature review of InSAR related information is given in section 2.2.1 to 2.2.4.

2.2.1 The basic principle of Synthetic Aperture Radar

A Synthetic Aperture Radar (SAR) system operates in a side-looking imaging geometry with its antenna pointing towards the earth surface perpendicular to the movement direction of the antenna. The flight track is known as the “along-track” or “azimuth” direction, while the distance between the sensor and target on the surface in the pointing direction is called the “cross-track” or “range” direction (Bamler and Hartl, 1998) (Figure 2.1). The SAR system is based on a pulsed radar structure. As the radar system moves along the platform trajectory, it sequentially transmits high power electromagnetic pulses, e.g. chirp signals, into the so-called “antenna’s illumination footprint”, and then receives the echoes of the backscattered signals at a rate of *PRF* (pulse repetition frequency), where *PRF* is the reciprocal of the pulse repetition interval *PRI*, that is $PRF = 1/PRI$. By taking advantage of the Doppler effects inherent, the stream of echoes received from multiple positions can be recombined to form a virtual synthesised aperture (maintain physical integrity and size limits), which is extremely large compared to the physical antenna length, and hence a higher resolution can be achieved. Since both the times and positons of the echoes scattered from the ground have been recorded, the array of echoes can be considered as a two-dimensional raw data matrix with two coordinates: 1) *echo delay time*, which is associated with the distance from the sensor to the target on the ground in range direction, and 2) *pulse number*, which represents the various positions along the azimuth direction. In other words, the raw data matrix can also be treated as a raw image, and the range resolution is limited to the length of the transmitted pulse while the azimuth resolution is given by the size of the antenna footprint. The pulse compression and synthetic aperture concepts are further applied to improve the spatial resolution of the raw image, and hence the typical Level-1 SAR image is formed. However, it is worth noting that these techniques are related to the SAR focusing steps, which is beyond the scope of this thesis, and readers are referred to Moreira et al. (2013) for more information.

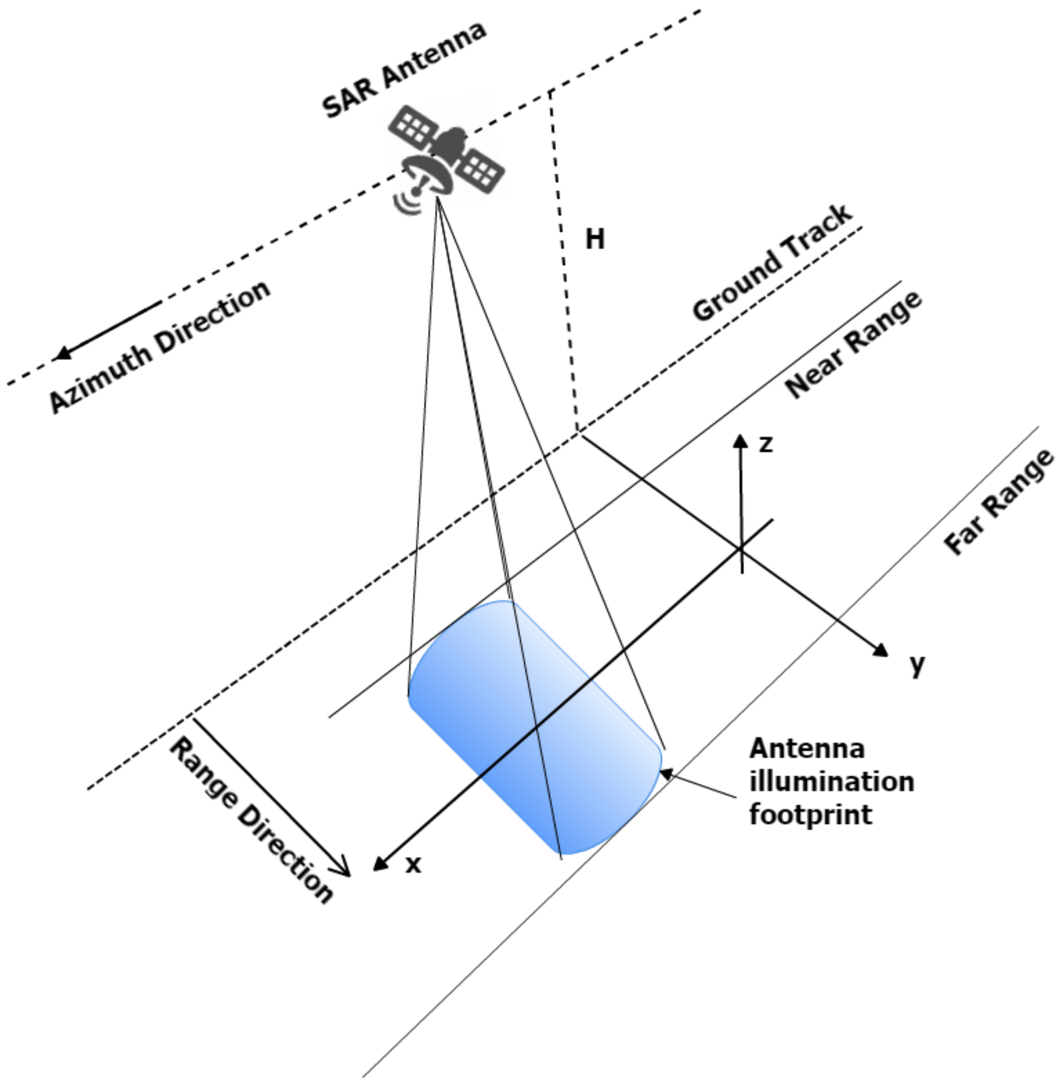

Figure 2.1 The side-looking geometry of synthetic aperture radar system

SAR systems have been utilised extensively for the past decades to map the earth's surface and capture information about its physical properties, e.g. morphology, roughness and topography of the backscattering layer (Bamler and Hartl, 1998). The NASA SEASAT satellite, launched by NASA's Jet Propulsion Laboratory in June 1978, was the first civilian earth-orbiting satellite designed for ocean studies and had the very first space-borne SAR on board. European remote sensing satellite-1 (ERS-1), the first SAR system of the European Space Agency (ESA), was then launched in

July 1991. Several more SAR satellites were operated in the 1990s, including the Canadian Space Agency (CSA)'s Radarsat-1, National Space Development Agency of Japan (NASDA)'s JERS-1, the Soviet Union's Almaz-1 and ESA's ERS-2. Of which, Radarsat-1 was the first commercial SAR satellite. The early 2000s was a boosting period for SAR satellite development, in total seven satellites were launched during these time, namely, ESA'S ENVISAT, Japan Aerospace Exploration Agency (JAXA)'s ALOS-1, CSA's RADARSAT-2, German Aerospace Center (DLR)'s TerraSAR-X, Italian Space Agency (ASI)'s COSMO-SkyMed-1/4, JAXA's ALOS-2 and ESA's Sentinel-1A/B. Until now, more than 15 spaceborne SAR systems are being released all over the world, and another 15 new SAR platforms will be launched within the next ten years (Moreira et al., 2013). The detailed information concerning the selected SAR satellites is given in Table 2-1.

Table 2-1 Overview of the most commonly used space-borne platforms for InSAR (modified from (Moreira et al., 2013))

SATELLITE/ SENSOR	OPERATION	BAND FREQUENCY	ORGANIZATION COUNTRY	ORBIT HEIGHT (km)	INCIDENCE ANGLE (°)	REPEAT CYCLE (d)	RESOLUTION (m) / MODE	INCLINATION (°)
SEASAT	Jun. – Oct. 1978	L (HH)	NASA/JPL, USA	800	22		~ 25	108
ERS-1/2/AMI	1991 – 2000 1995 – 2011	C (VV)	ESA, Europe	785	20 – 26	35	~ 25	98.5
JERS-1	1992 – 1998	L (HH)	NASDA, Japan	568	32 – 38	44	~ 18	97.7
Radarsat-1	1995 – 2013	C (HH)	CSA, Canada	798	20 – 49	24	~ 25/Standard	98.6
ENVISAT/ASAR	2002 – 2012	C (dual)	ESA, Europe	790	15 – 45	35	~ 30/IMS	98.4
ALOS/PALSAR	2006 – 2011	L (quad)	JAXA, Japan	692	8 – 60	46	~ 10/FBS/FBD	98
TerraSAR-X	2007 – present	X (quad)	DLR/Astrium, Germany	515	15 – 60	11	~ 3/ Stripmap	97.44
Radarsat-2	2007 – present	C (quad)	CSA, Canada	798	30 – 50	24	~ 10/Fine	98.6
COSMO-SkyMed-1/4	2007 … 2010 – present	X (dual)	ASI/MiD, Italy	619	20 – 60	1 – 15	~ 3/ Stripmap	97.9
ALOS-2	2014 – present	L (quad)	JAXA, Japan	628	8 – 70	14	~ 10/FBS/FBD	97.9
Sentinel-1A/1B	2014 … 2016 – present	C (dual)	ESA, Europe	693	18.3 – 46.8	6, 12	~ 20/IWS	98.18

2.2.2 Synthetic Aperture Radar Interferometry

A conventional SAR system can only be used to measure the location of targets (two dimensional), while InSAR is the synthetic combination of conventional SAR technique and the concept of phase interferometry, with the ability to measure the three-dimensional position of objectives. The very first InSAR application was proposed by Graham (Graham, 1974; Rosen et al., 2000), and he designed an imaging interferometer by augmenting an additional physical antenna to the conventional SAR platform. This method strongly proved the status of InSAR as a tool for high-resolution topographic mapping. However, the main drawback was that the topographic contours were not identical due to the relative phase changes. Zebker and Goldstein (Zebker and Goldstein, 1986) developed an InSAR system to solve the relative phases ambiguity by recording both the complex amplitude and phase information for each antenna. An 11 km x 10 km region around the San Francisco Bay Area was exploited to conduct the experiment, and the obtained topographic map proved to be 10 m accuracy. Later in 1988, crossed orbit interferometry was invented by Gabriel to reduce the limitations of parallel orbits (Gabriel and Goldstein, 1988). Li and Goldstein (Li and Goldstein, 1990) assessed the performance of InSAR system by capturing SAR data at various baseline separations and signal to noise ratio, and eventually came up with a model for phase residual errors analysis. Rodriguez optimised some parameters of Li’s model and improved the accuracy of the derived topographic map (Rodriguez and Martin, 1992). Indeed, InSAR technique was initially being used for the topographic mapping. Nevertheless, the ground deformation mapping has become the primary application of InSAR technique since 1993 (Ng, 2010; Massonnet et al., 1993).

2.2.3 Differential Synthetic Aperture Radar Interferometry

Differential Interferometric SAR (DInSAR) is an evolution of the conventional InSAR technique which is used for measuring earth surface deformation, and the typical two-pass DInSAR approach is carried out by utilising an external provided Digital Elevation Model (DEM) to remove the topographic information from the IFG and capture the ground surface changes. The concept of DInSAR was first mentioned by Gabriel (Gabriel et al., 1989). However, it was until four years later that Massonnet demonstrated the first DInSAR result for the 1992 earthquake in Landers, California using the two-pass procedure. The accuracy was proved in the order of centimetre, which was extremely competitive to conventional field survey techniques (Massonnet et al., 1993; Massonnet et al., 1994; Zebker et al., 1994). Zebker then proposed the three-pass DInSAR technique in 1994, and the main idea was to calculate the topographic phase signal by taking advantage of an extra InSAR pair with very short temporal baseline (Zebker et al., 1994). Since then, DInSAR has been applied to many applications with great successes. Notable examples are glacier motion monitoring (Gray et al., 1998; Joughin et al., 2004), volcanic activities observing (Massonnet et al., 1996; Lanari et al., 1998; Hu et al., 2009; Hooper et al., 2012), earthquake deformations measuring (Massonnet et al., 1993; Massonnet et al., 1994; Zebker et al., 1994; Suga et al., 2001; Ge et al., 2008; Hensley et al., 2009; Lindsey, 2014), underground mining detection (Ge et al., 2001; Ge et al., 2007; Hu et al., 2013), and underground water extraction monitoring (Chang et al., 2004; Ge et al., 2014).

Essentially, DInSAR technique can measure topographic surface displacement with a greater likelihood of high accuracies when the time gap between two image acquisitions is relatively small. Therefore, the temporal baseline is reduced and a dense grid of pixels can be applied. However, there are certainly some limitations which restrict the effectiveness in some applications (Ferretti et al., 2001).

The main restrictions for DInSAR are de-correlation in the spatial and temporal domain, e.g. when monitoring low-velocity subsidence within a long term, the differential IFGs are focused to have large temporal and spatial baseline, and consequently degrading the IFG phase and only highly coherent area can be used to extract useful information. Additionally, signal phase delay due to Atmospheric Phase Screen (APS) could also degrade the quality of deformation estimation. It is worth noting that the changes in troposphere and ionosphere from one day to another could form different time delays similar to the deformation signals (Ding et al., 2008). Furthermore, the phase distortion induced by orbit error, which shares the similar characteristics with the long-wavelength phase in the spatial domain, can also lead to the estimation inaccuracy. A commonly accepted method to deal with this matter is by applying a lower-order polynomial fitting algorithm. Nevertheless, given the fact that the most significant difference between long-wavelength and orbital artefacts is that the former one is correlated in the temporal domain, the application of the lower-order polynomial fitting method can be considered more efficient if the temporally correlated components are being removed beforehand.

2.2.4 Time series Synthetic Aperture Radar Interferometry

To enhance the performance of DInSAR for land deformation mapping purpose through minimising atmospheric propagation effects and temporal/spatial decorrelation, Time-series InSAR (TS-InSAR), in which jointly analysed multi-SAR images acquired on different dates, was invented in the late 1990s (Ferretti et al., 2000). The phase gradient approach was the first attempt to increase the phase clarity and decrease the errors caused by atmospheric artefacts by averaging the differential IFGs, since atmospheric contribution is highly correlated in the spatial domain, but not correlated in temporal domain (Sandwell and Price, 1998). To further minimise DEM inaccuracy and spatial decorrelation, some works with small baseline IFG were carried out. However, an issue related to the subsets of differential IFGs may occur due to the multi-master strategy. Singular Decomposition Method (SVD) was applied by Berardino et al. (2002) to solve the subset problem by utilising minimum-norm criteria to estimate the deformation velocity for only coherent pixels.

Persistent Scatterer InSAR (PSInSAR^{TM}) technique was proposed by Ferretti et al. (2001) to monitor local deformation phenomena over the highly coherent structures, such as buildings, rail tracks and bridges (Ferretti et al., 2001; Kampes, 2006). By selecting a stack of acquisitions (generally >= 20 images) (Colesanti et al., 2003a), all the slave images are co-registered to only one master image. Pixels corresponding to one or two dominant scatterers are then selected from the prominent natural features, the precise location of each scatterer can be recorded after comparing to non-prominent features, thus making it possible to track the motion of each dominant scatterer and later solve for the ground deformation (Lanari et al., 2007). Such pixels that contain dominant scatterers are so-called Persistent Scatterer (PS) pixels, and the principle behind is that PS pixels are normally caused by dihedral and trihedral reflection. Therefore, the phase varying little due to temporal decorrelation, and the variation is also small even with different viewing angle and squint angle (hence large spatial baselines). It is worth mentioning that the accuracy could reach up to sub-millimetre level depends on the quality and number of image stacks (Colesanti et al., 2003a).

Since then many TS-InSAR techniques have been developed, which can more or less be segregated into three categories. (1) In the first category are techniques that make use of only one single master image to generate stacks of IFGs. These approaches estimate the ground deformation at the PS pixels, whose scattering characteristics remain stable even over long time intervals and large baseline separation, e.g., PSInSAR™ (Ferretti et al., 2001), Stanford method for Persistent Scatterers (StaMPS) (Hooper et al., 2004), the Spatio-Temporal Unwrapping Network (STUN) (Kampes, 2006), Stable Points Network (SPN) (Crosetto et al., 2008; Kuehn et al., 2010) and the GEOS-PSI method (Ng et al., 2012b). These techniques have the advantage of associating the deformation with a particular scatterer, rather than a multi-looked resolution cell. This allows displacement maps to be generated with high resolution and the achievable accuracy could be 1 $mm \cdot yr^{-1}$ or better where the subsidence over the study region is linear in time (Adam et al., 2009).

(2) The second category involves the usage of multi-master IFGs, and only the so-called Coherent Scatterer (CS) pixels were selected for further analysis. Unlike PS pixels whose scattering characteristics are insensitive to spatial and temporal baselines, CS pixels can only maintain their scattering characteristics with limited spatial and temporal baselines, and multi-look operation is always needed to enhance the signal-to-noise-ratio (SNR) of CS pixels, e.g., the Stacking Analysis method (Sandwell, 1998), the Small Baseline Subset (SBAS) method (Berardino et al., 2002; Lanari et al., 2004), the Coherent pixel technique (CPT) (Mora et al., 2003), Poly-Interferogram Rate And Time-series Estimator (π-RATE) (Biggs et al., 2007; Wang et al., 2012), the Temporally Coherent Point InSAR (TCPInSAR) (Zhang et al., 2011), the Intermittent SBAS (ISBAS) (Bateson et al., 2015).

(3) In the third category, single- and multi-master IFGs are combined to form the time series analysis (Hooper et al., 2012), e.g. full-resolution SBAS approach (Lanari et al., 2004), modified-StaMPS (Hooper, 2008), SqueeSAR method (Ferretti et al., 2011) and the GEOS-ATSA (Ge et al., 2014). These different TS-InSAR techniques have been applied to measure mean velocities and cumulative deformation in various applications that include groundwater extraction-induced land subsidence, landslide and volcanic deformation, and city urbanisation and expansion-induced deformation. However, it is worth mentioning that none of the error sources can be completely eliminated even with the TS-InSAR method, and researchers working on these techniques are trying to minimise the unfavourable phase components according to different geological situations.

Chapter 3

Technical Highlights of Differential SAR Interferometry and Time series SAR Interferometry

3.1 The principle of DInSAR

DInSAR interferometry is characterised by single-pass or repeat-pass interferometry according to the number of platforms pass over the same scene (Ahmed et al., 2011). Typically, repeat pass interferometry is operated using only one antenna to capture the same area twice at different times, and the time difference is called the revisit time. The basic geometry of the SAR system is illustrated in Figure 3.1, where S_M represents the master image while the slave image is denoted as S_S. λ is the carrier wavelength of radar pulses, θ and θ_0 are the incidence angle to the image pixel on the topographic surface and reference surface, respectively. R_M and R_S are the range distances between antenna positions and topography target, α is the angle between the baseline and horizontal direction, D is the displacement of the image pixel along LOS direction, B is the length of baseline whilst $B_\perp$ is the perpendicular vector of the baseline.

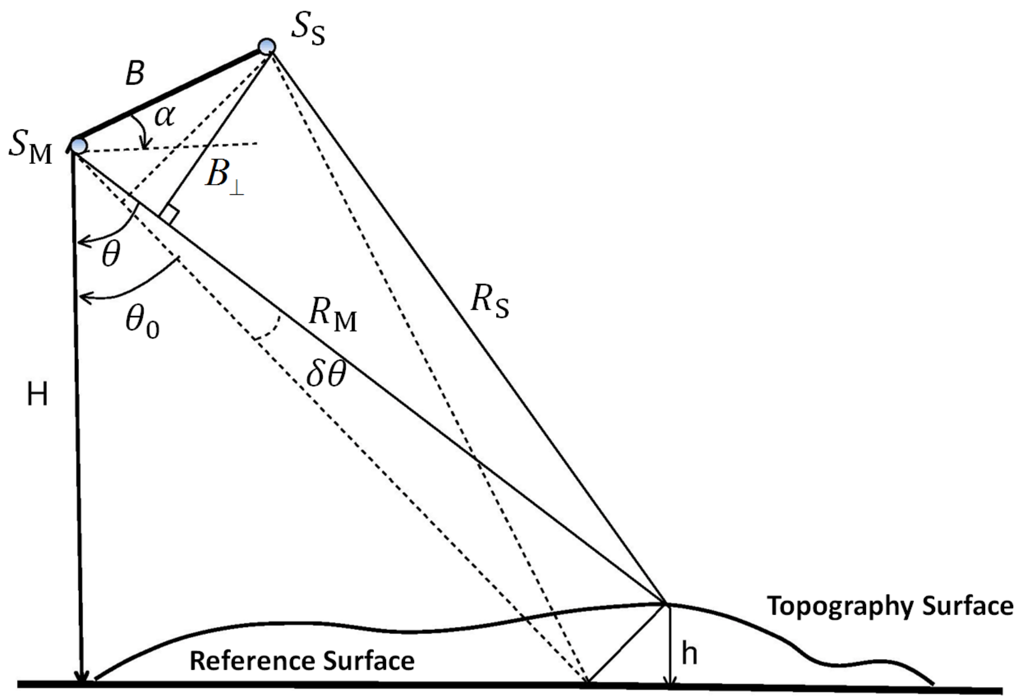

Figure 3.1 Geometry of repeat-pass InSAR System

The observed phase value $\emptyset_M$ (.) and $\emptyset_S$ (.) of the SAR images with respect to a resolution cell is determined by the length of the range, wavelength as well as the backscattering phase, and the associated equation can be expressed as:

$$\begin{cases} \phi_M(.) = -\dfrac{4\pi}{\lambda} R_M + \phi_{scat,M} \\ \phi_S(.) = -\dfrac{4\pi}{\lambda} R_S + \phi_{scat,S} \end{cases} \tag{3.1}$$

where $\phi_{scat,M}$ and $\phi_{scat,S}$ are the backscattering phase of both master and slave images. For two SAR images acquired under very similar condition, the backscattering phase $\emptyset_M$ (.) and $\emptyset_S$ (.) can be considered as identical to each other. The interferometric phase $\emptyset$ (.), therefore, is more sensitive to the range phase difference and can be rewritten as (Rosen et al., 1996):

$$\phi(.) = \phi_M(.) - \phi_S(.) = -\frac{4\pi}{\lambda}(R_M - R_S) \quad (3.2)$$

Additionally, $\phi(.)$ can also be written as equation (3.3) when assuming R_{M}, R_{S} (500 ~ 800 km) are >> B (< ~1 km).

$$\phi(.) \approx -\frac{4\pi}{\lambda} B\sin(\theta - \alpha) \quad (3.3)$$

The earth ellipsoid phase need to be simulated based on orbit parameters, which is also well known as the flat earth effect. The flat earth phase can be denoted as the following equation when assuming that the topography is absent from the reference surface:

$$\phi_{Flat} \approx -\frac{4\pi}{\lambda} B\sin(\theta_0 - \alpha) \quad (3.4)$$

where ϕ_{Flat} is referred to flat earth phase. By removing this phase component from $\phi(.)$, the resulted differential phase ϕ_{Diff} is given:

$$\phi_{Diff} = \phi(.) - \phi_{Flat} = -\frac{4\pi}{\lambda} B\cos(\theta_0 - \alpha)\delta\theta \quad (3.5)$$

The relationship between $\delta\theta$ and height of the target h is given under the assumption that there is no ground displacement between two acquisition times (Rosen et al., 1996):

$$\delta\theta \approx \frac{h}{R_M \sin\theta_0} \tag{3.6}$$

where θ_0 is also known as the local incidence angle, h is the topography target height referring to the reference surface, $\delta\theta$ is the difference between θ and θ_0.

It is worth mentioning that the above equation is purely based on geometric structure. In reality, several other phases may contaminate the differential phase and should be considered as well. Therefore, the new equation becomes:

$$\phi_{Diff} = \phi_{Topo} + \phi_{Defo} + \phi_{Orbit} + \phi_{Atm} + \phi_{Noise} \tag{3.7}$$

These five denoted phases are contributed by topography, deformation, orbital, atmosphere artefacts, and noise, respectively. Among them, topographic phase ϕ_{Topo} is typically removed by importing an external data contains terrain information. As a result, such component can be simulated from this external data, e.g. a one arc-second (approx. 30m resolution) Shuttle Radar Topography Mission (SRTM) Digital Elevation Model (DEM) or an external InSAR pair with relative short temporal baseline. However, due to the inaccuracy of the DEM, the residual topographic phase noise may remain in ϕ_{Diff} and we assume this part is included inside the ϕ_{Noise}. The phase component ϕ_{Orbit} consists of both linear-component dominant phase and nonlinear phase. The linear phase trend can be eliminated if ground control points are available, e.g. static GPS measurements. An alternative way is to measure the frequency of the signal with maximum power in both the azimuth and range direction by applying a Fast Fourier Transform (FFT) function to transfer the interferometric signals into the frequency domain, which is also referred to as linear phase gradient coefficients (Zhang et al., 2009; Ng et al., 2012b). The derived phase component is denoted as ϕ_{FFT} :

$$\phi_{FFT}(x,y) = 2\pi \cdot (x \cdot g_x + y \cdot g_y + \tau) \tag{3.8}$$

where x, y are the coordinates in slant-range radar coordinate system while the gradient coefficients along the range and azimuth directions are expressed as g_x and g_y. τ is a constant value.

Nevertheless, the nonlinear phase caused by orbital error is difficult to remove and therefore considered to be included in ϕ_{Noise}. The atmospheric phase component ϕ_{Atm} is composed of tropospheric phase and ionospheric phase, whilst tropospheric phase is made up of both stratified phase and turbulent phase (Jolivet et al., 2014). Global Atmospheric Model (GAM) is capable of eliminating the atmospheric phase to some extent and the detailed discussion can be found in Section 4. The last component ϕ_{Noise}, which is correlated in the spatial domain, can be eliminated following a low pass adaptive filtering operation.

Eventually, an optimised differential IFG mainly composed of deformation phase can be obtained. Since the differential interferometric phase is expressed in modulo 2π radians, the conversion process to resolve the 2π ambiguities is necessary, which is also known as the Phase Unwrapping (PU) operation. The relationship between the unwrapped differential phase and displacement value *D* is presented in equation

3.9 (Fornaro et al., 2009). The processing flowchart of DInSAR technique can be found in Figure 3.2.

$$\phi_{unwrapped,Diff} = -\frac{4\pi}{\lambda} D \tag{3.9}$$

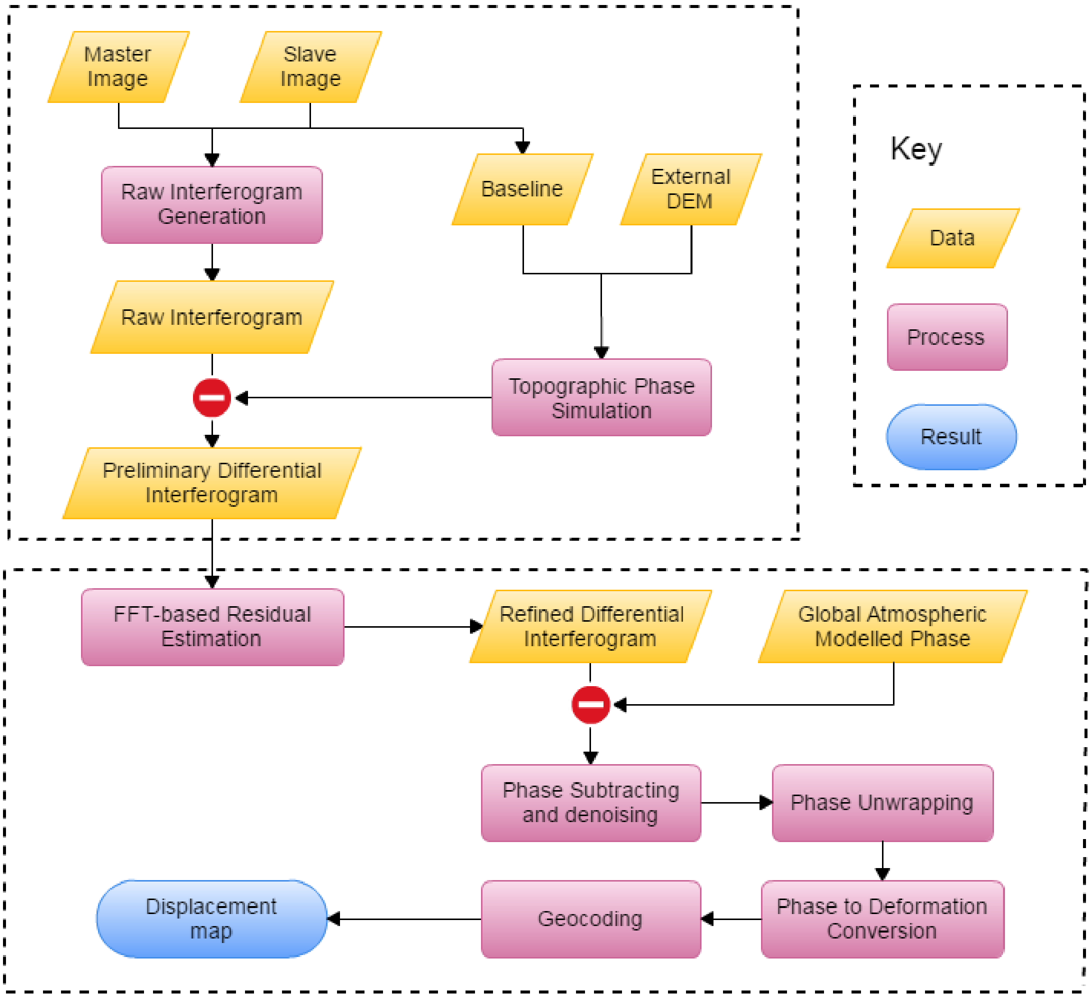

Figure 3.2 Processing flowchart of DInSAR technique

3.2 Time series InSAR Interferometry

3.2.1 SAR images co-registration and interferogram generation

Suppose there are N + 1 input SAR images available and one of them is selected as the reference image, the rest N scenes are co-registered and re-sampled to the same grid as the selected image using the Six Point Cubic Convolution (CC6P) kernel (Ng, 2010; Hanssen, 2001). Then the conventional two-pass DInSAR method is applied to estimate the IFG by conjugate multiplication between two scenes within the image stack, and the total number of possible IFG combination is M, which is given in equation 3.10.

$$N \leq M \leq N(N+1)/2 \tag{3.10}$$

The topographic phase is estimated using the one arc-second DEM (30 m posting) acquired from the SRTM (Farr et al., 2007) and removed from the IFGs.

3.2.1.1 Single-master stacking strategy

Under the single-master strategy, in order to achieve the TS-InSAR result with the best quality, an appropriate master image needs to be selected to maximise the stack coherence of the interferometric pairs (Hooper, 2006; Kampes, 2006; Ng, 2010). The stack coherence with respect to the master m can be simply modelled as:

$$\gamma_{total} = \gamma_{temporal}\gamma_{spatial} \approx \frac{1}{N}\sum_{n=1}^{N} f(B_{\perp}^{m,n}, B_C) \times f(T^{m,n}, T_C) \quad where \tag{3.11}$$

$$f(x,c) = \begin{cases} 1 - |x|/c & for\ |x| \leq c \\ 0 & for\ |x| \geq c \end{cases} \tag{3.12}$$

$B_{\perp}^{m,n}$ and $T^{m,n}$ are the perpendicular spatial baseline and temporal baseline, respectively. The divisor c is referred to as the critical value for B_C and T_C, and an IFG exhibits complete decorrelation with either parameter beyond this value. It is worth noting that these critical values are dependent on wavelength, look angle and bandwidth of SAR images, and the typical value for ALOS-1 PALSAR fine-beam single polarization (FBS−HH) in particular are T_C = 5 years (given the fact that the life time for this satellite is five years plus four months), and B_C = 13.1 km (Sandwell et al., 2008).

As the master image is selected which could give the largest stack coherence, an empirical SAR calibration is carried out for these re-sampled scenes (Cassee, 2004; Ge et al., 2014), whose amplitude value acquired at different time may vary due to the changes in characteristics of sensor as well as viewing geometry. The two-step calibration operation is: 1) the calibration constant C_n provided in the SAR parameter file of each SLC data is used to conduct the pre-calibration (equation 3.13), and 2) since the provided calibration constant may be poorly defined due to some systematic biases, another calibration factor K_n is introduced to ensure that the images are comparable by taking advantage of the mean value of these pre-calibrated SAR images (equation 3.14) (Ng, 2010).

$$A_{pre\_cal}^{n}(l,p) = \frac{C_m}{C_n} A_{orig}^{n}(l,p) \tag{3.13}$$

where $A_{pre\_cal}^{n}(l,p)$ and $A_{orig}^{n}(l,p)$ are the pre-calibrated and original amplitude value, respectively, with respect to the pixel at (l, p) and image acquisition n = 1, 2, 3 …

N+1. C_m and C_n are the calibration constant for the master image and the acquisition *n* image, respectively.

$$A^{n}_{cal}(l,p) = \frac{K_m}{K_n} A^{n}_{pre\_cal}(l,p) = \frac{\sum_{p=1,l=1}^{P,L} A^{m}_{orig}(l,p)}{\sum_{p=1,l=1}^{P,L} A^{n}_{pre\_cal}(l,p)} A^{n}_{pre\_cal}(l,p) \tag{3.14}$$

where $A^{n}_{cal}(l,p)$ is the final calibrated amplitude value with respect to the pixel at (*l*, *p*) while K_m and K_n are mean amplitude values of the pre-calibrated SAR image *m* and *n*, respectively.

3.2.1.2 Multi-master stacking strategy

For traditional SBAS technique (Berardino et al., 2002), *M* multi-looked interferograms (IFGs) and corresponding coherence maps are generated with both spatial baseline and temporal baseline smaller than a pre-defined threshold. After that, pixels with low-phase dispersion are selected for the subsequent process, and these pixels are also referred to as Coherent Scatterer (CS) pixels. To determine whether a multi-looked unit is a CS pixel, the temporal coherence magnitude $|\hat{\gamma}|$, a maximum likelihood estimator, is exploited to evaluate the phase dispersion. $|\hat{\gamma}|$ can be affected by many factors, such as the impact of volume scattering, geometric decorrelation, temporal decorrelation, as well as Doppler centroid difference between two images acquisitions (Zhang et al., 2013). CS pixels are selected with temporal mean value $|\hat{\gamma}|$ higher than a pre-defined threshold (equation 3.15).

$$|\hat{\gamma}| = \frac{1}{M}\sum_{m=1}^{M} |\gamma_m(l,p)| \tag{3.15}$$

where $\gamma_m(l,p)$ represents the coherence magnitude at (l,p) of mth IFGs, and the detailed definition of $\gamma_m(l,p)$ can be found in Section 3.2.3.

3.2.1.3 Modified Multi-master stacking strategy

It is worth mentioning that the traditional SBAS technique only takes the magnitude of spatial and temporal baselines as decorrelation indicators, and the selection of possible IFG combinations is achieved by setting a pre-defined threshold for spatial and temporal baselines (Berardino et al., 2002). However, there are certainly other factors that might degrade the correlation of IFG, e.g., the orbital error and atmospheric phase screen disturbance (Zhang et al., 2013). Therefore, the global gross coherence (GGC) can be exploited to evaluate the de-correlation level with respect to each IFG (modified from LGC mentioned in (Zhang et al., 2013)). The GGC for the *M*th IFG is given as follow:

$$\gamma_{GGC}^{M} = \sum_{l=1,p=1}^{L,P} |\gamma|^{M}\ (l,p) \tag{3.16}$$

where L, P are the line number and pixel number with respect to the *M*th IFG, respectively, $|\gamma|^{M}$ (l, p) is coherence value of the pixel at (l, p) while γ_{GGC}^{M} is the overall coherence value for the *M*th IFG.

After obtaining all these GGC values and sorting them into ascending order, the bottom *"$\hat{p}$"* percentage IFGs are selected as the optimal combination for the subsequent process. Generally, the value of *"$\hat{p}$"* needs to satisfy two requirements: (1) includes all the image acquisitions, and (2) cannot be too large, otherwise, would degrade the coherence selection.

3.2.1.4 Estimate the maximum annual subsidence rate

Indeed, before conducting the TS-InSAR analysis, it is always necessary to estimate the achievable maximum subsidence with the current dataset. The simplest model is given in equation 3.17.

$$D_{\max} = \pm \frac{365}{\Delta T_{\max}} \cdot \frac{\lambda}{4} \tag{3.17}$$

where $\Delta T_{\max}$ is the maximum temporal baseline of all IFGs, λ is the wavelength of the sensor, while $D_{\max}$ is the maximum annual subsidence which can be estimated.

3.2.2 Measurement scatterer pixel selection

For all the TS-InSAR methods, the phase ambiguity is actually resolved over the so-called MS pixels, which could remain the low-phase dispersion in the temporal domain. The following are the most commonly used techniques for selecting MS pixels under different conditions.

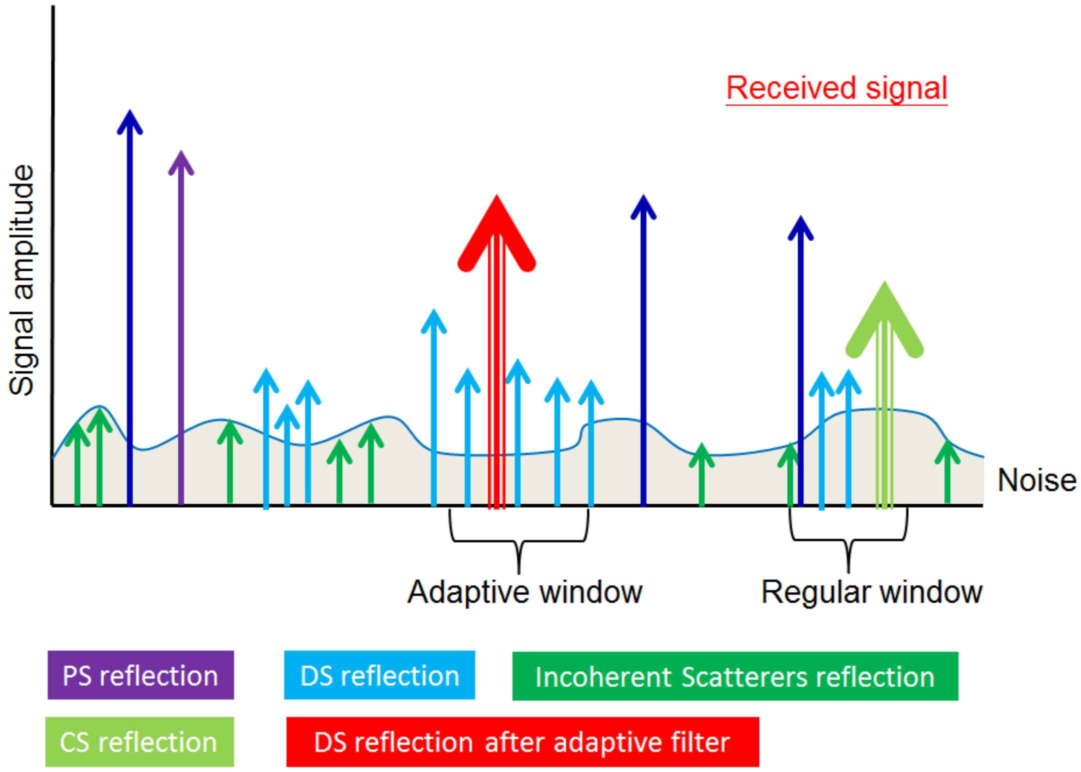

Figure 3.3 Reflected signals received from PS, DS, CS, refined DS and Incoherent Scatterers pixels.

3.2.2.1 Persistent scatterer pixel selection

Suppose that N input slave SAR images have been co-registered to a common master image and N IFGs have generated accordingly. Since the interferometric phase detected by the SAR sensor is modulo 2π and can be affected by various factors, such as deformation and DEM error, it is very difficult to assess the interferometric phase stability along the image stack for individual pixels. Ferretti et al. (2000) noted that the phase dispersion of a pixel exhibits to be small with little variation if the corresponding amplitude value along the image stack is relatively large. This suggests that the time series amplitude values of each pixel can be analysed to evaluate the phase stability. The amplitude dispersion method invented by Ferretti et al. (2001) can be exploited to select PS pixels based on their amplitude stability along the image stacks.

$$D_A \equiv \frac{\sigma_A}{\mu_A} \cong \sigma_\phi \tag{3.18}$$

where μ_A is the mean value, σ_ϕ and σ_A are the phase and amplitude standard deviation value with respect to the pixel along image stacks, respectively. D_A is the amplitude dispersion index.

A numerical simulation carried out by Ferretti et al. (2001) and Kampes (2006) shows that Equation 3.18 can be considered as a good estimation of the phase dispersion when $D_A < 0.25$ (Figure 3.6) while the correlation between D_A and σ_ϕ is getting weaker once the value goes beyond 0.25. Ferretti et al. (2001) pointed out that the theoretical limit of $\sqrt{(4-\pi)/\pi} \simeq 0.52$ can be approached for D_A under Rayleigh distribution. Nevertheless, D_A has been exploited by the majority of the single-master based TS-InSAR methods and the typical threshold is between 0.25 and 0.4. It is worth mentioning that the amplitude dispersion method for selecting PS pixels is applied over full resolution pixel (where one or two dominant scatterers may exist) without considering the neighboring pixels. Due to the distinctive characteristics of this method, these dominant scatterers are often man-made structures, such as buildings, bridges, metallic objects, pylons, etc., which mostly located in urban regions. As a result of it, the density of PS pixel is usually very high (> 100 PS km^{-2}) in urban areas while the counterpart density is typically very low (< 10 PS km^{-2}) over rough terrain and non-urban areas which are characterized by surface or volume scattering phenomena, or reflectivity inhomogeneous scatterers.

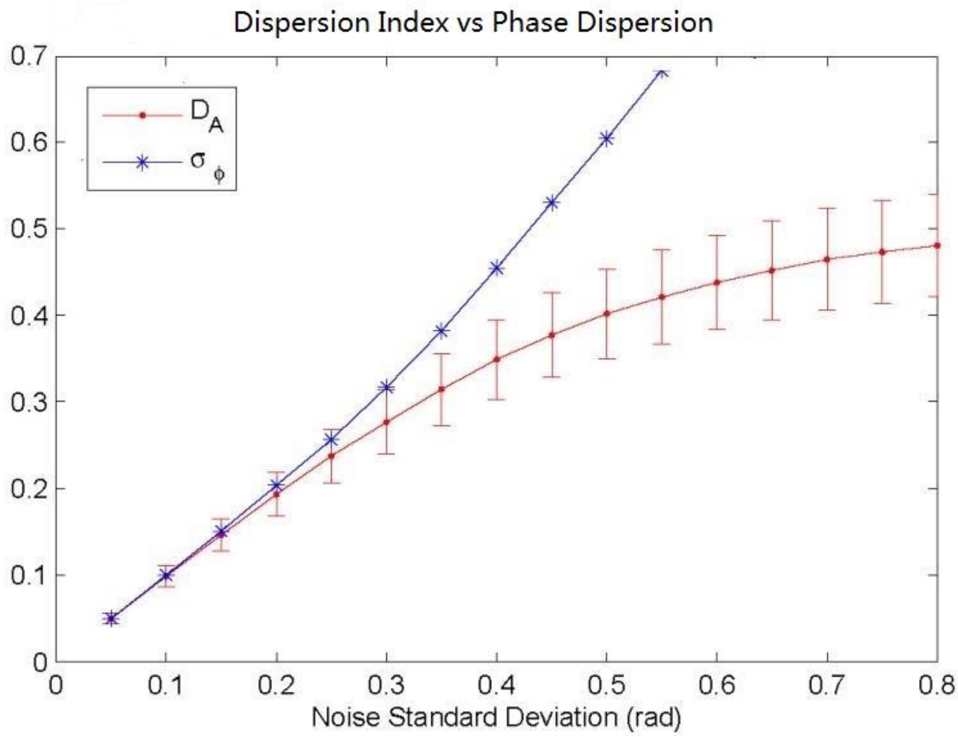

Figure 3.4 Amplitude dispersion simulation result modified from (Ferretti et al., 2001; Ng, 2010).

where signal model: $z_k = g + n_k$ (k =1, 2, …, K, where K is the number of simulated images used and is set to 34), the value of g is fixed to 1, while the noise standard deviation with respect to both the real and imaginary part of n_k is gradually increased from 0.05 to 0.8. In total 5000 estimates of the mean phase standard deviation $\boldsymbol{\sigma_{\emptyset}}$ (blue line) and the average amplitude dispersion index $\boldsymbol{D_A}$ (black line) is carried out for the simulation. The x-axel represents the noise standard deviation while the y-axel is the mean value of the amplitude dispersion index and the phase standard deviation, respectively.

3.2.2.2 Distributed scatterer pixel selection

To overcome the issue of low density of PS pixels over non-urban regions, the concept of Distributed Scatterer (DS) pixels was first introduced by Ferretti et al. (2011), which typically can be detected from homogeneous field, such as debris flow, desert regions, scattered outcrops etc. (the magnitude difference of DS and PS pixels can be referred to Figure 3.5). Unlike PS pixel, DS pixel is a group of homogeneous scatterers within a specified search window which share similar homogenous behaviours (Goodman, 1976) and is often modelled by a complex circular Gaussian return (Bamler and Hartl, 1998). Distributed scatterer mechanism is trying to find these statistical homogenous (SH) small scatterers within a kernel box centred at the distributed point, whose SNR can be significantly improved through an adaptive filtering operation.

The most commonly used method for DS pixel selection is Kolmogorov-Smirno (KS) test (Ferretti et al., 2011) and the equation is given as:

$$D_{KS} = \max_{x \in \{x_{m,i}, x_{n,i}\}} \left| \hat{F}_m(x) - \hat{F}_n(x) \right| \tag{3.19}$$

where *m* is the targeted pixel, *n* is the pixel within a specified search window centred at *m*, *i* = 1,…, *N*+1, $\hat{F}_m(x)$ and $\hat{F}_n(x)$ are the empirical cumulative distribution functions (ECDFs) of amplitude with respect to the pixels at *m* and *n*, respectively. The null hypothesis will be accepted with level α if the equation 3.20 is satisfied. In other words, pixels *m* and *n* can be considered as homogeneous candidates under this circumstance.

$$D_{KS} < \sqrt{\frac{2}{N+1}} K_{\alpha} \tag{3.20}$$

where *N+1* is the number of image stacks, K_a is the Kolmogorov distribution at the α percentile level, and the values of the most common K_a are given in Table 3-2.

Table 3-1 The value of K_a for the most common levels of $\boldsymbol{\alpha}$

α	0.10	0.05	0.025	0.01	0.005	0.001
K_a	1.22	1.36	1.48	1.63	1.73	1.95

An alternative nonparametric test used for DS identification is Anderson-Darling (AD) test other than KS test (Parizzi and Brcic, 2011). AD test considered to be more powerful for testing normality because KS test can lead to blurry features over low contrast areas once the difference among homogeneous targets is small. The equation for selecting DS pixels using AD test is given in equation 3.21.

$$A = \sqrt{\frac{N+1}{2} \sum_{x \in \{x_{m,i}, x_{n,i}\}} \frac{(\widehat{F}_m(x) - \widehat{F}_n(x))^2}{\widehat{F}_{mn}(x)(1-\widehat{F}_{mn}(x))}} \tag{3.21}$$

where $\widehat{F}_{mn}(x)$ is the ECDF of the pooled distribution by integrating two independent datasets, $x_{m,i}$ and $x_{n,i}$, $i = 1, 2, ..., N+1$, into a compound one. The null hypothesis will be rejected with the AD statistic value *A* less than a threshold value.

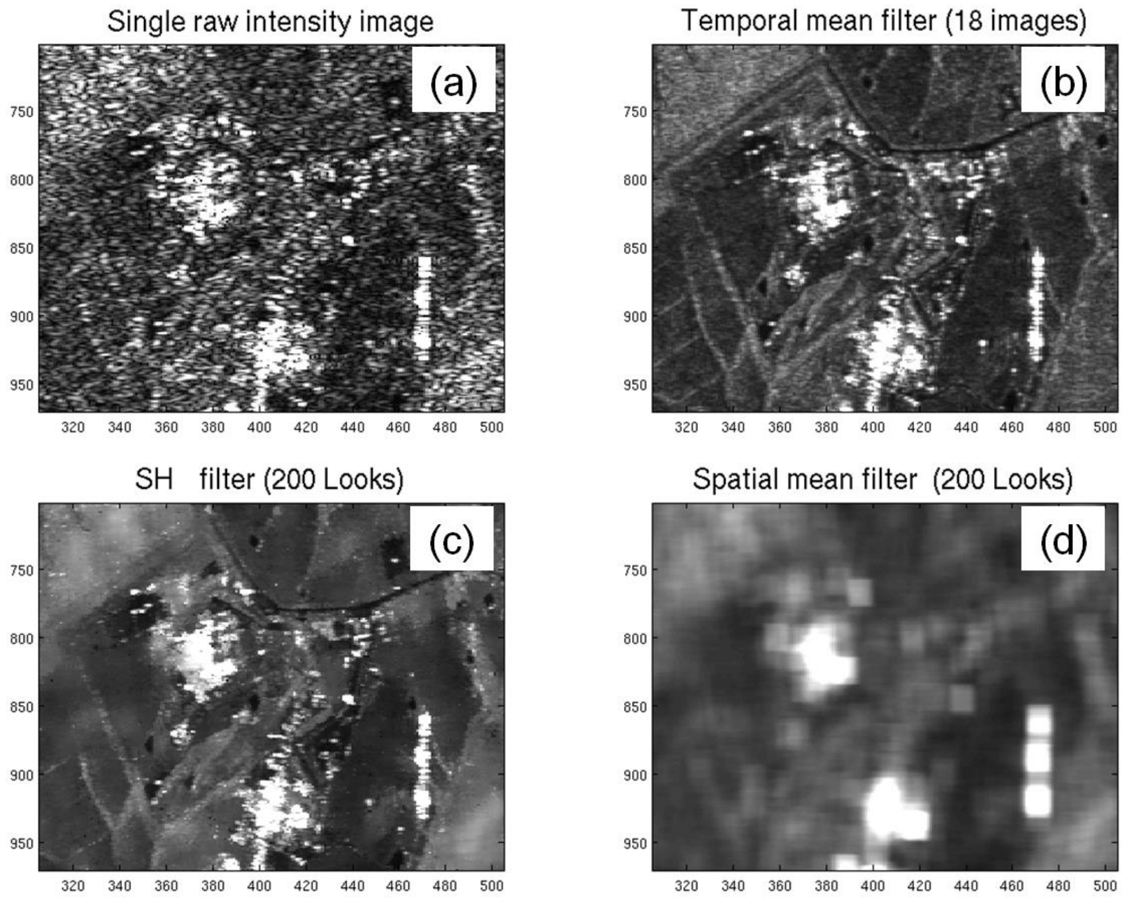

Figure 3.5 Comparison of the (a) individual ALOS-1 Intensity image, (b) after temporal mean filtering, (c) after the SH filtering (20 × 10), and (d) after the spatial mean filtering (20 × 10)

In addition, during the SH pixels selection, the dimension of the spatial widow for the search of neighbouring SH pixels is based on the actual line & pixel number multiplying a proper coefficient (e.g. the typical search window size for ALOS-1 PALSAR FBS, ENVISAT ASAR and Sentinel-1 Interferometric Wide Swath (IWS) are 20 × 10, 31 × 6 and 10 × 20, respectively) and image pixels are considered as DS candidates with SH pixels higher than a certain threshold 20 (at which level PS pixels can be least affected). Following Ferretti et al. (2011), a maximum likelihood

(ML) estimator is then exploited to estimate the optimal phase based on the coherence matrix by using all possible interferometric phase combinations and the equation can be expressed as:

$$\hat{\lambda} = \arg\min_{\lambda}\{\Theta^H (\left|\hat{\Gamma}\right|^{-1} \circ C)\Theta\} \tag{3.22}$$

where ^{H} and ° stand for the conjugate transpose and Hadamard operator, respectively. The *N+1* unknown phase observations with respect to each InSAR image are given as $\lambda = [\theta_1, \theta_2, \cdots, \theta_{N+1}]^T$. Θ is the complex counterpart of λ and is expressed as $\Theta = \exp(j\lambda)$. To decrease the complexity of the solution space, the first unknown θ_1 generally can be fixed to zero (Zhang et al., 2016). Γ and C are the coherence and covariance matrix, respectively. The relationship between them is as follows:

$$C = \Gamma \circ (\sigma\sigma^H) \tag{3.23}$$

where the vector $\sigma = [\sigma_1, \sigma_2, \cdots, \sigma_{N+1}]^T$ represents the data standard deviations. To solve equation 3.23, normally a quasi-Newton based LBFGS (Limited memory Broyden-Fletcher-Goldfarb-Shannon) algorithm would be adopted, which is basically designed for unconstrained nonlinear optimization issues. At last, the good-of-fitness value γ_P is used to assess the quality of the optimized phase of DS candidates.

$$\gamma_P = \frac{1}{N^2 + N} \sum_{m=1}^{N+1} \sum_{n \neq m}^{N+1} e^{j\varphi_{mn}} e^{-j(\theta_m - \theta_n)} \tag{3.24}$$

where φ_{mn} is the spatially filtered phase; θ_{m} and θ_{n} are the optimized phases with respect to images m and n, respectively. The null hypothesis will be accepted if γ_P is higher than a certain threshold, and DS candidates thus can be considered as DS pixels.

3.2.2.3 Coherent scatterer pixel selection

InSAR coherence is commonly used to assess the quality of the local IFG, which is also being used to select the Coherent Scatterer (CS) candidates when the multi-master stacking strategy, e.g. SBAS approach, is applied. The basic estimation is conducted over a pre-defined window $M \times N$ and the coherence value is obtained by estimating the correlation values within the search window:

$$|\gamma| = \frac{\left| \sum_{m=1,n=1}^{M,N} y_M^{m,n} y_S^{m,n*} \right|}{\sqrt{\sum_{m=1,n=1}^{M,N} |y_M^{m,n}|^2 \sum_{m=1,n=1}^{M,N} |y_S^{m,n}|^2}} \tag{3.25}$$

where $y_M^{m,n}$ and $y_S^{m,n}$ are the complex values with respect to the master and slave image at the position m and n within the search window (the full size is $M \times N$), * is the complex conjugate operator. It can be seen from the equation 3.25 that the maximum value of 1 for $|\gamma|$ can only be achieved when both $y_M^{m,n}$ and $y_S^{m,n}$ are identical. Any changes that make these two values different will result in decreasing the coherence value.

Figure 3.7 (c) and (d) demonstrate the efficiency of using both the SH filtering and the spatial mean filter over the intensity image stacks. The kernel box for both analyses is 20 × 10, which is dependent on the ratio value between the line number and pixel number of the real single-polarized ALOS-1 dataset. It is clear that SH filtering is entirely capable of preserving high-quality information compare to the counterpart spatial mean filtering.

3.2.2.4 Maximum likelihood scatterer selection

The Maximum Likelihood Estimation (MLE) approach is first suggested by Shanker and Zebker (2007) to identify coherent points for their TS-InSAR processor, and the basic model is a function of the signal-to-clutter ratio γ, which is given in equation 3.26.

$$P(\phi) = \frac{\cos^2\phi - \beta_\phi^2}{2\pi\cos^2\phi} \cdot \frac{1}{1-\beta_\phi^2} \cdot \left\{ 1 + \frac{\beta_\phi \cdot \arccos(-\beta_\phi)}{\sqrt{1-\beta_\phi^2}} \right\} \tag{3.26}$$

$$where \qquad \beta_\phi = \frac{\gamma}{\gamma+1}\cos\phi$$

Given a total number of N IFGs, the value of γ is achieved by maximizing $P(\gamma \mid \phi_{n_1}, \phi_{n_2}, ..., \phi_{n_N})$, where $n_1, n_2, ..., n_N$ are the differential interferometric phase value at pixel n in N IFGs. $P(R|Q)$ is the conditional probability of R for event Q. According to Bayers' rule, the following equation is derived:

$$P(\gamma \mid \phi_{n_1}, \phi_{n_2}, ..., \phi_{n_N}) = \frac{P(\phi_{n_1}, \phi_{n_2}, ..., \phi_{n_N} \mid \gamma) \cdot P(\gamma)}{P(\phi_{n_1}, \phi_{n_2}, ..., \phi_{n_N})} \tag{3.27}$$

Within equation 3.27, since the term $P(\phi_{n1},\phi_{n2},...,\phi_{nN})$ is independent of γ, the equation can be solved by maximizing the numerator with respect to each value of γ. Under the assumption that $P(\gamma)$ is constant for all γ, equation 3.27 can be resolved by maximizing the following component.

$$P\left\langle \phi_{n_1} \middle| \gamma \right\rangle \cdot P\left\langle \phi_{n_2} \middle| \gamma \right\rangle ....P\left\langle \phi_{n_N} \middle| \gamma \right\rangle, \qquad \forall\gamma \tag{3.28}$$

The estimated maximum likelihood value γ is then compared to the pre-defined threshold value $\gamma_{threshold}$ which is also dependent on various situations, and the MS candidates with γ exceeding the threshold can be accepted as the MS pixels.

3.2.2.5 Offset deviation estimation

Given the fact that the majority of the TS-InSAR analyses are human-involved approaches and many parameters, e.g. the patch size and critical threshold values, are highly dependent on individual's experience, it is challenging to balance the phase quality and the proper spatial density of the MS pixels without a priori knowledge. Based on the fact that the offsets estimated from strong scatterers are less sensitive to the oversampling factor and the window size compared to those incoherent scatterers (Bamler and Hartl, 1998), Zhang et al. (2011) proposed an amplitude based method to select the MS candidates by taking advantage of the standard deviation of the estimated co-registration offsets. The detailed algorithm contains two steps: 1) for each individual SAR image, the co-registration function is applied to estimate an offset vector at pixel *i* by changing the window size gradually from small patches to large patches (from 8 × 8 to 64 × 64 indicating t_{i1} to t_{i4}) and the associated equation is as equation 3.29 and 2) the standard deviation value of the vector OT_i is estimated and individual pixel can be selected as MS pixel only if the corresponding $std(OT_i)$ is smaller than $std_{threshold}$, which is an experience-based value.

$$
\begin{aligned}
&OT_i = \left[ot_{i1}, ot_{i2}, ..., ot_{iN}\right] \\
&std(OT_i) < std_{threshold}
\end{aligned}
\tag{3.29}
$$

where ot_{ij} , $j = 1, 2, 3 \ldots, N$ represents the iteration times at the ith pixel.

3.2.3 Parameters estimation

3.2.3.1 Parameters solved over points

Least squares (LS) approach is the basic model adopted by the SBAS method to solve the unknown parameters mean velocity (v_x) and DEM error (h_x) since an increasing number of deformation parameters would decrease the stability of the estimation process (Van Leijen and Hanssen, 2007). $\Delta\phi^N_{unwrapped,x}$ is the unwrapped observation phases at the multi-looked xth CS pixel, and can be modelled as in the equation 3.30:

$$
\Delta\phi^N_{unwrapped,x} = -\frac{4\pi}{\lambda}(v_x T^N + d^N_x - \frac{B^N_{\perp,x}}{R_x \sin\theta_x} h_x) + \phi^N_{Atm,x} + \phi^N_{Orbit,x} + \phi^N_{Noise,x} \tag{3.30}
$$

where T^N is the time difference between two acquisitions, v_x is the mean velocity, $B^N_{\perp,x}$, θ_x are the local perpendicular baseline and local incidence angle, respectively; and h_x is the DEM error at pixel x. The last three parts are phase contributions from atmospheric artefacts, orbit error and random noise. Considering a set of unwrapped differential IFGs, equation 3.30 can be rewritten as:

$$\Phi_{unwrapped,x} = A_x \begin{bmatrix} h \\ v \end{bmatrix} + \varepsilon_x \quad (3.31)$$

where $\Phi_{unwrapped,x}$ represents the input observations, which are unwrapped at CS pixels, A_x is a the constant term whose elements include $B_{\perp,x}^{N}$, θ_x, T^N, R_x, and λ while ε_x represents the remaining components, which are contributed by nonlinear deformation, atmospheric artefacts, orbital error and noise. These two parameters can be estimated through a LS approach:

$$\begin{bmatrix} h \\ v \end{bmatrix} = \left(A^T A\right)^{-1} A^T \Phi_{unwrapped,x} \quad (3.32)$$

3.2.3.2 Parameters solved over arcs

For single-master based TS-InSAR methods, the phase expression $\Delta\varphi_x^N$ in differential IFG N at pixel x can be denoted as:

$$\Delta\phi_{wrapped,x}^{N} = -\frac{4\pi}{\lambda}(v_x T^N + d_x^N - \frac{B_{\perp,x}^{N}}{R_x \sin\theta_x} h_x) + \phi_{Atm,x}^{N} + \phi_{Orbit,x}^{N} + \phi_{Noise,x}^{N} \quad (3.33)$$

where $\Delta\phi_{wrapped,x}^{N}$ is ambiguous and denoted as the wrapped interferometric phase at single-looked xth MS pixel.

Since the phase observation of each MS pixel is wrapped, sparse phase unwrapping algorithm proposed by Costantini and Rosen (1999) can be applied to solve the phase ambiguity over these sparse MS pixels. The successful application of this algorithm requires the phase difference between adjacent pixels within the interval $\left(-\pi, \pi\right]$ (Chen and Zebker, 2002). However, this situation can hardly be met, especially for 1) IFGs with large temporal baseline, and 2) SAR data acquired in short wavelength, e.g., C-band and X-band, resulting in the unwrapped phase difference larger than π. To solve this problem, triangluar irregulation network (TIN), which is constructed based on a nearly optimal and unique triangulation – Delaunary triangulation, was introduced to link all these MS pixels and estimate the phase difference between nearby pixels, e.g. x, y. Each pair of nearby pixels is referred to as arc in this context. Under the assumption that atmospheric and noise artefacts are spatially correlated, the double-difference phases are estimated over arcs in order to reduce the effect of atmospheric and noise effects that may invalidate the velocity/DEM-error model. Thus, the phase difference between two adjacent pixels can be obtained as:

$$\Delta\phi^{N}_{wrapped,x,y} = -\frac{4\pi}{\lambda}(\Delta v_{x,y}T^{N} - \frac{B^{N}_{\perp,x,y}}{R_{x,y}\sin\theta_{x,y}}\Delta h_{x,y}) + \sigma^{N}_{sum,x,y} \tag{3.34}$$

where $\Delta v_{\mathrm{x,y}}$ is the velocity difference; $B^{\mathrm{K}}_{\perp,\mathrm{x,y}}$ and $\theta_{\mathrm{x,y}}$ are the mean local perpendicular baseline and local incidence angle, respectively; and $\Delta h_{\mathrm{x,y}}$ is the average DEM error corresponding to pixels *x* and *y*. The last term $\sigma^{N}_{sum,x,y}$ is the residual phase contributed by un-modelled nonlinear displacement component, atmospheric error, orbit error and noise error.

Indeed, most of the TS-InSAR method, e.g. PSInSAR™ and Spatio-Temporal Unwrapping Network (STUN) methods (Kampes, 2006; Ferretti et al., 2001), estimate the two unknown values (v_x) and (h_x) at the *x*th single-looked MS pixel over the arcs of TIN. Alternatively, Liu et al. (2009a) proposed a freely connected network (FCN) to connect all nearby pixels whose distances are less than a pre-defined length. This method is fully capable of generating 30 times more observations compare to the TIN based cases, and can be considered useful when dealing with small stacks of MS pixels as there are more redundant observations to enhance the reliability of the measurements. However, the computational load will significantly increase once dealing with larger stacks of MS pixels, e,g., more than 20, 000, 000 points (Ge et al., 2014) and FCN based analysis is not suited anymore.

At this stage, the first two parameters $\Delta h_{\mathrm{x,y}}$ and $\Delta v_{\mathrm{x,y}}$ with respect to each arc can be estimated from the IFG stacks by solving a minimization problem:

$$
\begin{aligned}
\arg\max_{v_{x,y},\Delta h_{x,y}} &= \frac{1}{N}\left|\sum_{n=1}^{N} e^{-j.(\Delta\phi^N_{wrapped,x,y}-\Delta\phi^N_{model,x,y})}\right| \\
\Delta\phi^N_{\mathrm{mod}el,x,y} &= -\frac{4\pi}{\lambda}(\Delta v_{x,y}\cdot T^N - \frac{B^N_{\perp,x,y}}{R_{x,y}\cdot\sin\theta_{x,y}}\cdot\Delta h_{x,y})
\end{aligned}
\tag{3.35}
$$

where $j=\sqrt{-1}$, $\Delta\varphi^{\mathrm{N}}_{\mathrm{wrapped,x,y}}$ is the observed phase while $\Delta\phi^N_{\mathrm{mod}el,x,y}$ is the phase generated from the deformation model. Since the above equation represents the phase differences between two adjacent pixels within one IFG, and the observed phase value is modulo 2π, the phase model along the IFG stack can be considered as a linear system.

3.2.3.2.1 Two-dimensional Search Solution

The two-dimensional search solution was proposed by Ferretti et al. (2001) to solve the minimization problem. Based on a priori knowledge, appropriate variation ranges (h_1, h_2 & v_1, v_2) with small sampling intervals (s_1 & s_2) can be set for $\Delta h_{\mathrm{x,y}}$ and $\Delta v_{x,y}$, respectively. The whole searching area can be considered within a window size of

$\left|(h_1 - h_2)/s_1\right| \times \left|(v_1 - v_2)/s_2\right|$ and the searching process will not stop until the appropriate $\Delta h_{x,y}$ and $v_{x,y}$ is found that could maximise equation 3.35. It is worth noting that the search solution can only be successfully performed under the assumption that $\sigma^N_{sum,x,y} < \pi$, which is true in most cases.

3.2.3.2.2 Integer Least-Squares approach

Alternatively, an integer least-squares (ILS) estimator, AMBiguity Decorrelation Adjustment (LAMBDA) was exploited by Kampes (2006) to estimate $\Delta v_{x,y}$ and $\Delta h_{x,y}$. LAMBDA was originally developed by Teunissen (1995) for fast GPS double difference integer ambiguity estimation. Kampes and Hanssen (2004a) then adopted this estimator for the time-series InSAR analysis to unwrap the phase in time. The modelled system of observation equation can be written as equation 3.36 considering the 2π integer.

$$\underset{N\times 1}{\begin{bmatrix} \Delta\phi^1_{x,y} \\ \vdots \\ \Delta\phi^N_{x,y} \end{bmatrix}} = \underset{N\times N}{\begin{bmatrix} -2\pi & & \\ & \ddots & \\ & & -2\pi \end{bmatrix}} \underset{N\times 1}{\begin{bmatrix} n^1_{x,y} \\ \vdots \\ n^N_{x,y} \end{bmatrix}} + (-\frac{4\pi}{\lambda}) \underset{N\times 2}{\begin{bmatrix} T^1 & \dfrac{B^1_{\perp,x,y}}{R_{x,y}\sin\theta_{x,y}} \\ \vdots & \vdots \\ T^N & \dfrac{B^N_{\perp,x,y}}{R_{x,y}\sin\theta_{x,y}} \end{bmatrix}} \underset{2\times 1}{\begin{bmatrix} \Delta v_{x,y} \\ \Delta h_{x,y} \end{bmatrix}} + \sigma \tag{3.36}$$

where $[\Delta\varphi^1_{x,y}, \ldots, \Delta\varphi^N_{x,y}]^T$ are N observed phase difference between pixel x and pixel y along IFG stack, while $[n^1_{x,y}, \ldots, n^N_{x,y}]^T$ are N integer phase components of the observed phase, σ is the combination of the residual phase component. For simplicity, equation 3.36 can be considered as a linear system of equation and thus rewritten as:

$$\Phi = An + Bp + \sigma \tag{3.37}$$

where Φ is the matrix of the double-difference phase observation between pixel x and pixel y, A and B are constant terms, n and p are the vector of integer-valued and real-valued unknown ambiguities, respectively.

Since there are a total number of $N + 2$ unknown variables within the N equations in equation 3.37, two pseudo-observations for each unknown parameters are added based on a priori information to the system of equations to give the design matrix full rank. Followed by a three-step procedure to resolve the system of equations: 1) the "float solution" for the integer parameter, $\breve{n}$, can be computed using the corresponding variance-covariance matrix (VC-matrix) $Q_{\hat{n}}$, 2) the "fixed solution", $\hat{n}$,can be determined from $\breve{n}$ and $Q_{\hat{n}}$ using LAMBDA, and 3) the "fixed solution" for the real-valued parameter, $\hat{p}$, can be estimated through a least-squares estimator: $\hat{p} = \left(B^T Q_\Phi B\right)^{-1} B^T Q_\Phi^{-1}(\Phi - A\hat{n})$, where Q_Φ is the VC-matrix of the observed phase difference Φ and is used to weight the contribution of each SLC image. It is worth mentioning that the correctly constructed VC-matrix could result in more accurate estimation (Kampes and Hanssen, 2004b).

According to Kampes (2006), the stochastic model of a SAR interferometric phase can be considered due to only the noise effect, whilst the variation of the atmosphere is neglected given the fact that all estimation are performed between points and the distances between them are small. Q_{Φ} is given as:

$$Q_{\Phi} = \sum_{n=0}^{N} \sigma_{Noise,n}^{2} Q_{n} \qquad where \quad Q_{n} = \begin{cases} 2E_{N} & if \quad n = 0 \\ 2i_{n}i_{n}^{T} & if \quad n = 1, \ldots, N \end{cases} \tag{3.38}$$

where $\sigma_{Noise,n}^{2}$ is the phase variance of the estimated noise within image acquisition *n*, and σ_{Noise}^{2} of $(20°)^2$ and $(30°)^2$ are normally given to master and slave images, respectively (Kampes, 2006), E_N is a $N \times N$ matrix of ones, while $i_n i_n^T$ is a $N \times N$ matrix with a single one at position (*n*, *n*). In other words, the whole estimation process can be considered as a two-step empirical method. Firstly, a weighted ILS estimator is applied to estimate the unknown two parameters and the weighting matrix is known as a priori VC-matrix, which is calculated based on a stochastic model (3.38). Secondly, the phase residuals with respect to arcs within each IFG can be estimated using an ordinary Least Squares estimation. Later, the derived estimation will be used to determine the variance component of each SAR scene.

Assume that all the $\Delta h_{x,y}$ and $\Delta v_{x,y}$ values have been estimated over arcs of the network. The ensemble phase coherence (EPC) also known as $\gamma(x, y)$ is then introduced to assess the reliability of the corresponding arc, which is first mentioned by Ferretti et al. (2001). As the value of EPC ranges from 0 to 1, and higher value of EPC represents more accurate estimation, arcs with EPC less than a certain threshold are assumed to be unreliable and would be removed from further analysis.

Afterwards, isolated MS pixels as a result of stability assessment shall be deleted as well (Ng et al., 2012b).

$$\gamma(x,y) = \frac{1}{N} \cdot | \sum_{n=1}^{N} e^{-j\cdot(\Delta\varphi_{x,y}^{N} - j\cdot\varphi_{\mathrm{model},x,y}^{N})} \tag{3.39}$$

3.2.4 Parameters integration

After that, the absolute value $v_x(v_y)$ and $h_x(h_y)$ with respect to each MS pixel need to be recovered from $\Delta v_{x,y}$ and $\Delta h_{x,y}$, and the basic function for the absolute inversion (take $v_x(v_y)$ as an example) is shown in Equation 3.40. Since $v_{x,y}$ is actually the velocity difference between pixels x & y and the absolute velocity with respect to each MS pixel can be calculated once the reference MS pixel was selected with deformation value assumed to be 0.

$$\Delta V = AV + \varepsilon \qquad where$$

$$\Delta V = \begin{bmatrix} v_{2,1} \\ v_{3,1} \\ \vdots \\ v_{3,2} \\ v_{4,2} \\ \vdots \\ v_{s,s-1} \end{bmatrix} \quad A = \begin{bmatrix} -1 & 1 & 0 & \cdots & 0 \\ -1 & 0 & 1 & \cdots & 0 \\ \vdots & \vdots & \vdots & \vdots & \vdots \\ 0 & -1 & 1 & \cdots & 0 \\ 0 & -1 & 0 & \cdots & 0 \\ \vdots & \vdots & \vdots & \vdots & \vdots \\ 0 & 0 & 0 & -1 & 1 \end{bmatrix} \quad V = \begin{bmatrix} v_1 \\ v_2 \\ v_3 \\ \vdots \\ v_{s-1} \\ v_s \end{bmatrix} \tag{3.40}$$

where s is the number of measurement points, ε is the residual value, the vector on the left hand side is the estimated velocity differences at the arcs, the design matrix on the right hand side relates to the estimated arcs, while the vector on the right hand side is the absolute velocity value corresponds to each individual MS pixel in LOS direction.

3.2.4.1 Ordinary Least Squares

Ordinary Least Squares (OLS) method is a standard approach to solve the overdetermined systems under the assumption that there is constant variance in the errors, and the 'LS' typically means to minimise the sum of the squares of the residuals with respect to every single equation. Therefore, the ordinary least squares solution can be applied to solve Equation 3.40 and is given as (*P* is the number of arcs):

$$\widehat{V}_{OLS} = \arg\min_{V} \sum_{p=1}^{P} \varepsilon_p^{*2} = (A^T A)^{-1} A^T \Delta V \qquad (3.41)$$
$$where \qquad p = 1, 2, \cdots, P$$

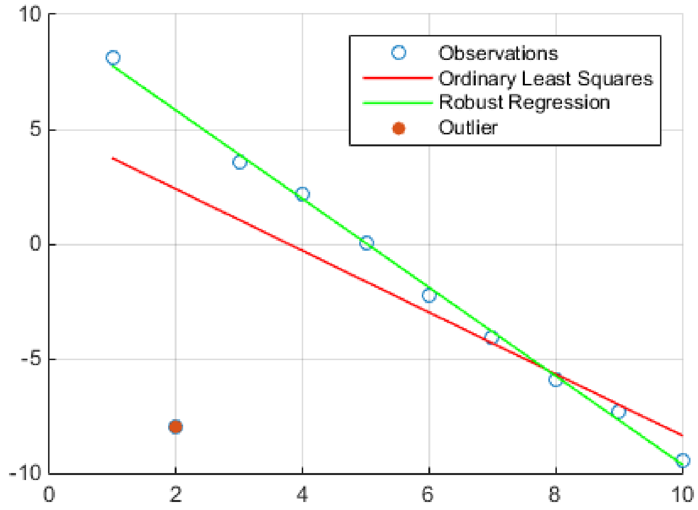

Figure 3.6 The Ordinary Least-Squares fit is more influenced by the outlier than the Robust Regression fit

3.2.4.2 Robust Regression

It is worth mentioning that biased estimation on some arcs may degrade the accuracy of the estimated absolute velocity value (Figure 3.8). Therefore, a maximum likelihood regression-based M-estimator is introduced (Huber, 1964; Zhang et al., 2013). M stands for maximum likelihood.

Suppose there is a data set of *P* available such that;

$$\Delta V_p = A_p V + \varepsilon_p \Rightarrow \varepsilon_p(V) = \Delta V_p - A_p V, \quad p = 1, 2, \cdots, P \tag{3.42}$$

M-estimator attempts to minimise the sum of a chosen function $\beta(.)$, which is related to the likelihood function for a suitable assumed residual distribution. M-estimator is formally given by:

$$\widehat{V_M} = \arg\min_V \sum_{p=1}^{P} \beta(\varepsilon_p(V)) \quad p = 1, 2, \cdots, P \tag{3.43}$$

Minimization of Equation 3.43 is achieved primarily by the following two steps: 1) a set of *P* nonlinear equations can be derived by setting $\frac{\partial \beta}{\partial V_i}$ = 0 for each i = 0, 1, …., *P* – 1.

$$\sum_{p=1}^{P} \psi\left(\varepsilon_p(V)\right) = 0, \tag{3.44}$$

where $\psi(\cdot) = \beta'(\cdot)$, and $\psi(\cdot)$ is known as the influence function.

2) the weighted least squares can be iteratively estimated using iteratively reweighted least squares (IRLS) method until a stopping criterion is met, and the optimised $\widehat{V}$ is obtained following Equation 3.45.

$$\widehat{V}^{(t+1)} = (A^T \left[W^{-1}\right]^{(t)} A)^{-1} A^T \left[W^{-1}\right]^{(t)} \Delta V \qquad t = 1, 2, \cdots \tag{3.45}$$

where $\left[W^{-1}\right]^{(t)} = diag(w_1^{(t)}, ..., w_P^t)$ and t is the iteration numbers.

Given the fact that Huber's method (Huber, 1964) is the most commonly chosen function in the M-estimation, the associated parameters can be expressed as:

$$\begin{aligned}
\beta(r) &= \begin{cases} z^2, & if\ |z| < c; \\ |2z|c - c^2, & if\ |z| \geq c \end{cases} \\
\psi(r) &= \begin{cases} z, & if\ |z| < c; \\ c[\mathrm{sgn}(z)], & if\ |z| \geq c \end{cases} \\
w(r) &= \begin{cases} 1, & if\ |z| < c; \\ c / |z|, & if\ |z| \geq c \end{cases} \qquad where \quad c \approx 1.345
\end{aligned} \tag{3.46}$$

3.2.5 Including less reliable measurement points

Over the years, many times when processing real data, choosing the right trade-off between the selection of highly coherent pixels and the grid sparsity is a challenging task. Increasing thresholds allow selecting high coherent pixels, but the higher sparseness of the pixel grid may lead to unwrapping failures. On the other hand, the introduction of too noisy pixels can also lead to further unwrapping failures as well as integration uncertainty. To adequately address these issues, GEOS-ATSA

(Advanced Time Series Analysis) proposed by Ge et al. (2014) used a three-step processing to solve the phase ambiguity over MS candidates. 1) At the first stage, all these candidates are divided into two sub-groups based on the pre-defined threshold, which is an experience-based value, e.g., pixels satisfy either D_A<0.25 or γ_P>0.75 can be considered within high-quality group (hereafter referring to reliable candidates) while pixels met either 0.25≤ D_A<0.4 or 0.75≤ γ_P<0.4 can be divided into medium-low group (known as less reliable candidates), 2) only reliable candidates are selected to construct the initial traditional triangular irregular network (TIN) and the motion/height-error model is solved over these candidates, and 3) Less reliable pixels are added into the TIN network iteratively based on a gradually increased searching box and the motion/height-error parameters are computed for these new candidates.

3.2.6 Removal of orbit and topography-dependent atmospheric error

In the following context, symbols Φ, φ, ϕ have been used to represent the phase component; therefore, the differences among them should be first outlined here. 1) Φ stands for the phase vector in the spatial domain, 2) φ represents the phase vector in the temporal domain, and 3) ϕ is the individual phase value.

The time-series residual phase of each MS pixel can be estimated after removing the modelled absolute DEM error, and linear velocity from the single-difference phase observation and the referred equation now reads:

$$\underset{P\times 1}{\Phi_{residual}^{wrapped,N}} = \underset{P\times 1}{\Phi_{wrapped}^{N}} - \underset{P\times 1}{\Phi_{\mathrm{mod}el}^{N}} \tag{3.47}$$

where P is the number of MS pixels, $\Phi_{residual}^{N}$ is the residual phase over MS pixels at Nth IFG and mainly consists of atmsophere (mainly tropospheric turbulence and tropospheric stratification) and orbital artefacts, nonlinear motion as well as noise component. A sparse Minimum Cost Flow (MCF) method is applied to the wrapped residual phase $\Phi_{residual}^{wrapped,N}$ to derive the unwrapped residual phase stack $\Phi_{residual}^{unwrapped,N}$ (Ng et al., 2012a; Zhang et al., 2013; Ge et al., 2014).

Since topography plays a significant role in producing atmospheric artifact due to changes in humidity, pressure, temperature as well as the water vapour content between two SAR image acquisitions, this component can be considered as vertically stratified phase delay. According to Hanssen (2001), in most cases, a simple linear model can be used to model this part using the height and unwrapped phase values at the position (p,l):

$$\Phi_{unwrap} = k \cdot H + b \tag{3.48}$$

where $\Phi_{unwrap} = \left[\phi_{unwrap,1}, \phi_{unwrap,2} \ldots, \phi_{unwrap,p}\right]^T$, $H = \left[h_1, h_2 \ldots, h_p\right]^T$, p is the total of MS pixels, k and b are constant terms, respectively. However, purely based on this method may confound with other types of phases, such as tropospheric turbulent, inaccurate satellite orbit, etc.

In addition, a lower-order polynomial fitting method is always being used to remove the phase distortion induced by orbit error (Liu et al., 2014; Rosen et al., 1996; Doin et al., 2009), which is commonly used in the InSAR processing. The coefficients of the polynomial can be determined either under the assumption that there is no deformation occurred in some region of the IFG or by the ground control points (GCPs). In other words, whether the orbital error can be accurately removed is largely dependent on the validity of no-deformation assumption and the precision of GCPs. Nevertheless, it is worth noting that the characteristics of orbital errors is similar to long-wavelength artefacts induced by the inaccurate determination of the sensor position vector, which can hardly be removed from an unwrapped IFG by fitting a low-order polynomial to the long-wavelength signal (Lu and Dzurisin, 2014). Long-wavelength phase can be observed in some cases whilst it also can be obscured by other phase components in other cases. Since the most significant difference between long-wavelength and orbital artefacts is that the latter one is not correlated in temporal domain, the orbital phase error is estimated based on the unwrapped residual phase since the majority of the temporal correlated components have been removed (height information is also included since the vertically stratified phase also has very weak temporal correlation).

$$\Phi_{residual}^{unwrapped,N} = a_0 + a_1 r + a_2 c + a_3 rc + a_4 r^2 + a_5 c^2 + a_6 h(r,c) \tag{3.49}$$

where $\Phi_{residual}^{unwrapped,N}$ is the unwrapped residual phase stacks at the interfergram *N*; *r* and *c* are the row number of column number, respectively; $h(r,c)$ is the topographic height at (*r*, *c*) while a_0, …, a_6 are modelled parameters.

3.2.7 Temporal-spatial filtering operation

After removing the phase components contributed by the tropospheric and orbital effects, the remaining components are given as:

$$\widehat{\Phi}_{residual}^{refined,N} = \Phi_{residual}^{unwrapped,N} - \left\{\widehat{a}_0 + \widehat{a}_1 r + \widehat{a}_2 c + \widehat{a}_3 rc + \widehat{a}_4 r^2 + \widehat{a}_5 c^2 + \widehat{a}_6 h(r,c)\right\} \tag{3.50}$$

where the terms $\widehat{a}_0$, …, $\widehat{a}_6$ are the best fitting coefficients derived from equation 3.49

while $\widehat{\Phi}_{residual}^{refined,N} = \left[\widehat{\phi}_{residual,1}^{N}, \widehat{\phi}_{residual,2}^{N}, ..., \widehat{\phi}_{residual,p}^{N}\right]^T$ $p = 1, 2, ..., P$ is the refined residual phase contributed by tropospheric turbulence, nonlinear motion and noise. Of which, the tropospheric turbulence phase φ_{turb} is considered to be correlated in space and not correlated in time, noise phase φ_{noise} has very weak correlation in both temporal and spatial domain while nonlinear motion is correlated in both time and space. A temporal-spatial filtering, proposed by Ferretti et al. (2001), is carried out to estimate the un-favoured phase components (φ_{turb} + φ_{noise}) based on their specific characteristics. More specifically, the three-step processing is introduced to determine the tropospheric turbulence, and the refined phase over pixel *p* can be written as Equation 3.51.

$$\varphi_{residual,p} = \left[\widehat{\phi}_{residual,p}^{1}, \widehat{\phi}_{residual,p}^{2}, ..., \widehat{\phi}_{residual,p}^{N}\right]^T \tag{3.51}$$

1) First of all, the temporal mean residual phase $\overline{\varphi}_{residual,p}$ needs to be removed from $\varphi_{residual,p}$,

$$\widehat{\varphi}_{residual,p} = \varphi_{residual,p} - \overline{\varphi}_{residual,p} \cdot \kappa \tag{3.52}$$

where $\kappa = [1,1,...,1]^T$ is a N × 1vector of ones.

2) A temporal high-pass filter with a defined triangular window, e.g., 360 days, is applied to remove the temporal correlated component, and the resulted phase is

denoted as $\hat{\varphi}_{residual\_HP,p}$. After this step, the temporally correlated nonlinear motion is removed.

3) A spatial low-pass filter with pre-defined window size, e.g., 2 km × 2 km, is exploited to remove the spatial non-correlated component $\varphi_{noise,p}$ for $\bar{\varphi}_{residual,p}$ and $\hat{\varphi}_{residual\_HP,p}$ and resulting in $\bar{\varphi}_{residual\_LP,p}$ and $\hat{\varphi}_{residual\_HP\_LP,p}$. The estimated tropospheric turbulence phase delay $\varphi_{turb,p}$ at MS pixel p is derived by combining these two components together.

$$\varphi_{turb,p} = \hat{\varphi}_{residual\_HP,p} + \bar{\varphi}_{residual\_LP,p} \tag{3.53}$$

Finally, the nonlinear phase at pixel p can be estimated by subtracting both $\varphi_{turb,p}$ and $\varphi_{noise,p}$ from $\varphi_{residual,p}$ and the equation 3.54 is given as follows:

$$\varphi_{nonlinear,p} = LP\_spatial\left\{\varphi_{residual,p} - \varphi_{turb,p}\right\} \tag{3.54}$$

where $LP\_spatial\{\cdot\}$ is the low pass operator. The nonlinear motion is obtained by multiplying the nonlinear phase component with $-\frac{\lambda}{4\pi}$.

3.3 Tropospheric turbulence and stratified phase delay

As all the current SAR satellites are operated at an altitude of 500 – 800 km (Table 2-1), the electromagnetic wave transmitted from these platforms must go through the atmosphere twice and can be easily affected by the small variation in the index of refraction in the line-of-sight (LOS) propagation (Zebker et al., 1997b). Differences in water vapour content, atmospheric temperature and pressure at two different observations will result in variations of phase values, which will remain in the observed IFG (Ding et al., 2008).

Essentially, the atmospheric phase is caused by electromagnetic wave delay/acceleration when travelling through the troposphere/ionosphere. The detailed information of these two layers is provided in Figure 3.9. Zebker et al. (1997a) reported that particularly for the SIR-C/X-SAR, a variation of 20% in the relative humidity of troposphere could lead to an error of 10 cm to ground subsidence and 80 − 290 m to DEM measurements for baselines ranging from 100 − 400 m when using favourable baseline geometry (Ding et al., 2008; Zebker et al., 1997a). Tropospheric and ionospheric artefacts can be characterised as spatially correlated and temporally uncorrelated due to the fluctuated medium as most atmosphere filters are designed on the basis of these characteristics.

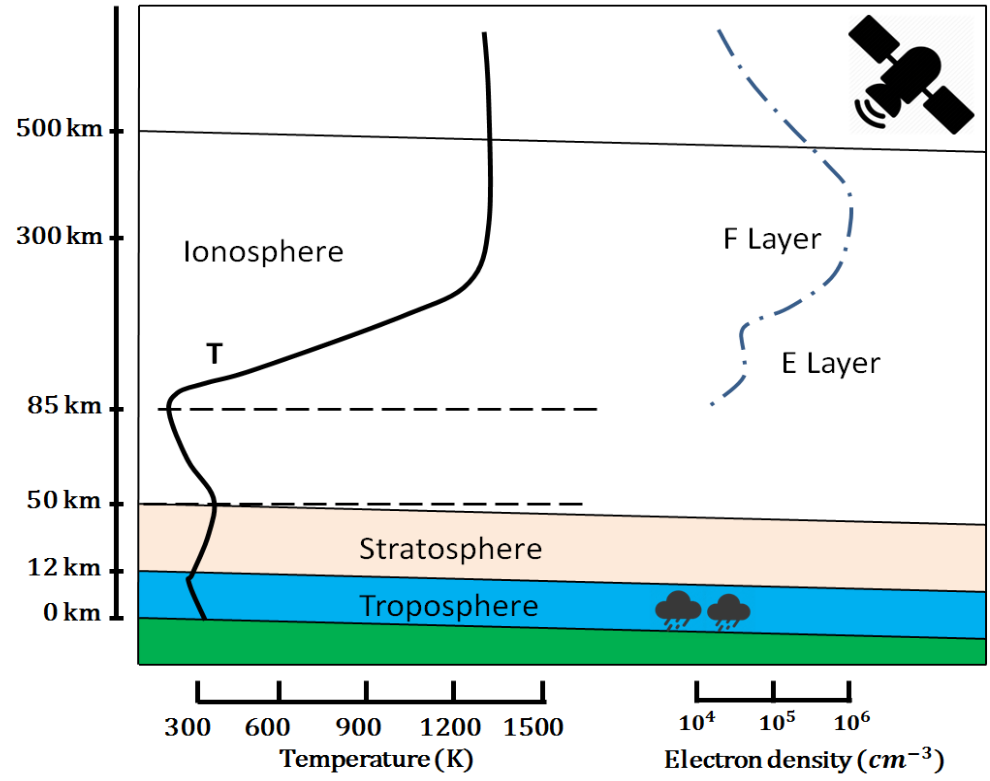

Figure 3.7 Representation of atmospheric layers

More specifically, tropospheric artefact mainly consists of tropospheric turbulence and tropospheric stratification (Jolivet et al., 2011), of which, localised water vapour is considered as the dominant factor to the tropospheric turbulence induced artefact (Li et al., 2006a). Water vapour is generally contained in the near-ground surface troposphere layer, basically up to 2 km from the ground with intense turbulent mixing phenomena. This can affect both flat and mountainous regions and can be eliminated by using statistical estimation method in both spatial and temporal domain (Ferretti et al., 2001; Ng et al., 2012a). The other tropospheric component is the tropospheric stratification, which has a significant impact on the changes in vertical direction. As the part is similar to orbital ramps and DEM errors, it is challenging to distinguish from linear orbit error, especially for longer wavelengths

SAR (Agram and Simons, 2015). It is worth noting that regions with strong topography changes can lead to more severe tropospheric delay as compared to humidity variation. Therefore, the two tropospheric components need to be carefully treated for precise subsidence measurement (Jolivet et al., 2011; Jolivet et al., 2014; Doin et al., 2009).

Also, ionospheric artefact behaves significantly distinct in comparison to tropospheric component as it tends to accelerate the phase of the electromagnetic wave. Theoretically, the ionospheric artefact is proportional to the total electron content (TEC) in the ionosphere layer. For example, a TEC of 1×10^{16} m^{-2} causes an acceleration of about half a cycle for C-band signal. The dispersive ionosphere can also affect the radio signal, which is inversely proportional to the square of the carrier frequency. For instance, if the ionosphere causes 17 m range errors to the L-band signals, it will only cause about 1 m range error to the C-band signals with the same atmospheric conditions and imaging geometry. In addition, 'azimuth streaks" is caused by an equivalent Doppler shift when going through the ionosphere and consequently lead to azimuth pixel shift within the IFGs (Chen and Zebker, 2012). Most studies have shown that the C-band sensors (ENVISAT ASAR, Radarsat-1/2 and Sentinel-1A) usually minimally influenced by the ionospheric delay, in the contrary, L-band sensors, e.g., ALOS-1/ALOS-2, often suffered from the ionospheric disturbance. In general, the local sun time of both ALOS-1 and ALOS-2 sensors is 10:30 am and 10:30 pm, and the ALOS-1/PALSAR observation is assigned to night-time orbit because of the optical sensor availability under the sunlight. Researches show that the amount of TEC at around 10:30 pm could be almost the half of the noon and moreover is unstable due to the TEC decay as the daily behaviour (Mannucci et al., 1998). Nevertheless, as the study of ionosphere is beyond the scope of this research, the ionosphere disturbance is not considered in this thesis.

Experiments have been conducted over the past two decades by many researchers to understand better and mitigate the atmospheric phase delay. Li et al. (2007) used both the Jarque-Bera and the Hinich methods to test the atmospheric signal in four SAR IFGs over Shanghai, and found that the atmospheric signals in all IFGs are non-Gaussian distribution. Onn and Zebker (2006) exploited the "frozen-flow" hypothesis first proposed by Taylor (1938) to correct the atmospheric bias, and proved that additional improvement could be obtained when both prior- and after-GPS measurements of each SAR acquisition are available. Ferretti et al. (2001) exploited the spectral characteristics in designing filters to model and remove atmospheric artefacts from nonlinear deformation.

Many other researchers use external data, namely, meteorological model, GPS, AQUA/TERRA Moderate-Resolution Imaging Spectroradiometer (MODIS) and ENVISAT Medium Resolution Imaging Spectrometer (MERIS) to mitigate these effects (Li et al., 2006b; Li et al., 2006c; Li et al., 2009). Li et al. (2006a) used the concept of power law nature of the atmospheric effects in designing algorithms to mitigate the atmospheric spectrum with meteorological and GPS data. Mathew et al. (2014) proposed a method to correct both tropospheric and ionospheric phase delay using MODIS and TEC data, the final result agrees well with GPS measurement.

Indeed, these methods were mainly based on external data to mitigate the atmospheric effect, and most of them can reduce the effect by about $20-40$ percentages (Ding et al., 2008). Nevertheless, the majority of the methods heavily rely on the atmospheric conditions (e.g. cloud coverage) and availability of other external datasets. Recently, many researchers tried to use Global Atmospheric Model (GAM) to predict the tropospheric stratified phase delays at the SAR image acquisition time (Jolivet et al., 2011; Jolivet et al., 2014; Li et al., 2009). Doin et al. (2009) quantitatively validated the potential of three GAMs: 1) ERA-Interim from ECMWF (European Centre for Medium-Range Weather Forecasts), 2) NARR (the North American Regional Reanalysis), and 3) MERRA (NASA's Modern Era-Retrospective Analysis for Research and Applications) by comparing with empirical corrections. Jolivet et al. (2014) further extended Doin's work and demonstrated the feasibility to predict the tropospheric stratified delay from GAM (~ 50 km). However, Due to the very coarse spatial resolution of the GAM datasets, only the tropospheric effect experiencing with large spatial wavelength can be effectively eliminated, while the counterpart effect with a short wavelength can hardly be influenced, e.g. tropospheric turbulence phase delay.

3.4 InSAR tropospheric stratification correction with GAMs

It is well known that the atmospheric phase delay is caused by air refractivity N between the satellite and the ground surface. The refractivity coefficient of air can be written as follows (Smith and Weintraub, 1953; Baby et al., 1988; Doin et al., 2009; Jolivet et al., 2014):

$$N = (n-1)\times 10^{6} = k_1 \frac{P_d}{T} + k_2 \frac{e}{T} + k_3 \frac{e}{T^2} + k_4 W_{cl} + k_5 \frac{ne}{f^2} \tag{3.55}$$

where T is the temperature in °K, P_d is the partial pressure of dry air in Pa, e is the partial pressure of water vapour in Pa, and n is the refraction index of air, W_{cl} is the cloud content in kg/m^3. ne is the electron density within the ionosphere layer while f is the frequency of the electromagnetic wave. k_1 = 0.776 K Pa^{-1}, k_2 = 0.716 K Pa^{-1}, k_3 = 3.75× 10^3 K^{2}Pa^{-1}, k_4 = 1.45× 10^3 m^{2}kg^{-1} and k_5 = -4.03×10^7 S^{-2} m^3 are constant parameters determined by (Smith and Weintraub, 1953). The first three components are due to the effect of both dry and wet air on air refractivity; the fourth term corresponds to the water content of clouds and is assumed to be included inside the turbulent delay; the fifth term is related to the dispersive effect of ionosphere, which is neglected as we discussed in section 3.3 (all the datasets used in the thesis are in C-band and L-band). Therefore, the modified Equation 4.2 now reads:

$$N = k_1 \frac{P_d}{T} + k_2 \frac{e}{T} + k_3 \frac{e}{T^2} \tag{3.56}$$

The expression of the excess path length $L(h)$ is estimated by calculating the refractivity N between the ground elevation h and a reference elevation h_{ref} (the air refractivity N above which is neglected), which consists of both dry and wet delays, and the equation can be expressed as:

$$L(h) = 10^{-6} \int_{h}^{h_{ref}} \left[k_1 \frac{P(h)}{T(h)} + (k_2 - k_1) \frac{e(h)}{T(h)} + k_3 \frac{e(h)}{T(h)^2} \right] dh \tag{3.57}$$

where the total pressure of moist air is denoted as $P = P_d + e$, according to Baby et al. (1988), Equation 3.57 can be rearranged as:

$$L(h) = 10^{-6} \left\{ \frac{k_1 R_d}{g_m} P(h_0) \left(1 - \frac{\beta}{T_s} h \right)^{\frac{g_m}{R_d \beta}} + \int_{h}^{h_{ref}} \left[(k_2 - \frac{R_d}{R_v} k_1) \frac{e(h)}{T(h)} + k_3 \frac{e(h)}{T(h)^2} \right] dh \right\} \tag{3.58}$$

where the specific gas constant for dry air and water vapour R_{d} and R_{v} are 287.05 J kg^{-1} K^{-1} and 461.495 J kg^{-1} K^{-1}, respectively. g_m = 9.8 m s^{-2}, $P(h_0)$ is the surface pressure at zero elevation, T_s is the surface temperature while β is the temperature lapse rate.

Thus, for a pixel at elevation h with the incidence angle of θ at a given time t, the LOS tropospheric phase delay $\phi_{LoS}^{total}(h,t)$, is given as a function of the excess path length L:

$$\phi_{LoS}^{total}(h,t) = \frac{-4\pi L(h,t)}{\lambda \cos\theta} \tag{3.59}$$

Based on auxiliary datasets like global meteorological records, GAMs is fully capable of estimating the atmospheric elements, such as water vapour pressure, geopotential height of pressure levels and temperature on a global or local grid at two individual acquisition times t_1 and t_2. The predicted absolute tropospheric stratified phase delay (TSPD) thus can be derived as:

$$\Delta\phi_{LoS}^{t_1,t_2}\left(h\right)=\phi_{LoS}^{total}\left(h,t_1\right)-\phi_{LoS}^{total}\left(h,t_2\right) \quad (3.60)$$

In the following experiments two GAMs, namely, ECMWF’s ERA-Interim and NASA’s MERRA will be exploited to estimate the tropospheric phase delay. One advantage of GAMs over external data such as MERIS or MODIS is that it will not be affected by cloudy region or problematic reflectance values. A python module PyAPS is exploited to estimate TSPD for correcting the SAR IFGs (Jolivet et al., 2011; Jolivet et al., 2014).

Chapter 4

Tropospheric turbulent phase correction with TS-InSAR

Beijing Metropolitan, the capital city of China, has suffered from groundwater-induced subsidence since the late 1930s and the over-exploration of groundwater could lead to subsidence as much as -12.0 cm yr^{-1}. Since the study areas were all plain regions and the elevation changes in the eastern Beijing were not significant (20 – 60 meters), the height related TSPD was not considered in this section. In other words, TSPD was not needed to be estimated by using either GAM based script PyAPS (Jolivet et al., 2014) or other height-related linear regression models (Ng et al., 2012b; Rosen et al., 1996; Liu et al., 2014). Apart from the tropospheric stratified component, the tropospheric turbulent phase delay was estimated by using the traditional temporal-spatial filtering operation (Ferretti et al., 2001), which was conducted by applying a low-pass and high-pass filtering operation in the spatial domain and temporal domain, respectively. The section is based on the material published in International Journal of Digital Earth (Du et al., 2017a).

4.1 Groundwater induced subsidence in Beijing City

Beijing municipality has suffered from groundwater-induced subsidence for decades, and the first record of groundwater level change was documented in the 1950s (Ng et al., 2012b; Gao et al., 2016). According to reports from the China Geological Survey (CGS), the groundwater level over the whole plain has dropped rapidly since the 1970s due to the large demands of the growing population and industrial development. Furthermore, the groundwater recharge rate experienced a severe reduction period between 1999 and 2009 due to consecutive years of drought. Eventually, the groundwater level had dropped up to 15 − 20 m from 1998 to 2005. Since the Beijing Plain is a typical Piedmont alluvial-pluvial plain, which consists mainly of coarse sandy gravel carried by Wenyu, Chaobai and Yongding rivers, local subsidence induced by the reduction of the groundwater level is to be expected (Ng et al., 2012b).

Many TS-InSAR methods have been applied to monitor the groundwater extraction induced gradual changes in Beijing City over the last decade. Ng et al. (2012b) exploited GEOS-PSI method to map the land subsidence in Beijing City with 44 ENVISAT and 24 ALOS images from 2003 to 2009, whereas the cross-validated results between these measurements agreed well. Then the three-dimensional analyses were carried out to discriminate the vertical and east-western deformation components, and the outcome confirmed that subsidence was mainly in the vertical direction ranging from -115 to 6 mm yr^{-1}. Gao et al. (2016) utilised the SBAS method to measure the ground deformation at Capital International Airport, Beijing between 2003 and 2013 with ENVISAT and TerraSAR-X SAR images. The study pointed out that the local subsidence rates were between -66.2 to 6 mm yr^{-1}. Later the authors verified these measurements with ground-levelling surveys and concluded that apart from excessive groundwater extraction, active faults and quaternary compressible layers might also have contributed to the land subsidence. Chen et al. (2017) then reported that the changes of groundwater level in the confined aquifer between 100 – 180 m contributed the most to the ground deformation by analysing the ENVISAT dataset from 2003 to 2010.

It is worth mentioning that previous studies on the field deformation at Beijing City mainly focused on the period before the year of 2014. Furthermore, there was a lack of detailed analyses relating the evolution of ground subsidence over particular trouble spots. According to Guardian (2016), the Beijing government inaugurated a mega-engineering project on 12 December 2014 to reduce the water shortage by constructing a 2,400 kilometres stretch of tunnels and canals, which was able to divert 44.8 billion m^3 of water annually to the capital. In addition, the Chaoyang district government declared it would phase out more than 360 water wells, which in turn reduced the annual consumption of groundwater by about 10 million m^3 (Guardian, 2015). Therefore, it is expected that the groundwater related subsidence should be reduced as a result of a reduction in groundwater extraction.

This section will focus on the subsidence monitoring in eastern Beijing City (Figure 4.1 (a)) and map the changes of the spatial deformation pattern among three temporal periods with respect to three different sensors: January 2007 – January 2011, September 2014 – February 2017 and June 2015 – November 2016 (the coverage of these three datasets is shown in Figure 4.1). Since eastern Beijing City and its surrounding areas are the area of interest (ROI), to examine the land-use types within the study region (approximate 30 km × 30 km), a maximum-likelihood based supervised classification method was exploited to classify the optical image acquired from Sentinel-2A with the resolution of 20 m, which has the similar coverage of

ALOS-1/2 image. Figure 4.1 (b) shows that the total area size of the urban and rural regions account for 527 km^2 and 419 km^2, respectively, which indicates that approximately 56 % of the processed area is covered by rural land-use type, of which the main uses are farmland and grasslands while the remaining 44% are urban regions covered with houses and buildings. In light of this, to achieve the best detail over both urban/non-urban areas, a DS pixels based TS-InSAR is implemented to conduct the time series analysis on Sentinel-1 and ALOS-1 datasets, which is initially modified from GEOS-ATSA (Ge et al., 2014; Du et al., 2016a). ALOS-2 dataset is processed using the CS pixels based TS-InSAR method since there are only nine images available (Zhang et al., 2013).

4.2 Geological settings and data description

Beijing City is located in the north-western portion of the North China Plain, with the north latitude ranging from 39°28' to 41°05' and the east longitude between 115°25' to 117°30' (Figure 4.1 (a)). The total coverage is about 16, 807 km^2 while the plain region accounts for 6, 390 km^2. The northern and western parts of Beijing are dominated by the Jundu Mountains and the Taihang Mountains, respectively. To the southeast direction, Beijing lies within alluvial-pluvial plains among five rivers, the Yongding, Ju, Juma, Wenyu and Chaobai. Beijing's climate belongs to the semi-humid continental type, with an annual average temperature of about 10°C. In addition, the terrain in the northwest region is generally higher than the southeast part and the elevation ranging from 20 – 80 meters above sea level (m.a.s.l) (Chen et al., 2016).

Nineteen ALOS-1 PALSAR images captured from 17 January 2007 to 28 January 2011, 24 Sentinel-1A/B scenes in interferometric wide swath (IWS) mode acquired between 17 June 2015 and 08 November 2016, as well as 9 ALOS-2 PALSAR scenes within 18 September 2014 and 2 February 2017 were utilised to map the ground deformation over eastern Beijing City, China. The ALOS-1 images (Track 447, Frame 790) were captured in ascending mode with mean incidence angle of 38.7°, the Sentinel-1 images (relative orbit 47) were acquired in descending orbit with a mean incidence angle of 33.9° (swath 1), while the ALOS-2 acquisitions (Track 137, Frame 790) were captured in ascending with a mean incidence angle of 31.4°. All the Sentinel-1 images were acquired in VV single polarisation with the azimuth and range pixel spacing of 13.96 m and 2.33 m, respectively, whereas all the dual-polarisation pairs (HH) for ALOS-1/2 were oversampled twice in the range direction with the final line and pixel spacing of 3.19 m and 4.68 m, respectively.

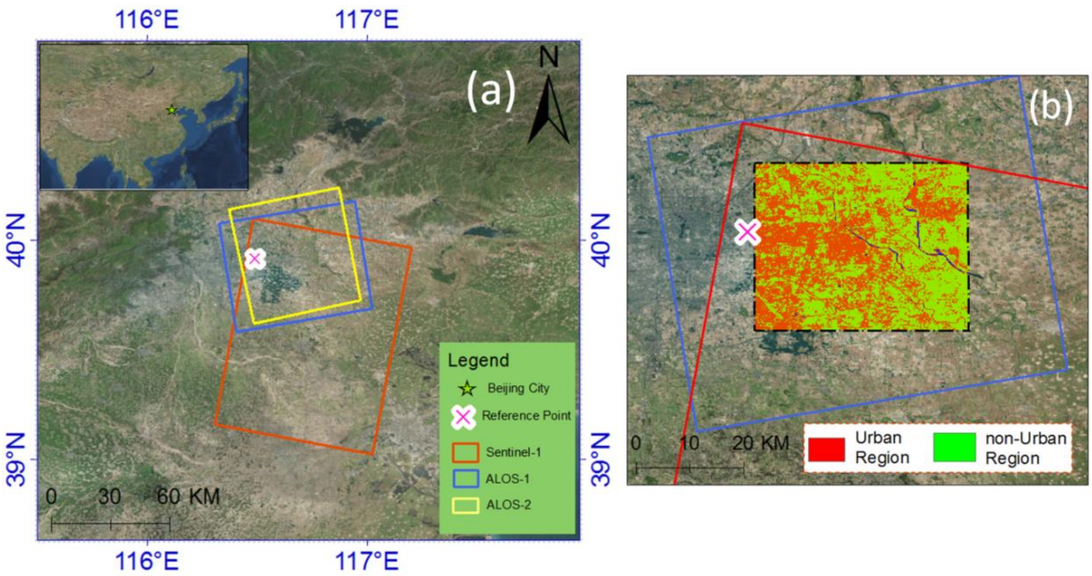

Figure 4.1 (a) The coverage of ALOS-1 (blue), ALOS-2 (yellow) and Sentinel-1 A/B (red) image stacks. The white pink cross represents the reference point. (b) Land cover classification result with respect to the coverage study region.

4.3 Result and analysis

4.3.1 Mapping land subsidence with ALOS-1/2 and Sentinel

Firstly, GEOS-DInSAR (Du et al., 2016b) and GMT5SAR (Sandwell et al., 2011) were used to process the 24 Sentinel-1, 19 ALOS-1 and 9 ALOS-2 datasets from single look complex (SLC) products to differential IFGs. The subsequent time series analysis was based on the in-house C++ scripts. The one arc-second DEM (30 meters) acquired from SRTM (Farr et al., 2007) were exploited to remove the topographic phase and geocode the TS-InSAR result from slant-range radar coordinate system to World Geodetic System (WGS) 1984 datum afterwards.

Images acquired on 06 September 2009 (ALOS-1), 12 February 2016 (Sentinel-1) and 17 September 2015 (ALOS-2) were picked as master images for the three image stacks to minimise the temporal and perpendicular baseline. The ALOS-1, Sentinel-1 and ALOS-2 InSAR-derived mean velocity maps in ALOS-1's LOS direction were given in Figure 4.2 (a), (b) and (c). The reference point was selected over a relatively stable region within the third east ring of Beijing, China and the mean displacement rate for the other MS pixels were relative to the reference point. The total number of MS pixels within the study region (marked with the black dash-line rectangle box) was about 2,310,200; 2,735,778 and 580,912 derived from the ALOS-1, Sentinel-1 and ALOS-2 TS-InSAR analyses, respectively. In other words, the corresponding densities of MS pixels obtained were 2567, 3040 and 645 MS km^{-2}, respectively. In addition, all these results were resampled onto 100 m $\times$100 m grid in order to achieve a reasonable comparison. It was clear that the highest subsidence rate from 2007 to 2011 exceeded –12.0 cm yr^{-1} in LOS direction, which correlated well with the measurements from Ng et al. (2012b) while the largest annual displacement from

2015 to 2016 was greater than –12.0 cm yr^{-1} as well. The distribution of the estimated linear deformation rate within the ROI for ALOS-1, Sentinel-1 and ALOS-2 can be seen in Figure 4.3(a), (b) and (c), respectively, while it was clear that the majority of the subsidence rates were between –2.0 to 0 cm yr^{-1}.

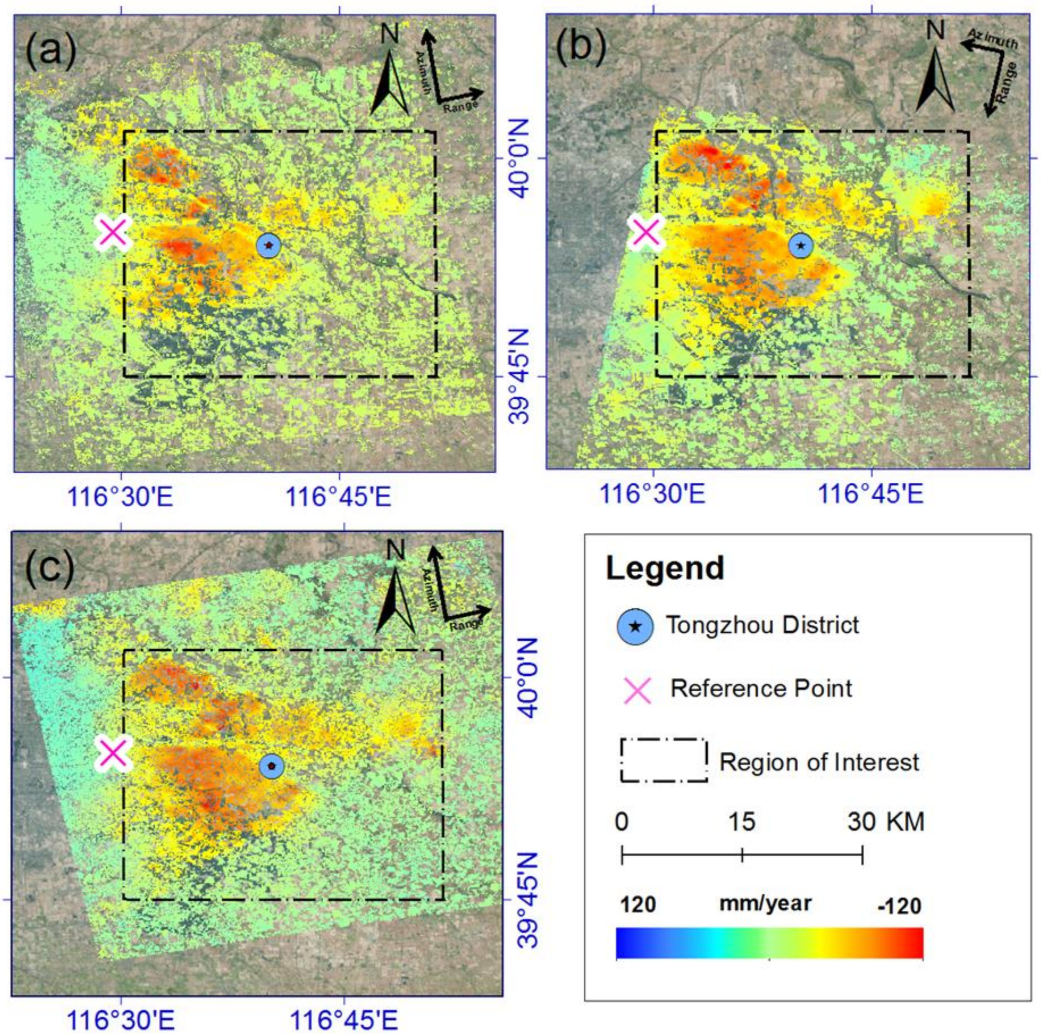

Figure 4.2 Three InSAR-derived subsidence rate maps over the eastern Beijing region on three-time spans were generated from SAR images acquired by: (a) ALOS-1 (January 2007 – January 2011), (b) Sentinel-1 (September 2014 – February 2017), and (c) ALOS-2 (June 2015 – November 2016) satellites. The blue circle represents the Tongzhou District, which is located in the eastern part of Beijing City. The resolution is 100 m × 100 m for all sub-maps.

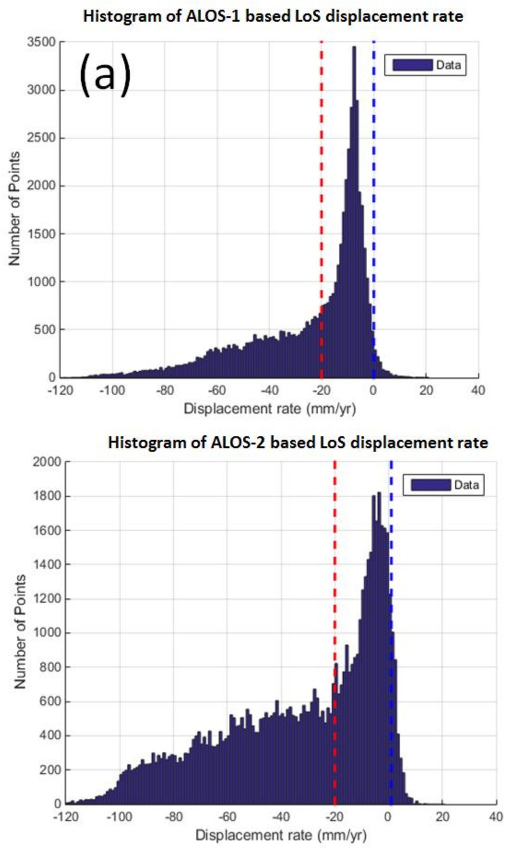

Figure 4.3 Histogram of the measured mean velocity maps in ALOS-1's LOS direction generated from (a) ALOS-1, (b) Sentinel-1 and (c) ALOS-2 dataset, respectively, over the ROI region.

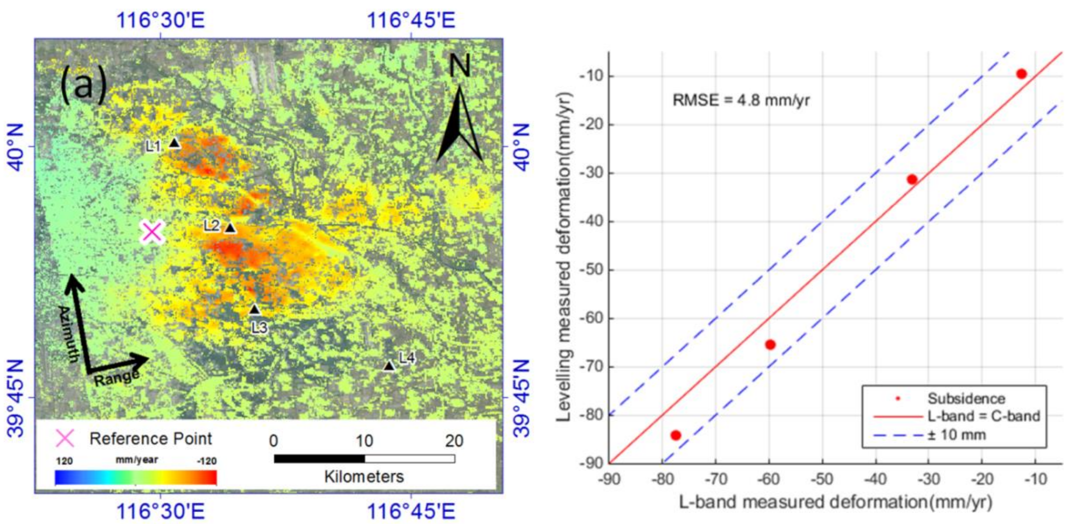

Figure 4.4 (a) Four levelling points (black triangles) superimposed onto ALOS-1 TS-InSAR derived velocity map (b) comparison of the land subsidence rate in ALOS-1's LOS direction between levelling and TS-InSAR measurements.

4.3.2 InSAR data validation

To evaluate the quality of the InSAR-derived mean velocity map from ALOS-1 image stacks, a comparison was conducted with the ground survey of levelling method. A total of four levelling points surveyed from April 2008 to June 2010 were exploited as checkpoints, which was originally used in Guo et al. (2016). The linear subsidence rates of these levelling points were estimated and later converted into ALOS-1's LOS direction. It is worth noting that since the resolutions of these two methods were different, the InSAR-derived land subsidence rate map was resampled onto a 100 m × 100 m grid, and the location of both levelling and InSAR measurement points were assigned. The InSAR measurements with respect to the corresponding levelling points were then identified and selected. Figure 4.4 demonstrates the scatter plot of levelling-InSAR solution over four levelling points. A strong correlation between the InSAR and levelling measurements were observed and the Root-mean-square-error (RMSE) was about 4.8 mm yr^{-1}, which suggests the reliability of ALOS-1 InSAR-derived subsidence rates. Nevertheless, Sentinel-1 derived InSAR measurements were verified with the TS-InSAR result from ALOS-2 datasets under the assumption that no displacement occurred at the reference point during the 2.5 year period.

4.3.3 Spatial-temporal analysis of land subsidence

Figure 4.5(a) demonstrates the correlation between Sentinel-1 and ALOS-1 mean velocity maps. Since the image acquisition times for these two datasets were not the same, the derived RMSE was about 1.8 cm yr^{-1}, and the value of R^2 is equal to 0.6.

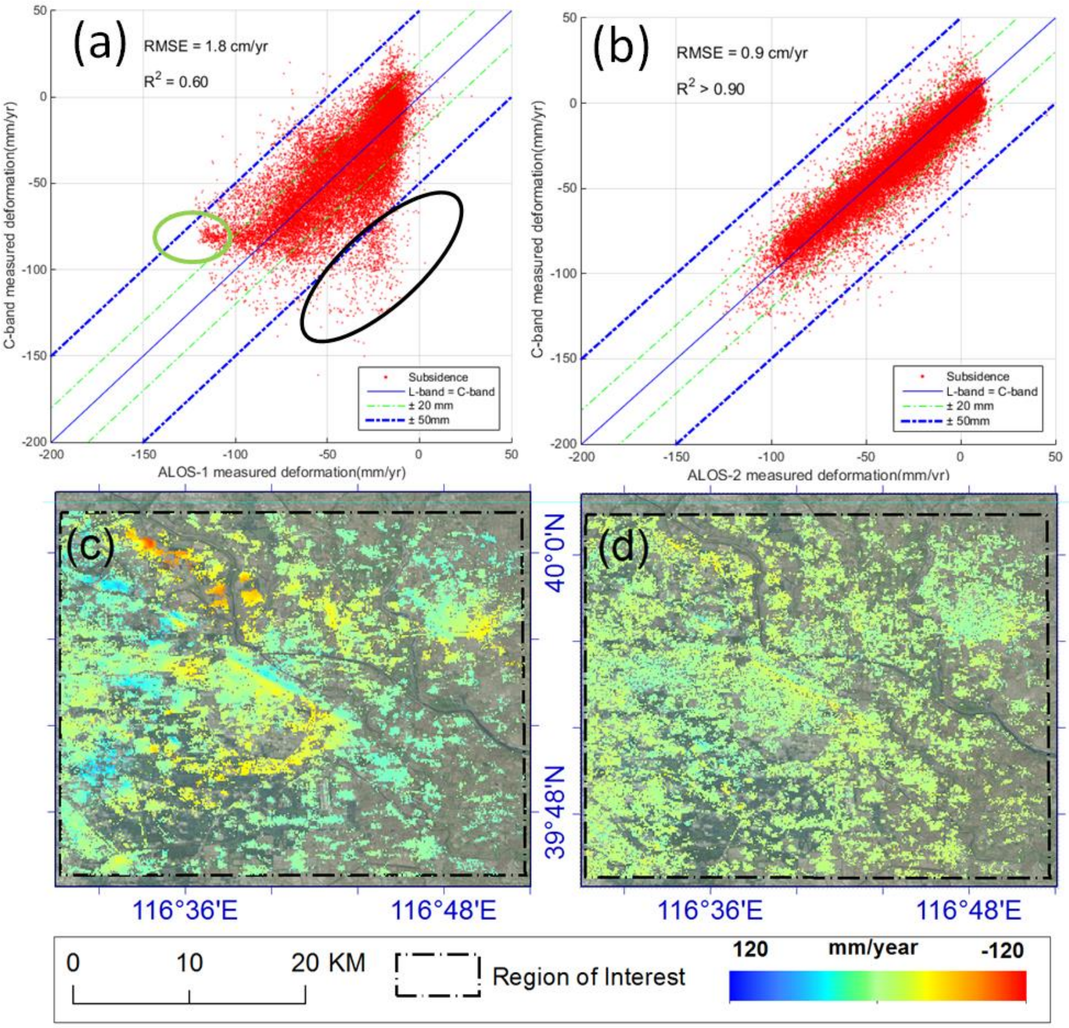

Figure 4.5 Pixel-by-pixel comparison between (a) Sentinel-1 and ALOS-1, and (b) Sentinel-1 and ALOS-2 mean velocity maps both in the ALOS-1's LOS direction, mean velocity differences of (c) Sentinel-1 – ALOS-1, and (d) Sentinel-1 – ALOS-2

R-squared (R^2) is the coefficient of determination in general regression analysis, which describes how well the velocity maps derived from both TS-InSAR analyses can be correlated with each other. Even with a medium value of R^2, we could still observe a linear trend from Figure 4.5 (a), as well as some additional information. For example, regions covered with a black circle indicate areas with rapidly increasing subsidence, whilst the range of the subsidence has changed from –60 – 0 cm yr^{-1} before 2011 to –120 – –60 cm yr^{-1} after 2015. Additionally, regions marked with green circle indicate that the previously rapidly subsiding areas were experiencing a reduced subsiding rate. In other words, these inconsistencies illustrate that the large subsidence rates over some regions were decelerating. The possible explanation for this was due to some government actions, for example, the reduction of groundwater extraction or the acceleration of the groundwater flow system has made some progress. On the contrary, as the temporal coverage between Sentinel-1 and ALOS-2 products are partially overlapped, Figure 4.5(b) illustrated a positive relationship between these two mean velocity maps with the RMSE value account for 0.9 cm yr^{-1} and $R^2 > 0.9$, which proved the reliability of both measurements. Figure 4.5 (c) and (d) are the mean velocity differences of (c) Sentinel-1 – ALOS-1 and (d) Sentinel-1 – ALOS-2, and regions covered with a red/blue colour indicates the subsidence accelerating/decelerating areas.

It can be seen from Figure 4.2 (a) and (b) that the spatial deformation patterns for both Sentinel-1 and ALOS-1 maps have the similar distribution from the first glimpse, which was mainly around the Tongzhou District. To have a clearer view of the subsiding regions within Tongzhou District, Beijing, the whole subsiding zone, has therefore been divided into four targeted zones, which were numbered Zones I, II, III and IV (Figure 4.6 (a)).

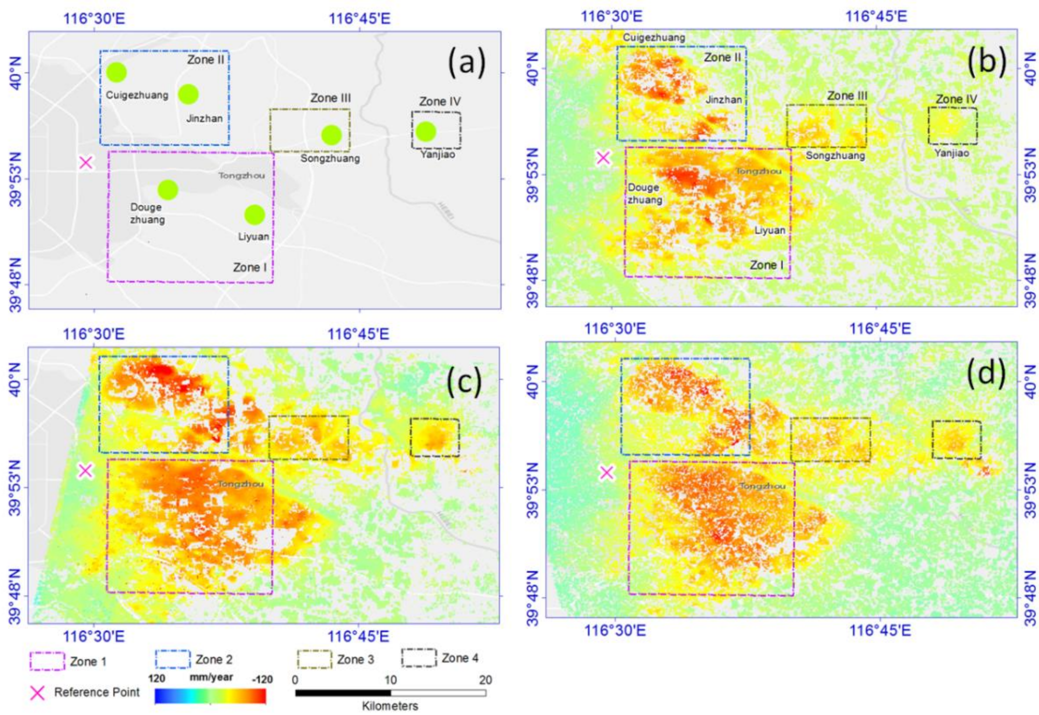

Figure 4.6 Four subsiding zones were marked with rectangle boxes I, II, III and IV, respectively (a) The relative locations with respect to these township centres, (b) ALOS-1 LOS displacement rate map, (c) Sentinel-1 displacement rate map and (d) ALOS-2 displacement rate map. Both (c) and (d) were converted into the ALOS-1's LOS direction.

As can be seen from Zone I to IV in Figure 4.6 (b), (c) and (d), the spatial coverages of the four deforming areas have all increased from the period of 2007 – 2011 to 2014 – 2017. More specifically, it was quite clear from Zone I that the most subsiding areas were around Dougezhuang township and Liyuan township, respectively, during the two temporal-period while the largest subsidence rate decreased from over –12.0 cm yr^{-1} to just above –10.0 cm yr^{-1}, which occurred in the centre of Dougezhuang township (located in the right corner of Zone I). The reason for the subsidence reduction was possibly due to the inauguration of the mega-engineering project, which was designed to bring water from the southern region of the country to the relatively arid northern part, including Beijing City. Moreover, the coverage of the subsiding regions has extended a lot, and it was quite obvious that the subsidence expanding trend was still going on towards the southwest direction centred at these two townships. Additionally, the land subsidence affecting regions within Zone II has become much more severe, especially near the two townships: Cuigezhuang and Jinzhan, where the largest subsidence rate was approximately –12.0 cm yr^{-1} from the year 2007 to 2011, whilst after 4 years of urban expansion and population growth, the largest subsidence exceeded –14.0 cm yr^{-1} in particular spots. What was more, the spatial pattern of the subsidence in the eastern part of Jinzhan township has experienced a booming growth towards the easterly direction, and eventually, Zone II and Zone III linked up together.

Besides, it is worth mentioning that some previously moderate subsidence regions within Zone I and Zone II became trouble spots (the subsidence rate over which position is reasonably large) at rates as high as –10.0 to –12.0 cm a year while in contrast, some other trouble spots experienced a decreasing period. Significant subsidence changes were observed along two subsidence funnels. Two profile lines a-a’ and b-b’ were chosen to illustrate the spatial characteristics of land subsidence, which can be found in Figure 4.7. The profile map in Figure 4.8 (a) shows the evolution of the displacement rate along the profile line a-a’ with the maximum displacement rate almost reaching –12.0 mm yr^{-1}. Moreover, at a distance between 2500 to 4500 m, the Sentinel-1 measurements were lower than the ALOS-1 counterpart, which agreed well with our previous conclusion. On the contrary, the subsidence along profile b-b’ within Figure 4.8 (b) exhibits a significantly increasing trend with the maximum subsidence rate of –12.5 cm yr^{-1}.

Furthermore, the subsidence rate over the gap region between Zone II and Zone III has increased from ~ –3 to ~ –8 cm yr^{-1}, and the growth ratio was more than 200%. Songzhuan township was within Zone III, and the local subsidence spatial pattern was moving from south to north with the maximum subsidence of –8.2 cm yr^{-1}. More specifically, the northern part of Songzhuan shows a relatively stable displacement rate of around –3.0 cm yr^{-1} within 2007 – 2011, but currently, the whole zone has been affected by the ground deformation. Last but not least, the most noticeable subsidence changes have been observed in Zone IV, where the largest displacement range changed from –2.9 to –6.0 cm yr^{-1}. Yanjiao township was within this zone, and the largest subsiding region occurred near the town centre (centre of Zone IV).

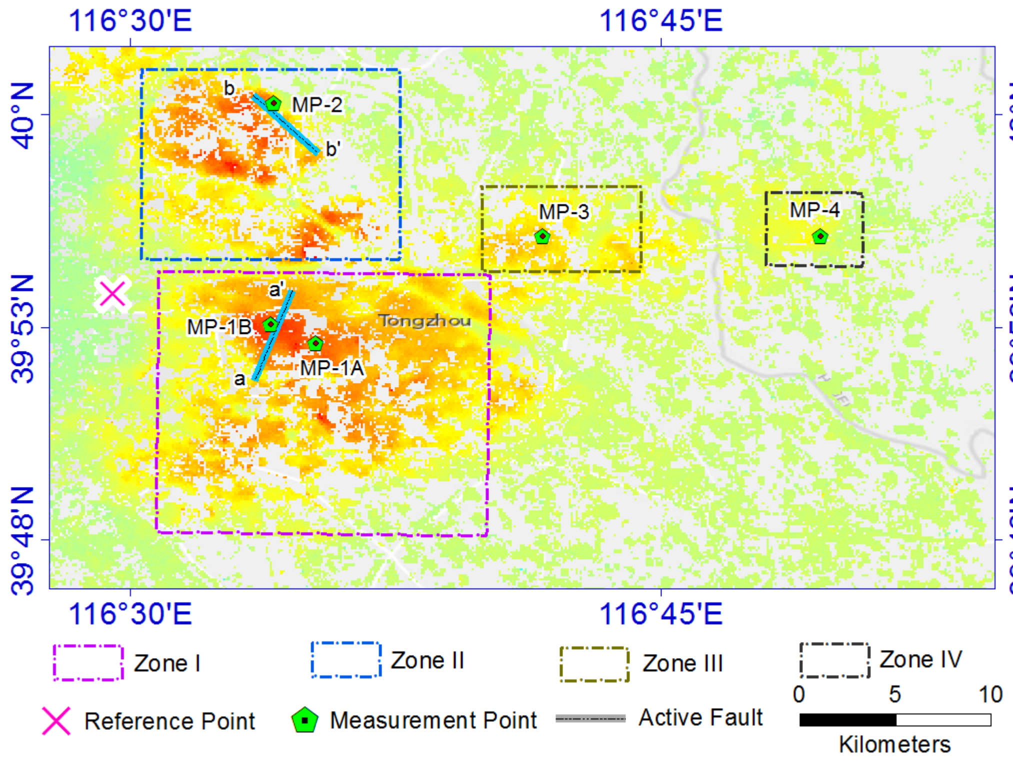

Figure 4.7 Five measurement points within each zone and two profile lines a-a' and b-b' crossing the targeted subsiding regions.

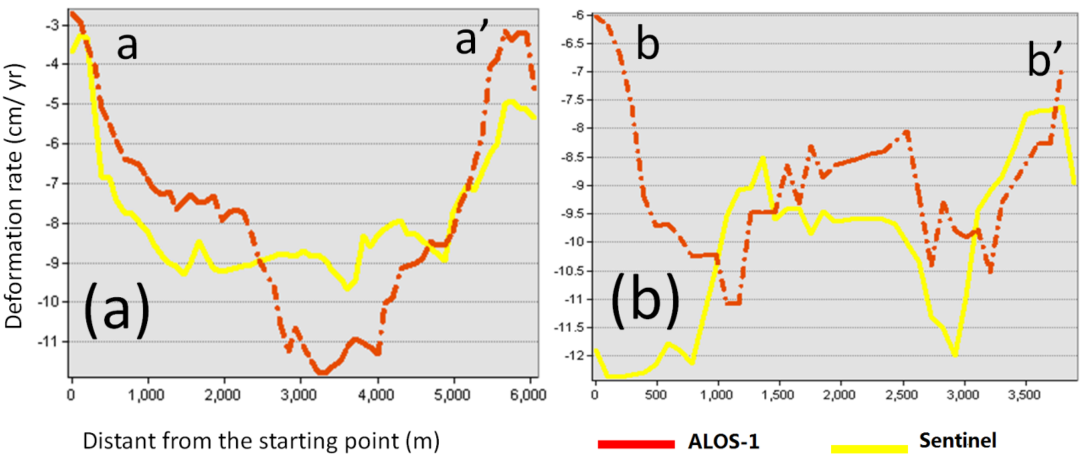

Figure 4.8 Subsidence profile: (a) along the profile line a-a' within Zone 1, and (b) along the profile line b-b' within Zone 2.

In order to map the subsidence time series, five MS pixels have been selected within each zone, and the position with respect to each of them can be found in Figure 4.7. Figure 4.9 shows the time series subsidence obtained by ALOS-1/2 and Sentinel-1 dataset at the five measurement points. It is worth mentioning that since the line and pixel spacing for both L-band and C-band sensors were different, each common pixel exploited was indeed a group of pixels within a 100 m × 100 m square box centred at the referred pixel. All the pixels within this window were utilised and their averaged value was estimated as well. Furthermore, since there was a big temporal gap between these three processing periods, the three time series measurements were not aligned together in the same graph, but separated into two sub-graphs. From Figure 4.9, the time series results from ALOS-2 and Sentinel-1 agreed well with each other, except over MS-2, where the difference of the mean velocity is account for 1.6 cm yr^{-1}, and this could be due to the nine-month temporal difference (September 2014 to June 2015). The following comparison was conducted between ALOS-1 and Sentinel-1 measurements. It can be seen that MS-1A and MS-3 selected from Zone I and Zone III have similar deformation value, and the subsidence rates did not change that much. The differences between them were 0.3 and 0.4 cm yr^{-1}, respectively. MS-1B, which was located in the centre of Douge Zhuang township, decreased from –10.3 to –8.6 cm yr^{-1}. For those two chosen points from Zone II and Zone IV, it was quite clear that the subsidence rate has increased a lot, from –5.8 and –2.9 cm yr^{-1} to –12.4 and –6.2 cm yr^{-1}, respectively. In other words, the increased rate was more than 100% during the four-year gap period.

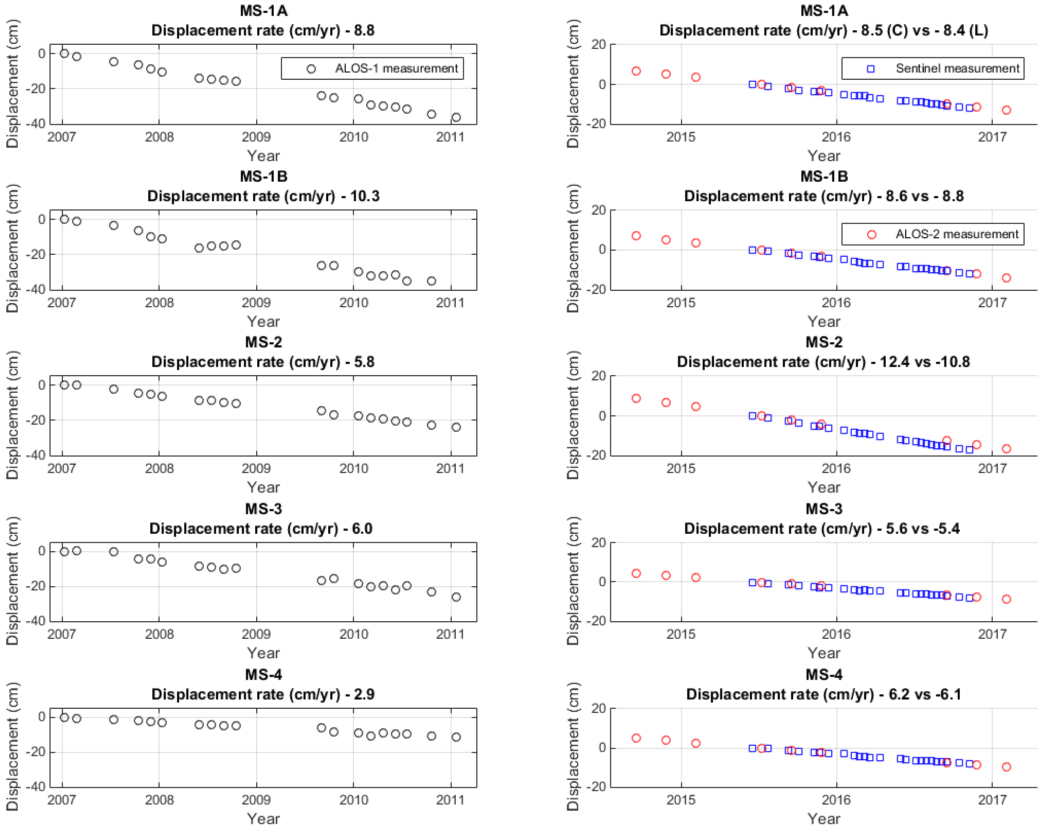

Figure 4.9 Time series deformation over the five measurement points; (left) ALOS-1 based measures; (b) ALOS-2 and Sentinel-1 based measures.

4.4 Discussion and conclusion

It needs to be pointed out that the subsidence trends over several townships within Tongzhou District, Beijing were still going on, namely, Cuigezhuan, Jinzhan, Liyuan, Songzhuang and Yanjiao, and the largest subsidence rates could easily reach to –8.0 cm yr^{-1}, except for Yanjiao, where the subsidence rate changed from less than –3.0 cm yr^{-1} (2007 to 2011) to over –6.0 cm yr^{-1} (2015 to 2016). Nevertheless, the largest changing ratio of land subsidence also occurred in the centre of Yanjiao township despite the moderate magnitude, which accounted for more than 100%. Given the fact that the Beijing Capital International Airport was about 6 km from Jinzhan township in the southeast direction, the affected region may extend to the airport sooner or later if the subsiding trend goes on. Therefore, particular attention should be paid to these townships in order to avoid further economic loss due to land subsidence induced hazards. The reason for these accelerating phenomena could be many, and according to the National Bureau of Statistics of China (NBSC) (NBSC, 2017a), the population of Beijing City has risen from 16.95 million in 2008 to 21.73 million in 2016, which was an increase of about 30%. Besides, it can be seen from NBSC (2017b) that the average per capita living space in Beijing rose from 20.5 m^2 in 2008 to 31.7 m^2 in 2016 as well. In other words, the total area of buildings almost doubled compared to eight years ago. Due to an increase in population as well as the skyscrapers, ring-roads and other development in Beijing City, the supporting infrastructures, e.g., water pipelines, gas-pipelines, and telecommunications cables beneath the man-made structures, may increase to meet this demand. All of these constructions could potentially cause the land subsidence in a major way. If this kind of sinking continues, the 20 million people in Beijing City will face severe safety threats. For instance, the city's train operations will be massively affected.

On the contrary, many places are experiencing a decreasing trend in subsidence. For example, the subsidence rate at the town centre of Dougezhuang township changed from over –12 mm yr^{-1} to just above –10 mm yr^{-1}. Similar findings have not been reported to the best of the authors' knowledge; a possible explanation is the mega-engineering project launched by the Chinese government in December 2012 to reduce the water shortage, and to recharge the groundwater. As is well known, it is a slow process for the groundwater system to recover: it may take years for subsidence to slow down due to the long delays for recharge to reach the groundwater (Yang et al., 1999). Therefore, further continuous monitoring, e.g., in-situ, ground survey or InSAR measurements from November 2016 to the near future, are still needed to have a close study of the land subsidence over Dougezhuang township.

Chapter 5

Tropospheric stratified and turbulent phase correction for TS-InSAR

5.1 Tropospheric stratified phase correction with DInSAR

ERA-Interim is a global reanalysis of ECMWF, which can provide a global 0.7° grid's estimation of water vapour partial pressure, temperature and geopotential elevation along 37 pressure levels every 6 h daily (start at 0:00 UTC). MERRA is also a global atmospheric reanalysis, which can be utilised to estimate the same variables during the same period. The only difference is that MERRA is along 42 pressure levels on a global grid (0.5° × 0.75° along longitude and latitude, respectively). The detailed description of ERA-Interim and MERRA can be found in Dee et al. (2011) and Rienecker et al. (2011), respectively.

Table 5-1 Detailed information of the interferometric pairs

Site	Satellite	Track/Frame	Date (dd/mm/yyyy)	Incidence Angle (°)	A/D	$B_{\perp}$ (m)
Qinghai	ALOS-1	477/714	13/06/2009-29/07/2009	38.7	A*	112.5
North China Plain	ALOS-1	447/750, 760,770	25/01/2010-12/03/2010	38.7	D**	602.9
Ordos	ENVISAT	176/2805	04/12/2011-02/02/2012	23	D	110.7

Note: $B_{\perp}$ is the perpendicular spatial baseline
*A indicates ascending
**D indicates descending

In this section, the experiments were conducted over the Qinghai Mountains, North China Plain and Ordos Basin, China, respectively, with three SAR pairs acquired from L-band ALOS-1 PALSAR and C-band ENVISAT ASAR (Table 5-1). Since the acquisition time for ALOS-1 and ENVISAT were 2:00 p.m. UTC and 3:00 a.m. UTC, respectively, the TSPD (both derived from GAMs) for ALOS were estimated at 12:00 p.m. UTC while the TSPD for ENVISAT were estimated at 6:00 a.m. UTC.

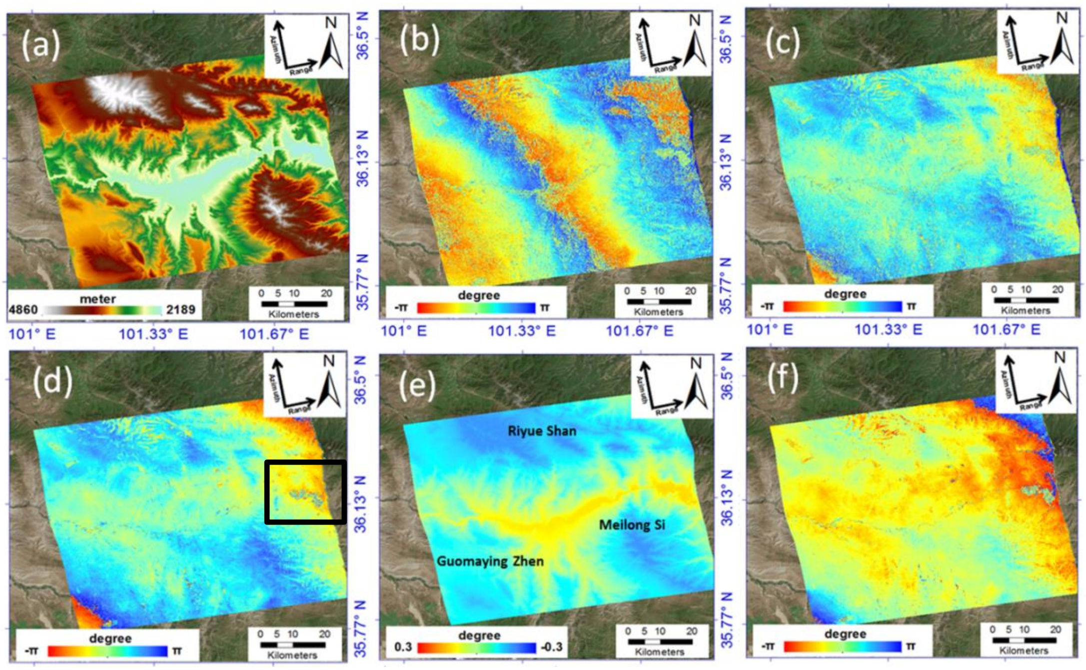

Figure 5.1 (a) DEM over Qinghai Mount; (b) The primary differential IFG; (c) The de-ramped differential IFG without denoising; (d) The de-ramped differential IFG; (e) TSPD derived from MERRA; (f) Differential IFG after TSPD correction. The de-ramped IFG is generated from the ALOS-1 pair of 13 June 2009 and 29 July 2009.

Figure 5.1 demonstrates a 46-day IFG covering an area in the Qinghai Mountains, extending from Guoyaming Zhen in the southwest to the Riyue Shan in the north. The elevation change is from 2189 to 4860 m and $B_{\perp}$ is about 112.5 m. Due to the relatively short temporal baseline, the deformation signal is considered to be negligible. An example of linear orbit error overspreading of the tropospheric stratified signal is shown in Figure 5.1 (b) and (c). The TSPD prediction derived from MERRA (Figure 5.1 (e)), reproduces the refined de-ramped differential IFG reasonably well (after low-pass filtering operation) (Figure 5.1 (d)). It is evident that most blue fringes near Riyue Shan, Guomaying Zhen and Meilong Si are correlated with elevation, which is related to the atmospheric stratified phase delay. However, some of the predicted patterns are not seen in Figure 5.1 (d), e.g. the northeastern phase delay marked with a black rectangular box. Figure 5.1 (f) is the differential IFG after the TSPD correction. At this stage, most elevation related atmospheric fringes have been removed. Also, phase unwrapping process can be applied to Figure 5.1 (f).

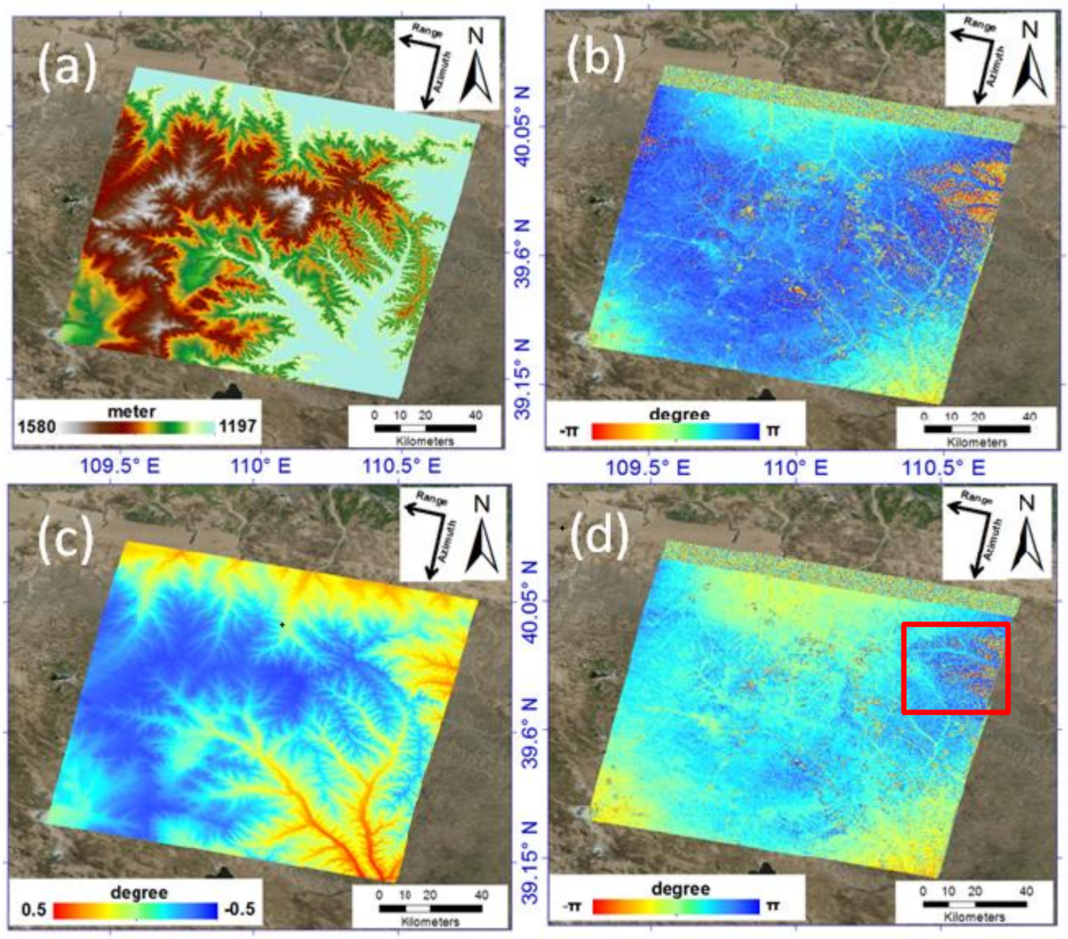

Figure 5.2 (a) DEM over Ordos Basin (b) The de-ramped differential IFG (c) TSPD derived from MERRA (d) Differential IFG after TSPD correction. The de-ramped IFG is generated from ENVISAT pairs of 4 December 2011 and 2 February 2012.

Figure 5.2 depicts a 60-day IFG over Ordos Basin. The elevation change is ranging from 1197 to 1580 m, which is not significant (Figure 5.2 (a)), while the spatial perpendicular baseline $B_{\perp}$ is approximately 110.7 m. Figure 5.2 (b) is the de-ramped IFG. The blue fringes of the IFG from the west to the middle part, which are correlated with elevation to a certain extent have been removed from Figure 5.2 (d). However, no clear correlation is visible in the northeast parts marked with a red rectangular box. Besides, the TSPD, predicted from the outputs of MERRA (Figure

5.2 (c)), effectively reproduces the observed phase in the de-ramped differential IFG with a reduction of the standard deviation of 31.5% in Figure 5.2 (d). It is worth noting that some tropospheric stratified signals are not well modelled, especially over the northeast parts, which are in low-elevation terrains. In this case, MERRA produces a poor correlation between phase and elevation on low-elevation terrains.

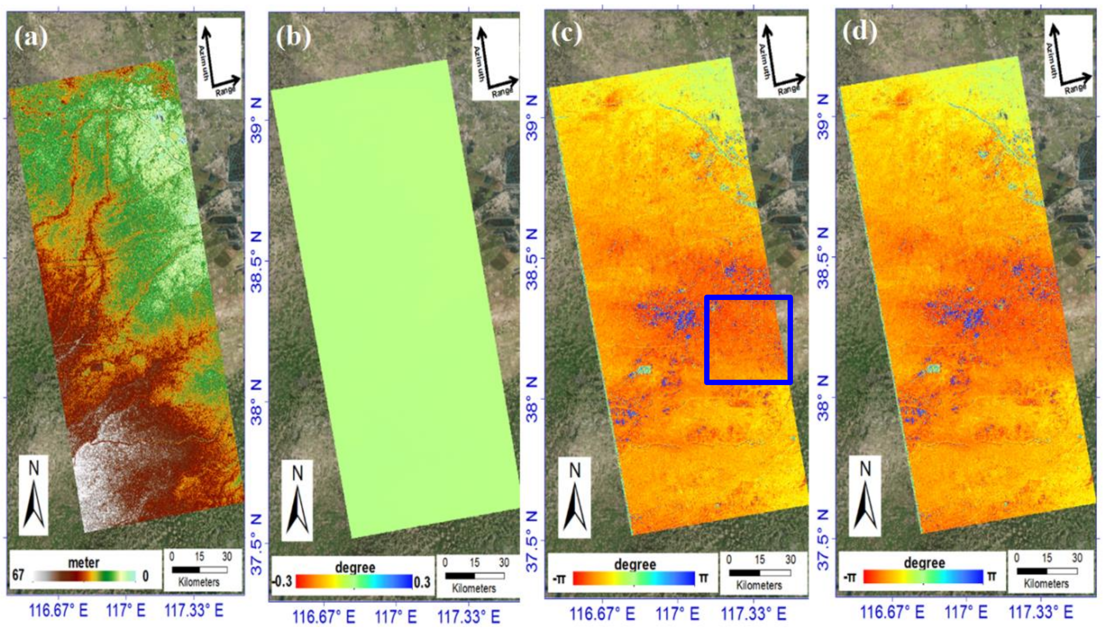

Figure 5.3 (a) DEM over North China Plain; (b) TSPD derived from ERA-Interim; (c) The de-ramped differential IFG; (d) Differential IFG after TSPD correction. The de-ramped IFG is generated from ALOS-1 pair of 9 August 2009 and 9 February 2010.

Figure 5.3 (a) shows the DEM information over North China Plain and the range of the elevation is from 0 to 67 m. Figure 5.3 (b) is the predicted TSPD from ERA-Interim reanalysis. The image contains some noises due to the large perpendicular baseline of 602.9 m. Figure 5.3 (c) is the de-ramped differential IFG, while Figure 5.3 (d) is the refined differential IFG after the TSPD correction. It is evident that

ERA-Interim fails to predict the atmospheric phase delay. A possible explanation is that the entire study region is located within low-elevation terrains with the elevation change of 67 m. Therefore, tropospheric turbulence phase delay should be the dominant factor. In addition, some anthropogenic activities marked by the blue rectangular box could also cause the phase difference.

To summarise, SAR images acquired from two satellite radar sensors – ALOS-1 PALSAR and ENVISAT ASAR were utilised in this section in order to generate the differential IFGs over three test sites with different topographic conditions – North China Plain, Ordos Basin and Qinghai Mountains. MERRA and ERA-Interim were exploited for estimating the atmospheric stratified phase delay. Both of them provide reasonable results; for instance, a reduction of standard deviation accounting for 31.5% was estimated in Ordos Basin. However, there are still some residual tropospheric phases that are not well modelled by these two GAMs for three plausible reasons, 1) certain anthropogenic activities over these regions; 2) parts of the study area are within low-elevation terrains, where tropospheric turbulence is the dominant factor, and 3) The estimation time for TSPD is different from SAR image acquisition time. GEO-ATSA (Ng et al., 2014) has been modified by adding a TSPD correction module.

From the next sub-section, the tropospheric stratified phase delay and the linear orbital error were taken into consideration and eliminated subsequently during the processing of an application of TS-InSAR at a coalbed methane site. The tropospheric turbulent phase delay was eliminated followed by a spatial-temporal operation. This section is based on the material published in International Journal of Digital Earth (Du et al., 2017b).

5.2 Introduction

Coalbed methane (CBM) exploration refers to a technique that extracts natural gas from coal beds. The world first CBM project began in the early 1980s, when a three-well research program was funded by the American Public Gas Association to produce CBM at Pleasant Grove, Alabama, USA with the aim to recover gas for the commercial usage. Later on, the CBM-producing areas extended to other countries, such as Australia, Canada, United Kingdom, India and so on (IESC, 2014). CBM exploration and development began in China in the early 1990s when the Deep CBM Exploration project was conducted by the North China Petroleum Bureau (Li et al., 2015). The application of CBM has experienced significant growth during the past two decades. Previous CBM production mainly focused on the southern Qinshui Basin, which has an abundance of high-rank coals reservoirs (Su et al., 2005; Meng et al., 2014). It is worth mentioning that the rank of coal is primarily determined by the temperature as well as the depth of burial and the increase in coal rank is normally achieved by increasing the amount of moisture in the coal, for example, the moisture content for high-rank, medium-rank and low-rank coal are > 75%, 8−75% and < 8%, respectively. However, latter research studies pointed out that medium-rank coal resources are also cost-efficient for CBM development (Murray, 1996; Palmer, 2010). China has abundant medium-rank coal reservoirs, especially within Ordos Basin and North China Basin (Li and Zhang, 2013; Meng et al., 2014). Liulin area is within the Lishi-Liulin mining area and lies in the middle part of Hedong Coalfield in eastern Ordos Basin. It is a typical medium-rank CBM exploration site and has gained a lot of attention in terms of the extraction sustainability and safety concerns from all over the country.

Indeed, Liulin region was one of the selected target areas in 1991, and seven CBM wells were drilled after hydraulic fracturing (Su et al., 2003). The total local recoverable CBM resources within Liulin district is about 210.83×10^8 m^3 within 72.2 km^2 region (Li et al., 2015). However, the CBM extraction process stagnated for almost a decade until the China United CBM Co. Ltd started their project in this region in the early 2000s. By 2013, more than 80 coal wells and 100 CBM wells were fully constructed and operational by China United Coalbed Methane Corporation, Fortune Liulin Gas Company and Coal Geological Bureau of Shanxi Province (Meng et al., 2014). Previous studies of CBM in Liulin mainly focused on the coal geological background or some improvement related to CBM technique. However, it is possible that these extraction activities might cause some impact on the local ground surface, for example, underground mining operations (Du et al., 2016b; Du et al., 2016a) and multi-discipline research is still needed in Liulin area.

It is well known that land subsidence occurs when the coal seam compact due to pressure changes in the ground. CBM production normally involves the withdrawal of groundwater to depressurise the target coal seam and liberate the gas. At the same time, the reduction in pressure and liberation of gaps results in compaction of the geological structures beneath the land surface. Using InSAR method, a study conducted by Grigg and Katzenstein (2013) showed that up to 4.7 cm of subsidence from 3 July 1997 to 27 July 2000 was observed near the CBM pumping well in

Wyoming's Powder River Basin, and the primary reason being that the aquifer compacted during groundwater removal. In contrast, the modelling results by Case et al. (2000) suggested that the largest subsidence was less than 13 mm, the reason being that not every aspect of the compaction was taken into consideration. Indeed, ground subsidence is dependent on a number of factors, such as the magnitude, direction and depth-interval of the compaction, as well as the geotechnical characteristics of the geological structure throughout the depth profile (IESC, 2014).

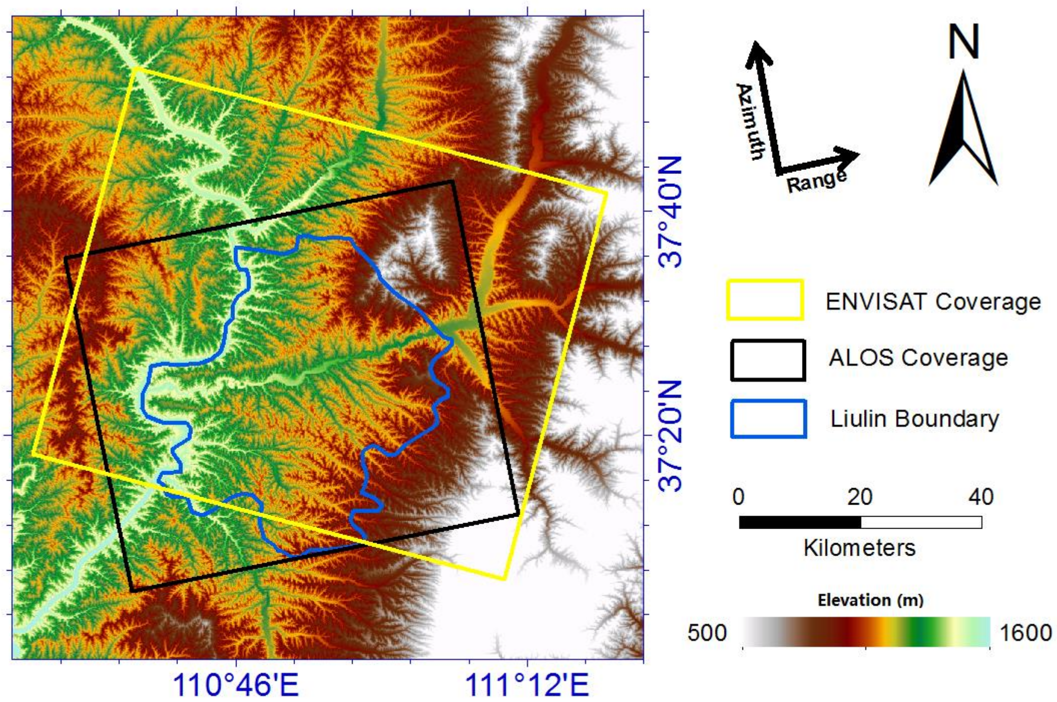

Figure 5.4 The coverage of Liulin County superimposed on SRTM DEM map

5.3 Geological setting and dataset

Liulin County is located in the western part of Shanxi Province, China and about 200 km away from the capital of Shanxi Province, Taiyuan City. The study region in general can be considered as a sloped zone since the topographical slopes over these areas range between 10° and 30°. The elevation of the eastern part of Liulin is higher than the western part (Figure 5.4), and the ground surface elevation change is from the north-eastern Wife Mountain (1522 m) to the south-western Sanjiao Town (607 m). The local annual precipitation is about 456 mm with about 65% of the total precipitation falling during the summer period.

Liulin County was one of the top-ranked counties in gross domestic product (GDP) in China and the storage of Permo-Carboniferous coal and CBM resources are abundant. The main cola-bearing stratum occurs in the upper Pennsylvanian Taiyuan Formation and the lower Permian Shanxi Formation, respectively. Of which, the Shanxi Formation was deposited in a fluvial-deltaic environment with a total thickness of 43−80 m and five coal seams while the Taiyuan Formation was deposited in a tidal flat and sandbar depositional environment with a combined thickness of 81−116 m and seven coal seams (Zhang et al., 2010). According to Figure 5.5, the main coal seams in the Shanxi formation are No. 3, 4 and 5 seams whilst those in Taiyuan Formation are No. 8, 9 and 10 seams (Li et al., 2015). Twenty CBM wells exploited in this study are within No. 4 coal seam (Meng et al., 2014).

The dataset covering the CBM site consists of 21 ALOS-1 PALSAR (L-band) scenes captured from 22 December 2006 to 2 January 2011 as well as 14 ENVISAT ASAR (C-band) images between 29 October 2003 and 07 November 2007. All the L-band acquisitions (Track 459 Frame 740) were acquired in ascending orbit with the mean incidence angle of 38.7 ° while all the C-band dataset (Track 118 Frame 2853) were captured in descending orbit with the average incidence angle of 28.8°.

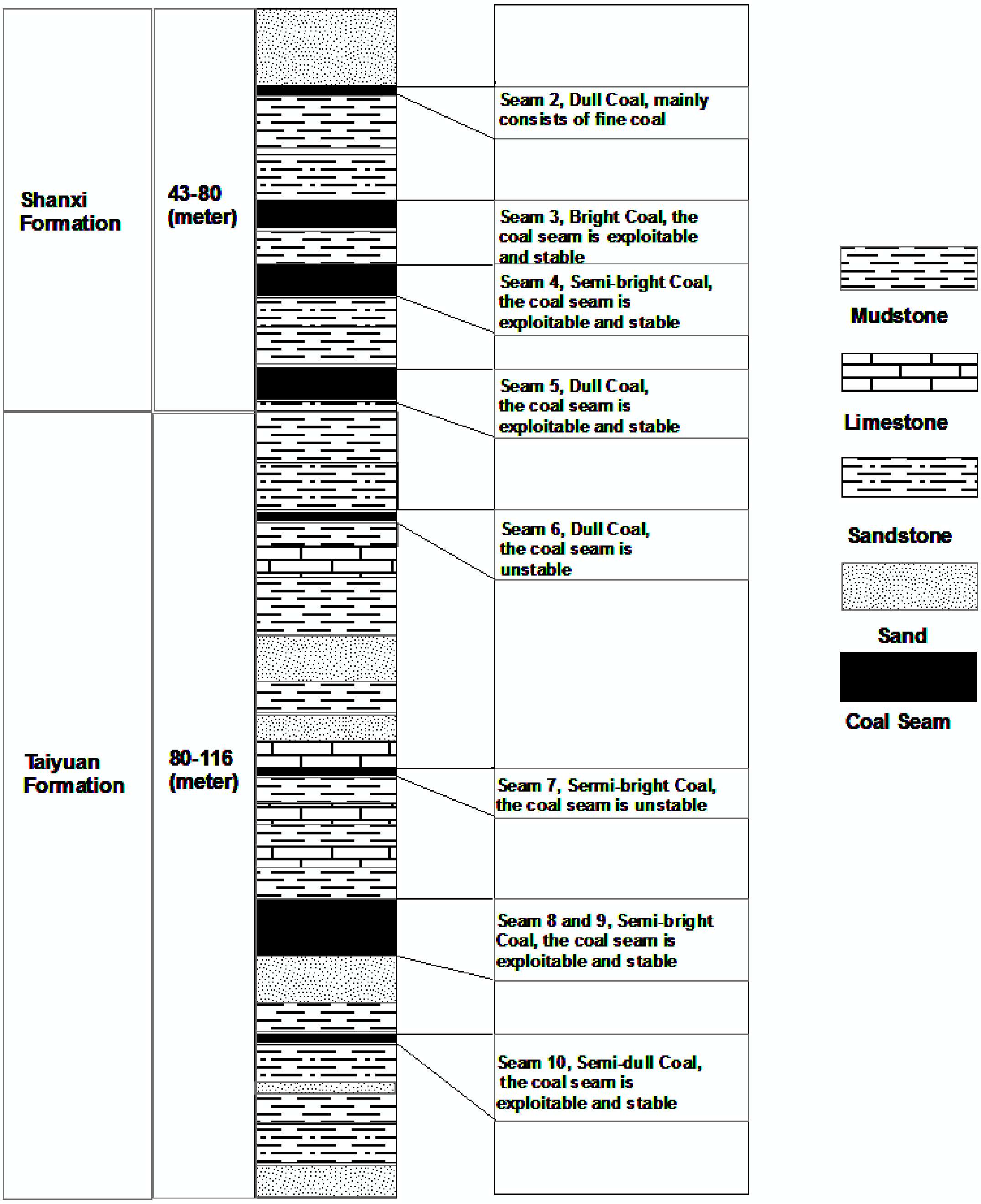

Figure 5.5 Stratigraphic column of the coal-bearing sequences in Liulin area (modified from (Meng et al., 2014))

5.4 Methodology flowchart

An overview of the core steps of the TS-InSAR method for estimating subsidence in Liulin County, China is shown in Figure 5.6 in this study.

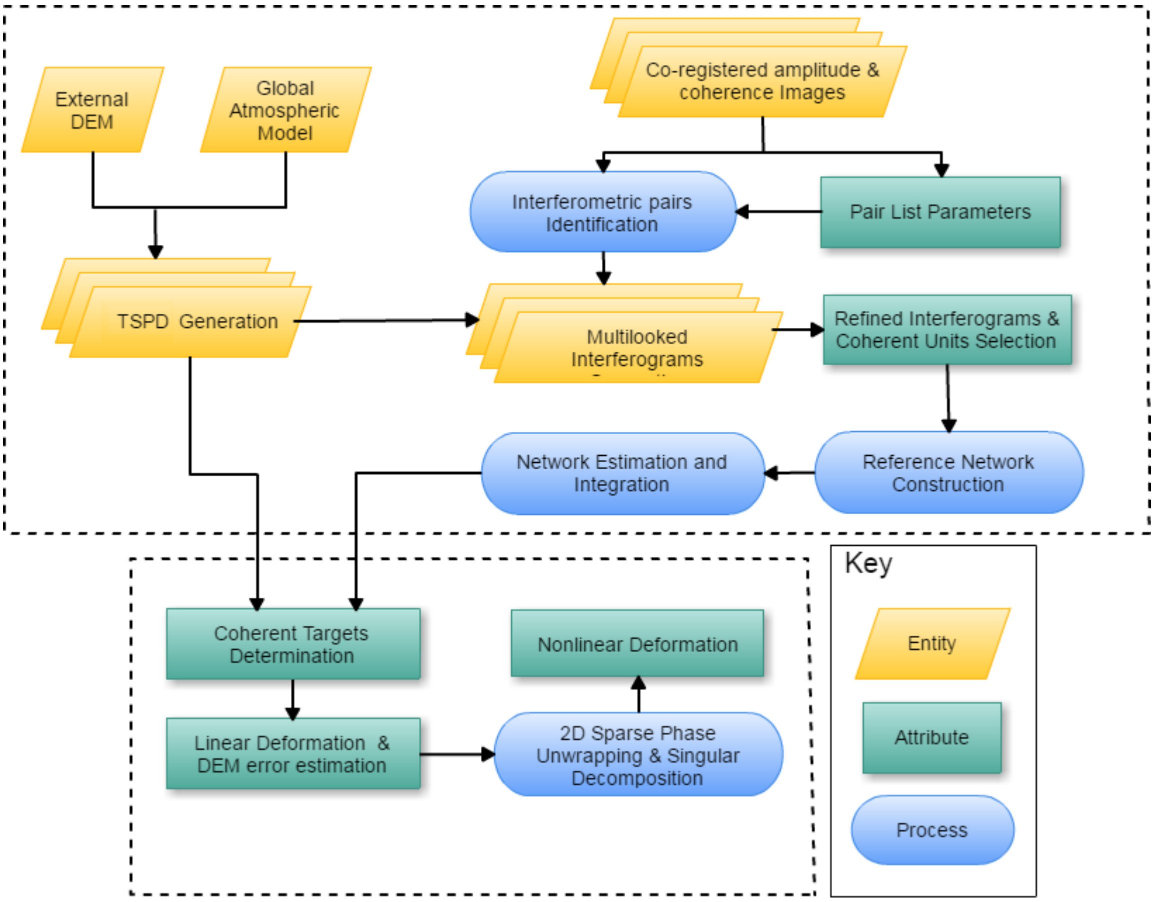

Figure 5.6 The flowchart of Time series InSAR approach used in this study

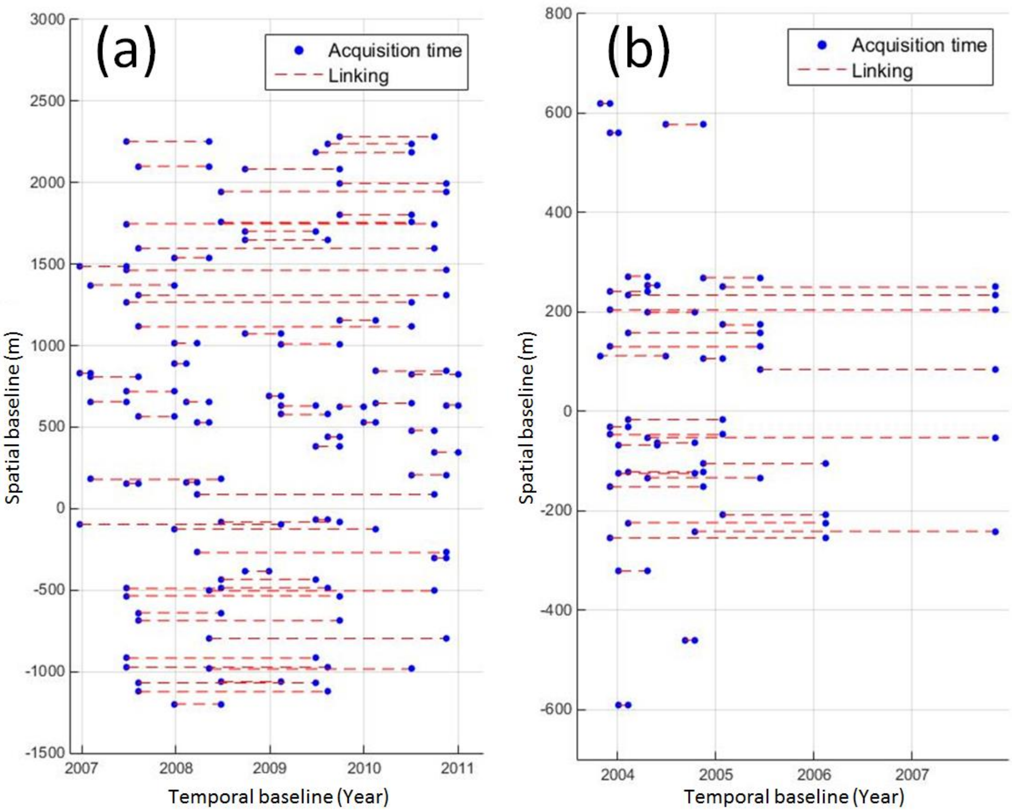

Figure 5.7 (a) Time-baseline plot of the 21 ALOS PALSAR scenes, the red dash lines represent the consecutive interferometric pair combinations out of 67. (b) Time-baseline plot of the 14 ENVISAT ASAR images, the red dash lines represent the consecutive interferometric pair combinations out of 36.

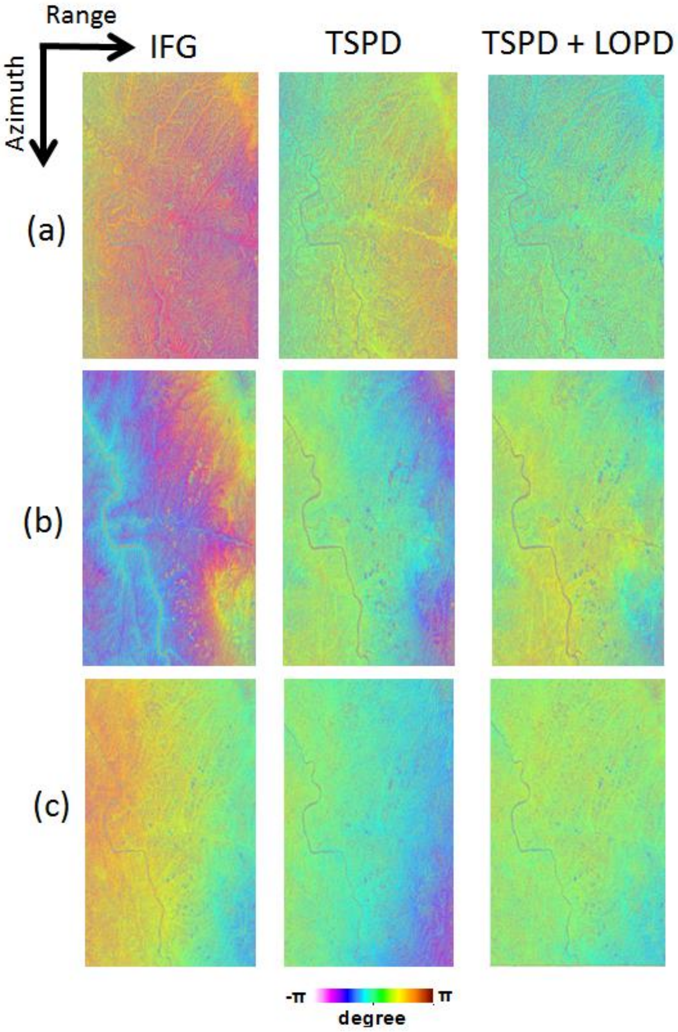

Figure 5.8 Three selected interferometric pairs in radar coordinates for L-band ALOS-1: (a) 25 December 2007 and 26 March 2008; (b) 2 July 2010 and 17 November 2010; and (c) 2 October 2010 and 17 November 2010 from the preliminary differential IFG, corrected for TSPD, corrected for TSPD and LOPD.

Table 5-2 Standard deviations of phase value for coherent points ($\boldsymbol{\gamma}$>0.7 with respect to each IFG) with various phase correction, the detailed information about these three IFG can be found in Figure 5.8.

IFG	Raw (rad)	After TSPD correction (rad)	After TSPD+LOPD correction (rad)	Improvement (%)
Figure 5.8 (a)	2.18	1.80	1.16	46.8
Figure 5.8 (b)	1.53	1.13	1.10	28.1
Figure 5.8 (c)	1.95	0.98	0.89	54.4

5.5 Experimental results and discussion

The images acquired on 27 December 2008 and 13 October 2004 were utilised as the reference image to co-register the other 20 L-band images and 13 C-band counterparts, respectively. The possible IFGs which can be formed were 210 and 91 in total, respectively, and eventually 67 and 36 multi-looked interferometric pair combinations and corresponded coherent maps were selected for further analysis, as their GGC values were relatively small (p = .32/.40). The time-baseline plot of the 21 ALOS PALSAR scenes and 14 ENVISAT ASAR acquisitions are demonstrated in Figure 5.7 (a) and (b). The three arc-second DEM derived from SRTM (Farr et al., 2007) was exploited to remove the topographic phase. To have a better representation of the TSPD, ECMWF's ERA-Interim (Dee et al., 2011) was utilised as the GAM to calculate TSPD maps. It can provide the estimation of all those atmospheric elements on a 37 pressure level every 6 h daily (Start at 0:00 UTC). In this work, all the TSPD products were acquired at 18:00 p.m. UTC (L-band) and 6:00 a.m. UTC (C-band) because these images were captured at around either 15:30 p.m. or 3:00 a.m. UTC, and individual relative TSPD map corresponding to each IFG was then subtracted from it through a conjugated multiplication operator. In addition, the linear orbital error estimated using Equation (5) was also excluded. To demonstrate the efficiency of both TSPD and linear orbital phase delay (LOPD) correction, L-band IFGs were served as an example in this study. Figure 5.8 shows three selected interferometric combinations without any correction (raw), with TSPD correction and with both TSPD and LOPD correction, respectively. The Figure illustrated that TSPD and LOPD correction reduced the atmospheric gradient by 46.8 %, 28.1% and 54.4%, respectively (Figure 5.8 third column compared to the first column) and demonstrated the importance of this correction for InSAR IFGs.

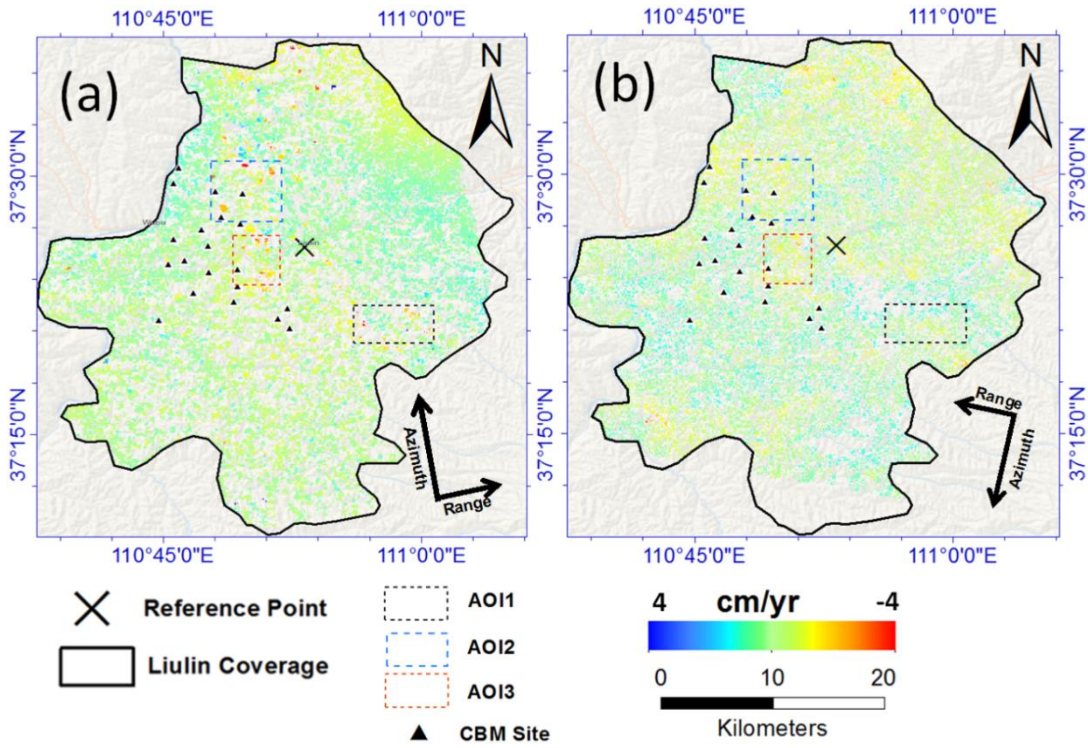

Figure 5.9 InSAR-derived linear deformation rate map with respect to coherent targets. (a) L-band ALOS PALSAR (b) C-band ENVISAT ASAR. Three regions with noticeable subsidence are marked with blue, red and black dash line rectangular boxes, respectively.

To select the multi-looked CUs, the threshold of the temporal mean $|\hat{\gamma}|$ was set to 0.7 and 0.75 for L-band and C-band analysis, respectively, and the total number of 90, 728 and 40, 742 units were identified as candidates accordingly. Delaunay TIN networks were constructed with each node represented by a candidate CU. The maximum length for the nearby CU was set to 2.0 km, and only the largest network was subsequently selected. Candidate CUs outside of the network were removed from further analysis and resulting in 88, 814 (35, 526) CUs and 245, 506 (60, 911) arcs. Then the absolute linear deformation rate and DEM error with respect to each CU were obtained using the LAMBDA and robust linear regression method described in the network integration section. It is worth noting that all these deformation values were with respect to the reference point in the central Liulin County (see the black cross in Figure 5.9), which was selected over a relatively stable region. To achieve full resolution accuracy, the absolute linear deformation rate and DEM error corresponding to each single-looked CT was estimated using the three nearest CUs and resulting in the total number of 1, 100, 096 (245, 386) CTs. The InSAR-derived linear deformation rate maps for both L-band and C-band are shown in Figure 5.9 (a) and (b).

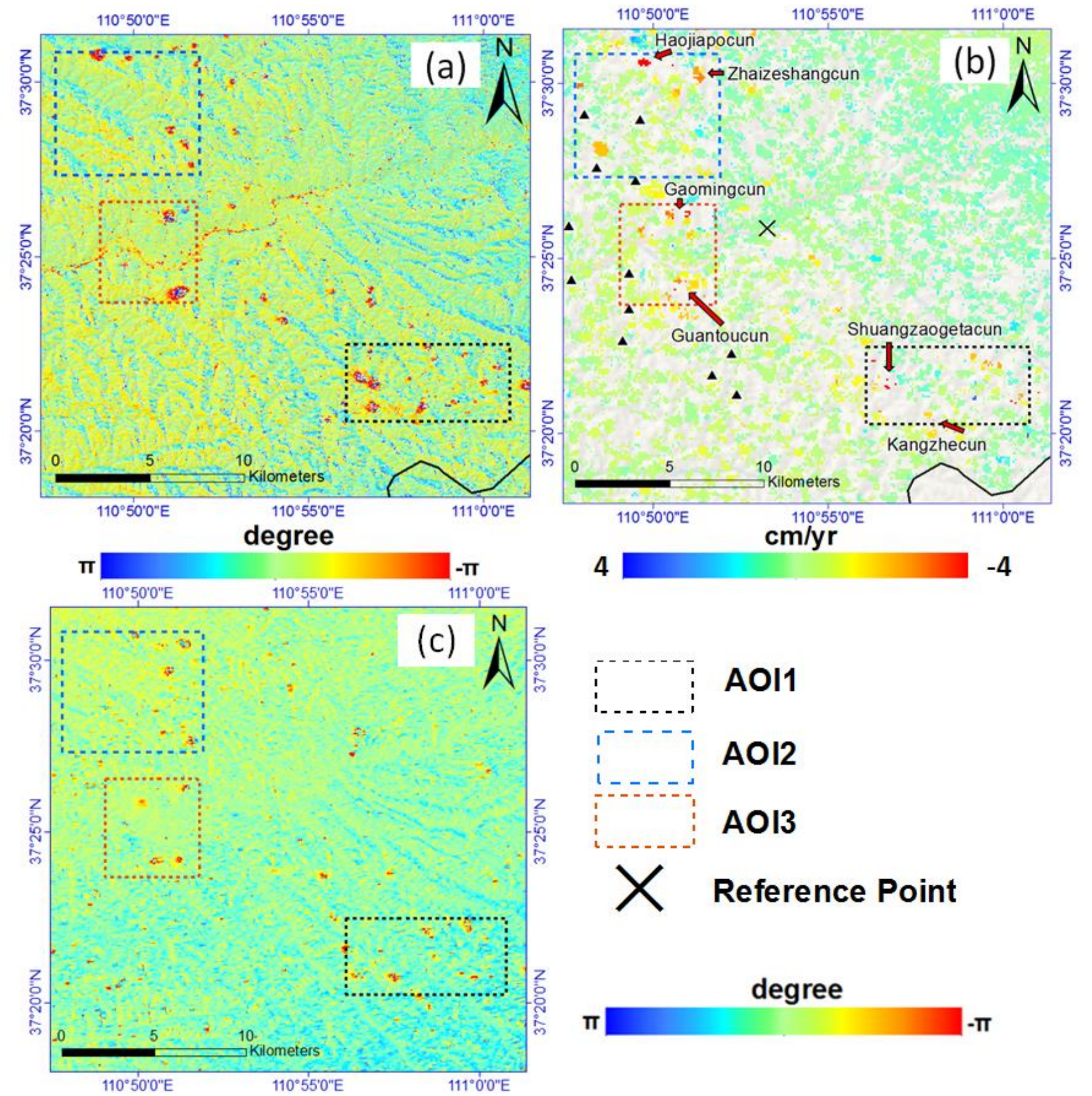

Figure 5.10 Three InSAR products derived from L-band ALOS-1 dataset (a) DInSAR IFG generated with two images acquired on 9 February 2008 and 26 March 2008 (b) InSAR-derived linear deformation rate map around AOI 1, AOI 2 and AOI 3 within Figure 5.11 and (c) DInSAR IFG generated with two images acquired on 30 December 2009 and 14 February 2010, Black cross represents the reference point.

5.5.1 L-band InSAR result interpretation

First and foremost, the deformation velocity map derived from L-band TS-InSAR analysis was illustrated in Figure 5.9 (a). It was clear that the deformation magnitude of this map, especially in the central part, was much larger compared to the counterpart C-band result (Figure 5.9 (b)), and the local deformation ranging from 15.0 to −40.0 mm yr^{-1} was identified. Besides, the south-western and north-eastern parts of Liulin region were quite stable during this four-year period while there were several areas within eastern and north-western parts suffering from land subsidence, which has been marked with blue, red and black dash line rectangles, respectively (Figure 5.9 (a) and (b)). These regions include Haojiapocun, Zhaizeshangcun, Gaomingcun, Guantoucun, Shuangzaogetacun and Kangzhecun (Figure 5.10 (b)), where the deformation rates were mainly between −20.0 and −40.0 $mm \cdot yr^{-1}$. Furthermore, the largest deformation of −40.8 and −29.9 mm yr^{-1} has been detected in Shuangzaogetacun and Haojiapocun, respectively. To explain the potential causes of the subsidence, traditional two-pass DInSAR result was generated with the master image acquired on 9 February 2008 and the slave image on 26 March 2008. It can be seen from Figure 5.10 (a) that many typical mining-induced sinking zones have been identified, for example, near Haojiapocun, Gaomingcun, Guantoucun, Kangzhecun and Shuangzaogetacun, whereas the subsidence pattern was not clear in the InSAR-derived mean deformation rate map (some rapid subsidence may seriously degrade the temporal mean coherence).

In addition, the mining-induced subsidence pattern was not found over Zhaizeshangcun in Figure 5.10 (a), whilst medium subsidence rates ranging from −10 to −20 mm yr^{-1} near Zhaizeshangcun were detected in the mean velocity map in Figure 5.10 (b), which was the zoomed in result of Figure 5.9 (a). The possible explanation was that: either the mining site was (1) not operating, or (2) was still active, but there was no underground mining activity between 9 February 2008 and 26 March 2008. Therefore, to prove the statement above, another IFG was formed with two SAR scenes acquired on 30 December 2009 and 14 February 2010, respectively (the result is shown in Figure 5.10 (c)). It is evident to us that the subsidence signal over Zhaizeshangcun region, which was not shown in the previous DInSAR result, has been confirmed at this stage. In addition, we could conclude that the mining activity over Zhaizeshangcun commenced sometime between 26 March 2008 and 14 February 2010. Last but not least, four coal mining sites have been observed from © Google Earth that were geologically close to these sinking regions (Figure 5.11), indicating that human-involved mining activities are the dominant factor that caused these local deformations. However, to further prove this argument, ground surveying measurements are still needed to verify this result.

5.5.2 Compare L-band result with C-band result over CBM sites

To match up the C-band time series outcome with the L-band counterpart, C-band result is projected into L-band LOS direction by multiplying a conversion factor cos θ_L/cos θ_C with the assumption that the East-West deformation movements are really small and are neglected in this circumstance. It is worth noting that θ_L and θ_C are the incidence angles of L-band and C-band image stacks, respectively. More specifically, the exact values for θ_L and θ_C are 38.7° and 28.8°, which result in the final conversion factor of 0.88.

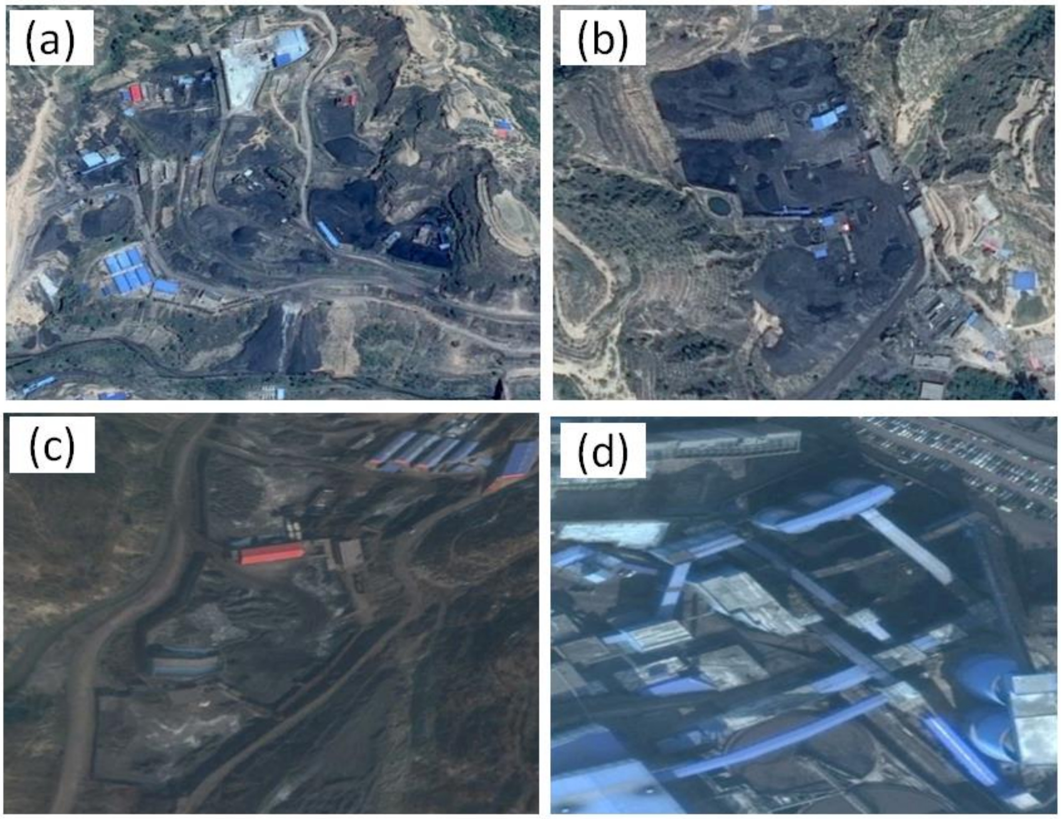

Figure 5.11 Coal mining sites identified on the optical images acquired from Google Earth (© Google Earth) near (a) Haojiapocun and Zhaizeshangcun (b) Gaomingcun, (c) Guantoucun and (d) Shuangzaogetacun and Kangzhecun.

By sharp contrast, the subsidence magnitude of C-band time series result was relatively small, and no clear subsidence patterns have been detected around the previous detected underground mining sites. A possible explanation was that the mining activities were not significant from 2003 to 2007. To measure the potential subsidence caused by the extraction operation of CBM, the following experiment was conducted over 20 CBM wells selected within this study according to Zhang et al. (2010) (Figure 5.12). All these CBM wells were constructed in the western part of Liulin Country (see Table 5-2). It is worth mentioning that the CBM well sites and the InSAR CTs were not likely to be located at the same locations due to the following reasons: (1) the natural distribution of InSAR scatterers, (2) the resolutions of both maps are different, and (3) uncertainty in geocoding process. To derive the ideal subsidence rate with respect to each CBM well, a 100 m × 100 m search window was used to identify CTs centred at CBM well site under the assumption that the displacements of all these nearby single-looked CTs were spatially correlated and had universal deformation signals. Given the fact that the resolution for C-band and L-band images is about 30 and 10 m, respectively, the corresponding maximum CTs that can be selected within the search window, are 10 and 100, respectively. After that, the average displacement values of CBM wells were calculated by averaging all these selected CTs. Nevertheless, only 14 and 13 out of 20 were covered with C-band and L-band InSAR measurements, respectively. In addition, only 8 CBMs out of 20 had the continuous measurements from 2003 to 2011, including CBM6, CBM7, CBM8, CBM9, CBM15, CBM17, CBM18 and CBM20, respectively (see Table 5-3 and Table 5-4), and would be exploited to conduct the time series analysis.

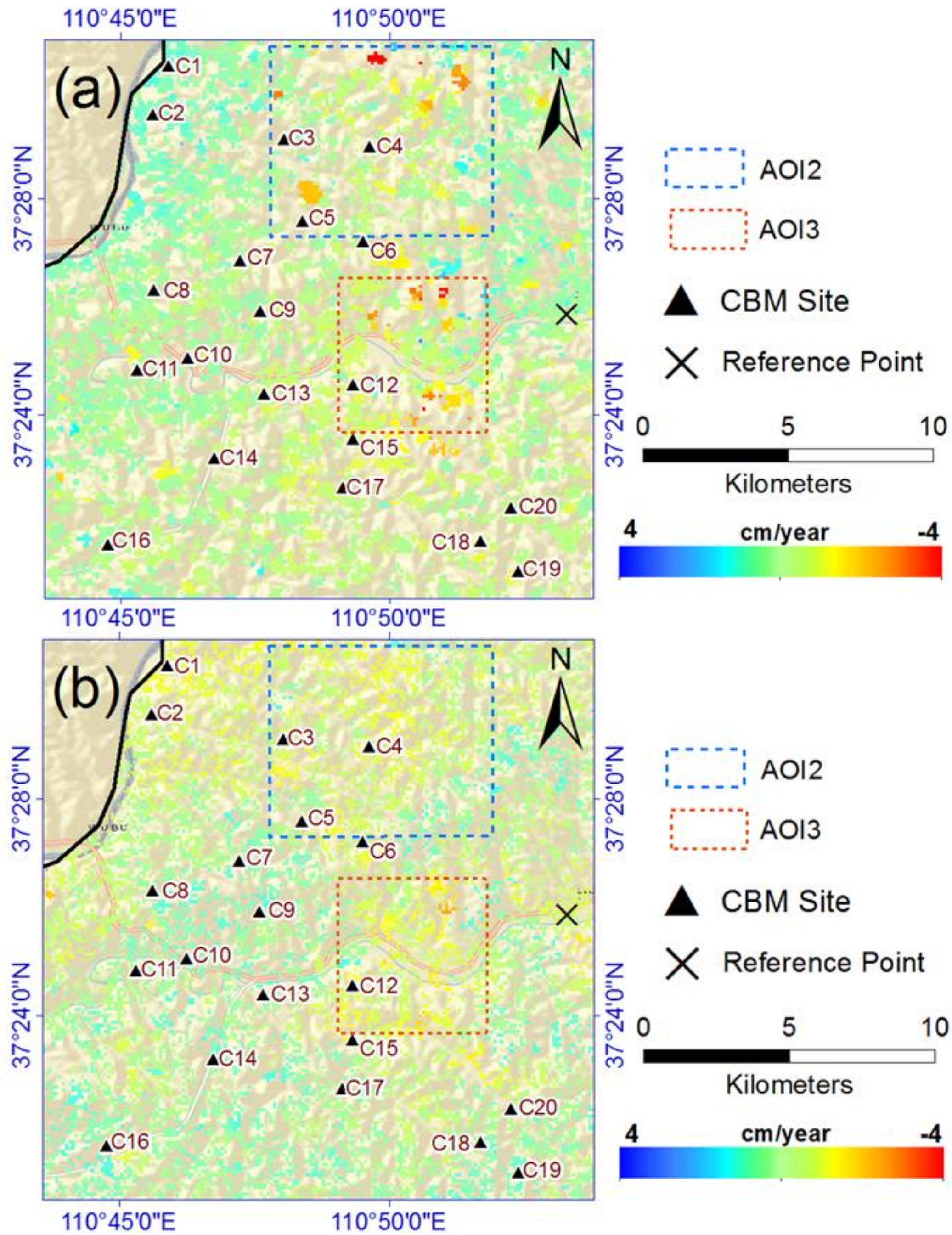

Figure 5.12 Twenty CBM sites superimposed on InSAR-derived linear deformation rate map (a) L-band outcome (b) C-band outcome.

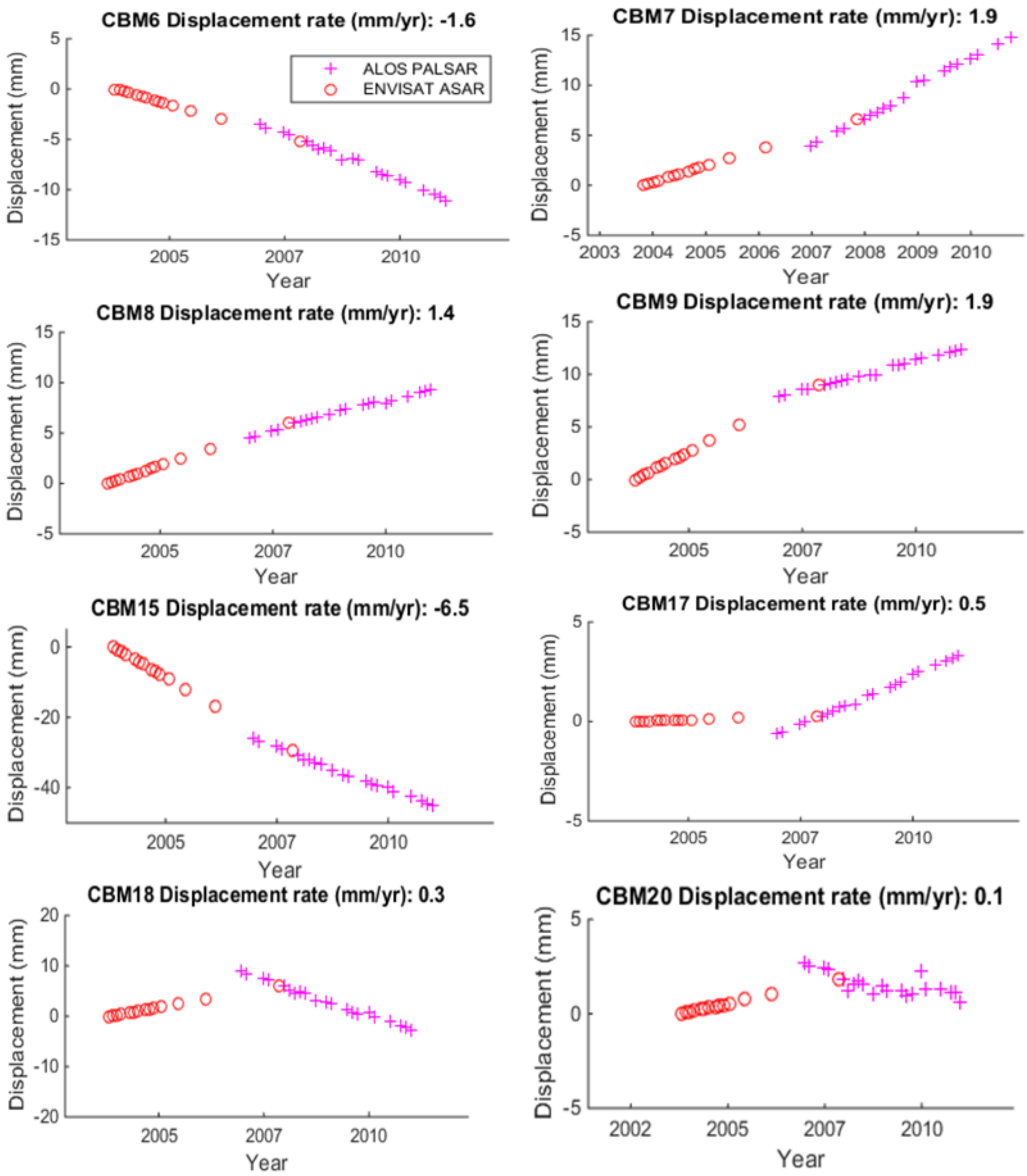

Figure 5.13 Time series measurements over eight selected CBM sites

The average deformation rates derived from L-band TS-InSAR analysis with respect to the 13 corresponding CBM sites were from 3.9 mm yr^{-1} (at CBM1) to −6.5 mm yr^{-1} (at CBM12), while the counterpart values from C-band product were between 5.6 mm yr^{-1} (at CBM14) to −7.3 mm yr^{-1} (at CBM15). Then the Mean Value (MV) and

Standard Deviation Value (SDV) with respect to these multi-CBMs were calculated based on three different circumstances (Table 5-5): 1) when considering the mere C-band result, MV of −0.3 mm yr^{-1} and SDV of 3.6 mm yr^{-1} were demonstrated, 2) For L-band outcome, MV and SDV were account for −0.9 and − 3.0 mm yr^{-1}, respectively, and 3) It was clear that only 8 CBMs out of 20 continuously had InSAR measurement from 2003 to 2011 when combining C-band and L-band measurements together, and MV and SDV over this long-time span were −3.0 and 2.6 mm yr^{-1}, respectively. Thus, it was worth noting that the ground deformations induced by these CBMs were not that significant in terms of the magnitude in any cases.

Table 5-2 Average subsidence derived from L-band InSAR over CBM sites (Unit mm $year^{-1}$)

CBM1	3.9	**CBM2**	None	**CBM3**	None	**CBM4**	None
CBM5	None	**CBM6**	−1.6	**CBM7**	1.5	**CBM8**	1.4
CBM9	1.0	**CBM10**	None	**CBM11**	None	**CBM12**	−6.0
CBM13	0.3	**CBM14**	None	**CBM15**	−4.7	**CBM16**	0.8
CBM17	0.8	**CBM18**	−3.0	**CBM19**	−6.0	**CBM20**	−0.5

Table 5-3 Average subsidence derived from C-band InSAR over CBM sites (Unit mm $year^{-1}$)

CBM1	None	**CBM2**	-1.9	**CBM3**	-6.0	**CBM4**	-5.6
CBM5	1.3	**CBM6**	-1.2	**CBM7**	2.0	**CBM8**	1.1
CBM9	2.5	**CBM10**	None	**CBM11**	3.0	**CBM12**	None
CBM13	None	**CBM14**	5.6	**CBM15**	-7.3	**CBM16**	None
CBM17	0.1	**CBM18**	1.6	**CBM19**	None	**CBM20**	0.9

Table 5-4 Mean and SDV derived from InSAR over CBM sites (Unit mm year^{-1})

	Time period	Number of CBMs	Mean value	Standard deviation
C-band	2003/10/29 – 2007/11/07	14	-0.3	3.6
L-band	2006/12/22 –2011/01/02	13	-0.9	3.0
C-band + L-band	2003/10/29 –2011/01/02	8	-0.3	2.6

The time series accumulated subsidence of eight common CBMs are displayed in Figure 5.13. It can be seen that the majority of them had experienced a linear deformation period in either towards satellite or against satellite direction with the average subsidence rate ranging from −6.0 to 1.9 mm yr^{-1}, while CBM18 and CBM20 did not illustrate linear deformation trend, but the magnitudes of the displacement over these two CBMs were quite small (< 5 mm yr^{-1}). All these measurements above demonstrated the fact that there was no clear deformation being identified with both C-band and L-band TS-InSAR products, suggesting that the basic structure of these CBM extraction sites were quite stable from October 2003 to January 2011, and the local subsidence within Liulin district was mainly caused by underground mining activities, which has been confirmed with DInSAR analysis in the previous stage.

5.5.3 Errors respect to TS-InSAR measurement

It is well known that the L-band sensor is less sensitive to the ground deformation as compared to C-band, and the accuracy of the TS-InSAR-estimated LOS deformation rate depends on three main components: the phase stability of MP pixel, temporal baseline distribution, and sensor wavelength. The equation to estimate the standard deviation of error for TS-InSAR-derived LOS deformation rate can be expressed as Equation 5.1.

$$\sigma_{\mathrm{V}} = \frac{\lambda \sigma_{\varphi}}{4\pi\sqrt{N}\sigma_{\mathrm{T}}^{2}} \tag{5.1}$$

where N is the number of images in the stacks; σ_{V} is the standard deviation of the estimated LoS displacement rate; λ is the wavelength of the sensor; σ_{φ} is the standard deviation of phase residuals; and σ_{T} is the standard deviation of the temporal baseline. Under the assumption that σ_{T}^{2} and $\sigma_{\varphi}$are constant, the precision of the measured deformation of the C-band dataset is about four times better than equivalence for the L-band dataset. In other words, the TS-InSAR measurement derived from the ENVISAT dataset was expected to achieve more precise results than the counterpart from the ALOS dataset.

On the other hand, InSAR can only be utilised to measure the ground subsidence in the LOS direction because of its side-looking system, which consists of vertical, easting and northing displacement components. The equation can be expressed as Equation 5.2.

$$D_{LoS} = [\cos\theta \quad -\sin\theta\cos\alpha \quad \sin\theta\sin\alpha]\begin{bmatrix} D_V \\ D_E \\ D_N \end{bmatrix} \tag{5.2}$$

within this equation, θ is the incidence angle while α is the heading angle (clockwise from north), D_{V} is the vertical displacement, D_{E} is the displacement in the eastern direction, while D_{N} is the displacement in northern direction. D_{LoS} is the displacement in the LOS direction.

As the LOS displacement vector is insensitive to the deformation in the north–south direction with current satellite viewing geometries, the northing displacements were assumed negligible. For ENVISAT descending pairs, the heading angle and mean incidence angle are 255° and 28.8°, respectively, resulting in the coefficients of 0.88 and 0.12 for vertical and eastern displacements. For ALOS-1 ascending pairs, the heading angle is −10°, while the mean incidence angle is 38.7°, which means the coefficients are 0.78 and −0.62, respectively. As the eastern movements are assumed to be neglected in this paper, in other words, an easting displacement of −5 mm yr^{-1} would cause an error of −0.6 and 3.1 mm yr^{-1} for C-band and L-band in the final product.

5.6 Concluding remarks

To conclude, the development of CBM in Liulin, China was started in the early 1990s and most associated research studies have mainly focused on the coal geological background or purely CBM techniques. This work presents the long term displacements in Liulin district using TS-InSAR technique to explore the potential land deformation induced by CBM extraction from 2003 to 2011. In total 21 ALOS-1 PALSAR images acquired from 22 December 2006 to 2 January 2011 and 14 ENVISAT ASAR scenes captured between 29 October 2003 and 7 November 2007 were used to measure the time series subsidence in Liulin District, China, with the tropospheric stratification phase delay and the linear orbital error being taken into consideration during the processing. An annual deformation rate ranging from 15 to −40 mm yr^{-1} was detected over the study region. Several locations were experiencing land subsidence − including Haojiapocun, Zhaizeshangcun, Gaomingcun, Guantoucun, Shuangzaogetacun and Kangzhecun − and the potential causes of these deformations were mainly due to mining activities. In addition, optical images captured from Google Earth were exploited to support the previous argument. Then the time series deformation evolutions were analysed over 8 CBM sites out of 20 and the subsidence rates were between 1.9 and −6.5 mm yr^{-1} from 2003 to 2011. In addition, the average subsidence rate and standard deviation among these eight measurements were −3.0 and 2.6 mm yr^{-1}, respectively, which means that these CBM extraction sites were quite stable and no apparent subsidence had been observed during this eight-year period. Further investigation and potential improvement in the future is necessary by comparing the TS-InSAR outcome with surveying measurements, e.g. static GPS and digital levels.

Chapter 6

C-band and L-band based TS-InSAR method over coalmine

This section reports the findings from TS-InSAR results over the Southern Coalfield, Australia using both ALOS-1 PALSAR and ENVISAT ASAR datasets. TS-InSAR has been applied to both rural and urban areas with great success, but very few of them have been applied to regions affected by underground mining activities. It is accepted that PSInSAR^{TM}, STUN and GEOS-PSI techniques are very compelling in city areas with many man-made structures where the density of PS pixels can be high enough (Ng et al., 2012b; Kampes, 2006). SqueeSAR and GEOS-ATSA can be applied to non-urban regions with good results because they select not only PS pixels, but also DS pixels (Ferretti et al., 2011; Ge et al., 2014). The TS-InSAR method utilised in this research is based on SqueeSAR and GEOS-ATSA (Ge et al., 2014). The Wollongong city area, Appin underground mining site and Tahmoor town region are our areas of interest. Appin and Tahmoor are mostly in rural areas where low density of PS pixels is expected. MS pixels are thus selected according to the different geophysical information. More specifically, since the DS pixels selection process is time-consuming, PS pixels are selected over the entire study region while DS pixels are selected around the Appin underground mining site and Tahmoor town region in order to achieve the best details. The section is based on the material published in Remote Sensing (Du et al., 2016a).

6.1 Study regions within southern coalfield and dataset

Australia is a country with many land subsidence issues, and most of them are related to anthropogenic activities including the extraction of natural resources, such as coal, natural gas and iron ore (Ng et al., 2010; Ng et al., 2014). The Sydney-Gunnedah Basin, which is 500 km long and 150 km wide, has the largest coal resource storage in New South Wales (NSW). There are five major coalfields inside the basin: Newcastle, Western, Hunter, Southern and Gunnedah. It covers an area south of Berrima and Sutton Forest to the north of Campbelltown, west of Tahmoor town and east of Wollongong, and has the only source of hard coking coals in NSW, which is favourable for steel production (Ng et al., 2010). Many previous InSAR studies were conducted over the Southern Coalfield (Ng et al., 2009; Ng et al., 2010; Ng et al., 2011). More specifically, both DInSAR and small stacks of InSAR methods were exploited to study the local subsidence mainly near Appin, Tahmoor and West Cliff collieries in the Southern Coalfield of NSW. Single-master-based TS-InSAR technique was not used for these earlier analyses due to two major reasons: (1) The number of ALOS PALSAR images were limited (10 acquisitions) while normally much larger image stacks (more than 20) are required by these TS-InSAR methods to achieve precise deformation measurement, and (2) most of these collieries in the Southern Coalfield are located within rural areas where very few PS pixels were expected by using these methods.

Regarding the geological settings, all three regions of interest are within the Southern Coalfield (Figure 6.1). Wollongong city area is in the Illawarra region of New South Wales, Australia, and is situated adjacent to the Tasman Sea and the South Coast railway line (orange rectangular box in Figure 6.2). Appin is a town in the Macarthur Region of New South Wales, Australia and it is situated about 35 kilometres Northwest of Wollongong. The underground coal mining site Appin Colliery is located about 25 kilometres Northwest of Wollongong (blue rectangular box in Figure 6.2). Tahmoor town is located in the Macarthur Region of New South Wales and to the southwest of Appin coal mining site. The Tahmoor Colliery, located to the south of North Bargo, is the primary source of its regional economy growth (purple rectangular box in Figure 6.2). The topographical slopes over these three sites are ranging between 0° and 3°, which indicates that the study regions are relatively flat (Figure 6.2 (c)).

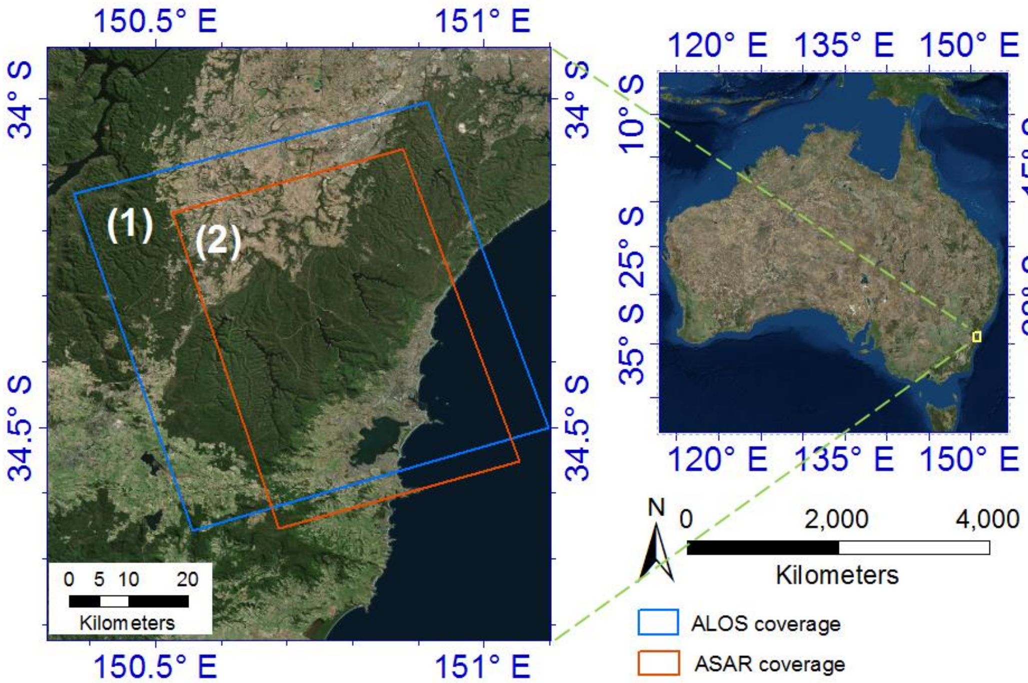

Figure 6.1 The coverage of ALOS-1 PALSAR image stacks (1) and ENVISAT ASAR image pairs (2).

In order to map the land displacement over the Southern Coalfield, Australia, twenty-three L-band ALOS-1 PALSAR scenes acquired between 29 June 2007 and 7 January 2011 and twenty-four C-band ASAR images acquired between 8 July 2007 and 5 September 2010, are analysed. All the ALOS-1 images (Track 370, Frame 649) were captured in ascending orbit with the average incidence angle of 38.7° while all the ASAR images (Track 381, Frame 6492) were acquired in ascending orbit with the incidence angle of 28.8°, which means both ALOS and ENVISAT sensors are only sensitive to LOS displacement (Figure 6.2 (a) and Figure 6.2 (b)). Eleven ALOS-1 images were acquired in HH and HV dual-polarisation while the other twelve were acquired in HH single polarisation. The dual-polarisation data (HH) were oversampled by a factor of two in range direction (Ng et al., 2012b) and the final pixel spacing in azimuth and range were 4.82 m and 5.55 m, respectively. All the ASAR images were acquired in VV single polarisation with the azimuth and range pixel spacing of 7.80 m and 4.06 m, respectively.

Table 6-1 ALOS and ENVISAT dataset.

Date (ALOS)	**Bperp (m)**	**Btemp (days)**	**Date (ENVISAT)**	**Bperp (m)**	**Btemp (days)**
29/06/2007	−2102.1	552	08/07/2007	244.5	−560
14/08/2007	−2067.8	−506	12/08/2007	274.8	−525
29/09/2007	−2572.8	−460	16/09/2007	−166.8	−490
14/11/2007	−2688.5	−414	21/10/2007	300.5	−455
30/12/2007	−3429.9	−368	25/11/2007	73.7	−420
14/02/2008	−3417.3	−322	30/12/2007	457	−385
31/03/2008	−4058.8	−276	03/02/2008	103.2	−350
16/05/2008	−4025.9	−230	09/03/2008	341.5	−315
01/07/2008	−1120.5	−184	13/04/2008	−70	−280
01/10/2008	740.6	−92	18/05/2008	185.6	−245
16/11/2008	680.2	−46	31/08/2008	78.3	−140
01/01/2009	0	0	05/10/2008	188.5	−105
16/02/2009	−303.4	46	09/11/2008	186.9	−70
04/07/2009	−872.4	184	14/12/2008	397.2	−35
04/10/2009	−1343.6	276	**18/01/2009**	0	0
19/11/2009	−1654.6	322	22/02/2009	129.8	35
04/01/2010	−2174.1	368	29/03/2009	−396.2	70

22/05/2010	−3149.4	506	29/11/2009	128.6	315
07/07/2010	−3164.7	552	14/03/2010	231.9	420
22/08/2010	−3262.4	598	18/04/2010	−57.3	455
07/10/2010	−3564.2	644	23/05/2010	143.6	490
22/11/2010	−4138.7	690	27/06/2010	122.5	525
07/01/2011	−4518.7	736	01/08/2010	419.1	560
			05/09/2010	142.2	595

6.2 Experimental results and analyses

Images acquired on 1 January 2009 (ALOS-1 PALSAR images) and 18 January 2009 (ENVISAT ASAR scenes) are picked as master images for the two image stacks to minimise the temporal and perpendicular baselines. Figure 6.2 (a) & (b) presents the TS-InSAR results using the ALOS-1 PALSAR and ENVISAT ASAR datasets, respectively, and both of them are resampled onto a grid with a resolution of 100 m × 100 m for further comparison. Regions marked with red, blue and purple rectangular boxes are the Wollongong city area, Appin underground mining site and Tahmoor town region. The measured displacements are with respect to the reference point (pink point in Figure 6.2) centred at 34˚ 22' 04" S and 150˚ 55' 25" E. The total number of MS pixels obtained from ALOS-1 dataset is 1,652,180, of which 88,003 are PS pixels. There are 403,857 MS pixels estimated from ENVISAT dataset, and 83,304 of them are PS pixels. The reason for this is because the wavelengths of the two sensors are different. L-band PALSAR sensor with longer wavelength has less decorrelation than C-band under the same baseline condition, therefore, it offers a much higher density of DS pixels (the density of PS pixels are similar). The total number of refined arcs is 4,921,872 and 1,184,997 for PALSAR and ASAR datasets, respectively. Therefore, the density of MS pixels at the three sites are 355, 8004, 6686 MS km^{-2} and 398, 423, 1557 MS km^{-2} for ALOS-1 and ENVISAT, respectively (only PS pixels are selected in Wollongong city area while both PS pixels and DS pixels are selected in the Appin underground mining site and Tahmoor town region). To compare the time series performances between C-band and L-band products, both time series displacements in LOS direction (Figure 2 (a) & (b)) are converted into the vertical direction by dividing the cosine of its incidence angle.

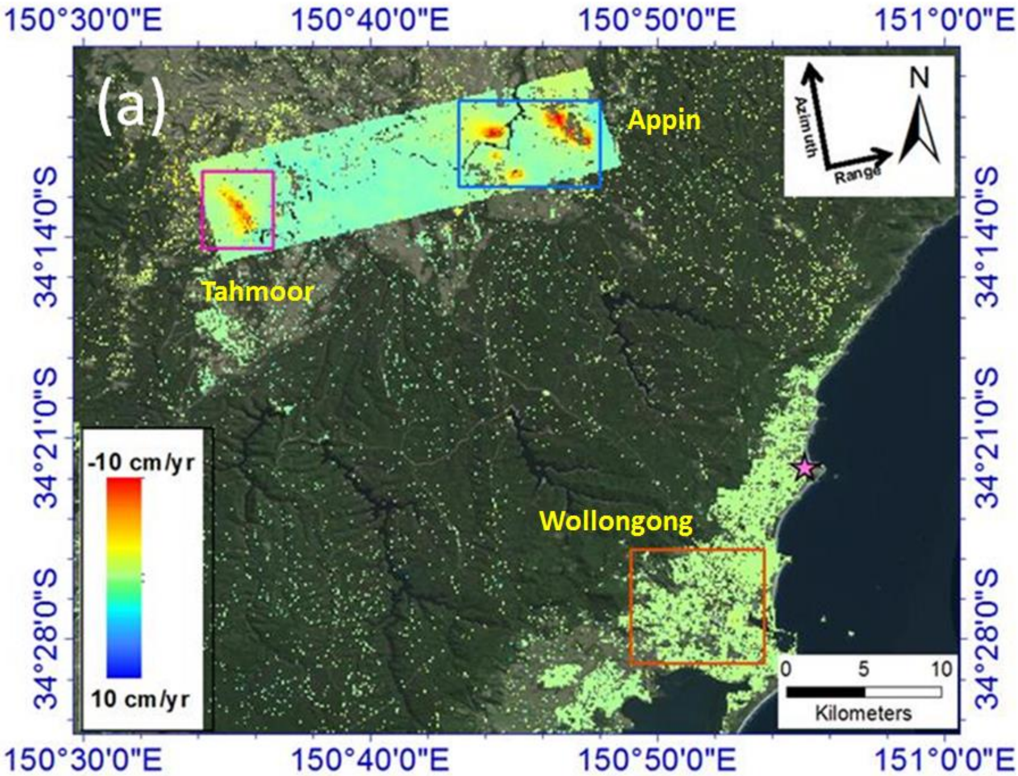

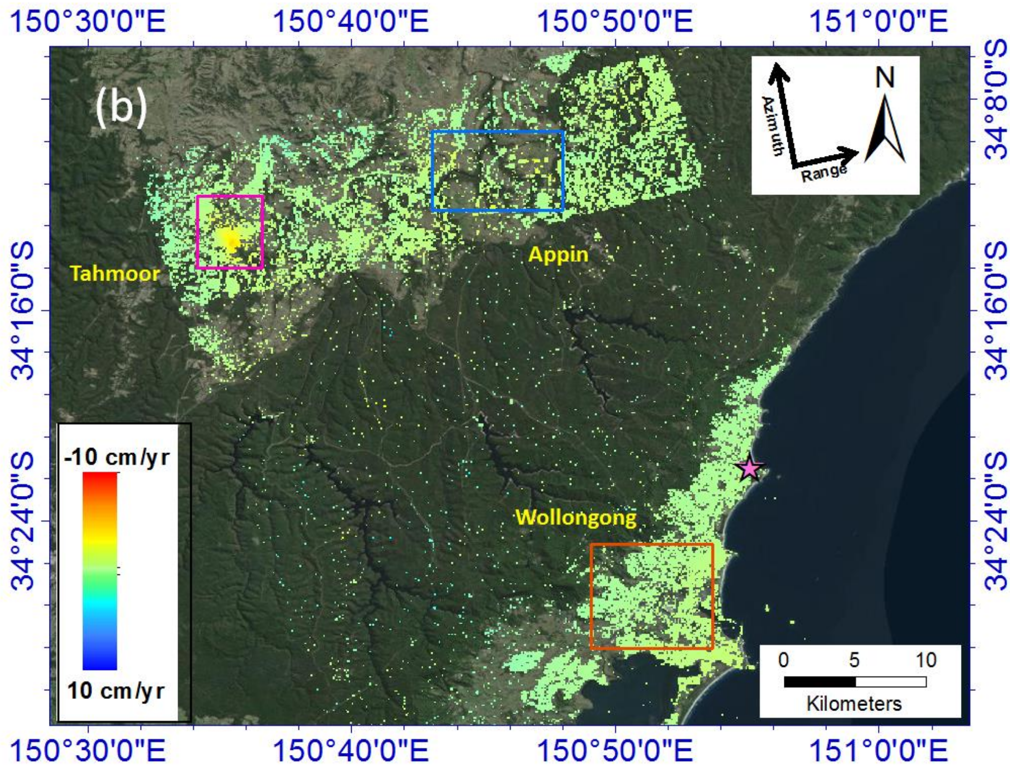
150°30'0"E
150°40'0"E
150°50'0"E
151°0'0"E
34°8'0"S
34°16'0"S
34°24'0"S
(b)
Azimuth
Range
N
Tahmoor
Appin
Wollongong
-10 cm/yr
10 cm/yr
0 5 10
Kilometers

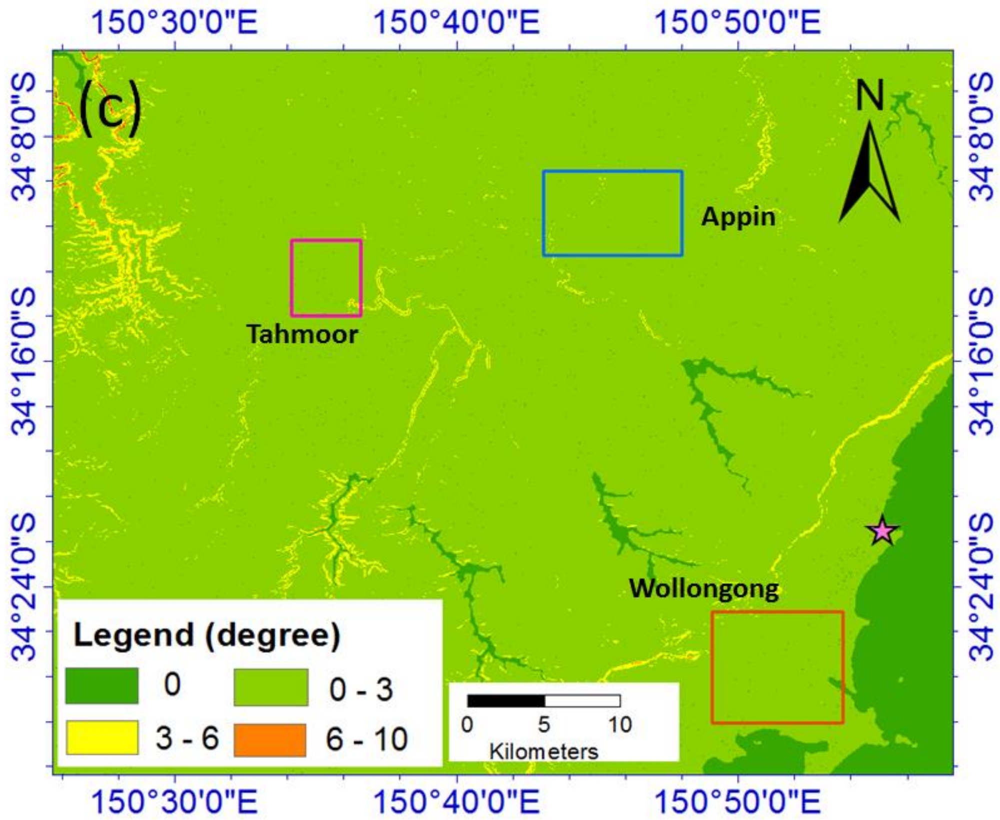
150°30'0"E
150°40'0"E
150°50'0"E
34°8'0"S
34°16'0"S
34°24'0"S
(c)
N
Appin
Tahmoor
Wollongong
Legend (degree)
0
0 - 3
3 - 6
6 - 10
0 5 10
Kilometers

Figure 6.2 (a) ALOS-1 PALSAR mean velocity result in LOS direction. (b) ENVISAT ASAR mean velocity result in LOS direction. The pink star represents the reference point while regions marked with red, blue and purple rectangular boxes are Wollongong city area, Appin mining sites and Tahmoor town region, respectively. The displacement results are resampled onto a grid of 100 m × 100 m resolution. (c) Slope Map generated from SRTM DEM.

6.2.1 Deformation over Wollongong City

The ground cover in Wollongong City is mainly made up of low vegetation and man-made structures, where a large number of PS pixels are expected because high coherence in the IFGs can be preserved over these regions. Figures 6.2 (a) to (c) show the displacement rate distribution between ALOS and ENVISAT time series measurements in Wollongong City. It is worth noting that the resolution of both displacement maps is resampled onto 100 m × 100 m and only common MS pixels have been taken into consideration. Figure 6.3 shows the time series measurement over one MS pixel marked by a red cross where a similar subsidence trend has been observed from both C-band and L-band results. Figure 6.4 illustrates good agreement between these two datasets. A root-mean-square-error (RMSE) (equation 6.1) of 3.11 $mm \cdot yr^{-1}$ has been obtained, showing that the L-band and C-band time series subsidence is comparable over Wollongong. During the estimation, the unmatched MS pixels are not included in the calculation of RMSE. In addition, the majority of subsidence in the city is between −10 to 10 $mm \cdot yr^{-1}$, which suggests that the local subsidence rate is quite stable. The difference between observations could be due to three reasons: (1) The different measurement precision is due to different sensors, (2) the horizontal movement is neglected, and (3) there is a mis-match in geolocation between individual MS pixels.

$$\text{RMSE} = \sqrt{\frac{1}{P}\sum_{p=1}^{P}(D_p^M - D_p^S)^2} \tag{6.1}$$

where P is the total number of common MS pixels within the region for RMSE estimation, D_p^M and D_p^S are the pth pixels within master and slave images, respectively.

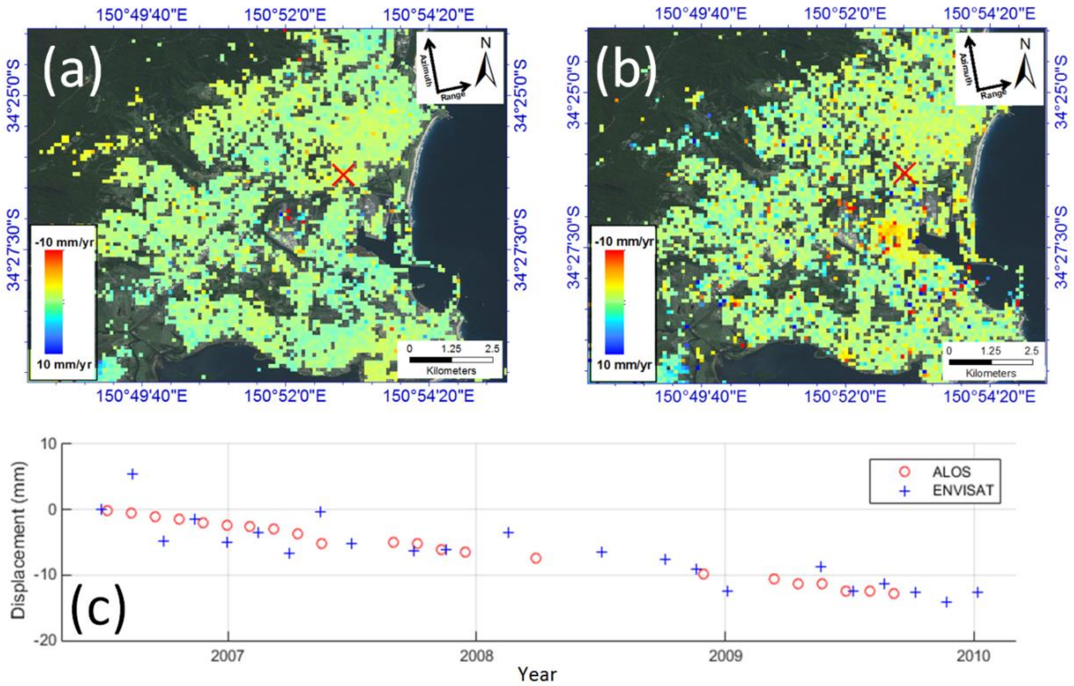

Figure 6.3 L-band (a) and C-band (b) measurement over Wollongong city region in the vertical direction (c) time series evolution over one MS pixel marked with the red cross.

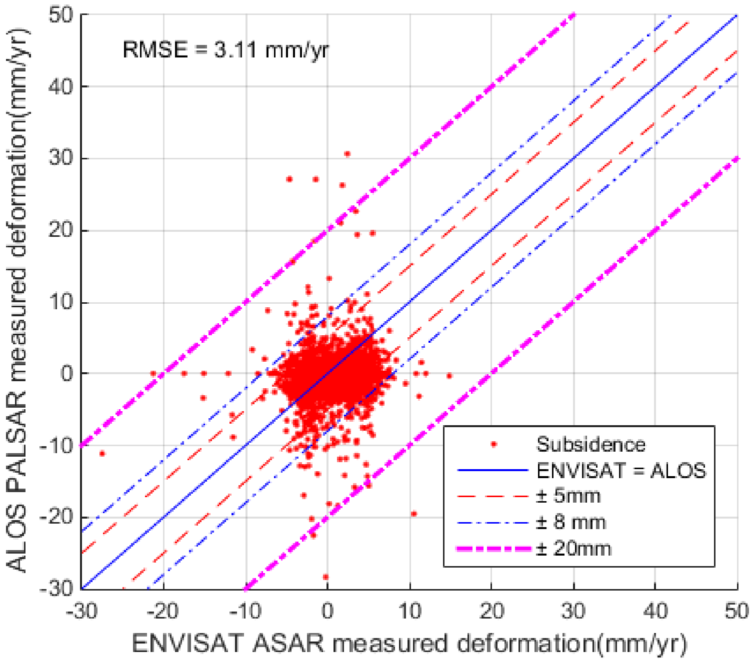

Figure 6.4 Comparison over Wollongong between L-band and C-band TS-InSAR results.

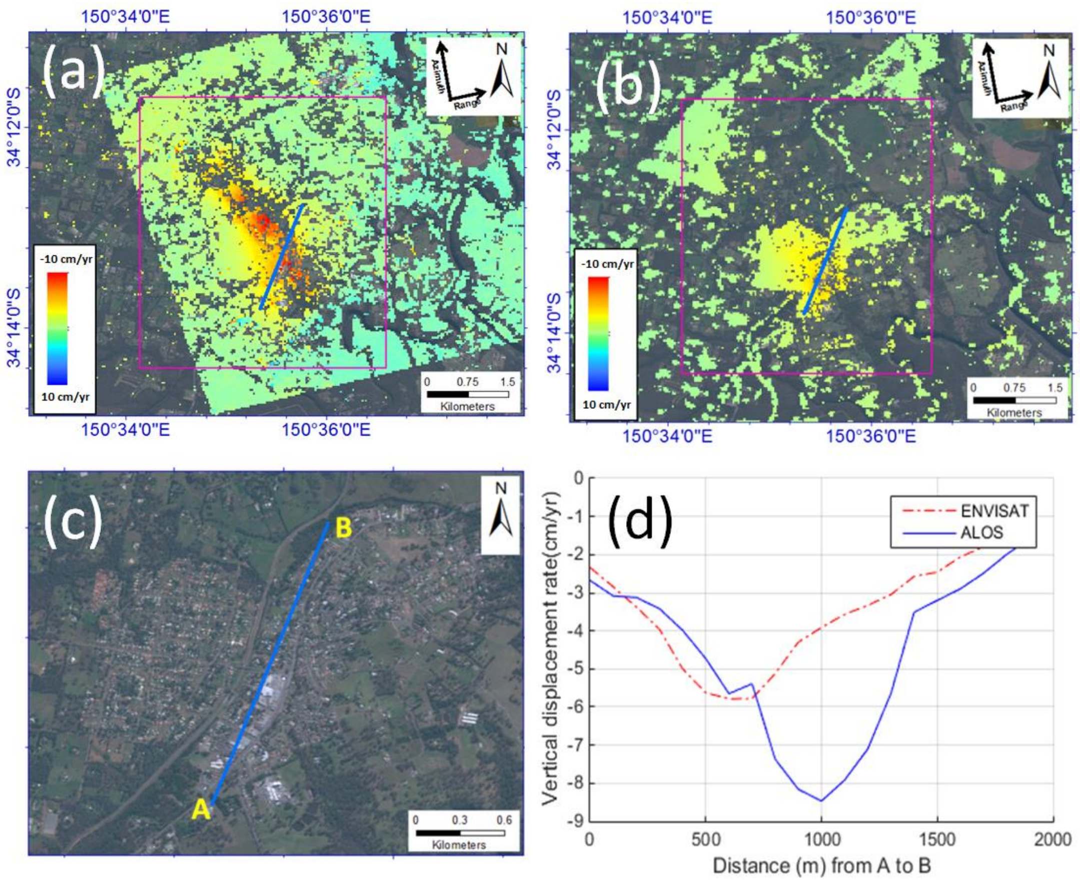

Figure 6.5 (a) L-band and (b) C-band measurements over Tahmoor region, the resolution of each pixel is 30 m × 30 m (c) Google map over Tahmoor town (© Google Earth) (d) the profile line through Tahmoor town.

6.2.2 Deformation over Tahmoor

Figure 6.5 (a) & (b) illustrate the vertical time series measurements in the Tahmoor town region with ALOS-1 and ENVISAT, respectively. It can be observed in both figures that vast areas around Tahmoor's centre are suffering from significant fall in ground elevation. In addition, L-band result indicates the western parts of Tahmoor town have experienced large subsidence with the maximum subsidence higher than –10 $cm \cdot yr^{-1}$ in the vertical direction, whereas it is not found in the C-band result. A 2 km profile line is drawn through the entire Tahmoor town (Figure 6.5 (c)). Figure 6.5 (d) shows the time series subsidence on this profile line for both datasets. The largest subsidence of –8.5 $cm \cdot yr^{-1}$ and –5.8 $cm \cdot yr^{-1}$ has been detected, respectively. It is clear that the left and right parts agree with each other well. However, there is a huge difference in the middle of the profile from 600 m to 1300 m, with the largest difference reaching –4.5 $cm \cdot yr^{-1}$ at 1000 m.

The difference is mainly caused by several reasons: (1) Signal saturation issue should be the most significant reason since the maximum detectable subsidence is different for both sensors (the detailed analysis can be found in Section 5.3) (2) A searching window with the same size of 100 m × 100 m is applied to find the point targets closet to the profile line for comparison, which means each value within the profile line does not reflect the subsidence of one single MS pixel, but a group of MS pixels. In addition, the numbers of MS pixels are different for both sensors within a searching window due to the threshold difference for “ensemble phase coherence” and we hold the assumption that L-band could preserve a higher coherence compared to C-band. (3) The middle part may suffer from some rapid changes during the 4-year period. However, compared to the L-band sensor, pixels with large displacement rate are less likely to be considered as MS pixels for a C-band sensor. In other words, within the searching window, L-band TS-InSAR result contains MS pixels with larger deformation that C-band TS-InSAR cannot capture. (4) According to the eastern part of Figure 6.6 (a-f), the loss of coherence in the high-gradient region in C-band dataset which resulted in underestimation of the mean velocity.

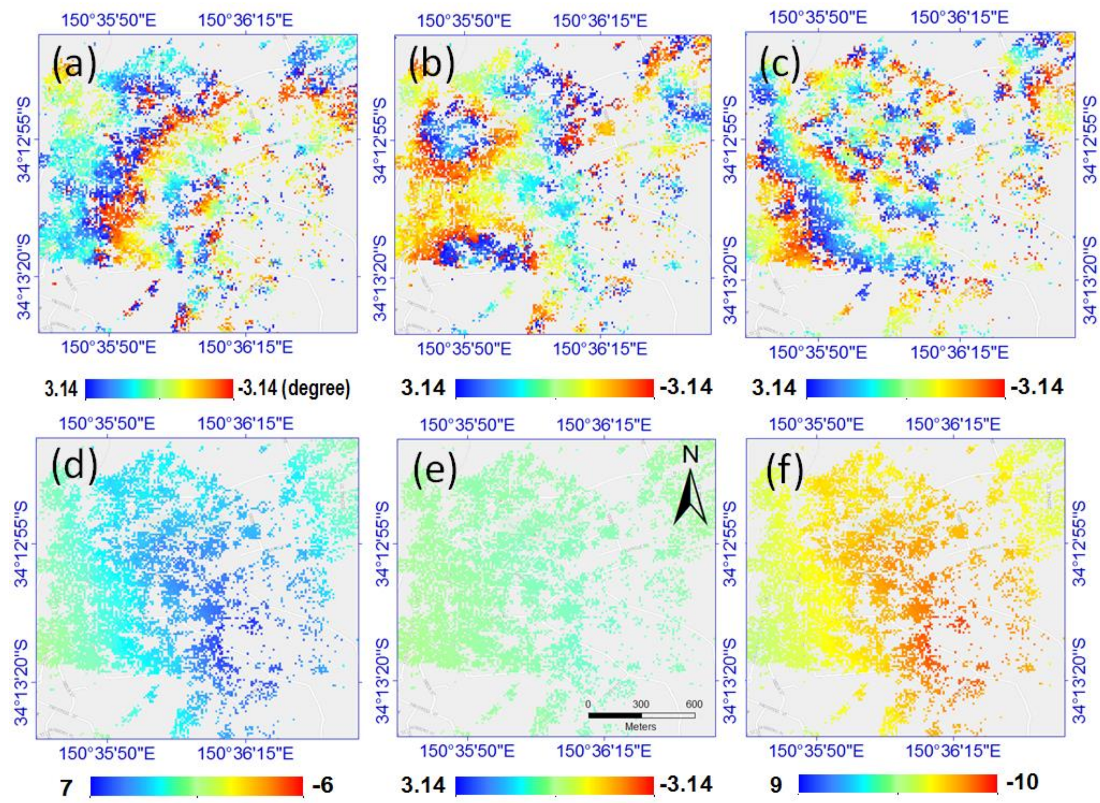

Figure 6.6 Three selected IFGs within the study region of Figure 6.5 (a–c) interferometric phase after the interferometric phase optimization; (d–f) unwrapped

phase from deformation; (a, d) 3 February 2008 and 18 January 2009; (b, e) 9 November 2008 and 18 January 2009; (c, f) 18 January 2009 and 1 August 2010.

6.2.3 Deformation over Appin underground mining site

One of the limitations of TS-InSAR techniques is related to resolving the phase ambiguity in regions suffering from rapid subsidence (Colesanti et al., 2002), for example, underground mining-induced subsidence. In other words, the deformation signal may not be correctly estimated if the subsidence of the MS pixel between any two image acquisitions within the image stack is larger than one-half cycle (5.9 cm/46 days for L-band satellite while 1.4 cm/35 days for C-band satellite). In this circumstance, the TS-InSAR technique can only be used to identify the occurrence time and location with respect to each MS pixel, but it may not be able to calculate the correct subsidence value. The above problem can be solved if *a-priori* knowledge is available (Colesanti et al., 2003b), which is significantly limited or even unavailable in most TS-InSAR analysis cases.

Land subsidence in the Appin mine site is mostly related to underground mining activities. Figure 6.7 (a) & (b) show the time series displacement of L-band and C-band measurements at the Appin site and the resolution is resampled onto 30 m × 30 m from original datasets, respectively. In general, the deformation patterns observed from the two measurements are not the same. In Figure 6.7 (a), several clear oval deformation patterns were found in the middle and right parts of the image, which is due to underground mining activity. However, there is no such subsidence pattern observed in Figure 6.7 (b), where the MS pixels are identified at the roads and residential areas and are reasonably stable. A possible explanation is that the deformation gradient is too large and highly nonlinear over the subsidence area. According to Ng et al. (2010), the mining-induced subsidence in the Southern Coalfield could reach up to 20 to 60 cm within the first 1 – 2 months and up to 80 – 100 cm in a one-year period. Therefore, no MS pixels can be obtained over the areas that were experiencing significant subsidence from C-band TS-InSAR product.

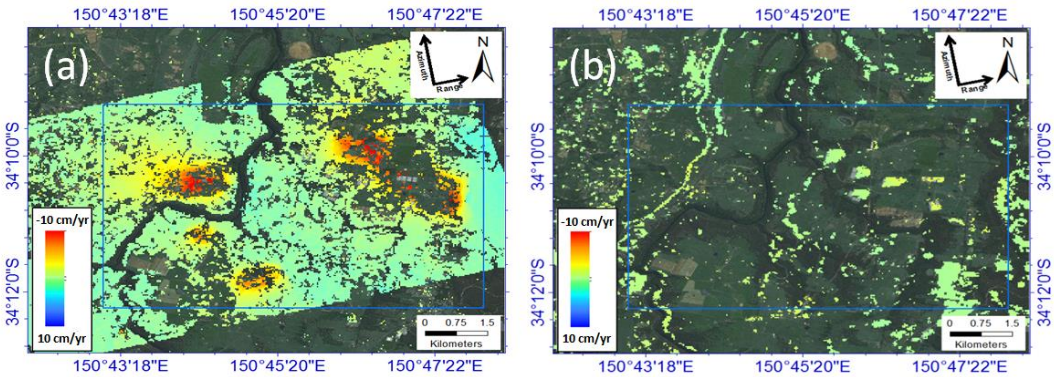

Figure 6.7 Comparison over Appin mining site between (a) L-band and (b) C-band, the resolution of each pixel is 30 m × 30 m.

Figure 6.8 (a) shows the typical fringe patterns caused by mine subsidence derived from DInSAR IFGs with two obvious characteristics: (1) The earth surface where underground mining occurs will sink as the colour of the deformation pattern changes from yellow to blue (from the centre to the edge), and (2) the subsidence magnitude increases from the edge to the centre, therefore forming an oval or round shape (Hu et al., 2013). Figure 6.8 (b) illustrates the underground mining subsidence pattern from the TS-InSAR velocity map. Regions suffering from rapid changes within a short period of time will de-correlate and therefore form gaps in the subsidence zones. Two characters are described in this chapter to identify underground mining-induced subsidence regions: (1) The subsidence zones are commonly rectangularly or quadrilaterally shaped (related to the shape of longwall mining sites), and (2) the magnitude of subsidence rate over the subsidence zone edges is relatively large (the actual subsidence in the center is much larger than the counterparts at the edges, nevertheless, the subsidence in the center experiences a nonlinear trend and cannot be captured with TS-InSAR method). By using the methodology described above, four mine subsidence bowls have been detected within Figure 6.7 (a) with a maximum subsidence rate in excess of -10 cm yr^{-1}.

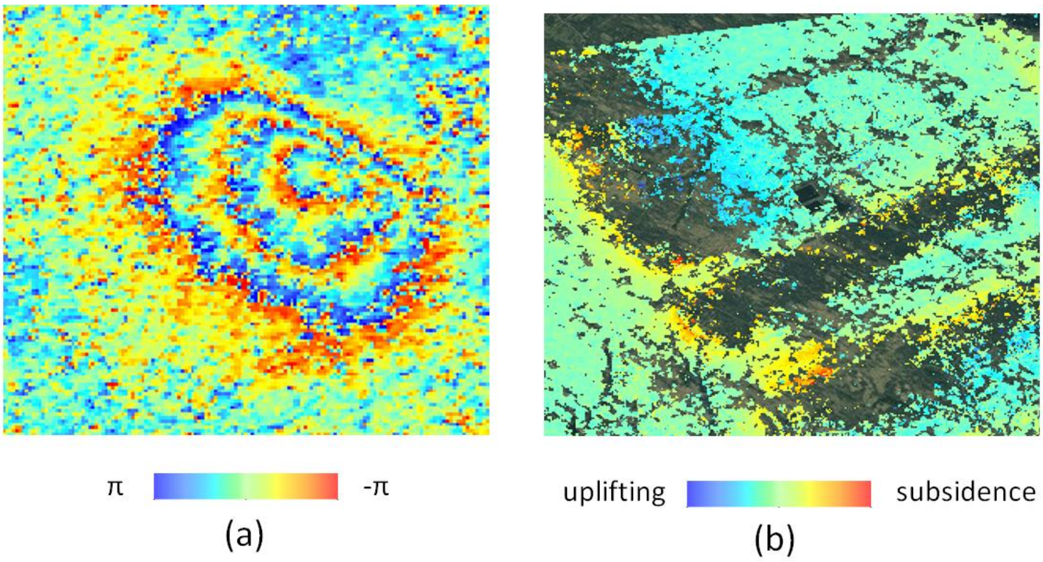

Figure 6.8 Typical patterns of underground mining subsidence in (a) DInSAR differential IFG. (b) TS-InSAR velocity map (Du et al., 2016b).

6.2.4 Conclusion remarks

In this section, the land surface stability over three test sites with different geological settings within the Southern Coalfield region was investigated using TS-InSAR technique. These three regions are: (1) Wollongong City, which is a relatively stable area, (2) Tahmoor Town, a small town affected by underground mining activities and (3) Appin underground mining site, a region with many underground mining operations. Both C- and L-band derived measurements are compared over these three sites. Within the process, a first-order linear function is utilised to remove the linear phase “ramp” induced by residual orbital error. From the experiment result, we could see that the performance of both C- and L-band is equally good over Wollongong City, where the dynamic range of subsidence is not significant, and the subsidence rate is mostly between -10 to $10\ \mathrm{mm \cdot yr^{-1}}$. However, over Tahmoor and the Appin mine, their performances differ. Since the maximum displacement gradients that can be detected are different for L- and C-band-based TS-InSAR, some rapid changes in land surface could cause the TS-InSAR to fail to estimate the correct displacements. It is well known that the L-band can perform better especially in underground mining regions and mining-affected regions where the deformation rate is much higher than city areas. L-band datasets are able to provide better results and achieve detailed deformation signals about the spatial distribution of the ground surface subsidence phenomenon. The traditional DInSAR subsidence pattern is then compared with the TS-InSAR subsidence pattern induced by underground mining activities. The comparison shows a promising way to identify illegal mining sites using TS-InSAR techniques. For example, DIMDS proposed by Hu et al. (2013) could be exploited to detect still-active illegal underground mining sites between two image acquisitions, while both still-active and ceased-illegal underground mining sites could be identified with the TS-InSAR subsidence pattern described in this research.

TS-InSAR results derived from an L-band dataset can indeed be used to measure the subsidence around underground mining zones; possible future research is therefore to form the three-dimensional analyses and observe the time series horizontal subsidence around underground mine sites with both descending and ascending L-band image stacks. ALOS-2, the successor of ALOS-1 launched on 24 May 2014, could be utilised to conduct TS-InSAR analysis over underground mining areas. In addition, it is possible that both L- and C-band datasets can be used together to detect the horizontal movement at certain locations, where good InSAR coherence can be preserved for C-band datasets, e.g., Sentinel-1A satellite, which has a short revisit time.

Chapter 7

DInSAR and TS-InSAR for mining subsidence detection

7.1 Integration of DInSAR with TS-InSAR

The aim of this section is to investigate ground deformation in Ordos, China by applying both DInSAR and TS-InSAR algorithms for images computational processing. TS-InSAR has been successfully used to monitor long term earth surface deformation in either urbanised or non-urban areas for a decade, such as Las Vegas, Beijing or Bandung (Kampes, 2006; Ng, 2010; Ge et al., 2014). The problem with TS-InSAR was that some rapid surface subsidence happening in a relatively short period lead to loss of InSAR coherence, and therefore gaps would appear in such areas because no scatters could be selected (chapter 6). A new method is proposed here to fill these gaps by exploiting DInSAR integration with the TS-InSAR. The subchapter is based on the material published in Remote Sensing Letters (Du et al., 2016b).

However, there is a problem with DInSAR measurement accuracy. It was related to its atmospheric phase screen (APS). Although the APS can be estimated via using data from Medium-Resolution Imaging Spectrometer (MERIS) or Moderate Resolution Imaging Spectroradiometer (MODIS), and the reduction of atmospheric effect could be 20 – 40%, these methods often depend on the atmospheric conditions (Ding et al., 2008). Recently, many researchers have tried to use Global Atmospheric models (GAM) to predict the tropospheric stratified phase delays at the SAR image acquisition time (Li et al., 2006c; Jolivet et al., 2014). Doin et al. (2009) have quantitatively validated the potential of a number of GAMs by comparing with empirical corrections. Jolivet et al. (2014) further extended Doin's work and demonstrated the feasibility of predicting the tropospheric stratified delay from GAM. DInSAR result was exploited after removing the tropospheric stratified phase delay using Jolivet's method and later integrated with TS-InSAR outcome to form a new product.

7.1.1 Geological settings and dataset

Ordos is located along the boundary between Inner Mongolia and Shaanxi Province, China (Figure 7.1 (a)), with coal mining and coal-to-liquids (CTL) industries playing an important role in regional economic growth in recent decade. However, it has been reported recently that this region is suffering from a significant drop in earth surface elevation. In April 2014, the Ordos government forced Shenhua Company, the world's biggest coal producer, to stop their CTL project from pumping groundwater in Ordos (Damian, 2014). Zhao et al. (2013) reported that from 2006 to 2011, the maximum vertical subsidence over the mining sites of Ordos reached 4.5 m with the image offset tracking method. However, such method can lead to bias in terms of its accuracy (0.2 m in slant range direction).

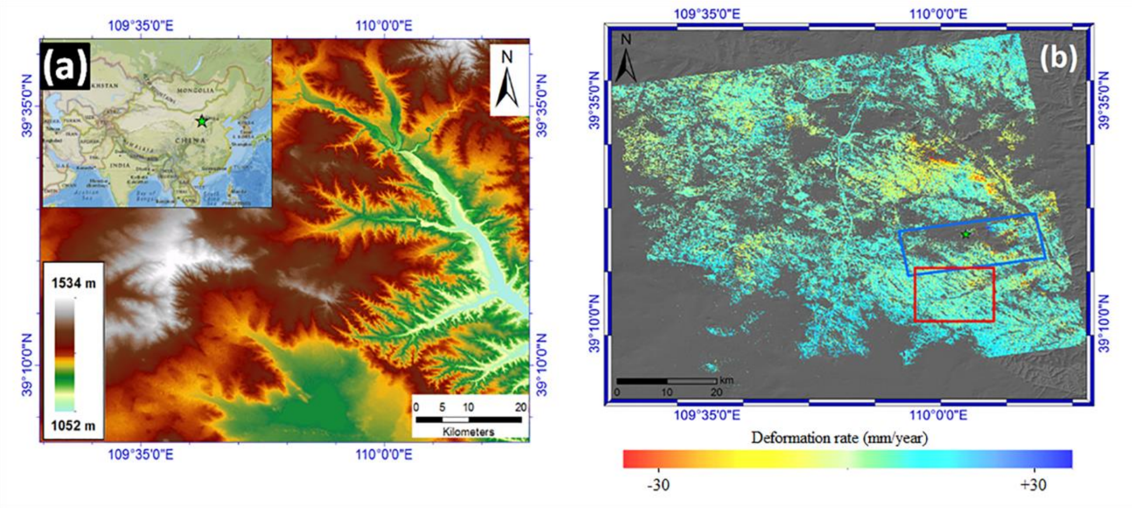

Figure 7.1 (a) Ordos region superimposed with DEM (b) Deformation maps over Ordos using GEOS-PSI with D_A < 0.4. The blue rectangle indicates the region with Advance Time Series Analysis (GEOS-ATSA) analysis. The red rectangle indicates the relatively stable region, which will be used for further analysis.

Twenty L-band ALOS-1 PALSAR images acquired between 8 January 2007 and 19 January 2011, were processed and analysed in this study. All these acquisitions (Track 460, Frame 78) were captured in ascending orbit with the same incidence angle of 38.7°. Eleven of them were acquired in HH and HV dual polarisation while the other nine were acquired in HH single polarisation. The dual polarisation data were oversampled by a factor of two in range direction (Ng, 2010), and the final azimuth and range resolutions were 4.82 m and 5.55 m, respectively.

7.1.2 Tropospheric stratified phase mitigation for DInSAR

The DInSAR technique has demonstrated its potential as a land subsidence monitoring tool with millimetre accuracy in the last twenty years (Ge et al., 2014). However, DInSAR mapping result is affected by tropospheric stratified and tropospheric turbulence delay (Jolivet et al., 2014), which is spatially correlated and temporally uncorrelated due to the fluctuated medium. ERA-Interim (one type of GAM) from European Center for Medium-Range Weather Forecasts (hereafter ECMWF) was used to calculate TSPD (Doin et al., 2009). Figure 7.2 (a) is IFG after removing the linear orbit error using a FFT based approach (Ng, 2010), while Figure 7.2 (b) is a TSPD example derived from ERA-Interim in Ordos. Figure 7.2 (c) is the result after TSPD correction; however, the tropospheric phase removal is not obvious. This pattern seems to be the phase variation due to the ionospheric disturbance, especially related to the Medium Travelling Ionospheric Disturbance (MTID), which is the slowly moving ionospheric layer in north direction.

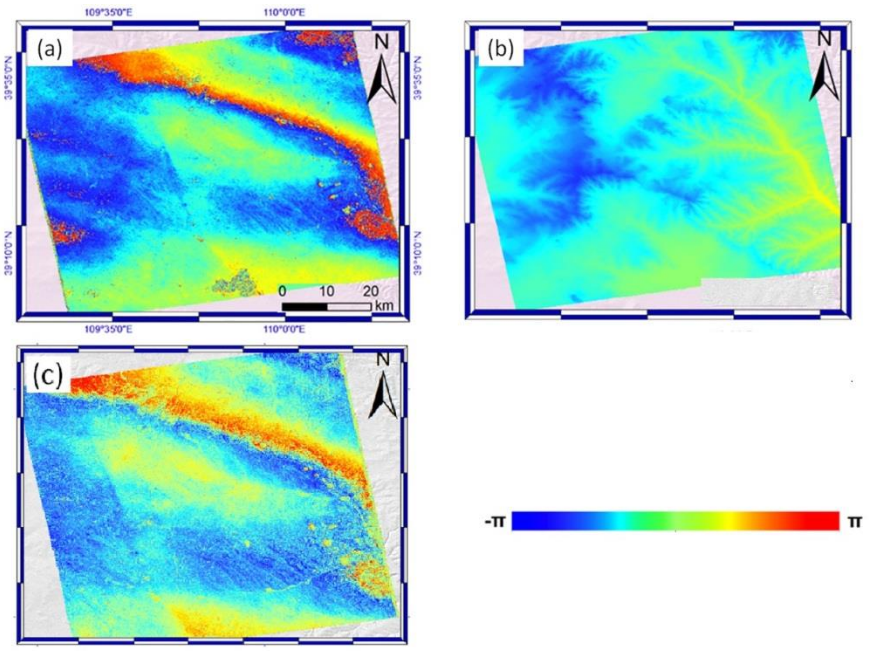

Figure 7.2 (a) The de-ramped differential IFGs, (b) TSPD obtained from the ERA-Interim, and (c) After TSPD correction. The de-ramped differential IFGs of (a) is generated from SAR pair of 16 July 2009 and 31 August 2009.

7.1.3 Result and analysis

The image acquired on 16 October 2009 was selected as the master image to minimise the temporal and spatial perpendicular baseline. The TS-InSAR results (Figure 7.1 (b) and Figure 7.3) were generated based on GEOS-PSI and GEOS-ATSA, respectively (Ge et al., 2014). In total 190 differential IFGs were generated using a DInSAR processing system named Automatic DInSAR Processing System (ADPS) developed by the GEOS group and six pairs with good coherence were picked to form the successive time series DInSAR displacement maps (Figure 7.4 (b-g)) near Qu Jia Liang coalmine (Box B in Figure 7.4 (a)).

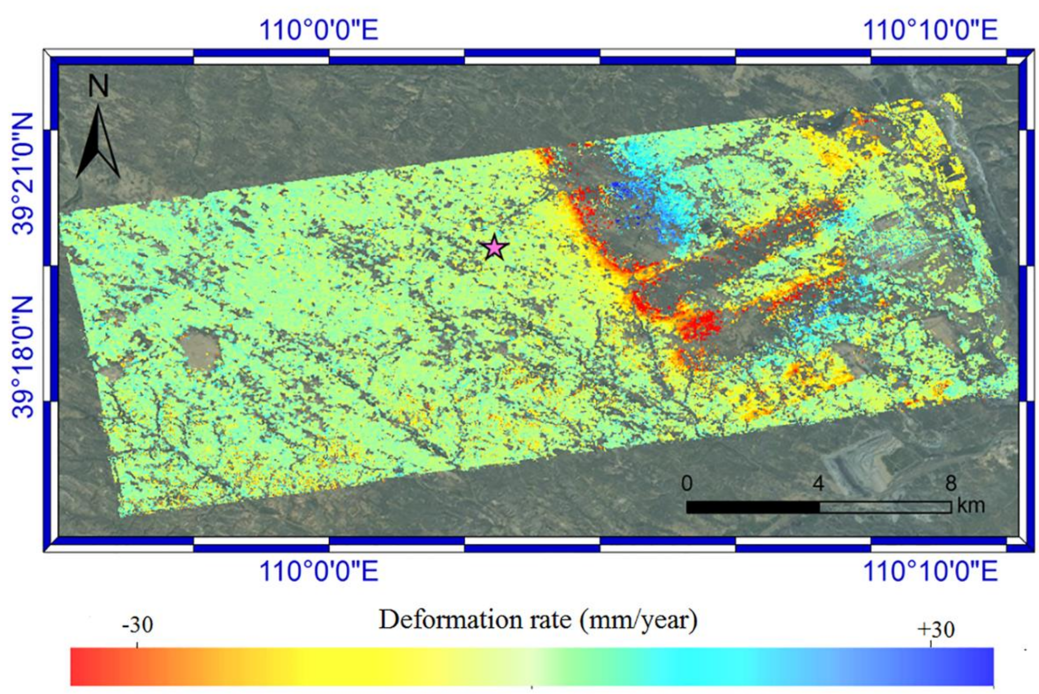

Figure 7.3 Deformation mapping result with the GEOS-ATSA for Ordos over the blue rectangle region in Figure 7.1 (b).

The TS-InSAR measurement showed that several locations in the eastern Ordos experiencing substantial land subsidence were identified including Huo Luo Wan coalmine and Qu Jia Liang coalmine. The subsidence rates ranging from −30 mm year^{-1} to 30 mm year^{-1} in LOS direction were detected. The comparison between TS-InSAR and DInSAR measurements, although showing good agreement in general pattern over mining regions, revealed gaps in TS-InSAR map near Qu Jia Liang coalmine (region A within Figure 7.4 (a)). Figure 7.5 (a) demonstrated the time series deformation for points 'a' and 'b', which were located within the Qu Jia Liang coalmine. Nonlinear subsidence from 2008 to 2010 has been observed. The average subsidence rates for them were 175 and 88 mm yr^{-1}, respectively. However, it was clear that both points ‘a’ and ‘b’ experienced a rapid change during the image taking. The highest vertical displacement rate for points ‘a’ and ‘b’ were 793 and 525 mm yr^{-1} within February 2009 – July 2009 and February 2008 – April 2008, respectively, which has exceeded the maximum deformation rate TS-InSAR technique can detect (Ng, 2010). Therefore, many gaps occurred in the TS-InSAR output.

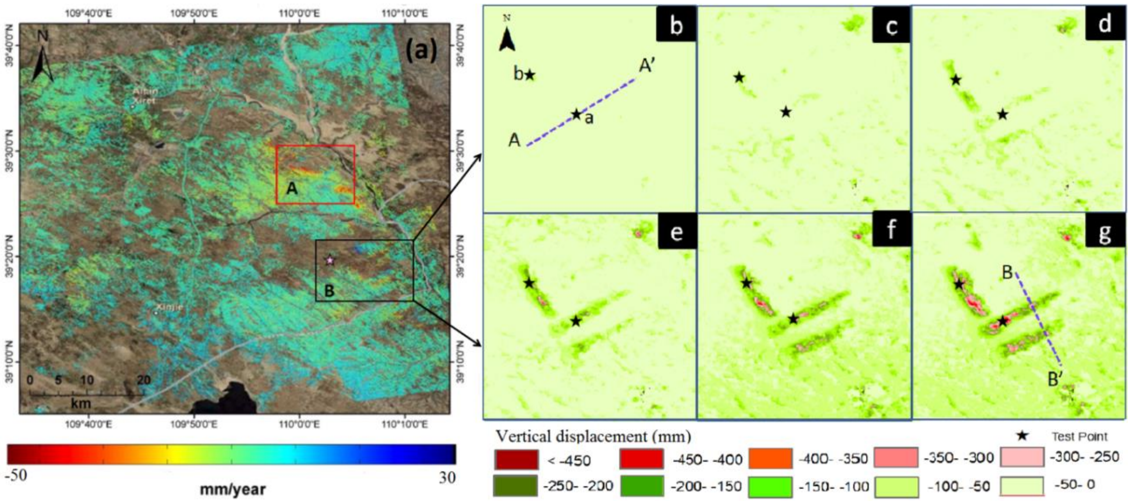

Figure 7.4 (a) GEOS-PSI time series deformation map for Ordos (A) Huo Luo Wan coalmine (B) Qu Jia Liang coalmine (b-g) Accumulated DInSAR subsidence map for Qu Jia Liang coalmine within Ordos where no signal detected by TS-InSAR from February 2008 to (b) April 2008 (c) July 2008 (d) February 2009 (e) July 2009 (f) January 2010 (g) July 2010 The two black stars are selected points ‘a’ and ‘b’.

The results derived from accumulative deformation time-series over profile A-A′ and B-B′ were illustrated in Figure 7.5 (b) and (c). Figure 7.5 (b) demonstrated the deformation between February 2008 and April 2008 along profile A-A′, the length of the deformation region was around 5.5 km, and the maximum deformation was

0.045 m, which was close to point ‘a’. The subsidence pattern can be correctly fitted by a parabolic curve (Zhao et al., 2013), a generally accepted mining curve, which has been widely utilised to predict mining subsidence. Besides, the regularity cross long wall pattern has been observed along profile B-B′ (Figure 7.5 (c)). The length of the profile was about 4.8 km and the maximum deformation was around 0.30 m.

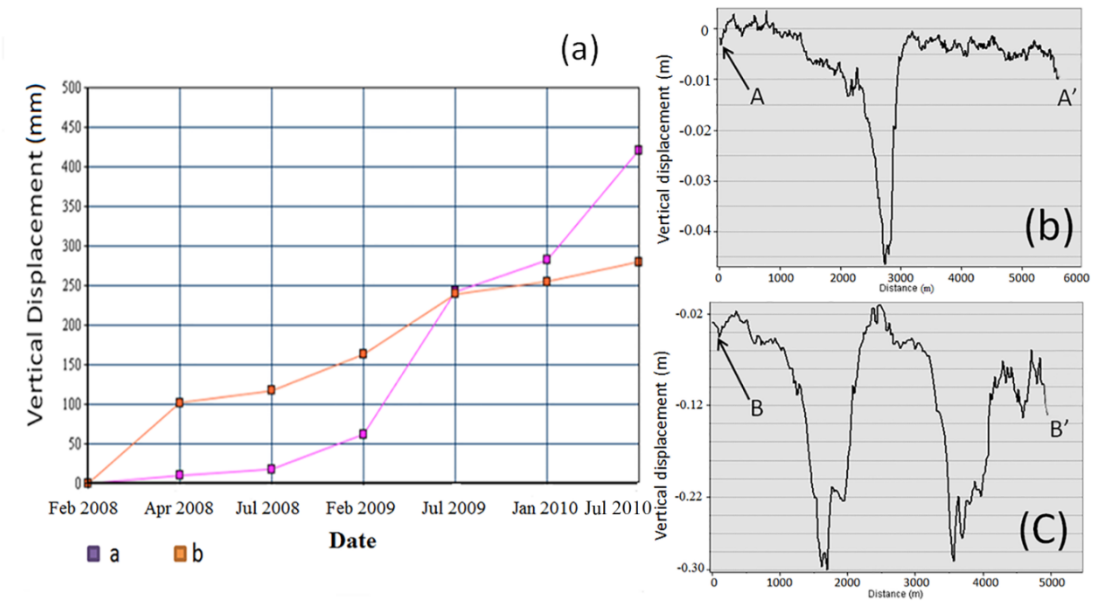

Figure 7.5 (a) Ground deformation at points ‘a’ and ‘b’ within Qu Jia Liang coalmine with no signal detected by TS-InSAR between 26 February 2008 and 19 July 2010. (b) and (c) Deformation results along two profiles denoted in Figure 7.4 (b-g): (b) Profile A-A′ along one of the long wall over Qu Jia Liang coalmine. (c) Profile B-B′ perpendicular to the long wall direction. The solid black lines indicate the deformation over these two profiles.

Figure 7.6 (b) was the refined DInSAR result after removing the TSPD component (Figure 7.2 (b)). Since the temporal baseline and spatial perpendicular baseline were 46 days and 112.5 m, respectively, spatial/temporal de-correlation induced phase errors were negligible. The remaining subsidence was mainly due to tropospheric turbulent effect, which was generally mitigated with numerous acquisitions. However, in this study, turbulent troposphere cannot be removed over gap regions due to the loss of InSAR coherence. Over the relatively stable region identified with TS-InSAR analysis (Region covered with red rectangular box in Figure 7.1 (b) with mean LOS velocity of -0.4 cm year^{-1}), the mean velocity value of the stable region within Figure 7.6 (c) was -1.5 cm year^{-1} while it was -1.2 cm year^{-1} for the counterpart of Figure 7.6 (b) after the TSPD correction. In other words, the improvement of the LOS deformation was 0.3 cm, which was equivalent to the total reduction of the atmospheric effect of about 21%. This result was competitive to the result generated from MODIS or MERIS (Ding et al., 2008).

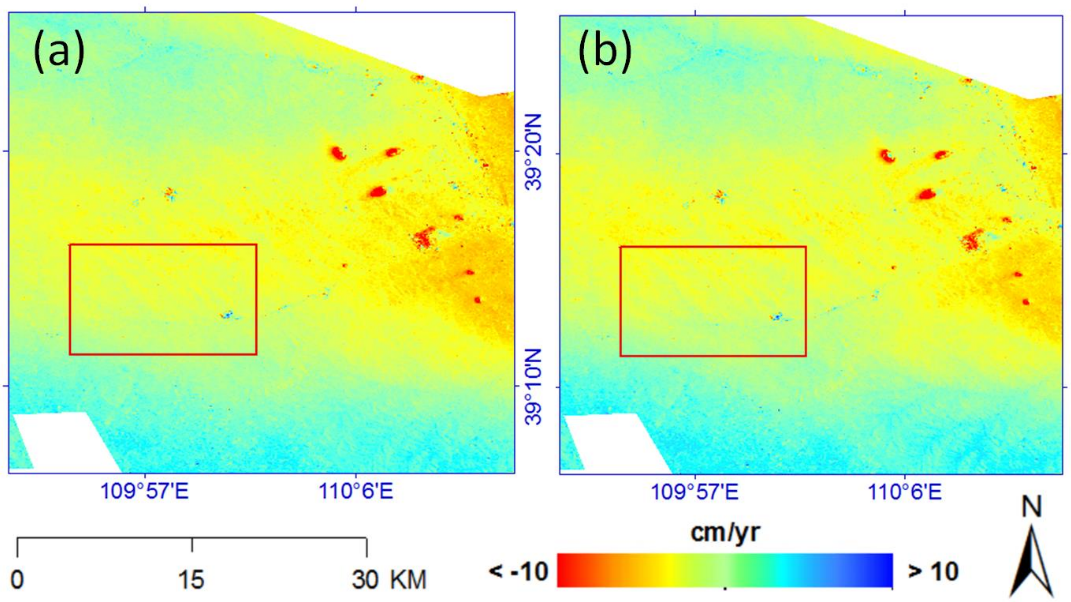

Figure 7.6 DInSAR results (a) Original (b) After TSPD correction are generated from SAR pairs of 13 June 2009 and 29 July 2009. The red rectangular boxes are stable region identified by GEO-PSI (Figure 7.1).

7.1.4 Integration of DInSAR and TS-InSAR

At last, DInSAR technique was exploited to fill in the gaps identified by TS-InSAR analysis. Take the refined DInSAR output between 26 February 2008 and 12 April 2008 as an example (Figure 7.4 (b)). First of all, the DInSAR measurement was converted from deformation value to deformation rate pixel by pixel by applying Equation 7.1, and then an oversampling factor was implemented in both the azimuth and range directions to match up with the pixel size of TS-InSAR measurements. After that, TS-InSAR result was superimposed onto DInSAR output to form the final product. Thus, the gaps within TS-InSAR are filled with DInSAR values (Figure 7.7 (b)). Figure 7.7 (c) shows that the deformation rate difference at 95% of the measurement points is between -10 mm/year to 10 mm/year, suggesting that the accuracy between these two methods are comparable.

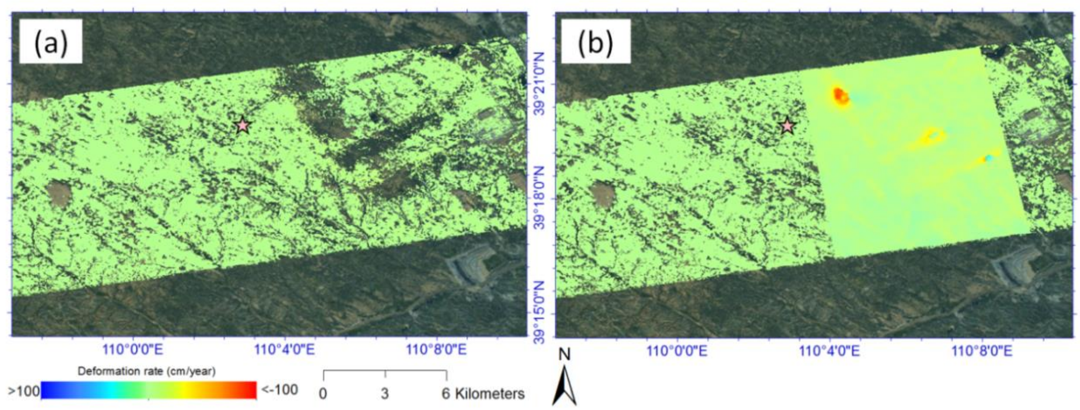

Figure 7.7 (a) GEOS-ATSA deformation map for Ordos (February 2007 ~ February 2011) near Qu Jia Liang coalmine (b) GEOS-ATSA deformation map for Ordos incorporating information from DInSAR output (February 2008 ~ April 2008)

$$V_{vel} = \frac{365}{\Delta T} D_{defo} \tag{7.1}$$

Where ΔT is the time difference between two consecutive acquisitions, D_{defo} is the deformation value for each pixel, and V_{vel} is the velocity value obtained.

To sum up, DInSAR and TS-InSAR technique are both interferometry methods for monitoring land subsidence with fine accuracy. DInSAR is suitable for short term measurement, while TS-InSAR uses phase information to map surface subsidence and requires SAR image acquisitions maintain high coherence, and hence is mainly applicable to slow changes. Given the fact that some rapidly changing surface subsidence can lead to the loss of InSAR coherence, and no signal can be detected in such a region, such gaps in TS-InSAR result can be resolved by combining refined DInSAR and TS-InSAR measurements.

7.2 Modified TS-InSAR method for C-band SAR images

The section is based on the material submitted to International Journal of Remote Sensing. Longwall mining technique is the most widely implemented underground mining method in Australia due to its productivity and safety considerations. The mining-induced subsidence could commonly reach –20 to –60 cm within the first 1–2 months after the fall down of the roof of the longwall panels (Ge et al., 2004; Ng et al., 2017), and over –80 cm in 12 months after mining has ceased. It is worth mentioning that when it comes to the stability evaluation and safety control for the longwall mining activities, two of the most concerning parameters for the mining industry and government are: 1) the maximum subsidence at the centre of the subsiding funnel and 2) the total affected region of the ground surface. The former can be estimated using DInSAR method while Ng et al. (2017) suggested that Sentinel-1A/B constellation with stripmap (SM) mode and ALOS-2 (any modes) are the ideal datasets for the rapid deformation mapping. On the contrary, the latter can be achieved with TS-InSAR technique over the far field of the subsidence funnel, which is considered as slow deforming area (Sowter et al., 2013; Bateson et al., 2015; Gama et al., 2015).

Nevertheless, Du et al. (2016a) reported that when using ATS-InSAR to map the ground displacement over the Appin underground mining regions, the density of MS pixels derived from C-band ENVISAT based ATS-InSAR method is much less in comparison to the counterpart result from L-band ALOS-1 dataset, even with the same thresholds settings. Indeed, working with either approach, one can get worse results with higher frequency data (e.g. C-band) in areas experiencing serious temporal decorrelation. The reason for that is C-band is more easily affected by temporal decorrelation, especially around the longwall mining sites, where short vegetation is dominant. Therefore, no clear subsidence pattern can be derived from the ATS-InSAR result (if not specified, ATS-InSAR hereafter refers to traditional ATS-InSAR). In other words, the problem lies with its higher sensitivity to vegetation regions instead of lower frequency data (e.g. L-band). In light of this, in order to offer the best detailed deformation information to associated councils and departments for risk management purpose regarding the ENVISAT ATS-InSAR analysis, this work introduces a modified MS pixel selection approach by including less reliable MS pixels through an IDW (Inverse Distance Weighted)-based integration method. Considering the fact that ENVISAT ceased communication with earth on 8 April 2012, the proposed method is also applied to C-band Sentinel-1 stacks for testing purposes. It is worth noting that the proposed method has been incorporated with GEO-ATSA (Ng et al., 2014) as an independent module.

7.2.1 Dataset and study region

A total number of 23 L-band ALOS-1 PALSAR scenes acquired between 29 June 2007 and 7 January 2011 (Track 370, Frame 649), 24 C-band ENVISAT ASAR images (Track 381, Frame 6489 & 6492) acquired from 8 August 2007 to 5 September 2010, and 22 C-band Sentinel-1A scenes (relative orbit 147) captured between 30 July 2015 to 6 June 2016 are utilized in this experiment (Table 7-1). The image stack of ENVISAT has been re-arranged compared to the dataset used in Du et al. (2016a) by including six scenes from Track 381 and Frame 6489, since the common spatial coverage between Frame 6489 and 6492 is > 90% with the same mean incidence angle. All the slave images are co-registered to the master image captured on 1 January 2009, 18 January 2009 and 14 January 2016 for ALOS-1, ENVISAT and Sentinel-1, respectively. The one arc-second DEM (30 meters) acquired from the Shuttle Radar Topography Mission (SRTM) is exploited to remove the topographic phase and later geocode the ATS-InSAR or modified ATS-InSAR result from slant-range radar coordinate system to World Geodetic System (WGS) 1984 (Farr et al., 2007). In addition, all the mean velocity maps (MVMs) mentioned in this work is in the radar line-of-sight (LOS) direction.

The study site, the Appin & West Cliff Colliery, is located in the southeastern corner of the Southern Coalfield, New South Wales (NSW), Australia (Figure 7.8). The colliery is about 50 kilometers southwest of Sydney City and 25 kilometers northwest of Wollongong City. In general, coal is extracted from the top coal seam layer of the Southern Coalfield and the direction of mining is from northwest to southeast, resulting in serious ground deformation. InSAR researches have been continuously conducted in this region to study the ground subsidence phenomena over the past ten years (Ge et al., 2007; Ng, 2010; Ng et al., 2011; Du et al., 2016a). Since the spatial extent of these two active mining longwalls in this study is about two kilometres, the atmospheric artefact is assumed to be insignificant (Ng et al., 2017).

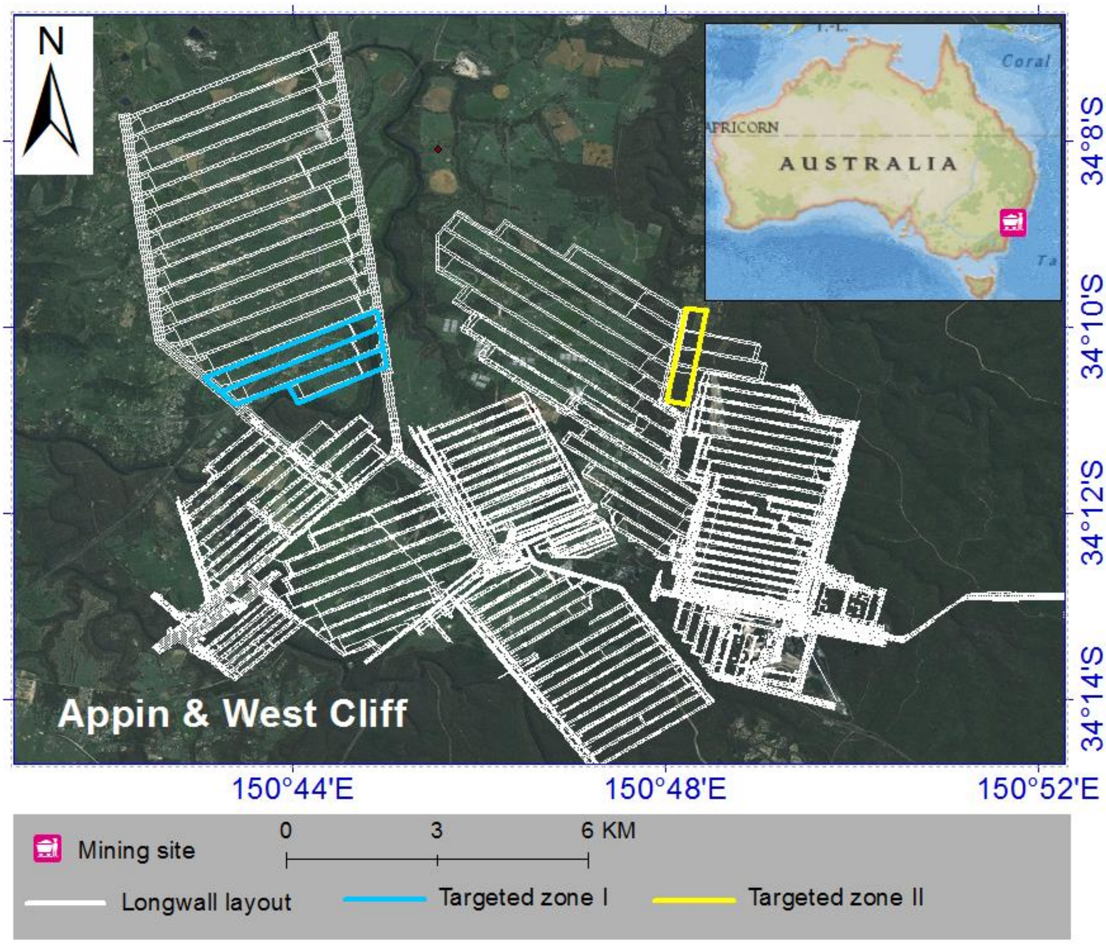

Figure 7.8 Geographical location of the Appin & West Cliff Colliery at Southern Coalfield in Australia overlaid on ©Google Map. Longwall panels highlighted with blue colour were mining active between June 2007 and January 2011 while panels marked with yellow colour were mining active between July 2015 and June 2016

Table 7-1 ALOS-1, ENVISAT and Sentinel-1 dataset

ALOS-1	Bperp (m)	Btemp (days)	ENVISAT	Bperp (m)	Btemp (days)	Sentinel-1	Bperp (m)	Btemp (days)

Note: * represents the ENVISAT images acquired from Frame 6489 while the rest in the same column are captured from Frame 6492

29/06/2007	–2102.1	–552	12/08/2007	154.6	–560	30/07/2015	–34.2	–168
14/08/2007	–2067.8	–506	21/10/2007	177	–490	11/08/2015	14.2	–156
29/09/2007	–2572.8	–460	25/11/2007	–63.6	–455	23/08/2015	92.5	–144
14/11/2007	–2688.5	–414	03/02/2008	–40.4	–385	10/10/2015	–28.1	–96
30/12/2007	–3429.9	–368	09/03/2008	218.6	–350	03/11/2015	46.4	–72
14/02/2008	–3417.3	–322	13/04/2008	199.5	–315	15/11/2015	37	–60
31/03/2008	–4058.8	–276	18/05/2008	66.4	–280	27/11/2015	–46.7	–48
16/05/2008	–4025.9	–230	22/06/2008*	–127.5	–245	09/12/2015	–39.1	–36
01/07/2008	–1120.5	–184	31/08/2008	–77.2	–175	21/12/2015	–41	–24
01/10/2008	740.6	–92	05/10/2008	66.3	–140	**14/01/2016**	**0**	**0**
16/11/2008	680.2	–46	09/11/2008	66.6	–105	26/01/2016	–92.6	12
01/01/2009	**0**	**0**	14/12/2008	272.1	–70	07/02/2016	–58.1	24
16/02/2009	–303.4	46	18/01/2009	–129.8	–35	19/02/2016	–12.9	36
04/07/2009	–872.4	184	**22/02/2009**	**0**	**0**	02/03/2016	70.7	48
04/10/2009	–1343.6	276	03/05/2009*	100.3	70	14/03/2016	53.9	60
19/11/2009	–1654.6	322	07/06/2009*	–194	105	26/03/2016	47.8	72
04/01/2010	–2174.1	368	16/08/2009*	52.4	175	07/04/2016	39.2	84
22/05/2010	–3149.4	506	25/10/2009*	63	245	19/04/2016	–19.1	96
07/07/2010	–3164.7	552	29/11/2009	27.3	280	01/05/2016	32.2	108
22/08/2010	–3262.4	598	03/01/2010*	90.6	315	13/05/2016	84.2	120
07/10/2010	–3564.2	644	14/03/2010	107.2	385	25/05/2016	–28.9	132
22/11/2010	–4138.7	690	18/04/2010	–186.8	420	06/06/2016	–26.4	144
07/01/2011	–4518.7	736	23/05/2010	40.8	455			
			27/06/2010	–30.5	490			

7.2.2 Add less reliable MS pixels

The flowchart of the proposed method is shown as follows (Figure 7.9).

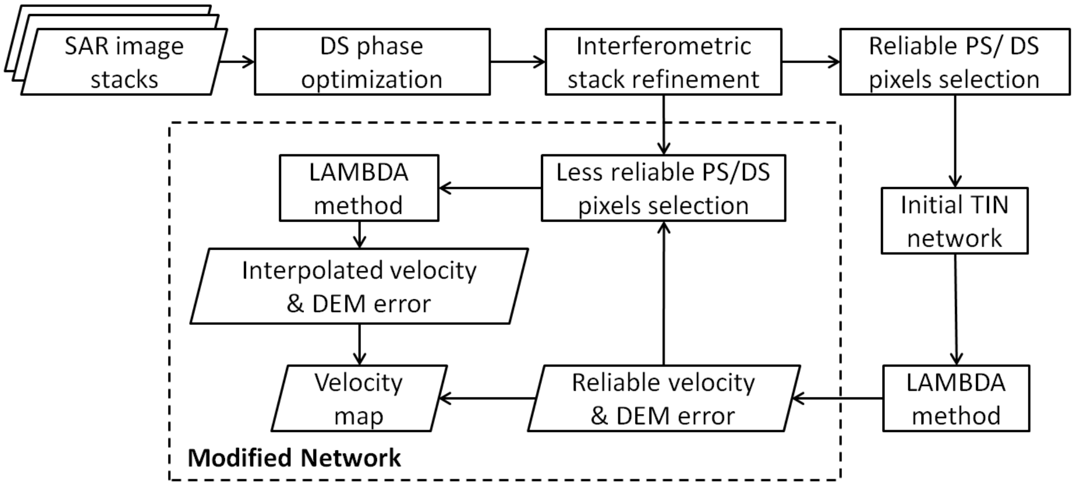

Figure 7.9 Flowchart of the proposed method

As we stated in previous section, the density of MS pixels produced by ENVISAT based ATS-InSAR method is not sufficient enough over the underground mining site, and no clear subsidence pattern can be derived (Du et al., 2016a). Therefore, in this section, an IDW (Inverse Distance Weighted)-based technique is proposed by including less reliable MS pixels to deal with this matter.

7.2.2.1 Add less reliable MS pixels

As is known, Kriging and IDW are two of the most commonly used interpolation methods in geographic information science (GIS) discipline (O'Sullivan and Unwin, 2014). According to Stein (2012), Kriging is one of the most complex interpolators, and it applies sophisticated statistical methods that consider the unique characteristics of datasets. However, many researchers have reported that IDW is more suitable for smaller dataset and is able to offer more accurate estimations compared to the Kriging method (Brusilovskiy, 2013; O'Sullivan and Unwin, 2014). More specifically, IDW takes the concept of spatial autocorrelation literally and is generally considered as a deterministic method for multivariate interpolation through a bunch of scattered set of known points. The third dimensional value of unknown points is calculated with a weighted average value in some surrounding neighbourhood points. Also, weighting assigned to points usually varies with distance as a negative exponential or reciprocal. Considering a group of samples $\mu_i = \mu(x_i) \quad for \quad i = 1, 2, ..., N$, a general form of estimating an interpolated value μ at a given point x using IDW now reads:

$$\mu(x) = \frac{\sum_{i=1}^{N} w_i(x)\mu_i}{\sum_{i=1}^{N} w_i(x)} \tag{7.2}$$

where $w_i(x) \propto 1/d(x, x_i)^p$ is a simple IDW weighting function; p is the exponent and the value of 'p' greater/lesser than 1.0 will decrease/increase the relative effect of distance points (O'Sullivan and Unwin, 2014). The concept of IDW will be exploited in the following context since the interpolation process can be considered within a small pitch (smaller dataset).

7.2.2.2 Estimate the velocity over less reliable MS pixels

As there are no redundancy pairs, it is necessary to squeeze out as much information as possible from every obtained IFG. Therefore, in order to achieve the best details over the mining-affected study area, less reliable MS pixels are also included for further analysis. Given the fact that one of the fundamental assumptions of TS-InSAR method is that the ground subsidence is correlated in the spatial domain, at least within a small patch, in this work, it is assumed that a small group of nearby MS pixels have similar deformation signals. Let s = *1, 2, ... , S* and *S* denotes the number of reliable MS pixels (either PS or DS pixels), which are the closest neighbours to the less reliable pixel *t*. It is worth noting that this selection is not based on any adaptive search windows centred on the targeted pixel, but relies on the actual Euclidean distance. Thus, for the *N*th interferometric pair combination, the double-differenced observations among them can be expressed as Equation 7.3:

$$\Delta\varphi_{t,s}^{N} = \varphi_{t}^{N} - \varphi_{s}^{N} = -\frac{4\pi}{\lambda}(\Delta v_{t,s} \cdot T^{N} - \frac{B_{\perp,t,s}^{N}}{R_{t,s} \cdot \sin\theta_{t,s}} \cdot \Delta h_{t,s}) + \sigma_{t,s} =$$

$$-\frac{4\pi}{\lambda}[(v_t - v_s) \cdot T^{N} - \frac{B_{\perp,t,s}^{N}}{R_{t,s} \cdot \sin\theta_{t,s}} \cdot (h_t - h_s)] + \sigma_{t,s} \tag{7.3}$$

$$s = 1, 2, \ldots, S$$

$$\sigma_{t,s} = \sigma_{Nonlinear,t,s} + \sigma_{Atmo,t,s} + \sigma_{Noise,t,s}$$

where λ is the sensor wavelength, $R_{x,y}$ is the distance between satellite and ground surface, T^{N} is the time difference between two acquisitions, $B_{\perp,x,y}^{N}$ and $\theta_{x,y}$ are the mean local perpendicular baseline and local incidence angle, respectively. $\Delta v_{x,y}$ is the velocity difference and $\Delta h_{x,y}$ is the DEM error difference of pixels *x* and *y*. $\sigma_{Nonlinear,t,s}$, $\sigma_{Atmo,t,s}$ and $\sigma_{Noise,t,s}$ are phase errors due to nonlinear, atmosphere and noise components, respectively. The double difference phase between t and s, $\sigma_{t,s}$, is the difference between the original phase $\Delta\varphi_{t,s}^{N}$ and the modelled phase $-\frac{4\pi}{\lambda}[(v_t - v_s) \cdot T^{N} - \frac{B_{\perp,t,s}^{N}}{R_{t,s} \cdot \sin\theta_{t,s}} \cdot (h_t - h_s)]$. LS approach described in Section 3.2.3 will be applied in the following section to estimate v_s and h_s by minimizing the value of $\sigma_{t,s}$".

$$\Delta\varphi_{t,s}^{N} - \frac{4\pi}{\lambda}[v_s \cdot T^{N} - \frac{B_{\perp,t,s}^{N} \cdot h_s}{R_{t,s} \cdot \sin\theta_{t,s}}] = -\frac{4\pi}{\lambda}[v_t \cdot T^{N} - \frac{B_{\perp,t,s}^{N} \cdot h_t}{R_{t,s} \cdot \sin\theta_{t,s}}] \quad s = 1, 2, \ldots, S \tag{7.4}$$

In addition, the weighting matrix is created following Equation 7.2 by setting the exponent 'p' to 1, which is given in Equation 7.5.

$$\mathbf{P} = diag\{\frac{1}{\hat{d}_1^1}\cdots\frac{1}{\hat{d}_1^N},\ldots,\frac{1}{\hat{d}_s^1}\cdots\frac{1}{\hat{d}_s^N}\}, s=1,2,\ldots,S \tag{7.5}$$

where $\frac{1}{\hat{d}_s^N}$ is the normalised reverse distance and the sum of all these distances is equal to 1, while $\mathbf{P}$ is a $NS \times NS$ weighting matrix (contain NS normalised reverse distances).

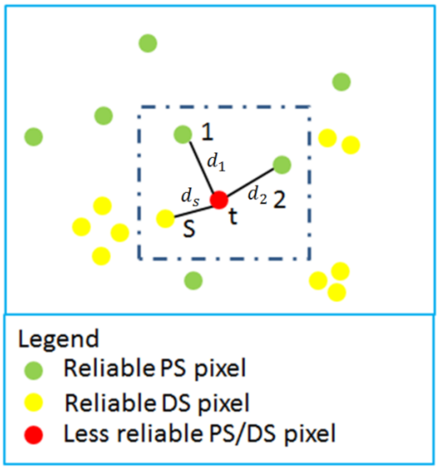

Figure 7.10 Simple geometry of including less reliable MS pixels

Furthermore, the way to add less reliable MS pixels into the initial TIN network is demonstrated in Figure 7.10 from Equations 7.6 to 7.8, the absolute linear velocity (ALV) v_s and DEM-error (DE) h_s with respect to each reliable MS pixel 's' are known values, whilst the (2 + NS) unknown elements are ALV v_t and DE h_t respect to 't', and the $N \times S$ integer values within matrix $\mathbf{B}$. Also, LAMBDA algorithm is applied to solve Equation 7.6, which has been implemented in Section 3.2.3 (Ng et al., 2012a).

$$\mathbf{P}\delta\widehat{\boldsymbol{\beta}} = \mathbf{A}\widehat{\boldsymbol{\beta}} + \mathbf{B} \tag{7.6}$$

$$\delta\widehat{\boldsymbol{\beta}} = \begin{bmatrix} \varphi_t^1 - \varphi_s^1 - \dfrac{4\pi}{\lambda}\cdot(v_s \cdot T^1 - \dfrac{B_{\perp,t,s}^1 \cdot h_s}{R_{t,s}\cdot \sin\theta_{t,s}}) \\ \varphi_t^2 - \varphi_s^2 - \dfrac{4\pi}{\lambda}\cdot(v_s \cdot T^2 - \dfrac{B_{\perp,t,s}^2 \cdot h_s}{R_{t,s}\cdot \sin\theta_{t,s}}) \\ \vdots \\ \varphi_t^N - \varphi_s^N - \dfrac{4\pi}{\lambda}\cdot(v_s \cdot T^N - \dfrac{B_{\perp,t,s}^N \cdot h_s}{R_{t,s}\cdot \sin\theta_{t,s}}) \end{bmatrix} \tag{7.7}$$

$s = 1, 2, \ldots, S$

$$\mathbf{A} = \begin{bmatrix} \dfrac{-4\pi}{\lambda}\cdot T^1 & \dfrac{-4\pi\cdot B_{\perp,t,s}^1}{\lambda\cdot R_{t,s}\cdot\sin\theta_{t,s}} \\ \dfrac{-4\pi}{\lambda}\cdot T^2 & \dfrac{-4\pi\cdot B_{\perp,t,s}^2}{\lambda\cdot R_{t,s}\cdot\sin\theta_{t,s}} \\ \vdots & \vdots \\ \dfrac{-4\pi}{\lambda}\cdot T^N & \dfrac{-4\pi\cdot B_{\perp,t,s}^N}{\lambda\cdot R_{t,s}\cdot\sin\theta_{t,s}} \end{bmatrix} \quad \mathbf{B} = \begin{bmatrix} -2\pi\cdot a_{t,s}^1 \\ -2\pi\cdot a_{t,s}^2 \\ \vdots \\ -2\pi\cdot a_{t,s}^N \end{bmatrix} \quad \widehat{\boldsymbol{\beta}} = \begin{bmatrix} \hat{v}_t \\ \hat{h}_t \end{bmatrix} \tag{7.8}$$

$s = 1, 2, \ldots, S$

where:

- $\delta\widehat{\boldsymbol{\beta}}$ is a $NS \times 1$ matrix,
- $\mathbf{A}$ is a $NS \times 2$ matrix,
- $\mathbf{B}$ is a $NS \times 1$ matrix, containing the integer ambiguity values.

The quality of the estimation is evaluated using Equation 7.9, and it is essential in estimating the quality of less reliable MS pixels. 't' can be selected as the final MS pixel only if $\widehat{\gamma}(t)$ is larger than a certain threshold.

$$\widehat{\gamma}(t) = \frac{1}{S}\sum_{s=1}^{S}\{\frac{1}{N}\cdot|\sum_{n=1}^{N} e^{j\cdot\Delta\varphi_{t,s}^{N} - j\cdot[-\frac{4\pi}{\lambda}(\Delta v_{t,s}\cdot T^{N} - \frac{B_{\perp,t,s}^{N}}{R_{t,s}\cdot\sin\theta_{t,s}}\cdot\Delta h_{t,s})]}\} \quad (7.9)$$

7.2.3 Experimental result and discussion

7.2.3.1 Performance of different sensors over rapidly subsiding region

It is worth mentioning that solving the issue of the intrinsic ambiguity of the phase signal due to rapidly subsiding deformation is a significant step of InSAR applications. According to Kampes (2006), if the displacement of two adjacent pixels between any interferometric combinations (within image stack) is larger than a half of the wavelength, the corresponding interferometric phase may not be correctly unwrapped in temporal domain or no MS pixels would be selected in such an area. In this case, TS-InSAR method can be exploited to identify the extent of the land displacement, but cannot resolve the correct displacement value (Ng et al., 2017).

Indeed, before conducting the TS-InSAR analysis, it is vital to estimate the achievable maximum subsidence rate $V_{\max}$ of the current dataset, especially when the study area contains rapid subsidence (Kampes, 2006; Ng et al., 2017). The simplest model for estimating $V_{\max}$ between two nearby points can be written as:

$$V_{\max} = \pm\frac{365}{\Delta T_{\max}}\cdot\frac{\lambda}{4} \quad (7.10)$$

where $\Delta T_{\max}$ is the maximum temporal baseline of all IFGs.

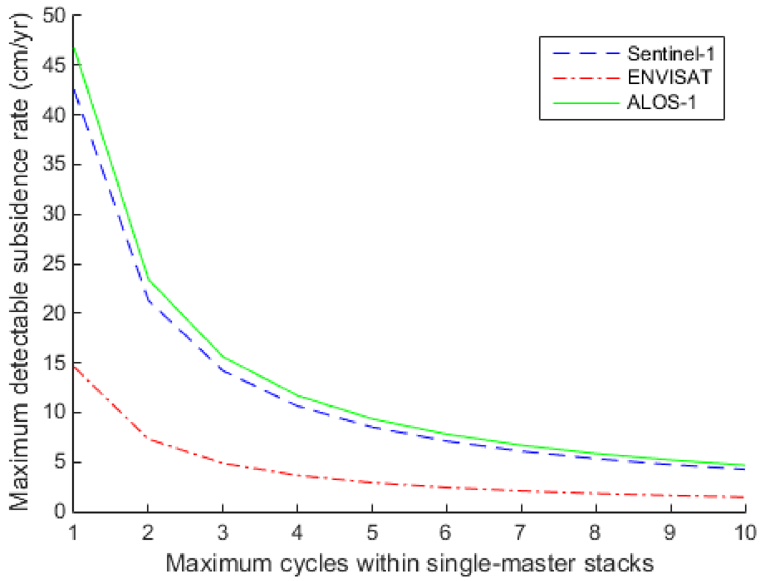

Figure 7.11 Correlation between the maximum detectable subsidence rate and maximum cycles within single-master stacks

Table 7-2 SAR satellite characteristics relevant to the expected detected subsidence

Satellite	Mode	Revisit time (days)	Maximum temporal baseline (days)	V_{max} (cm/yr)
ALOS-1	FBS[a]	46	138 (3 cycles)	15.6
ENVISAT	IM[b]	35	70 (2 cycles)	7.4
Sentinel-1	IWS[c]	12	48 (4 cycles)	10.6

[a] Fine Beam Single; [b] Image Mode; [c] Interferometric Wide Swath

Considering if an interferogram is available, under the assumption that the incidence angle is the same, the ideal performance for Sentinel-1A interferometric wide swath (IWS) mode is about four times better than the counterpart performance of ENVISAT image mode (IM) in terms of the maximum detectable subsidence per meter per day (Ng et al., 2017). This is given the fact that the spatial resolution and revisit time are 20 m & 14 days and 30 m & 35 days for Sentinel-1 and ENVISAT, respectively. Figure 7.11 demonstrates the correlation between the maximum detectable subsidence rate and maximum cycles within single-master stacks for ALOS-1, ENVISAT and Sentinel-1. It is clear that under the situation of the same maximum cycles, the performances of Sentinel-1 and ALOS-1 are a lot better in comparison to the counterpart of ENVISAT. In this work, as the maximum temporal baseline of these three image stacks are 138, 70, and 48 days for ALOS-1, ENIVSAT and Sentinel-1, respectively, the values of V_{max} are 15.6, 7.4, and 10.6 cm yr^{-1} accordingly (Table 7-2).

7.2.3.2 Performance of different sensors over rapidly subsiding region

In order to demonstrate the effectiveness of ATS-InSAR method for estimating the mining-affected areas, 23 ALOS-1 images (Track 370, Frame 649) used in Du et al. (2016a) are exploited in this experiment (the exact threshold settings can refer to the article above). The difference is that this time ATS-InSAR method is conducted over the entire SAR coverage. Eventually, 29, 218, 317 MS pixels are selected with $D_A <$ 0.25 or γ_P >0.75 and later resampled onto a grid with the resolution of 30 m × 30 m. All these measurements are relative values as regards to a stable point in Wollongong City (the same reference point is used for all the experiments afterwards). It can be seen clearly from Figure 7.12 that three regions marked with rectangular boxes are the highlighted trouble spots, and special attention should be paid to these regions. Nevertheless, it is impossible for ENVISAT based ATS-InSAR to detect such information even with the same thresholds (Du et al., 2016a).

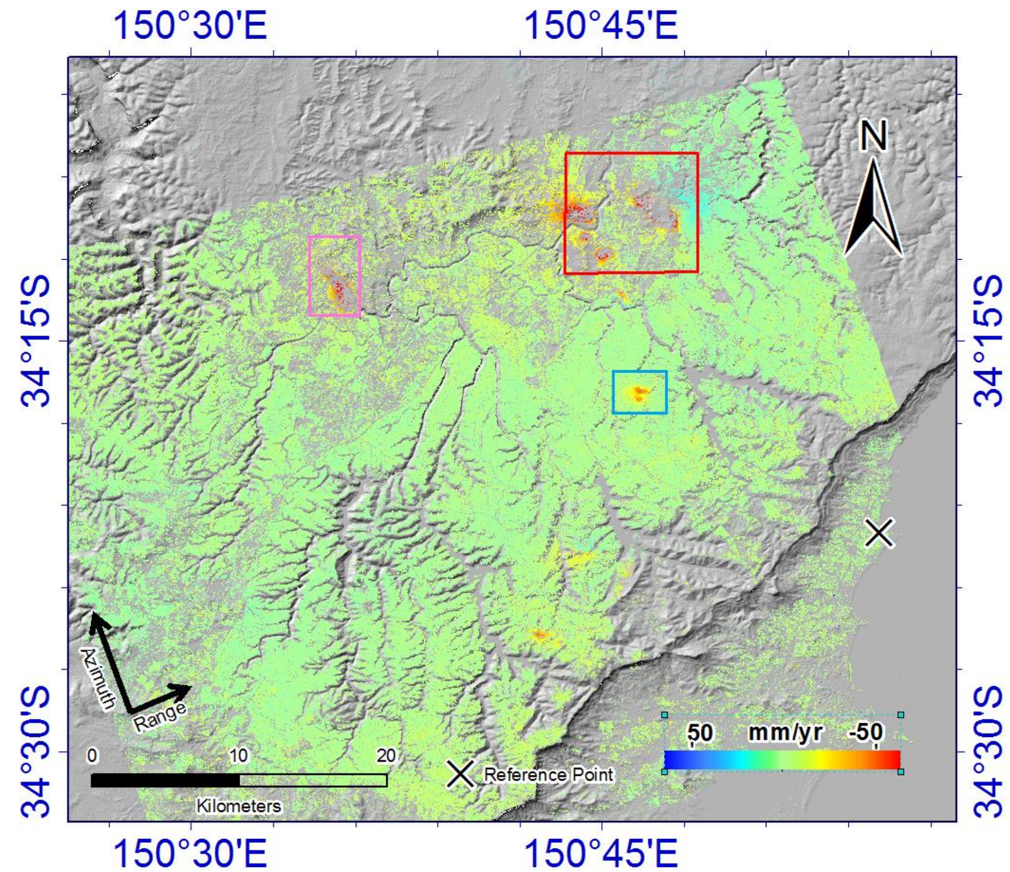

Figure 7.12 The MVM derived from ALOS-1 based ATS-InSAR method superimposed onto a DEM layer.

7.2.3.3 Modified ATS-InSAR method with ENVISAT and Sentinel-1

Over the years, many times when processing real data, choosing the right trade-off between the selection of highly coherent pixels and the grid sparsity is a challenge (Hooper et al., 2004). Increasing the threshold allows the selection of highly coherent pixels, but the higher sparseness of the pixel grid may lead to unwrapping failures. On the other hand, the introduction of too noisy pixels can lead to unwrapping failures as well as integration uncertainty. In this sub-section, TS-InSAR analyses are conducted under several circumstances with different threshold settings (from Figure 7.13 to Figure 7.15).

First and foremost, only relatively reliable MS pixels ($D_A < 0.25$ or $\gamma_P > 0.55$) are selected to conduct the ATS-InSAR analysis, resulting in the number of MS pixels and arcs of 851, 780 and 2,554,879, respectively. The final output MVM is shown in Figure 7.13 (a). In order to verify the reliability of the proposed method, the modified ATS-InSAR has been applied to monitor the ground deformation. Precisely, MS pixels with $D_A < 0.25$ or $\gamma_P > 0.6$ are selected to construct the initial network while pixels with $0.6 \geq \gamma_P > 0.55$ are included afterwards using the IDW-based integration method and the outcome is demonstrated in Figure 7.13 (b). It is evident that these two results are comparable with each other with the root-mean-square-error (RMSE) accounting for 2.4 mm yr^{-1} (Figure 7.13 (c)). Indeed, the above experiments are conducted with relatively reliable MS pixels and the performance of the modified ATS-InSAR method will be further tested by including less reliable MS pixels.

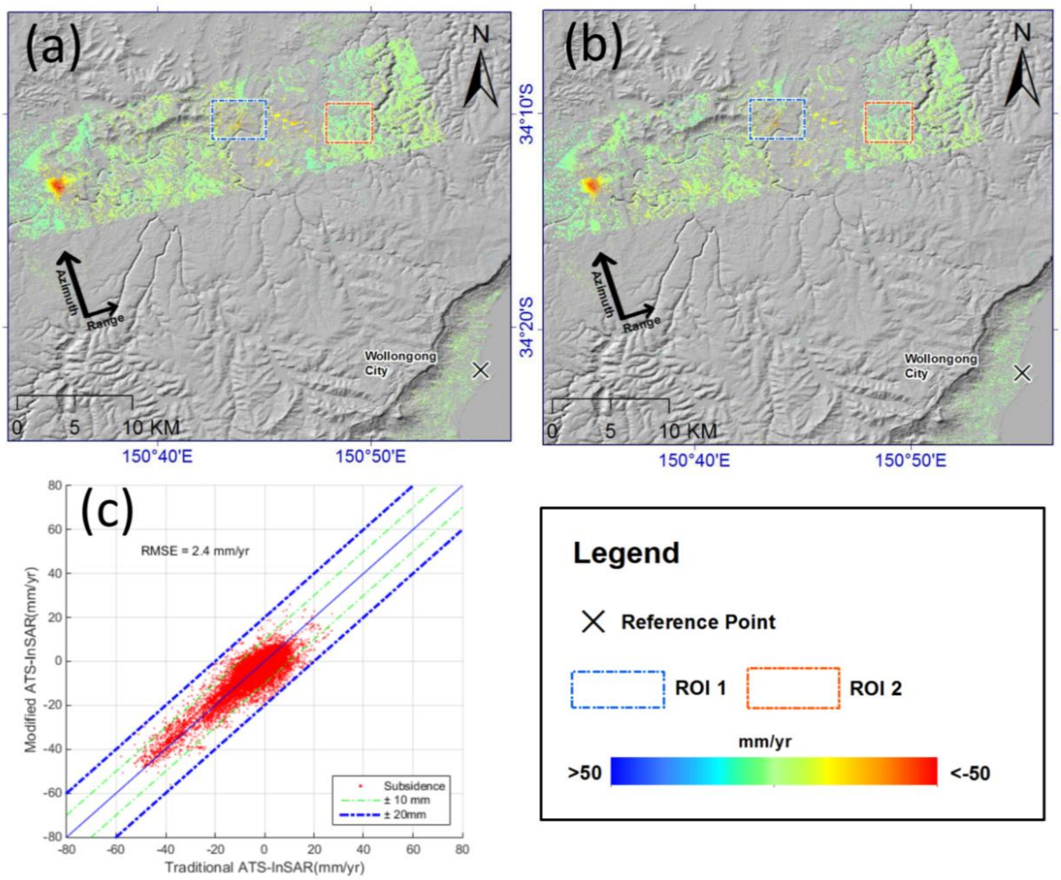

Figure 7.13 ENVISAT derived MVM using both traditional and modified ATS-InSAR method over Southern Sydney with different threshold settings (a) $D_A < 0.25$ or $\gamma_P > 0.55$ (b) $D_A < 0.25$ or $\gamma_P > 0.6$ & $0.6 \geq \gamma_P > 0.55$, and (c) Correlation between (a) and (b).

7.2.3.4 ATS-InSAR methods with less reliable MS pixels

Figure 7.14 is the zoom-in result of the blue dash-line covered region (ROI1) in Figure 7.13. According to the report from BHP (2014), the mining proposal for Longwalls 702 – 704 was approved on 1 November 2006, while the operation period was from 27 October 2007 to 29 July 2012. It can be seen from Figure 7.13 that ROI1 is rather sparse in terms of the density of MS pixels. To acquire more detailed information about the ground deformation, the threshold for ATS-InSAR has been changed to $D_A < 0.25$ or $\gamma_P > 0.5$ (Figure 7.14 (a)) and $D_A < 0.25$ or $\gamma_P > 0.4$ (Figure

7.14 (b)) for including more MS candidates to the initial TIN network. It is apparent that even the number of MS pixels has changed from 10, 051 ($\gamma_P > 0.55$) to 14, 229 ($\gamma_P > 0.5$) and 63, 454 ($\gamma_P > 0.4$), respectively, and the mining-induced subsidence pattern still cannot be clearly identified. As the initial TIN network is constructed using arcs and all these arcs have the same significance level, adding less reliable arcs directly into the initial TIN network can seriously degrade the accuracy of the integration processing and lead to incorrect estimation and integration uncertainty. The modified ATS-InSAR technique is applied by selecting not only reliable MS pixels ($D_A < 0.25$ or $\gamma_P > 0.4$) to construct the initial TIN network, but also less reliable MS pixels ($0.4 \geq \gamma_P > 0.25$), and the result is illustrated in Figure 7.14 (c). Overall, 103, 220 MS pixels have been selected with the corresponding value of $\hat{\gamma}(t)$ larger than 0.25, which means the improvement of this proposed method is nearly 39% in terms of the density of total MS pixels as compared to the reliable case. In this circumstance, the number of MS pixels seem enough, and the general mining-induced pattern can be seen.

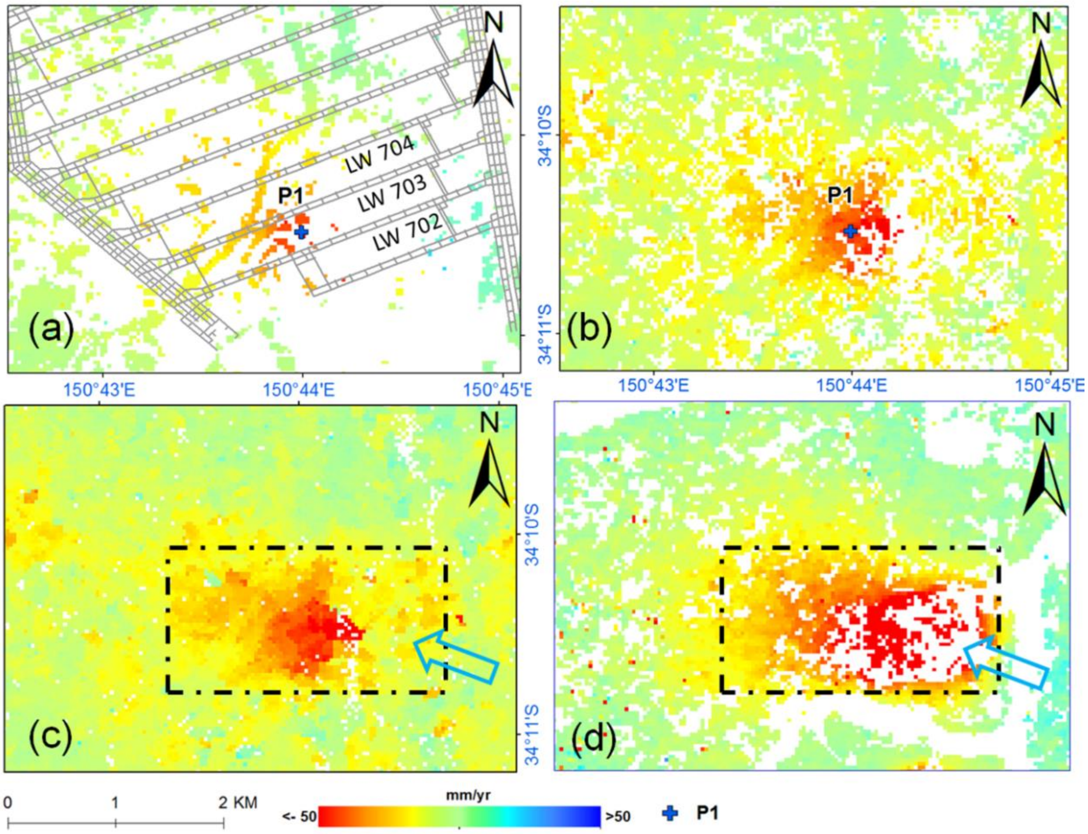

Figure 7.14 ENVISAT ATS-InSAR result over the longwall panel marked with blue colour with $D_A < 0.25$ or a) $\gamma_P > 0.5$, b) $\gamma_P > 0.4$, c) modified ATS-InSAR with $\gamma_P > 0.4$ and $0.4 \geq \gamma_P > 0.25$, and d) ALOS-1 with $\gamma_P > 0.75$. P1 is the selected hot-spot.

Figure 7.14 (d) is the ALOS-1 based ATS-InSAR outcome with $\gamma_P > 0.75$ and is primarily used for verification purpose. The black dash-line box within Figure 7.14 (c) & (d) represents the mining-affected regions, and the two subsiding patterns cannot be perfectly matched as is evident from these two figures. The difference between the two outcomes could be due to two reasons: 1) the temporal coverage between these two datasets is not identical — 2007.06 to 2011.01 (ALOS-1) vs 2007.08 to 2010.06 (ENVISAT) and 2) The maximum detectable subsidence is different for ALOS-1 and ENVISAT in this work — 15.6 vs 7.4 cm yr^{-1}. As the spatial resolution and revisit time are 10 m & 46 days and 30 m & 35 days for ALOS-1 and ENVISAT, respectively, the maximum detectable subsidence per meter per day is 34×10^{-3} and 7×10^{-3} mm m^{-1} day^{-1} accordingly. In other words, the capability of ALOS-1 for detecting mining-induced subsidence is nearly five times better than ENVISAT case.

Sentinel-1 satellite (April 2014 –) is the successor of ENVISAT satellite (March 2002 – April 2012) after the latter ceased communication with earth on 8 April 2012. The proposed method will be tested on the Sentinel-1 dataset in the following experiments. It is worth noting that since the operation periods for these two satellites are different, there is no way to conduct the experiment over LW702 – 704 as the active mining period was between 27 October 2007 and 29 July 2012. Nevertheless, considering that the geological structure of Appin & West Cliff Colliery and the longwall mining technique remained the same over the years, the Sentinel-1 based ATS-InSAR analysis thus essentially focuses on the targeted zone II (panels marked yellow in Figure 1), which is about 6 kilometres to the east of LW702.

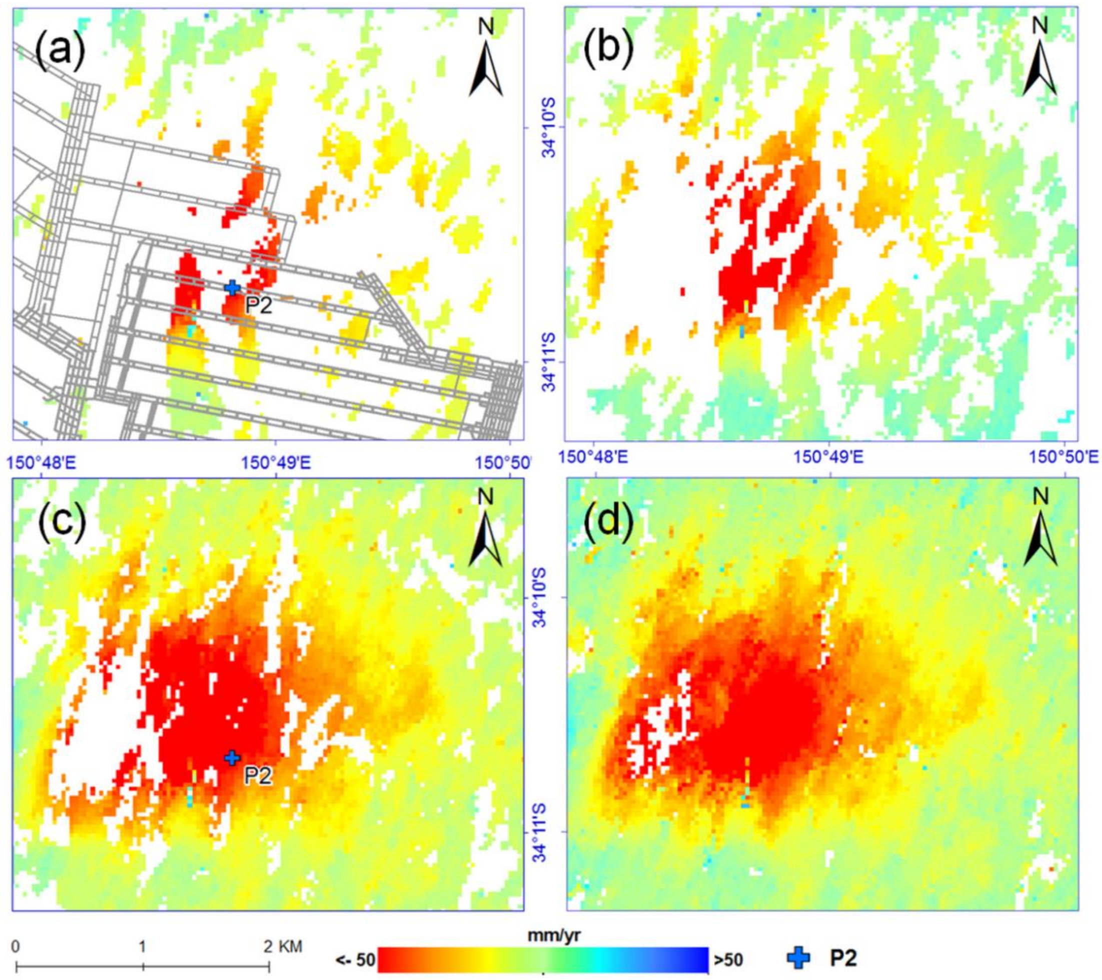

Figure 7.15 Sentinel TS-InSAR result over the longwall panel marked with yellow colour in Figure 1 with $D_A < 0.25$ or a) $\gamma_P > 0.7$, b) $\gamma_P > 0.6$, c) $\gamma_P > 0.5$ and d) modified ATS-InSAR with $\gamma_P > 0.5$ and $0.5 \geq \gamma_P > 0.4$. P2 is the selected hot-spot.

According to the report from BHP (2014), the operating time period for this longwall was between July 2015 and June 2016. Figure 7.15 (a) – (c) illustrate the Sentinel-1 based ATS-InSAR outcomes with $D_A < 0.25$ or $\gamma_P > 0.7$, $\gamma_P > 0.6$ and $\gamma_P > 0.5$, respectively. The corresponding number of MS pixels are 13, 919; 41, 823; and 107, 217, respectively. However, the exact outline of the eastern part is still not clear. Figure 7.15 (d) shows the modified ATS-InSAR result with $D_A < 0.25$ or $\gamma_P > 0.5$ &

$0.5 \geq \gamma_P > 0.4$. The total number of MS pixels is 171, 094, which is about 1.6 times more in comparison to the previous case ($\gamma_P > 0.5$), and the clear mining-induced subsiding pattern can be clearly observed in Figure 7.15 (d). Compared to ENVISAT based ATS-InSAR result in Figure 7.14 (c), the performance of Sentinel-1 is much better primarily due to two reasons: 1) Due to the relative short revisit time of Sentinel-1, even the maximum revisit cycle of Sentinel-1 data is 4 (48 days), however, it is still smaller than the two cycles of ENVISAT data (70 days), and 2) the extents of these two mining activities are not identical.

To test whether the drop of the threshold of γ_P would degrade the stability of the Initial TIN network, time series analysis is conducted over two hot-spots P1 (Figure 7.14 (a) and (b)) and P2 (Figure 7.15 (a) and (c)), respectively. As evident from Figure 7.16 (a), with the value of γ_P changing from 0.5 to 0.4 for ASAR datasets, the LOS displacement rate of P1 is consistent from August 2007 to June 2010, which is nearly –6.1 cm yr^{-1}. Also, a similar comparable result is observed over P2 between July 2015 and June 2016 under two different situations; 1) $\gamma_P > 0.7$ and 2) $\gamma_P > 0.5$ for Sentinel dataset, and the LOS subsidence rate is nearly –4.6 cm yr^{-1}. In other words, the TIN network is intact with the value of γ_P set to 0.4 and 0.5 for ASAR and Sentinel, respectively.

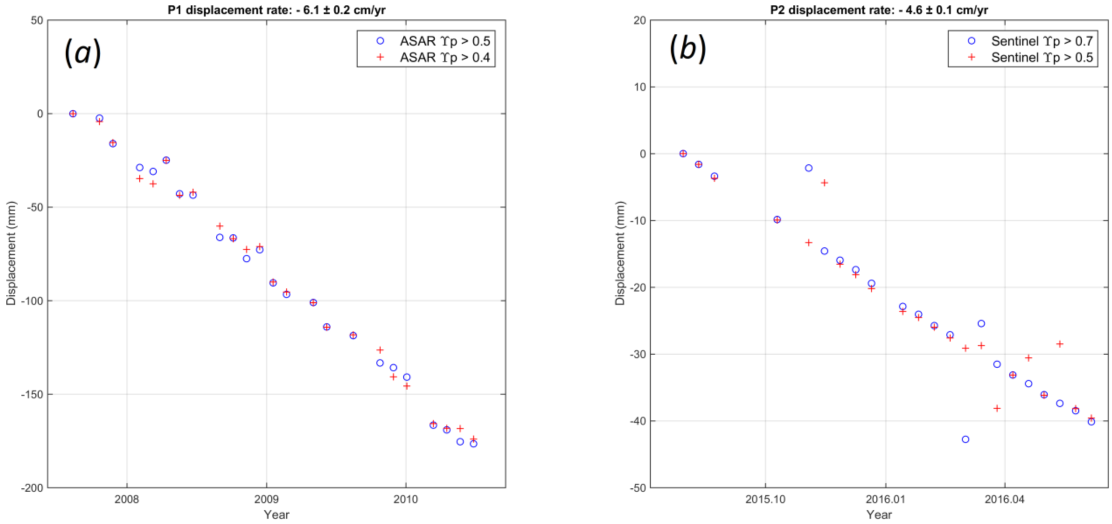

Figure 7.16 Time series displacement over two hot-spots P1 (Figure 7.14 (a) and (b)) and P2 (Figure 7.15 (a) and (c)), respectively.

7.2.4 ATS-InSAR methods with less reliable MS pixels

Basically, it is true that when it comes to the underground mining activities, a nonlinear deformation model should be a better choice to model the deformation phenomena (the subsidence follows a nonlinear trend due to the effect of some sudden deformation within a short period of time). However, a nonlinear deformation model is only applied when a-prior information is available. As the underground mining progress in this work was unknown to the authors (e.g. the exact start and end date, the nonlinear displacement rate, and how the process was going), it is not possible to use such a model because of the absence of significant information. Additionally, this is also the reason why there is a deficiency of MS pixels over the centre of the longwall mining sites (large subsidence within a short period cannot be well modelled using linear deformation model).

Moreover, during the estimation, all the thresholds used in the analysis are empirical values. Considering that the general temporal baseline for Sentinel-1 is much shorter than the counterpart of ENVISAT, the ranges of the reliable γ_P for EVNISAT and Sentinel-1 are set to 0.4 and 0.5, respectively, for selecting sufficient MS pixels. As evident from Figures 7.14 (a) and 7.15 (a), the ENVISAT and Sentinel-1 based MVMs derived from ATS-InSAR method are superimposed onto the local mine plan. It is apparent from Figures 7.14 (c) and 7.15 (d) that the longwall mining panels match pretty well with the two subsiding zones, which means that the local deformation is essentially induced by the underground mining activities. Due to the use of longwall mining technique, the mining-affected regions are predominantly around the longwall panel and can hardly be extended to areas outside the panels.

To produce reasonable contour maps with respect to the MVMs, a GIS-based interpolation method is introduced: 1) a good number of characteristic points are extracted from the original MVMs, 2) smoother mean velocity maps (SMVMs) are generated with these characteristic points, which are illustrated in Figure 7.17 (a) and (b), and 3) the 1-cm-interval contour maps are projected from SMVMs. After carefully calculating, the entire subsiding zone potentially affected (> 2.0 cm yr^{-1}) by underground mining activities approximately accounts for 2.28 and 3.14 km^2, respectively. Within the subsiding zone, a number of public facilities have been detected that are suffering from the ground deformation. These facilities include Hume Motorway and a railway-line in Figure 7.17 (c) as well as Wedderburn Airport in Figure 7.17 (d). As a result of the subsidence, the service ability of railways and roads may be affected by distortion of the rail foundation and road surface. Moreover, the continuous sinking of the airport ground may threaten flight safety and human lives to a large extent. Hence, special attention should be given by the mining industry and government to deal with this matter.

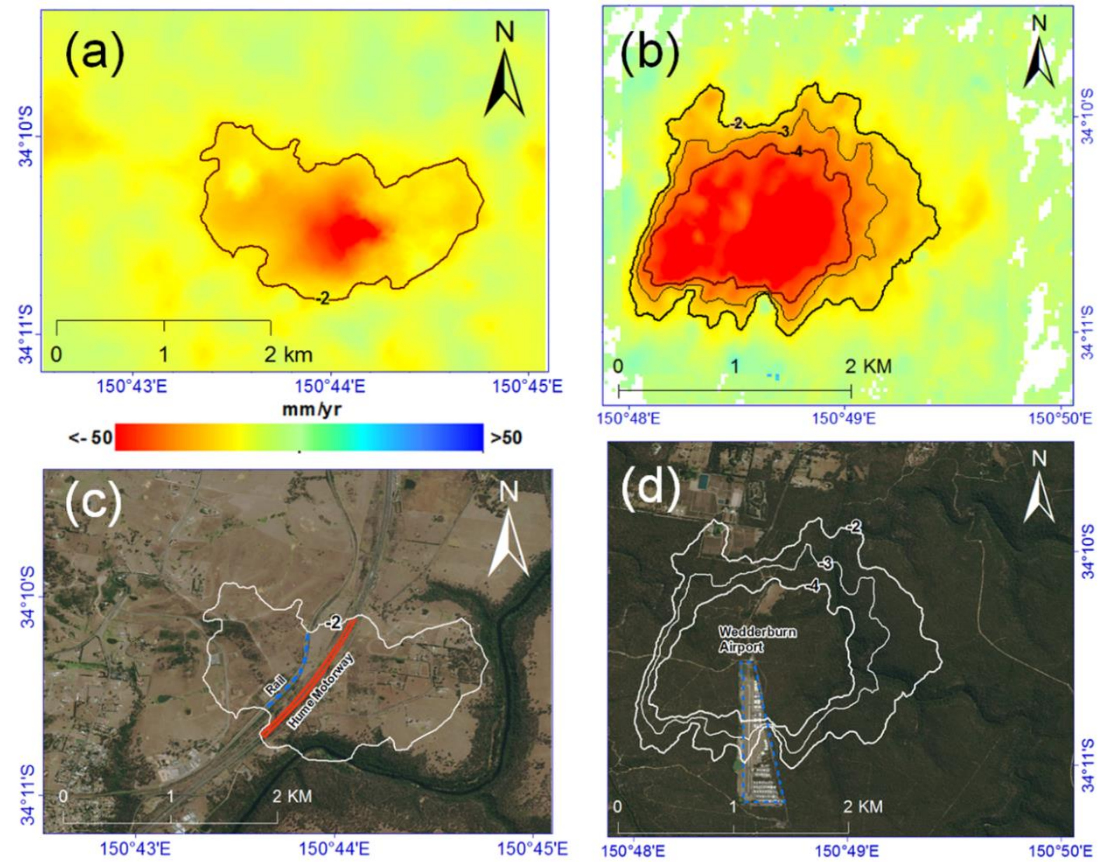

Figure 7.17 (a) – (b) 1-cm-interval contour maps superimposed on ENVISAT and Sentinel-1 based SMVMs, respectively. (c) – (d) 1-cm-interval contour maps superimposed on ©Google Map.

Chapter 8

Comparison between GRACE and InSAR

The Gravity Recovery and Climate Experiment (GRACE) twin satellite mission is a joint scientific project between NASA and DLR for providing precise, time-varying measurements of the Earth's gravitational field (JPL, 2016a). Recently, both GRACE-based technique and TS-InSAR method have been utilized for monitoring groundwater depletion phenomena and even groundwater induced subsidence (Ge et al., 2014; Chen et al., 2010; Rodell et al., 2009; Chaussard et al., 2013; Chaussard et al., 2014; Castellazzi et al., 2016). Ge et al. (2014) drew a conclusion that ground subsidence of 20 – 30 cm yr^{-1} in Bandung City is induced by a reduction in groundwater level of 100 cm yr^{-1} by exploiting the measurement from water wells and the TS-InSAR-derived ground deformation. Nevertheless, such result is only suited for local scale analysis because of the sparse density of utilized points. Castellazzi et al. (2014) first combined both GRACE and DInSAR technique to study the relationship between groundwater depletion series and groundwater induced land displacement. However, their result is rather limited as DInSAR cannot provide time series measurements. Also, Chaussard et al. (2014) utilised more than 600 ALOS-1 images between 2007 and 2011 in order to study the ground subsidence in Mexico covering over 200, 000 km^2 with SBAS method, and the largest subsidence of up to 5~30 cm yr^{-1} has been reported. The authors later concluded that the subsidence is mostly due to groundwater pumping for urban or industrial activities as the other factors, like surface water drainage, artificial sediment loading and mining activities are unlikely to induce such subsidence. Castellazzi et al. (2016)

further examined the correlation among official water budgets, SBAS-based measurements acquired from Chaussard et al. (2014), as well as the groundwater depletion rate derived from GRACE. The comparison result indicates that GRACE failed to detect the entire groundwater losses as reported by the other two methods, and the authors interpreted the difference as returns of wastewater to groundwater recharging system.

Nevertheless, mining activities are widespread in Mexico (Chaussard et al., 2014), and traditional SBAS does not have the ability to clearly identify the subsidence zone induced by underground mining (Du et al., 2017b). Therefore, this part, categorised as the localised subsidence, needs to be identified using other methods, e.g., ATS-InSAR (Du et al., 2016b) and further excluded before estimating the globally averaged value. Within this chapter, two significant facts that the previous research has neglected will be emphasised: 1) the impact of other human-involved activities, for example, underground mining, and 2) the way to integrate multi-path TS-InSAR results.

8.1 Overview of the GRACE satellite mission

The GRACE space gravity mission, which was launched in 2002, is a joint scientific satellite mission between NASA and DLR for providing precise, time-varying measurements of the Earth's gravitational field (JPL, 2016a). The spatial and temporal resolution of GRACE is approximately 160,000 km^2 and monthly, respectively. GRACE mass variation estimates quantify changes in total water storage (*TWS*) also expressed as an Equivalent Water Height (EWH) (Tregoning et al., 2012). Researchers have found that it is capable of observing water storage variations of all depths, including soil moisture, surface water, groundwater, snow and ice by exploiting either land-surface models or in situ observations (Rodell et al., 2009; Rodell et al., 2007; van Dijk et al., 2014; Famiglietti et al., 2011), and the accuracy is better than 1 cm of EWH (Swenson and Wahr, 2002). Furthermore, *TWS* can generally be considered as an integrative measure and estimating groundwater storage (*GWS*) from GRACE EWH requires separating the *TWS* changes into the components of surface water, soil moisture, snow and ice (Richey et al., 2015; Rodell et al., 2007). Rodell et al. (2007) used soil moisture storage (*SMS*) and snow and ice storage (*SIS*) simulated from the Global Land Data Assimilation System (GLDAS) to estimate the *GWS* changes over four major sub-basins of the Mississippi River basin and concluded that this approach is more suitable for regions larger than 900,000 km^2. Moreover, he pointed out that in regions such as the Middle East and China, where the rates of the extraction of *GWS* are unsustainable, this approach is invaluable. Rodell et al. (2009) further exploited external surface water storage (*SWS*) integrated with *SMS* and *SIS* to study the change of *GWS* in northwest India and found that the locally depleted *GWS* is about 4.0 ± 1.0 cm yr^{-1}. van Dijk et al. (2014) studied the global *GWS* changes from 2003 to 2012 and reported that glacier mass loss and subsurface storage decline could be the major uncertainties that constrain the accuracy of the GRACE product. A proper estimation of the each component from ΔTWS allows one to estimate ΔGWS:

$$\Delta GWS = \Delta TWS - (\Delta SMS + \Delta RWS + \Delta LWS + \Delta SIS) \quad (8.1)$$

where *GWS* is the groundwater storage

TWS is the GRACE – derived total water storage

SWS is consists of surface river water storage (*RWS*) and lake water storage (*LWS*)

SMS is the soil moisture storage

SIS is the snow and ice storage

Δ represents the difference between two time acquisitions

8.2 Geological settings

Ordos Basin (Figure 8.1), Inner Mongolia, is extremely rich in natural resources, with one sixth of China's national coal reserves (Yearbook, 2012). As one of the large sedimentary groundwater basins in China (about 280, 000 km^2), Ordos Basin mainly consists of three different aquifer systems: the Cretaceous Aquifer System, the Karst Aquifer System and the Carbonate-Jurassic and Quaternary Aquifer system (Hou et al., 2008). All these aquifer systems are superimposed with each other vertically. However, due to the effect of local arid and semi-arid climates, intense evapotranspiration and weak precipitation, Ordos Basin is suffering from a severe shortage of water resources (Hou et al., 2008). The study area (Figure 8.1) is located in the north part of the Ordos Basin.

Ordos municipality, located in the central part of the study area, was one of the richest cities in China, and even ranked ahead of Beijing in 2011 with a nominal per-capita GDP of US$ 25,239 (Yearbook, 2012). In recent decades, coal-to-liquids (CTL) industries are playing an important role in regional economic growth. CTL – a process also referred to as coal liquefaction – allows coal to be utilised as an alternative to oil, which is highly suited to cities that heavily rely on oil imports and have large domestic reserves of coal. There are a number of CTL projects around the world at various stages of development (GreenToGoFuel, 2015). In 2003, the Shenhua Group Corporation, one of the world's largest coal companies, began to construct the world's first commercial direct coal liquefaction project at Majata, Inner Mongolia, China (Figure 8.1). Majata is a typical coal mining zone and the local water resources have been significantly damaged due to the collective excavation of coal resources. Since 2006, the water resources for coal liquefaction have been heavily dependent on the groundwater from Haolebaoji, Inner Mongolia (red dash line in Figure 8.1), a region about 100 kilometres away in the heart of the Mu Us Sandy land. Twenty-two wells over 300 meters deep were utilised to extract groundwater in Haolebaoji, with a maximum capacity of 58,000 m^3 per day. In other words, the total annual extracted groundwater is about 14.4 million m^3. Recently, a field investigation found that a surrounding region of about 400 km^2 (red solid line in Figure 8.1) is suffering from a drop of ground surface level (Shenhua, 2013). More than 40% of the world's population lives in arid and semi-arid regions where groundwater is not only essential for the maintenance of ecosystem health, but also for human consumption (The Drum, 2015). Therefore, it is important to understand the relationship between groundwater change and surface subsidence. Previous researchers have utilised pixel offset method and TS-InSAR technique to study the underground mining related subsidence with ALOS-1 PALSAR dataset (Zhao et al., 2013; Du et al., 2015). However, the subsidence of Ordos Basin is caused not only by underground mining activities, but also by groundwater extraction. In other words, It is difficult to tackle the complexity of earth surface deformation on an individual, site-specific level or use a single technique or methodology. Rather, the problem needs to be approached by the integration of data taken with different techniques and the collaboration of researchers from multiple disciplines.

In order to map the subsidence in Ordos Basin, 42 L-band ALOS-1 PALSAR images acquired between 8 January 2007 and 19 January 2011 were selected to conduct the TS-InSAR analysis. All these images were captured in ascending orbit with the same incidence angle of 38.7° (Track 460, Frame 780 & 790).

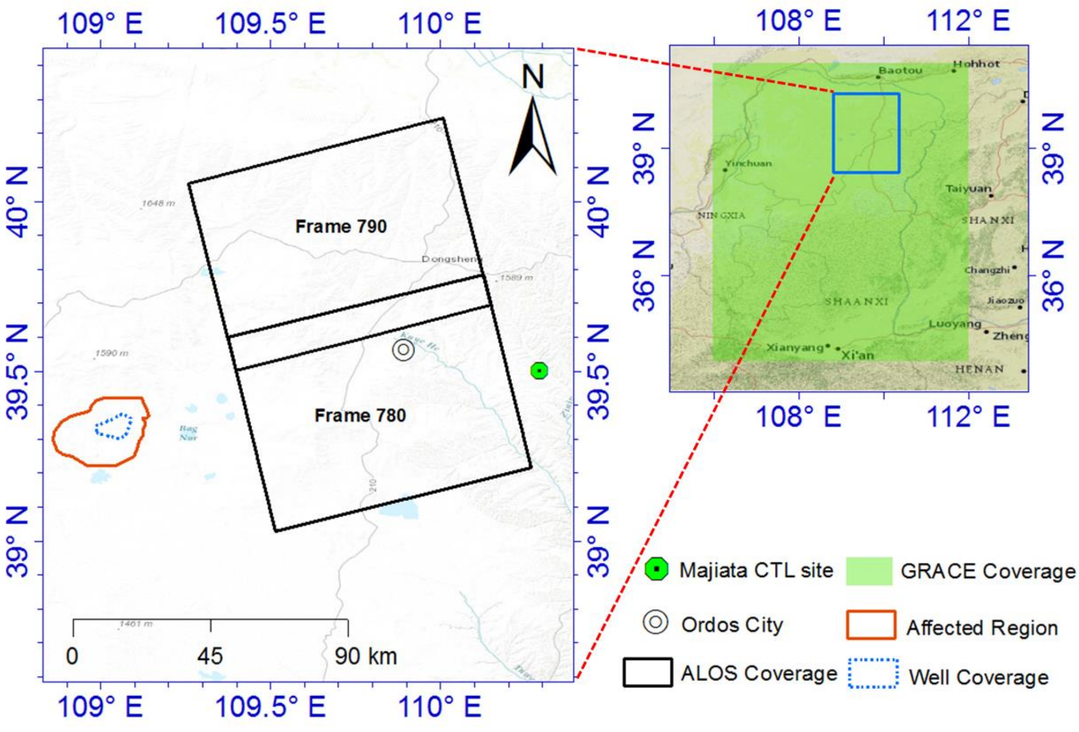

Figure 8.1 The area covered by TS-InSAR analysis is indicated by the rectangle with black solid lines. The light green rectangle refers to the coverage of GRACE product. Regions covered with red solid-line is known as Haolebaoji.

8.3 The procedure to generate GRACE time series measurements

In this study, since Ordos Basin is a semi-arid region, the error of GRACE product induced by glacier mass loss is considered to be negligible; we assume that the local TWS mainly consists of *SMS*, *GWS*, *RWS* and *LWS*. The GRACE monthly *TWS* data is pre-processed in order to eliminate the effect of atmosphere and ocean. To squeeze the systematic uncertainties associated with the data processing, recent studies found that the ensemble mean (simple arithmetic mean of JPL, CSR, GFZ fields after multiplying the scaling grid (JPL, 2016b)) was the most effective way of reducing the noise in the gravity field solutions within the available scatter of the solutions (Sakumura et al., 2014) (examples of these four components can be found in Figure 8.2 (a) to (d)). Thus, an ensemble average *TWS* is calculated with products from three processing centres, namely GFZ (GeoforschungsZentrum Potsdam), CSR (Center for Space Research at University of Texas, Austin) and JPL (Jet Propulsion Laboratory, NASA), from September 2006 to June 2012. All of them are based on the RL05 spherical harmonics with the spatial resolution of 1° in both latitude and longitude (approx. 111 km at the equator). The correct *TWS* is obtained by subtracting a historical mean of the monthly GRACE data (2004 – 2009). It is worth mentioning that low-pass filtering (e.g. destriping, filtering and truncation) may lead to the loss of GRACE signal. In order to estimate the accurate quantification of GRACE observed *TWS*, a scaling factors obtained from the National Center For Atmospheric Research (NCAR)'s Community Land Model 4.0 (CLM 4.0) is applied to correct and restore the signal.

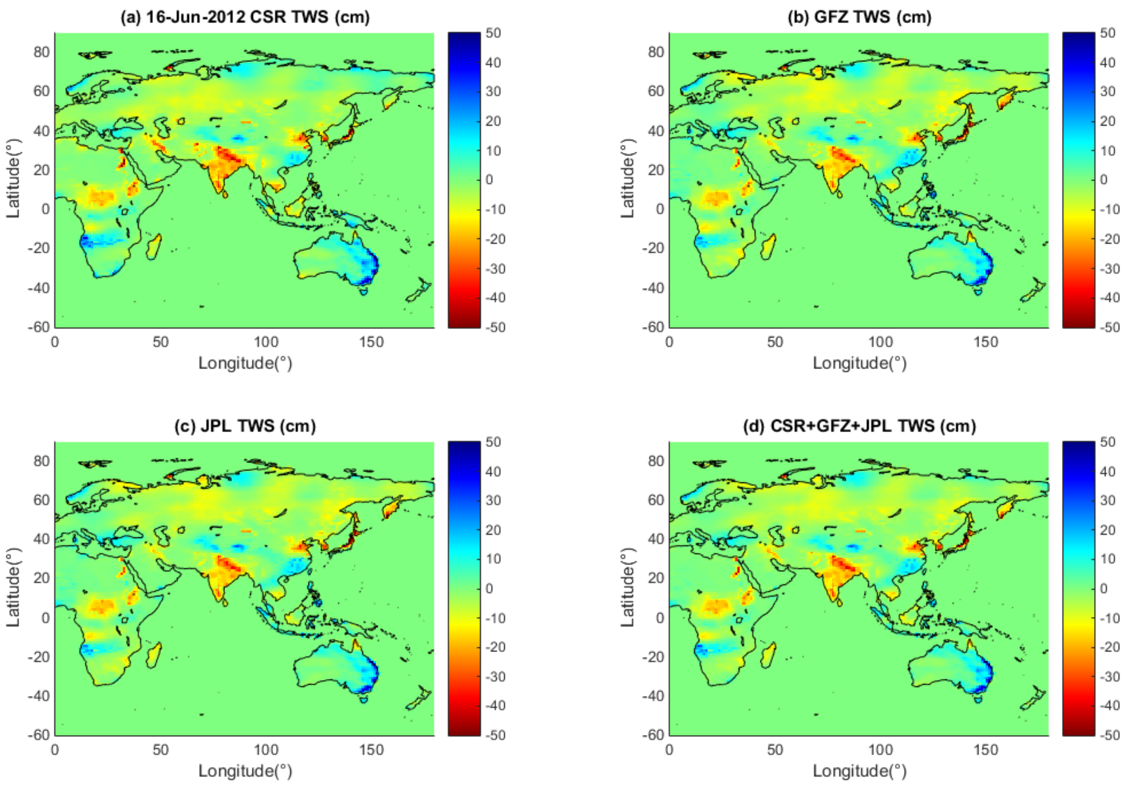

Figure 8.2 the *TWS* acquired on 16 June 2012 derived from (a) CSR, (b) GFZ, (c) JPL, and (d) CSR+GFZ+JPL, respectively.

SMS can be solved with a number of land surface models from GLDAS, namely, Community Land Model (CLM) (10 layers), NOAH (four layers), MOSAIC (three layers) and Variable Infiltration Capacity (VIC) (three layers) (Liu et al., 2009b). GLDAS derived estimates are 3-hourly products with 0.25° spatial resolution (down-sample to 1° spatial resolution in both latitude and longitude direction), while satellite based observations offer twice-daily instantaneous retrievals at similar spatial scales. The total *SMS* is extracted using the monthly output from the arithmetic mean of these four models while the rest components *RWS* and *LWS* are provided by Professor. van Dijk (van Dijk et al., 2014) (1° resolution and a 300 km wide Gaussian filter is applied) (examples of *RSW*, *LWS* and *SMS* can be seen in Figure 8.3 (a) to (d)).

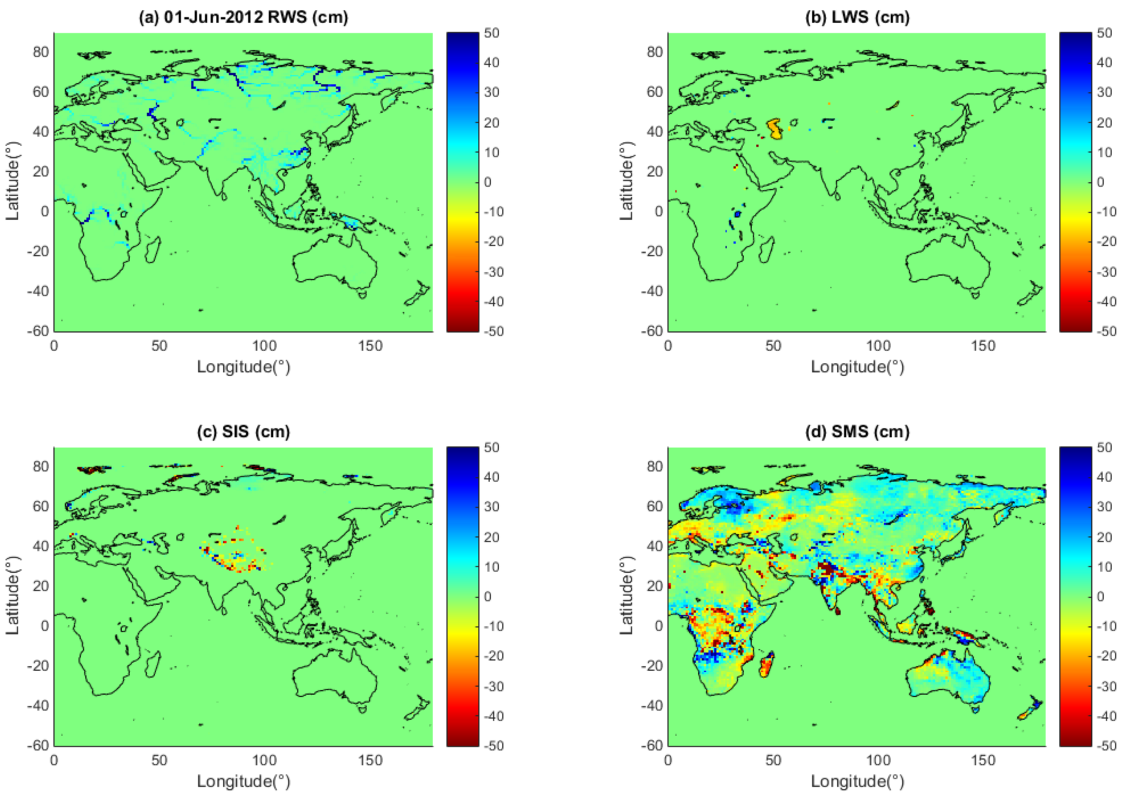

Figure 8.3 components included in *TWS* acquired on 01 June 2012 derived from (a) *RSW*, (b) *LWS*, (c) *SIS*, and (d) *SMS*, respectively.

To achieve a reasonable comparison among all these various layers, the data acquisition times for them should be exactly the same. However, given the fact that the temporal sampling rates for some of these layers are not consistent, the temporal gap refining method is carried out. More specifically, all these *TWS* products were acquired in the middle of months and several months were not recorded while for other layers, including *SMS*, *LWS*, and *RWS*, the dataset acquisition times were at the beginning of months and all months have been recorded (taking *SMS* as an example).

SMS is resampled in temporal domain to match up with the temporal sampling rate of *TWS* based on Equation 8.2.

The interpolation operation in time series is carried out under the assumption that the EWH changes experience a linear trend within a short period (e.g. one month in this context).

$$f(t)=\begin{cases} 0 & for \quad t>t_i,t_{i+1} \\ \left[y(t_{i+1})-y(t_i)\right]\left(\dfrac{t-t_i}{t_{i+1}-t_i}\right)+y(t_i) & for \quad t>t_i \,\&\, t<t_{i+1} \\ 0 & for \quad t<t_i,t_{i+1} \end{cases} \tag{8.2}$$

where t is the targeted time in *TWS*, while t_i and t_{i+1} are two adjacent times in *SMS*, $i+1$ is the number of *SMS* stack, $f(t)$, $y(t_i)$, $y(t_{i+1})$ are the corresponding two-dimensional values at time t, t_i and t_{i+1}.

Finally, to compute the *GSW* time series, all types of datasets are first adjusted so that their values were relative to the first image in September 2006. The ΔSMS, ΔRWS and ΔLWS are then subtracted from ΔTWS to derive the groundwater storage variation. The time series variations for ΔSMS derived from four models are given in Figure 8.4 and eventually, the averaged *SMS* is used for the final estimation. The time series *GWS* is estimated by calculating the averaged value among 42 one-degree pixels (~420, 000 km^2) covering the whole Ordos Basin (latitude ranges from 34.5^o to 40.5^o north while longitude ranges from 106.5^o to 111.5^o east, respectively) (light green rectangle region within Figure 8.1).

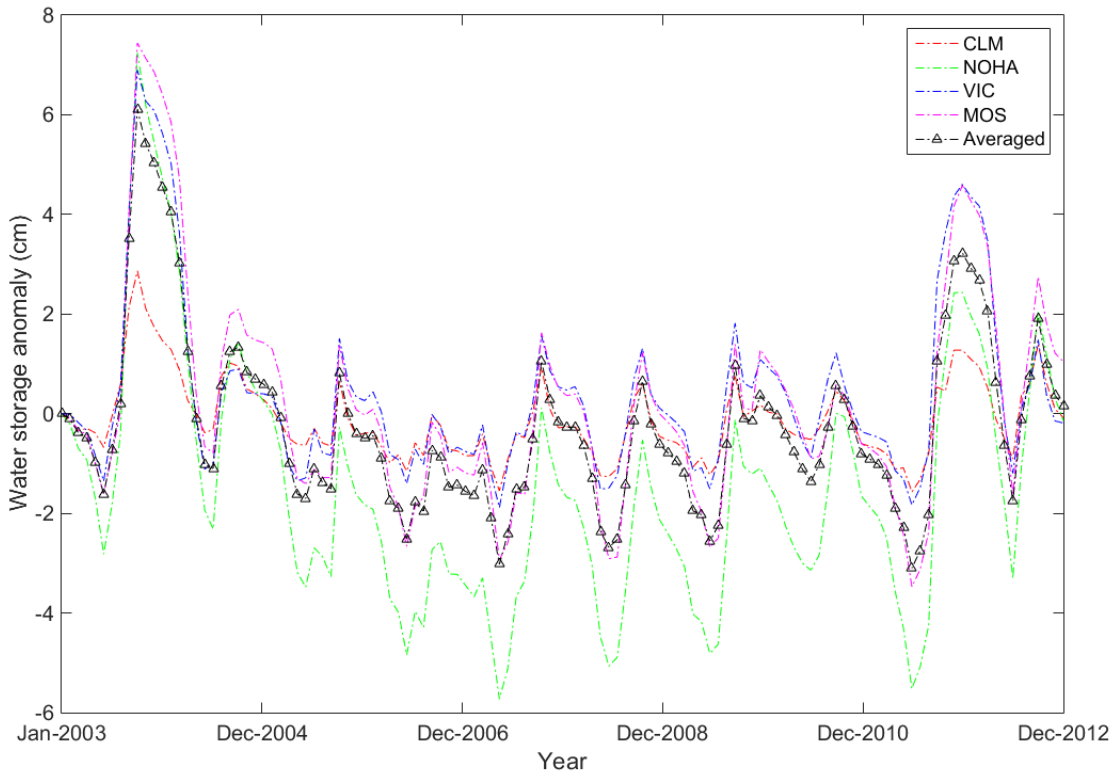

Figure 8.4 The 2003 – 2012 time series soil moisture variation over Ordos Basin estimated from four GLDAS models (including the averaged result)

Since the InSAR-derived result and GRACE-based outcome have a vast difference in spatial resolution, i.e. GRACE (~ 300 km) vs. InSAR (~ a few 10s of meters), the two measurements are not comparable over the same region. For example, even several meters of groundwater loss over a small area spanning a few kilometres might not be detectable by GRACE, which senses only regional patterns. Instead

Figure 8.5 (a) and (b) is the time series comparison among *SMS*, *TWS* and *RSW+LWS* layers over Ordos Basin between December 2016 and June 2012. It is clear that the change of *RSW+LWS* layer was not significant during this six-year period due to the fact that the study region lies within a semi-arid continental climate zone and the number of lakes and rivers taken into account are rather limited.

Furthermore, the trends of both *SMS* and *TWS* layers match up to each other to some extent, posing an apparent seasonal change. The monthly rainfall measurement over Ordos Basin is given in Figure 8.5 (c). Despite the differences in magnitude, it is worth noting that the general tendency between *SMS* and the monthly rainfall shows a relatively high consistency. The groundwater depletion series, also known as *GWS*, is estimated by subtracting *SMS* and *RSW+LWS* from *TWS* and the results indicate that groundwater induced subsidence rates in vertical direction is about −7.3 mm yr^{-1} (Figure 8.3 (b)), which is equivalent to a complete loss of 2,044 million m^3 water resources per year as the total size of Ordos basin is about 280,000 km^2. In other words, within Ordos Basin, a total amount of 2.9 million m^3 groundwater could be extracted from a 400 km^2 region in general. However, according to Shenhua's report (Shenhua, 2013), 14.4 million m^3 groundwater was actually extracted from the Haolebaoji surrounding region (region covered with red solid-line in Figure 8.1 with the total size of approximate 400 km^2), which is about five times the average annual depletion rate of the entire Ordos Basin, and this should serve as reliable evidence to explain the local ground subsidence. In conclusion, the experiment result agrees well with the fact that the region surrounding Haolebaoji is suffering from a drop of groundwater level after the groundwater extraction commenced in 2006 (Shenhua, 2013).

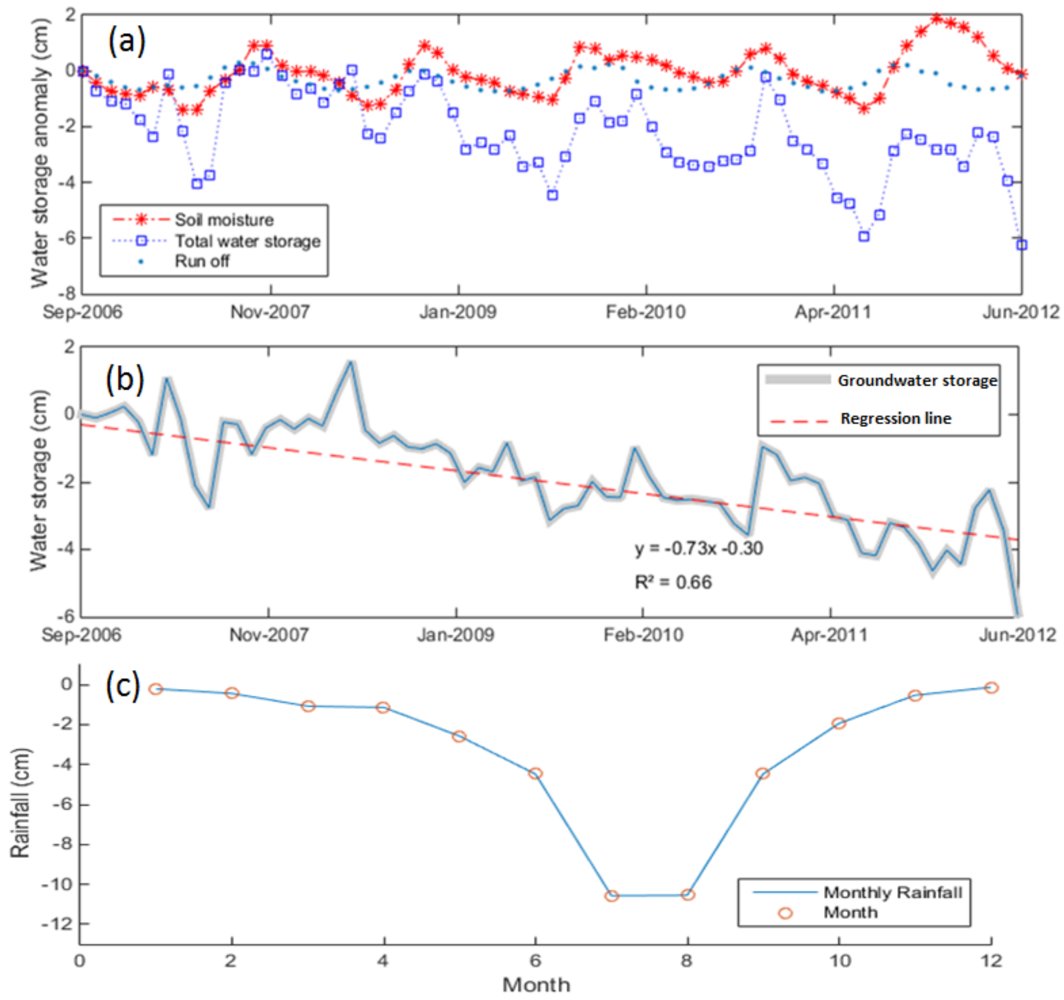

Figure 8.5 (a) *SMS*, *TWS* and *RSW+LWS* time series measurements and (b) groundwater depletion rate form GRACE between Sep. 2006 and Jun. 2012 (c) the monthly rainfall over Ordos Basin.

8.4 InSAR time series measurement

The subsidence rate map generated from ALOS-1 PALSAR data (both Frame 780 and Frame 790) between 08 January 2007 and 19 January 2011 is shown in Figure 8.6. The reference point is selected over a relatively stable region outside of the underground mining zone marked with empty white star. The linear displacement rates derived from TS-InSAR analysis are relative values with respect to the reference point. To combine the TS-InSAR results from two frames together, first and foremost, a common region is selected (marked with red rectangle dash-line box within Figure 8.6). The mean LOS velocities are estimated over the common region for both frames and the TS-InSAR result for Frame 780 is set as the reference layer. It is evident from Figure 8.7 (a) that the mean LOS velocity value estimated from Frame 780 is –5.4 mm yr^{-1}, and thereafter the final combined TS-InSAR result can be achieved by shifting the mean velocity value of Frame 790 to –5.4 mm yr^{-1} as shown in Figure 8.7 (b).

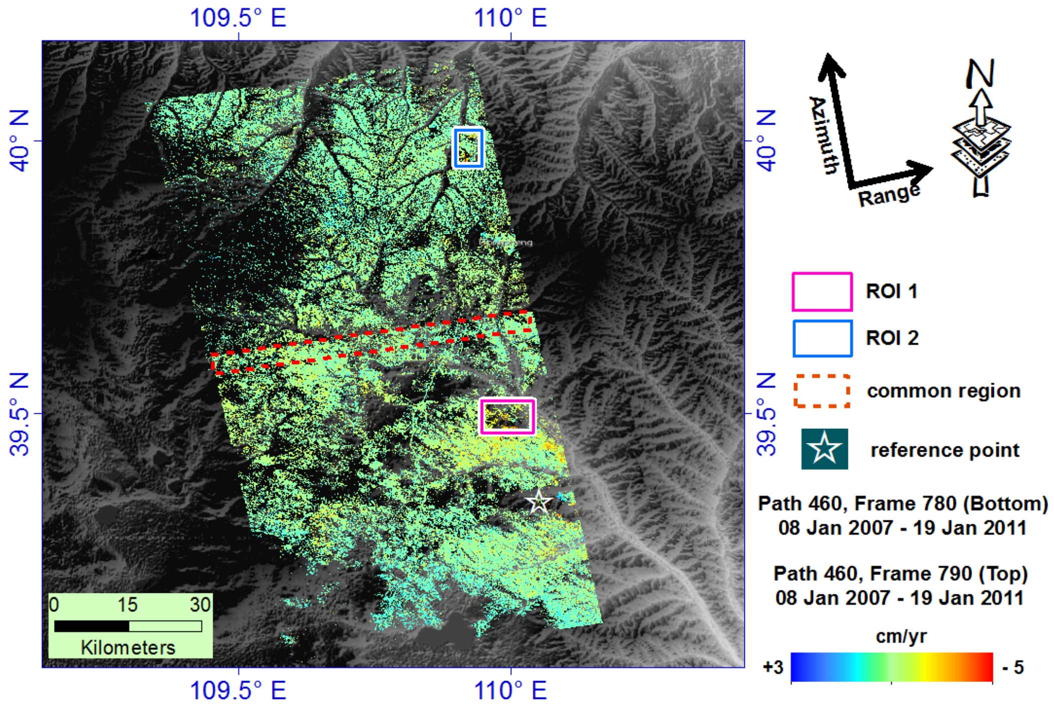

Figure 8.6 TS-InSAR mean velocity map in LOS direction superimposed on SRTM DEM map (SAR images acquired from 08 January 2007 to 19 January 2011)

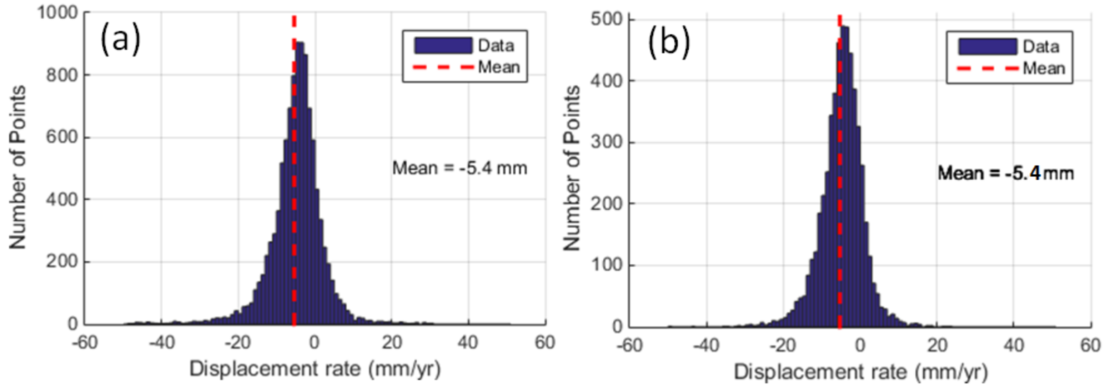

Figure 8.7 The histogram of TS-InSAR velocity over the common region (a) Frame 780; (b) Frame 790; marked with red rectangle dash-line box in Figure 8.6.

After deleting all the common MS pixels, a total number of 2,055,859 pixels is obtained, which means the density of scatterers is about 286 MS km^{-2} (286 is quite a good number because less reliable MS pixels were added to increase the density of scatterers). The majority of the ALOS-1 LOS displacement is between –20 mm yr^{-1} to 20 mm yr^{-1}, and two areas have been selected to demonstrate the detailed subsidence; Figure 8.8 (a) shows ROI 1 superimposed onto the optical image (© Google Earth), which is a rapidly subsiding zone as previously shown in Figure 8.6 covered with purple rectangle. It can be seen that the subsidence bowls are located over the rural regions, with the mean velocity of the subsidence region at –16 mm yr^{-1} in LOS direction. Furthermore, a RADARSAT-2 pair is used to generate the differential interferometric map using the two-pass DInSAR technique (Massonnet et al., 1993), and the interferometric pattern from the outcome can be used to provide some useful information for the more recent land deformation evolution over the region. Four typical subsiding funnels induced by underground mining activities have been detected in Figure 8.8 (b), suggesting the land subsidence may have continued over the same subsidence region even after one-year period.

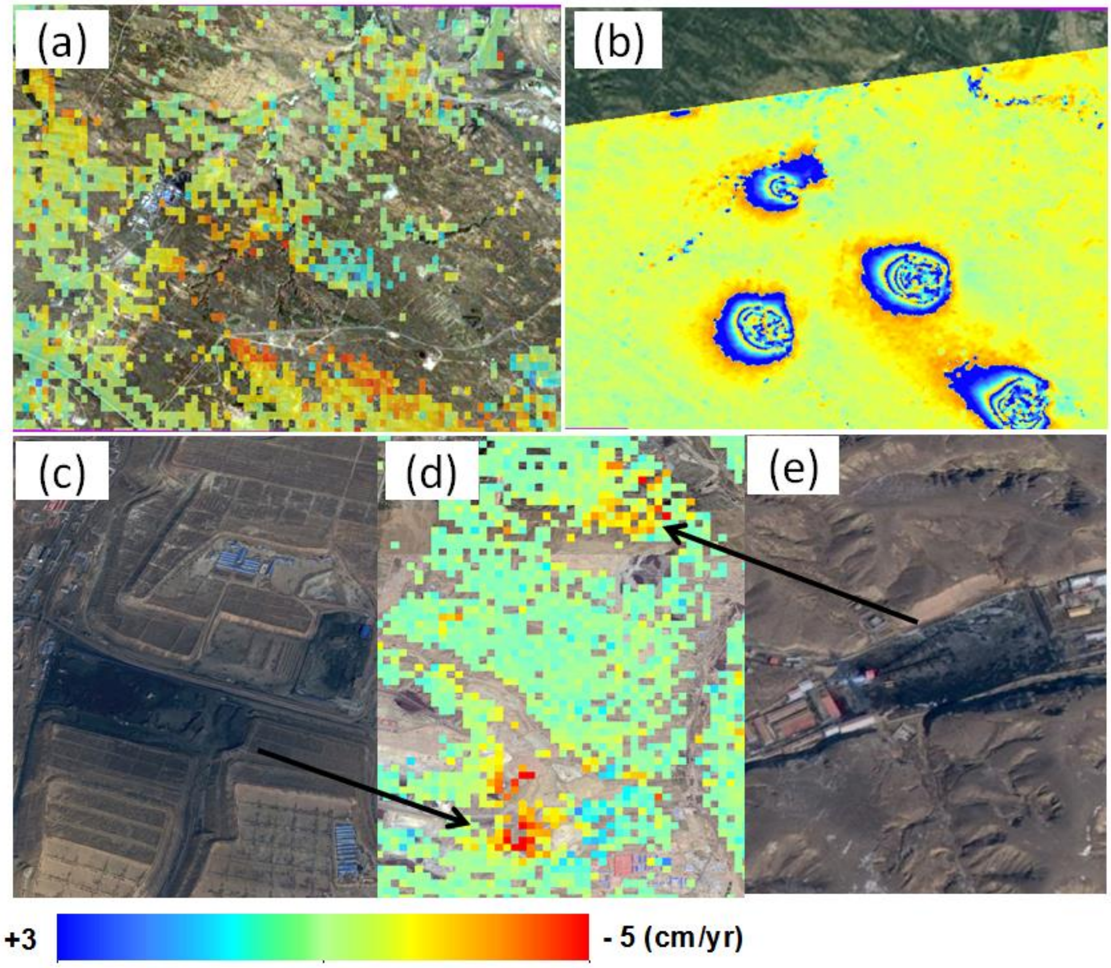

Figure 8.8 (a) (d) Subsidence rate map generated with ALOS-1 PALSAR data with optical image (© Google Earth) at the highlighted region AOI 1 and AOI 2 in Fig. 5. (b) represents the DInSAR IFG generated with two RADARSAT-2 images acquired on 13 February 2012 and 8 March 2012. (c) and (e) are optical image obtained from Google Earth.

The InSAR-derived subsidence over ROI 2 is shown in Figure 8.8 (d) and the magnitude of subsidence over –30 mm yr^{-1} in LOS direction has been found in some areas. Two coal mining sites illustrated in Figure 8.8 (c) and (e) that have been observed using Google Earth are geologically close to two sinking regions, indicating the local subsidence is also caused by mining related activities. According to (Du et al., 2016a), the typical fringe patterns caused by underground mining subsidence derived from DInSAR differential IFG with two obvious characteristics: 1) The earth surface where underground mining occurs will sink as the colour of the defomation pattern is changing from yellow to blue (from the centre to the edge); 2) The subsidence magnitude increases from the edge to the centre, therefore resulting in an oval or a round shape (Hu et al., 2013), while the detailed description of the underground mining subsidence pattern from TS-InSAR velocity map can be found in (Du et al., 2016a). Regions suffering from rapid changes within a short period of time will lose their InSAR coherence and therefore will form gap zones (see section 7.1).

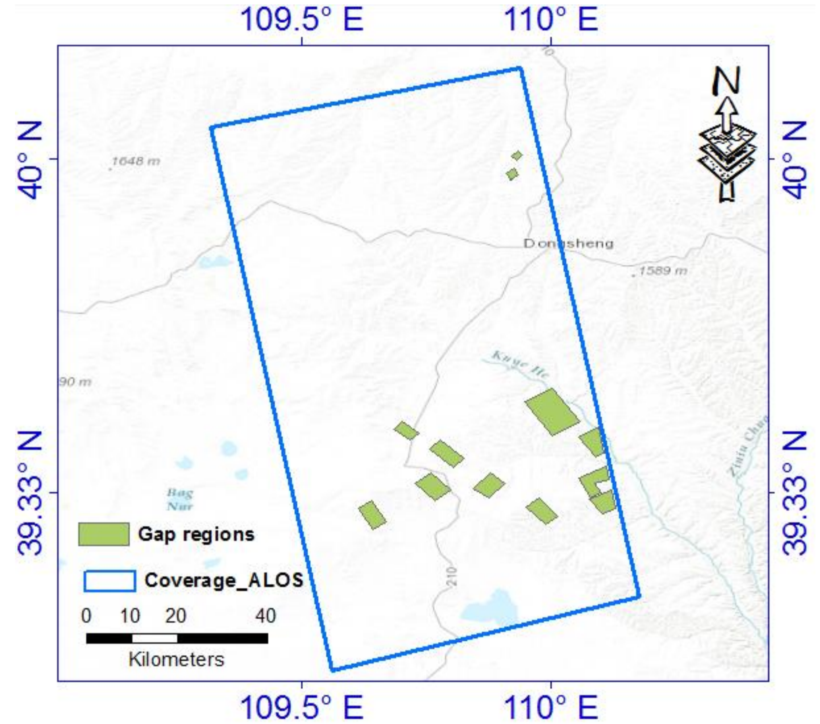

Figure 8.9 Twelve gap regions derived from TS-InSAR result

Figure 8.9 shows twelve gap regions derived from the TS-InSAR result (identified using the rules described in (Du et al., 2016a)). The total size of these areas is about 190 km^2, which only accounts for 2.6 % of the coverage of the TS-InSAR result (about 60 × 120 km^2). However, it is worth noting that the actual extent of underground mining induced land surface subsidence is larger than the extent of underground mining sites, and the affected regions are related to a number of factors, e.g. the angle of draw and the depth of longwall mining sites (Coal Mine, 2015). More importantly, this part of subsidence contributes a lot to the total velocity and should be excluded before estimating the final mean velocity (which accounts for –3.8 mm yr^{-1} in LOS direction in this paper). Due to the lack of various viewing geometry, e.g. a descending pair covering the study region, the deformation is assumed to be mainly in the vertical direction and the horizontal movement is negligible. Finally, the mean vertical velocity of –4.9 mm yr^{-1} is obtained by dividing the cosine of the angle of incidence (Du et al., 2015). Furthermore, given the fact that the groundwater extraction site and its affected region (about 400 km^2) are both outside of the coverage of ALOS measurement (Figure 8.1), it is still fairly difficult to conclude that the local subsidence is mainly induced by underground mining activities, unless no further impacts of groundwater changes on the surface subsidence were confirmed.

8.5 Further work

In the future, to make a rational comparison between the InSAR derived mean velocity with GRACE-based groundwater depletion trend together, the following conditions need to be satisfied: 1) The coverage of InSAR measurement shall be larger than the spatial resolution of GRACE product, taking L-band ALOS PALSAR data as an example, the minimum nearby image pairs is at least 18. Additionally, Sentinel-1A IWS mode with its relatively short revisit time of 12 days and large spatial coverage of 250 km $\times$ 250 km can be exploited to study the relationship between ground surface deformation and groundwater changes, as two or three adjacent sentinel-1A images together are fully capable of covering the spatial resolution of GRACE. 2) Local subsidence induced by human involved activities, e.g. underground mining, shall be excluded before the final estimation of the mean velocity.

Chapter 9

Concluding remarks

The main objective of this dissertation was defined in Chapter 1 as:

"This dissertation aims to identify ways to overcome the drawbacks of the TS-InSAR method for dealing with the moderate and rapid ground subsidence, as well as to investigate the potential cause of the subsidence by applying several established TS-InSAR techniques to different areas."

9.1 Summary

Land subsidence is an environmental, geological phenomenon that often refers to gradual settling or rapid sinking of the ground surface as a result of subsurface movement of earth materials. It is considered to be a global issue, and many cities of the world have been reported suffering from land subsidence to a large extent. The level of land subsidence can be simply categorised into three groups: rapid, moderate and slow changes, if one only takes the potential effects of the subsidence into consideration. Rapid land subsidence events, such as earthquake, are likely to cause serious problems. Moderate and slow ground surface subsidence may result in no evident consequence in a short time, but over a long period of time can lead to severe economic loss and shocking impact.

Differential Interferometric Synthetic Aperture Radar (DInSAR) method has been used to monitor such events over the past three decades. However, its result can be affected by spatial/temporal decorrelation and atmospheric disturbance. In recent decade, Time series InSAR (TS-InSAR) was proposed to minimise these biases by taking advantage of the principle of temporal and spatial statistical analysis. Nevertheless, TS-InSAR has issues due to the tropospheric stratification in high elevation regions and insufficient measurement pixels over rapid subsiding zones.

This dissertation mainly focused on optimisation of the TSInSAR-based technique for land subsidence measuring induced by the extraction of natural resources, such as coal, coalbed methane (CBM) and groundwater. We believe that the application of time series SAR interferometry will broadened greatly with the help of these research outcomes.

- DInSAR and TS-InSAR technique are both interferometry methods for monitoring land subsidence with fine accuracy. DInSAR is suitable for short term measurement, while TS-InSAR uses phase information to map surface subsidence and requires SAR image acquisitions to maintain high coherence, and hence is mainly applicable to slow changes. However, some rapidly changing surface subsidence can lead to the loss of InSAR coherence. Therefore, no signal can be detected in such a region. Such gaps in TS-InSAR result can be resolved by combining refined DInSAR and TS-InSAR measurements together.

- Secondly, ALOS-1 PALSAR and ENVISAT ASAR based TS-InSAR has been conducted to monitor the subsidence over underground mining regions. Since the maximum displacement gradients that can be detected are different for L-band and C-band-based TS-InSAR, some rapid changes in land surface could cause the TS-InSAR to fail to estimate the correct displacements. L-band datasets are able to provide better results and achieve detailed deformation signals about the spatial distribution of the ground surface subsidence phenomenon. Nevertheless, the result of the counterpart ENVISAT failed to produce reasonable outcome due to the underground mining effect. An approach has been developed and implemented to address this issue through an IDW (Inverse Distance Weighted)-based integration method. In addition, the proposed method is also applied to C-band Sentinel-1 image stacks for testing purpose, and the final result proved to be efficient to offer sufficient information to the mining industry and government for risk management purpose.

- Thirdly, several established TS-InSAR techniques have been applied to different areas, and these significant findings from the TS-InSAR analysis have led to new insights into the processes causing the deformation.

9.2 Future directions

It should be noticed that Stripmap (SM) (e.g. ALOS-1, ALOS-2) and Terrain Observation with Progressive Scan SAR (TOPSAR) (e.g. Sentinel-1) are the most commonly used modes of both single- and multi-master based TS-InSAR analysis. Nevertheless, there is no such TS-InSAR experiment conducted using Scanning SAR (ScanSAR) mode dataset. In fact, ScanSAR mode provides a much wider observation area as compared to the counterpart coverage of SM mode. Taking ALOS-2 satellite as an example, the swath of the former (~350 km) is nearly five times wider than the latter (~ 70 km) (Table 9-1), making it possible to resolve the continuous land subsidence covering a reasonably large area. Furthermore, it has been three years since the launch of ALOS-2 satellite on 24 May 2014. But until now, the maximum SM pairs with the same incidence angle over one particular site is less than 13 images whilst the counterpart pairs of ScanSAR is usually more than 25 scenes. Last but not least, the derived ScanSAR based TS-InSAR can also be used to solve the coefficient of correlation between land subsidence and groundwater depletion rate (GRACE measurement).

Table 9-1 ScanSAR Data information for the radar satellites that are still operating

	Spatial Coverage (km × km)	Spatial Resolution (m)
TerraSAR-X	100 × 150	~ 18.5
COSMO-SkyMed	100 × 100	~ 100
ALOS-2	350 ~ 490	~ 100
Radarsat-2	300 × 300	~ 100

On the other hand, earlier SAR satellites from SEASAT-SAR to RADARSAT-1 acquired images at single polarimetric channels, while the latest launched space-borne SARs operated with dual-polarization or even quad-polarization. Navarro-Sanchez et al. (2010) conducted the first dual-polarimetric based TS-InSAR using space-borne SAR based on Pipia et al. (2009) and showed that 60% more PS pixels were obtained as compared to single-pol data. Navarro-Sanchez and Lopez-Sanchez (2014) later reported that the quad-pol based TS-InSAR was fully capable of detecting 310% more PS pixels as compared to single-pol set over the urban area of Barcelona, Spain. Considering that the former pol- based TS-InSAR experiments were conducted over the metropolitan regions, this technique can be adopted into

ATS-InSAR and applied over non-urban areas for achieving more detailed observation.

Furthermore, it is evident that the static GPS or Continuously Operating Reference Station (CORS) can provide very accurate measurement in North-South (N-S) and West-East (W-E) direction (< 5 mm) while levelling is fully capable of providing accurate detection in vertical direction (< 5 mm) (more close the Term Bench Mark (TBM), more accurate measurement can be achieved). Imagine that there is a network combining both CORS & TBM, and each GPS station has one or more nearby TBM (both measurements can later be resampled into monthly or yearly products); such a system can indeed be used to retrieve the 3D movements over individual GPS stations, and further cross validate/rectify the TS-InSAR outcomes.

Reference

Adam, N., Parizzi, A., Eineder, M. & Crosetto, M. 2009. Practical persistent scatterer processing validation in the course of the Terrafirma project. *Journal of Applied Geophysics,* 69**,** 59-65.

Agram, P. & Simons, M. 2015. A noise model for InSAR time series. *Journal of Geophysical Research: Solid Earth*.

Ahmed, R., Siqueira, P., Hensley, S., Chapman, B. & Bergen, K. 2011. A survey of temporal decorrelation from spaceborne L-Band repeat-pass InSAR. *Remote Sensing of Environment,* 115**,** 2887-2896.

Baby, H. B., Gole, P. & Lavergnat, J. 1988. A model for the tropospheric excess path length of radio waves from surface meteorological measurements. *Radio science,* 23**,** 1023-1038.

Bamler, R. & Hartl, P. 1998. Synthetic aperture radar interferometry. *Inverse problems,* 14**,** R1.

Bateson, L., Cigna, F., Boon, D. & Sowter, A. 2015. The application of the Intermittent SBAS (ISBAS) InSAR method to the South Wales Coalfield, UK. *International Journal of Applied Earth Observation and Geoinformation,* 34**,** 249-257.

Berardino, P., Fornaro, G., Lanari, R. & Sansosti, E. 2002. A new algorithm for surface deformation monitoring based on small baseline differential SAR interferograms. *IEEE Transactions on Geoscience and Remote Sensing,* 40**,** 2375-2383.

BHP 2014. Appin Longwalls 701 to 704 and 705 to 710. BHP Billiton Illawarra Coal, Australia.

Biggs, J., Wright, T., Lu, Z. & Parsons, B. 2007. Multi-interferogram method for measuring interseismic deformation: Denali Fault, Alaska. *Geophysical Journal International,* 170**,** 1165-1179.

Brusilovskiy, E. 2013. *Spatial Interpolation: A Brief Introduction* [Online]. Available: http://www.bisolutions.us/A-Brief-Introduction-to-Spatial-Interpolation.php [Accessed 15 June 2017].

Case, J. C., Edgar, T. V. & De Bruin, R. H. 2000. Subsidence potential related to water withdrawal in the Powder River Basin. *Wyoming Geo-Notes,* 68**,** 19-20.

Cassee, B. 2004. *Selection of permanent scatterer candidates for deformation monitoring; amplitude calibration of ERS SLC SAR images.* Master's thesis, Delft University of Technology, Delft, Netherlands, 2004.

Castellazzi, P., Martel, R., Galloway, D. L., Longuevergne, L. & Rivera, A. 2016. Assessing groundwater depletion and dynamics using GRACE and InSAR: potential and limitations. *Groundwater,* 54**,** 768-780.

Castellazzi, P., Martel, R., Garfias, J., Calderhead, A. I., Salas-Garcia, J., Huang, J. & Rivera, A. Groundwater deficit and land subsidence in central mexico monitored by grace and RADARSAT-2. Geoscience and Remote Sensing Symposium (IGARSS), 2014 IEEE International, 2014. IEEE, 2597-2600.

Chang, C., Chang, T., Wang, C., Kuo, C. & Chen, K. 2004. Land-surface deformation corresponding to seasonal ground-water fluctuation, determining by SAR interferometry in the SW Taiwan. *Mathematics and Computers in Simulation,* 67**,** 351-359.

Chaussard, E., Amelung, F., Abidin, H. & Hong, S.-H. 2013. Sinking cities in Indonesia: ALOS PALSAR detects rapid subsidence due to groundwater and gas extraction. *Remote Sensing of Environment,* 128**,** 150-161.

Chaussard, E., Wdowinski, S., Cabral-Cano, E. & Amelung, F. 2014. Land subsidence in central Mexico detected by ALOS InSAR time-series. *Remote sensing of environment,* 140**,** 94-106.

Chen, B., Gong, H., Li, X., Lei, K., Zhu, L., Gao, M. & Zhou, C. 2017. Characterization and causes of land subsidence in Beijing, China. *International Journal of Remote Sensing,* 38**,** 808-826.

Chen, C.-H., Wang, C.-H., Hsu, Y.-J., Yu, S.-B. & Kuo, L.-C. 2010. Correlation between groundwater level and altitude variations in land subsidence area of the Choshuichi Alluvial Fan, Taiwan. *Engineering Geology,* 115**,** 122-131.

Chen, C. W. & Zebker, H. A. 2002. Phase unwrapping for large SAR interferograms: Statistical segmentation and generalized network models. *IEEE Transactions on Geoscience and Remote Sensing,* 40**,** 1709-1719.

Chen, J. & Zebker, H. A. 2012. Ionospheric artifacts in simultaneous L-band InSAR and GPS observations. *Geoscience and Remote Sensing, IEEE Transactions on,* 50**,** 1227-1239.

Chen, M., Tomás, R., Li, Z., Motagh, M., Li, T., Hu, L., Gong, H., Li, X., Yu, J. & Gong, X. 2016. Imaging Land Subsidence Induced by Groundwater Extraction in Beijing (China) Using Satellite Radar Interferometry. *Remote Sensing,* 8**,** 468.

Coal Mine. 2015. *Coal Mine Subsidence Theory* [Online]. Available: http://inside.mines.edu/fs_home/tboyd/Coal/sub_theory/ [Accessed 16 November 2015].

Colesanti, C., Ferretti, A., Novali, F., Prati, C. & Rocca, F. 2003a. SAR monitoring of progressive and seasonal ground deformation using the permanent scatterers technique. *IEEE Transactions on Geoscience and Remote Sensing,* 41**,** 1685-1701.

Colesanti, C., Ferretti, A., Novali, F., Prati, C. & Rocca, F. 2003b. SAR monitoring of progressive and seasonal ground deformation using the permanent scatterers technique. *Geoscience and Remote Sensing, IEEE Transactions on,* 41**,** 1685-1701.

Colesanti, C., Locatelli, R. & Novali, F. 2002. Ground deformation monitoring exploiting SAR permanent scatterers. *Proceding of IGARSS.*

Costantini, M. & Rosen, P. A. A generalized phase unwrapping approach for sparse data. Geoscience and Remote Sensing Symposium, 1999. IGARSS'99 Proceedings. IEEE 1999 International, 1999. IEEE, 267-269.

Crosetto, M., Biescas, E., Duro, J., Closa, J. & Arnaud, A. 2008. Generation of advanced ERS and Envisat interferometric SAR products using the stable point network technique. *Photogrammetric Engineering & Remote Sensing,* 74**,** 443-450.

Damian, K. 2014. *Why the world's biggest coal company has stopped extracting Chinese groundwater* [Online]. Energydesk daily dispatch. Available: http://energydesk.greenpeace.org/2014/04/08/worlds-biggest-coal-company-stopped-extracting-chinese-groundwater/ [Accessed 25 June 2015].

Dee, D., Uppala, S., Simmons, A., Berrisford, P., Poli, P., Kobayashi, S., Andrae, U., Balmaseda, M., Balsamo, G. & Bauer, P. 2011. The ERA - Interim reanalysis: Configuration and performance of the data assimilation system. *Quarterly Journal of the Royal Meteorological Society,* 137**,** 553-597.

Ding, X.-l., Li, Z.-w., Zhu, J.-j., Feng, G.-c. & Long, J.-p. 2008. Atmospheric effects on InSAR measurements and their mitigation. *Sensors,* 8**,** 5426-5448.

Doin, M.-P., Lasserre, C., Peltzer, G., Cavalié, O. & Doubre, C. 2009. Corrections of stratified tropospheric delays in SAR interferometry: Validation with global atmospheric models. *Journal of Applied Geophysics,* 69**,** 35-50.

Du, Z., Ge, L., Li, X. & Ng, A. Land subsidence characteristics of Ordos using differential interferometry and persistent scatterer interferometry. Geoscience and Remote Sensing Symposium (IGARSS), 2015 IEEE International, 26-31 July 2015 2015. 314-317.

Du, Z., Ge, L., Li, X. & Ng, A. 2016a. Subsidence Monitoring over the Southern Coalfield, Australia Using both L-Band and C-Band SAR Time Series Analysis. *Remote Sensing,* 8**,** 543-559.

Du, Z., Ge, L., Li, X. & Ng, A. H.-M. 2016b. Subsidence monitoring in the Ordos basin using integrated SAR differential and time-series interferometry techniques. *Remote Sensing Letters,* 7**,** 180-189.

Du, Z., Ge, L., Ng, A. & Li, L. 2017a. Mapping land subsidence over the eastern Beijing City using satellite radar interferometry. *International Journal of Digital Earth*.

Du, Z., Ge, L., Ng, A. H.-M. & Li, X. 2018. Investigation on mining subsidence over Appin–West Cliff Colliery using time-series SAR interferometry. *International Journal of Remote Sensing,* 39**,** 1528-1547.

Du, Z., Ge, L., Ng, A. H.-M., Li, X. & Li, L. 2017b. Monitoring of ground deformation in Liulin District, China using InSAR approaches. *International Journal of Digital Earth***,** 1-20.

Famiglietti, J., Lo, M., Ho, S., Bethune, J., Anderson, K., Syed, T., Swenson, S., de Linage, C. & Rodell, M. 2011. Satellites measure recent rates of groundwater depletion in California's Central Valley. *Geophysical Research Letters,* 38.

Farr, T. G., Rosen, P. A., Caro, E., Crippen, R., Duren, R., Hensley, S., Kobrick, M., Paller, M., Rodriguez, E. & Roth, L. 2007. The shuttle radar topography mission. *Reviews of geophysics,* 45**,** 1-33.

Ferretti, Fumagalli, A., Novali, F., Prati, C., Rocca, F. & Rucci, A. 2011. A new algorithm for processing interferometric data-stacks: SqueeSAR. *IEEE Transactions on Geoscience and Remote Sensing,,* 49**,** 3460-3470.

Ferretti, Prati, C. & Rocca, F. 2000. Nonlinear subsidence rate estimation using permanent scatterers in differential SAR interferometry. *Geoscience and Remote Sensing, IEEE transactions on,* 38**,** 2202-2212.

Ferretti, Prati, C. & Rocca, F. 2001. Permanent scatterers in SAR interferometry. *IEEE Transactions on Geoscience and Remote Sensing,,* 39**,** 8-20.

Fornaro, G., Pauciullo, A. & Serafino, F. 2009. Deformation monitoring over large areas with multipass differential SAR interferometry: a new approach based on the use of spatial differences. *International Journal of Remote Sensing,* 30**,** 1455-1478.

Gabriel, A. K. & Goldstein, R. M. 1988. Crossed orbit interferometry: theory and experimental results from SIR-B. *International Journal of Remote Sensing,* 9**,** 857-872.

Gabriel, A. K., Goldstein, R. M. & Zebker, H. A. 1989. Mapping small elevation changes over large areas: differential radar interferometry. *Journal of Geophysical Research: Solid Earth (1978–2012),* 94**,** 9183-9191.

Gama, F. F., Cantone, A., Santos, A. R., Pasquali, P., Paradella, W. R., Mura, J. C. & Silva, G. G. Monitoring subsidence of waste piles and infrastructures of active open PIT iron mine in the Brazilian Amazon Region using SBAS interferometric technique and TerraSAR-X data. 2015 IEEE International Geoscience and Remote Sensing Symposium (IGARSS, 2015), 2015. Milan, Italy, 282-285.

Gao, M., Gong, H., Chen, B., Zhou, C., Chen, W., Liang, Y., Shi, M. & Si, Y. 2016. InSAR time-series investigation of long-term ground displacement at Beijing Capital International Airport, China. *Tectonophysics,* 691**,** 271-281.

Ge, L., Chang, H.-C. & Rizos, C. 2007. Mine subsidence monitoring using multi-source satellite SAR images. *Photogrammetric Engineering & Remote Sensing,* 73**,** 259-266.

Ge, L., Chang, H.-C., Rizos, C. & Omura, M. Mine subsidence monitoring: a comparison among Envisat, ERS, and JERS-1. Proceedings of 2004 ENVISAT Symposium, Salzburg, Austria, 2004. 6-10.

Ge, L., Han, S. & Rizos, C. 2000. Interpolation of GPS results incorporating geophysical and InSAR information. *Earth Planets and Space,* 52**,** 999-1002.

Ge, L., Ng, A. H.-M., Li, X., Abidin, H. Z. & Gumilar, I. 2014. Land subsidence characteristics of Bandung Basin as revealed by ENVISAT ASAR and ALOS PALSAR interferometry. *Remote Sensing of Environment,* 154**,** 46-60.

Ge, L., Rizos, C., Han, S. & Zebker, H. Mining subsidence monitoring using the combined InSAR and GPS approach. Proceedings of the 10th International Symposium on Deformation Measurements, 2001. 1-10.

Ge, L., Zhang, K., Ng, A., Dong, Y., Chang, H.-c. & Rizos, C. 2008. Preliminary Results of Satellite Radar Differential Interferometry for the Co-seismic Deformation of the 12 May 2008 Ms8.0 Wenchuan Earthquake. *Geographic Information Sciences,* 14**,** 12-19.

Goodman, J. W. 1976. Some fundamental properties of speckle. *JOSA,* 66**,** 1145-1150.

Graham, L. C. 1974. Synthetic interferometer radar for topographic mapping. *Proceedings of the IEEE,* 62**,** 763-768.

Gray, A., Mattar, K., Vachon, P., Bindschadler, R., Jezek, K., Forster, R. & Crawford, J. InSAR results from the RADARSAT Antarctic Mapping Mission data: estimation of glacier motion using a simple registration procedure. Geoscience and Remote Sensing Symposium Proceedings, 1998. IGARSS'98. 1998 IEEE International, 1998. IEEE, 1638-1640.

GreenToGoFuel 2015. Coal to Liquids.

Grigg, K. M. & Katzenstein, K. W. Using Insar And Groundwater Pumping Data To Model Land Subsidence From Coalbed Methane Production In The Powder River Basin, Wyoming. 2013 GSA Annual Meeting in Denver, 2013.

Guardian. 2015. *China's water diversion project starts to flow to Beijing* [Online]. Available: https://www.theguardian.com/world/2014/dec/12/china-water-diversion-project-beijing-displaced-farmers [Accessed 23 February 2017].

Guardian. 2016. *Beijing has fallen: China's capital sinking by 11cm a year, satellite study warns* [Online]. Available: https://www.theguardian.com/world/2016/jun/24/beijing-has-fallen-chinas-

capital-sinking-by-11cm-a-year-satellite-study-warns [Accessed 23 February 2017].
Guo, J., Zhou, L., Yao, C. & Hu, J. 2016. Surface Subsidence Analysis by Multi-Temporal InSAR and GRACE: A Case Study in Beijing. *Sensors,* 16**,** 1495.
Hanssen, R. F. 2001. *Radar interferometry: data interpretation and error analysis*, Springer Science & Business Media.
Hensley, S., Zebker, H., Jones, C., Michel, T., Muellerschoen, R. & Chapman, B. First deformation results using the NASA/JPL UAVSAR instrument. Synthetic Aperture Radar, 2009. APSAR 2009. 2nd Asian-Pacific Conference on, 26-30 Oct. 2009 2009. 1051-1055.
Hooper, A. 2008. A multi‐temporal InSAR method incorporating both persistent scatterer and small baseline approaches. *Geophysical Research Letters,* 35**,** L16302.
Hooper, A., Bekaert, D., Spaans, K. & Arıkan, M. 2012. Recent advances in SAR interferometry time series analysis for measuring crustal deformation. *Tectonophysics,* 514**,** 1-13.
Hooper, A., Zebker, H., Segall, P. & Kampes, B. 2004. A new method for measuring deformation on volcanoes and other natural terrains using InSAR persistent scatterers. *Geophysical research letters,* 31**,** L23611.
Hooper, A. J. 2006. *Persistent scatter radar interferometry for crustal deformation studies and modeling of volcanic deformation*.
Hou, G., Liang, Y., SU, X., Zhao, Z., Tao, Z., Yin, L., Yang, Y. & Wang, X. 2008. Groundwater systems and resources in the Ordos Basin, China. *Acta Geologica Sinica (English Edition),* 82**,** 1061-1069.
Hu, Z., Ge, L., Li, X., Zhang, K., NG, A. H.-M. & Rizos, C. 2009. ALOS PALSAR Observation of Kilauea Volcano activities from 2006 to 2009. *in International Conference on Geo-spatial Solutions for Emergency Management & 50th Anniversary of the Founding of the Chinese Academy of Surveying & Mapping.* Beijing, China.
Hu, Z., Ge, L., Li, X., Zhang, K. & Zhang, L. 2013. An Underground-Mining Detection System Based on DInSAR. *IEEE Transactions on Geoscience and Remote Sensing,* 51**,** 615-625.
Huber, P. J. 1964. Robust estimation of a location parameter. *The Annals of Mathematical Statistics,* 35**,** 73-101.
IESC. 2014. *Subsidence from coal seam gas extraction* [Online]. Available: http://www.iesc.environment.gov.au/publications/subsidence-coal-seam-gas-extraction [Accessed April 4 2017].
Jolivet, R., Agram, P. S., Lin, N. Y., Simons, M., Doin, M. P., Peltzer, G. & Li, Z. 2014. Improving InSAR geodesy using global atmospheric models. *Journal of Geophysical Research: Solid Earth,* 119**,** 2324-2341.
Jolivet, R., Grandin, R., Lasserre, C., Doin, M. P. & Peltzer, G. 2011. Systematic InSAR tropospheric phase delay corrections from global meteorological reanalysis data. *Geophysical Research Letters,* 38**,** L17311.
Joughin, I., Abdalati, W. & Fahnestock, M. 2004. Large fluctuations in speed on Greenland's Jakobshavn Isbrae glacier. *Nature,* 432**,** 608-610.
JPL. 2016a. *Grace Space Twins Set to Team Up to Track Earth's Water and Gravity* [Online]. Available: http://www.jpl.nasa.gov/news/news.php?release=2002-0174 [Accessed February 22 2016].

JPL. 2016b. *Monthly Mass Grids* [Online]. Available: http://grace.jpl.nasa.gov/data/get-data/monthly-mass-grids-land/ [Accessed Feburary 22 2016].

Kampes, B. M. 2006. *Radar interferometry: persistent scatterer technique,* Dordrecht, Netherlands, Springer, 211pp.

Kampes, B. M. & Hanssen, R. F. 2004a. Ambiguity resolution for permanent scatterer interferometry. *IEEE Transactions on Geoscience and Remote Sensing,* 42**,** 2446-2453.

Kampes, B. M. & Hanssen, R. F. 2004b. Ambiguity resolution for permanent scatterer interferometry. *Geoscience and Remote Sensing, IEEE Transactions on,* 42**,** 2446-2453.

Kuehn, F., Albiol, D., Cooksley, G., Duro, J., Granda, J., Haas, S., Hoffmann-Rothe, A. & Murdohardono, D. 2010. Detection of land subsidence in Semarang, Indonesia, using stable points network (SPN) technique. *Environmental Earth Sciences,* 60**,** 909-921.

Lanari, R., Casu, F., Manzo, M., Zeni, G., Berardino, P., Manunta, M. & Pepe, A. 2007. An overview of the small baseline subset algorithm: A DInSAR technique for surface deformation analysis. *Pure and Applied Geophysics,* 164**,** 637-661.

Lanari, R., Lundgren, P. & Sansosti, E. 1998. Dynamic deformation of Etna volcano observed by satellite radar interferometry. *Geophysical Research Letters,* 25**,** 1541-1544.

Lanari, R., Mora, O., Manunta, M., Mallorquí, J. J., Berardino, P. & Sansosti, E. 2004. A small-baseline approach for investigating deformations on full-resolution differential SAR interferograms. *Geoscience and Remote Sensing, IEEE Transactions on,* 42**,** 1377-1386.

Li, F. K. & Goldstein, R. M. 1990. Studies of multibaseline spaceborne interferometric synthetic aperture radars. *Geoscience and Remote Sensing, IEEE Transactions on,* 28**,** 88-97.

Li, G. & Zhang, H. 2013. The origin mechanism of coalbed methane in the eastern edge of Ordos Basin. *Science China Earth Sciences,* 56**,** 1701-1706.

Li, Y., Tang, D., Xu, H., Elsworth, D. & Meng, Y. 2015. Geological and hydrological controls on water coproduced with coalbed methane in Liulin, eastern Ordos basin, China. *AAPG Bulletin,* 99**,** 207-229.

Li, Z., Ding, X., Huang, C., Wadge, G. & Zheng, D. 2006a. Modeling of atmospheric effects on InSAR measurements by incorporating terrain elevation information. *Journal of Atmospheric and Solar-Terrestrial Physics,* 68**,** 1189-1194.

Li, Z., Ding, X., Huang, C., Zou, Z. & Chen, Y. 2007. Atmospheric effects on repeat-pass InSAR measurements over Shanghai region. *Journal of atmospheric and solar-terrestrial physics,* 69**,** 1344-1356.

Li, Z., Fielding, E. J. & Cross, P. 2009. Integration of InSAR time-series analysis and water-vapor correction for mapping postseismic motion after the 2003 Bam (Iran) earthquake. *Geoscience and Remote Sensing, IEEE Transactions on,* 47**,** 3220-3230.

Li, Z., Fielding, E. J., Cross, P. & Muller, J. P. 2006b. Interferometric synthetic aperture radar atmospheric correction: GPS topography ‐ dependent turbulence model. *Journal of Geophysical Research: Solid Earth (1978–2012),* 111.

Li, Z., Muller, J. P., Cross, P., Albert, P., Fischer, J. & Bennartz, R. 2006c. Assessment of the potential of MERIS near‐infrared water vapour products to correct ASAR interferometric measurements. *International Journal of Remote Sensing,* 27**,** 349-365.

Lindsey, H. 2014. *UC Berkeley System Gave Early Warning of South Napa Earthquake* [Online]. Available: http://blogs.kqed.org/science/2014/08/24/uc-berkeley-early-warning-system-predicted-south-napa-earthquake/.

Liu, G., Buckley, S. M., Ding, X., Chen, Q. & Luo, X. 2009a. Estimating spatiotemporal ground deformation with improved permanent-scatterer radar interferometry. *Geoscience and Remote Sensing, IEEE Transactions on,* 47**,** 2762-2772.

Liu, Y., McCabe, M., Evans, J., Van Dijk, A., De Jeu, R. & Su, H. Comparison of soil moisture in GLDAS model simulations and satellite observations over the Murray Darling Basin. Proceedings of the International Congress on Modelling and Simulation, 2009b.

Liu, Z., Jung, H.-S. & Lu, Z. 2014. Joint Correction of Ionosphere Noise and Orbital Error in L-Band SAR Interferometry of Interseismic Deformation in Southern California.

Lu, Z. & Dzurisin, D. 2014. InSAR imaging of Aleutian volcanoes. *InSAR Imaging of Aleutian Volcanoes.* Springer.

Mannucci, A., Wilson, B., Yuan, D., Ho, C., Lindqwister, U. & Runge, T. 1998. A global mapping technique for GPS-derived ionospheric total electron content measurements. *Radio science,* 33**,** 565-582.

Massonnet, D., Feigl, K., Rossi, M. & Adragna, F. 1994. Radar interferometric mapping of deformation in the year after the Landers earthquake. *Nature,* 369**,** 227-230.

Massonnet, D. & Feigl, K. L. 1998. Radar interferometry and its application to changes in the Earth's surface. *Reviews of geophysics,* 36**,** 441-500.

Massonnet, D., Rossi, M., Carmona, C., Adragna, F., Peltzer, G., Feigl, K. & Rabaute, T. 1993. The displacement field of the Landers earthquake mapped by radar interferometry. *Nature,* 364**,** 138-142.

Massonnet, D., Thatcher, W. & Vadon, H. 1996. Detection of postseismic fault-zone collapse following the Landers earthquake. Nature**,** 612-616.

Mathew, J., Majumdar, R. & Vinod Kumar, K. 2014. Estimating the atmospheric phase delay for quantifying co-seismic deformation using repeat pass Differential SAR Interferometry: Observations from 20th April 2013 Lushan (China) Earthquake. *ISPRS-International Archives of the Photogrammetry, Remote Sensing and Spatial Information Sciences,* 1**,** 57-64.

Meng, Y., Tang, D., Xu, H., Li, C., Li, L. & Meng, S. 2014. Geological controls and coalbed methane production potential evaluation: A case study in Liulin area, eastern Ordos Basin, China. *Journal of Natural Gas Science and Engineering,* 21**,** 95-111.

Mora, O., Mallorqui, J. J. & Broquetas, A. 2003. Linear and nonlinear terrain deformation maps from a reduced set of interferometric SAR images. *IEEE Transactions on Geoscience and Remote Sensing,* , 41**,** 2243-2253.

Moreira, A., Prats-Iraola, P., Younis, M., Krieger, G., Hajnsek, I. & Papathanassiou, K. P. 2013. A tutorial on synthetic aperture radar. *Geoscience and Remote Sensing Magazine, IEEE,* 1**,** 6-43.

Murray, D. K. 1996. Coalbed methane in the USA: analogues for worldwide development. *Geological Society, London, Special Publications,* 109**,** 1-12.
Navarro-Sanchez, V. D. & Lopez-Sanchez, J. M. 2014. Spatial adaptive speckle filtering driven by temporal polarimetric statistics and its application to PSI. *Geoscience and Remote Sensing, IEEE Transactions on,* 52**,** 4548-4557.
Navarro-Sanchez, V. D., Lopez-Sanchez, J. M. & Vicente-Guijalba, F. 2010. A Contribution of Polarimetry to Satellite Differential SAR Interferometry: Increasing the Number of Pixel Candidates. *Geoscience and Remote Sensing Letters, IEEE,* 7**,** 276-280.
NBSC. 2017a. *Beijing population statistics* [Online]. Available: http://www.stats.gov.cn/ [Accessed March 3 2017].
NBSC. 2017b. *Per capita living space* [Online]. Available: http://wenku.baidu.com/link?url=J67FycNDtpU2OPPGIM1oZn2gW4aaxVUD7jtsdpnAbQrfnI471NYlrqVwrvLClVum-JbSL4CqU271uzl6Fx9hYJhe2FSBSutDFX9YcIrQIJm [Accessed March 3 2017].
Ng, A. H.-M. 2010. *Advanced satellite radar interferometry for ground surface displacement detection.* PhD Thesis, The University of New South Wales, Sydeny. 244pp.
Ng, A. H.-M., Chang, H.-C., Ge, L., Rizos, C. & Omura, M. 2009. Assessment of radar interferometry performance for ground subsidence monitoring due to underground mining. *Earth, planets and space,* 61**,** 733-745.
Ng, A. H.-M., Ge, L., Du, Z., Wang, S. & Ma, C. 2017. Satellite radar interferometry for monitoring subsidence induced by longwall mining activity using Radarsat-2, Sentinel-1 and ALOS-2 data. *International Journal of Applied Earth Observation and Geoinformation,* 61**,** 92-103.
Ng, A. H.-M., Ge, L. & Li, X. 2014. Assessments of land subsidence in the Gippsland Basin of Australia using ALOS PALSAR data. *Remote Sensing of Environment,* 159**,** 86-101.
Ng, A. H.-M., Ge, L., Li, X., Abidin, H. Z., Andreas, H. & Zhang, K. 2012a. Mapping land subsidence in Jakarta, Indonesia using persistent scatterer interferometry (PSI) technique with ALOS PALSAR. *International Journal of Applied Earth Observation and Geoinformation,* 18**,** 232-242.
Ng, A. H.-M., Ge, L., Li, X. & Zhang, K. 2012b. Monitoring ground deformation in Beijing, China with persistent scatterer SAR interferometry. *Journal of Geodesy,* 86**,** 375-392.
Ng, A. H.-M., Ge, L., Yan, Y., Li, X., Chang, H.-C., Zhang, K. & Rizos, C. 2010. Mapping accumulated mine subsidence using small stack of SAR differential interferograms in the Southern coalfield of New South Wales, Australia. *Engineering Geology,* 115**,** 1-15.
Ng, A. H.-M., Ge, L., Zhang, K., Chang, H.-C., Li, X., Rizos, C. & Omura, M. 2011. Deformation mapping in three dimensions for underground mining using InSAR–Southern highland coalfield in New South Wales, Australia. *International journal of remote sensing,* 32**,** 7227-7256.
O'Sullivan, D. & Unwin, D. 2014. *Geographic information analysis,* John Wiley & Sons, 436pp.
Onn, F. & Zebker, H. 2006. Correction for interferometric synthetic aperture radar atmospheric phase artifacts using time series of zenith wet delay observations

from a GPS network. *Journal of Geophysical Research: Solid Earth (1978–2012),* 111.

Palmer, I. 2010. Coalbed methane completions: a world view. *International Journal of Coal Geology,* 82**,** 184-195.

Parizzi, A. & Brcic, R. 2011. Adaptive InSAR stack multilooking exploiting amplitude statistics: A comparison between different techniques and practical results. *Geoscience and Remote Sensing Letters, IEEE,* 8**,** 441-445.

Pipia, L., Fabregas, X., Aguasca, A., Lopez-Martinez, C., Duque, S., Mallorqui, J. J. & Marturia, J. 2009. Polarimetric differential SAR interferometry: First results with ground-based measurements. *Geoscience and Remote Sensing Letters, IEEE,* 6**,** 167-171.

Richey, A. S., Thomas, B. F., Lo, M. H., Reager, J. T., Famiglietti, J. S., Voss, K., Swenson, S. & Rodell, M. 2015. Quantifying renewable groundwater stress with GRACE. *Water resources research,* 51**,** 5217-5238.

Rienecker, M. M., Suarez, M. J., Gelaro, R., Todling, R., Bacmeister, J., Liu, E., Bosilovich, M. G., Schubert, S. D., Takacs, L. & Kim, G.-K. 2011. MERRA: NASA's modern-era retrospective analysis for research and applications. *Journal of Climate,* 24**,** 3624-3648.

Rodell, M., Chen, J., Kato, H., Famiglietti, J. S., Nigro, J. & Wilson, C. R. 2007. Estimating groundwater storage changes in the Mississippi River basin (USA) using GRACE. *Hydrogeology Journal,* 15**,** 159-166.

Rodell, M., Velicogna, I. & Famiglietti, J. S. 2009. Satellite-based estimates of groundwater depletion in India. *Nature,* 460**,** 999-1002.

Rodriguez, E. & Martin, J. M. 1992. Theory and design of interferometric synthetic aperture radars. *Radar and Signal Processing, IEE Proceedings F,* 139**,** 147-159.

Rosen, P. A., Hensley, S., Joughin, I. R., Fuk, K. L., Madsen, S. N., Rodriguez, E. & Goldstein, R. M. 2000. Synthetic aperture radar interferometry. *Proceedings of the IEEE,* 88**,** 333-382.

Rosen, P. A., Hensley, S., Zebker, H. A., Webb, F. H. & Fielding, E. J. 1996. Surface deformation and coherence measurements of Kilauea Volcano, Hawaii, from SIR‐C radar interferometry. *Journal of Geophysical Research: Planets,* 101**,** 23109-23125.

Sakumura, C., Bettadpur, S. & Bruinsma, S. 2014. Ensemble prediction and intercomparison analysis of GRACE time‐variable gravity field models. *Geophysical Research Letters,* 41**,** 1389-1397.

Sandwell, D., Mellors, R., Tong, X., Wei, M. & Wessel, P. 2011. Gmtsar: An insar processing system based on generic mapping tools. *Scripps Institution of Oceanography*.

Sandwell, D. T., Myer, D., Mellors, R., Shimada, M., Brooks, B. & Foster, J. 2008. Accuracy and resolution of ALOS interferometry: Vector deformation maps of the Father's Day intrusion at Kilauea. *IEEE Transactions on Geoscience and Remote Sensing,* 46**,** 3524-3534.

Sandwell, D. T. & Price, E. J. 1998. Phase gradient approach to stacking interferograms. *Journal of Geophysical Research: Solid Earth (1978–2012),* 103**,** 30183-30204.

Shanker, P. & Zebker, H. 2007. Persistent scatterer selection using maximum likelihood estimation. *Geophysical Research Letters,* 34.

Shenhua. 2013. *Shenhua's water grab* [Online]. Available: http://www.greenpeace.org/eastasia/Global/eastasia/publications/reports/climate-energy/2013/Thirsty%20Coal%202.pdf [Accessed February 24 2016].

Smith, E. K. & Weintraub, S. 1953. The Constants in the Equation for Atmospheric Refractive Index at Radio Frequencies. *Proceedings of the IRE,* 41**,** 1035-1037.

Sowter, A., Bateson, L., Strange, P., Ambrose, K. & Syafiudin, M. F. 2013. DInSAR estimation of land motion using intermittent coherence with application to the South Derbyshire and Leicestershire coalfields. *Remote Sensing Letters,* 4**,** 979-987.

Stein, M. L. 2012. *Interpolation of spatial data: some theory for kriging*, Springer Science & Business Media.

Su, X., Lin, X., Liu, S., Zhao, M. & Song, Y. 2005. Geology of coalbed methane reservoirs in the Southeast Qinshui Basin of China. *International Journal of Coal Geology,* 62**,** 197-210.

Su, X., Zhang, L. & Zhang, R. 2003. The abnormal pressure regime of the Pennsylvanian No. 8 coalbed methane reservoir in Liulin–Wupu district, eastern Ordos Basin, China. *International Journal of Coal Geology,* 53**,** 227-239.

Suga, Y., Takeuchi, S., Oguro, Y., Chen, A., Ogawa, M., Konishi, T. & Yonezawa, C. 2001. Application of ERS-2/SAR data for the 1999 Taiwan earthquake. *Advances in Space Research,* 28**,** 155-163.

Swenson, S. & Wahr, J. 2002. Methods for inferring regional surface‐mass anomalies from Gravity Recovery and Climate Experiment (GRACE) measurements of time‐variable gravity. *Journal of Geophysical Research: Solid Earth,* 107.

Taylor, G. I. The spectrum of turbulence. Proceedings of the Royal Society of London A: Mathematical, Physical and Engineering Sciences, 1938. The Royal Society, 476-490.

Teunissen, P. J. 1995. The least-squares ambiguity decorrelation adjustment: a method for fast GPS integer ambiguity estimation. *Journal of geodesy,* 70**,** 65-82.

The Drum 2015. Declining groundwater is a big problem for Australia.

Tregoning, P., McClusky, S., Van Dijk, A., Crosbie, R. & Peña-Arancibia, J. 2012. Assessment of GRACE satellites for groundwater estimation in Australia. *National Water Commission, Canberra,* 82.

van Dijk, A., Renzullo, L., Wada, Y. & Tregoning, P. 2014. A global water cycle reanalysis (2003–2012) merging satellite gravimetry and altimetry observations with a hydrological multi-model ensemble.

Van Leijen, F. J. & Hanssen, R. F. Persistent scatterer density improvement using adaptive deformation models. Geoscience and Remote Sensing Symposium, 2007. IGARSS 2007. IEEE International, 2007. IEEE, 2102-2105.

Wang, H., Wright, T. J., Yu, Y., Lin, H., Jiang, L., Li, C. & Qiu, G. 2012. InSAR reveals coastal subsidence in the Pearl River Delta, China. *Geophysical Journal International,* 191**,** 1119-1128.

Yang, Y., Lerner, D., Barrett, M. & Tellam, J. 1999. Quantification of groundwater recharge in the city of Nottingham, UK. *Environmental Geology,* 38**,** 183-198.

Yearbook, I. M. S. 2012. GDP 2011 figure of Inner Mongolian divisions.

Zebker, H. A. & Goldstein, R. M. 1986. Topographic mapping from interferometric synthetic aperture radar observations. *Journal of Geophysical Research: Solid Earth (1978–2012),* 91**,** 4993-4999.
Zebker, H. A., Rosen, P. A., Goldstein, R. M., Gabriel, A. & Werner, C. L. 1994. On the derivation of coseismic displacement fields using differential radar interferometry: The Landers earthquake. *Journal of Geophysical Research: Solid Earth (1978–2012),* 99**,** 19617-19634.
Zebker, H. A., Rosen, P. A. & Hensley, S. 1997a. Atmospheric effects in interferometric synthetic aperture radar surface deformation and topographic maps. *Journal of Geophysical Research: Solid Earth (1978–2012),* 102**,** 7547-7563.
Zebker, H. A., Rosen, P. A. & Hensley, S. 1997b. Atmospheric effects in interferometric synthetic aperture radar surface deformation and topographic maps. *Journal of geophysical research: solid earth,* 102**,** 7547-7563.
Zhang, K., Ge, L., Li, X. & Ng, A. H.-M. 2013. Monitoring ground surface deformation over the North China Plain using coherent ALOS PALSAR differential interferograms. *Journal of Geodesy,* 87**,** 253-265.
Zhang, K., Ng, A.-M., Li, X., Chang, H.-C., Ge, L. & Rizos, C. A new approach to improve the accuracy of baseline estimation for spaceborne radar interferometry. Geoscience and Remote Sensing Symposium, 2009 IEEE International, IGARSS 2009, 2009. IEEE, V-162-V-165.
Zhang, K., Song, R., Wang, H., Wu, D. & Wang, H. 2016. Interferometric phase reconstruction using simplified coherence network. *ISPRS Journal of Photogrammetry and Remote Sensing,* 119**,** 1-9.
Zhang, L., Ding, X. & Lu, Z. 2011. Ground settlement monitoring based on temporarily coherent points between two SAR acquisitions. *ISPRS Journal of Photogrammetry and Remote Sensing,* 66**,** 146-152.
Zhang, S., Tang, S., Tang, D., Pan, Z. & Yang, F. 2010. The characteristics of coal reservoir pores and coal facies in Liulin district, Hedong coal field of China. *International Journal of Coal Geology,* 81**,** 117-127.
Zhao, C., Lu, Z. & Zhang, Q. 2013. Time-series deformation monitoring over mining regions with SAR intensity-based offset measurements. *Remote Sensing Letters,* 4**,** 436-445.
Zhao, X. & Jiang, X. 2015. *Coal mining: Most deadly job in China* [Online]. Available: http://www.chinadaily.com.cn/english/doc/2004-11/13/content_391242.htm [Accessed June 3 2015].